Low Power Compact Dual Mode Detectors for Nuclear Security Applications

David Matthew Alan Bennett

Submitted in fulfillment of the requirements for the
Degree of Doctor of Philosophy

Nuclear Physics Group
School of Physics and Astronomy
College of Science and Engineering
University of Glasgow

2026

Abstract

The transportation and use of illicit Special Nuclear Material is a challenge that must be addressed in an increasingly nuclear world. To this end, different monitoring techniques of key nuclear signatures, such as neutron and gamma radiation, are being investigated to improve the likelihood of the detection of this material.

This thesis details the work undertaken to achieve the goal of creating a low power and sturdy detector solution that can be used for longer term passive monitoring or active field interrogation. This is possible using dual (or even triple) mode detectors, which are detectors that can use pulse shape discrimination (PSD), to separate gamma and neutron radiation species, using different timing characteristics that arise from each form of radiation. The detectors chosen for use in this investigation were the inorganic scintillation materials CLLBC and CLYC, and the organic scintillation materials EJ-276 and EJ-299-50.

Inorganic scintillators are primarily sensitive to gamma radiation and thermal neutrons, with these materials commonly having a high ^{6}Li enrichment, allowing for the thermal capture of these neutrons. Organic scintillators are sensitive to gamma radiation and fast neutrons, which have energies in excess of 1 MeV. The EJ-299-50 material alters slightly from these definitions, as whilst it is organic in nature, it also has a high enrichment of ^{6}Li, allowing it to act as a triple mode detector.

Both photomultiplier tubes (PMTs) and silicon photomultipliers (SiPMs) were used as photon detection technologies for recording scintillation photons throughout this investigation, with PMTs forming the significant majority due to operational difficulties with the available SiPMs. This was undertaken to evaluate the performance of each technology, as SiPMs are the natural choice for lower power performance. This is due to the lack of vacuum components and dynode chains required by a PMT, and a lower operating voltage of $\sim$40 V. This is a significantly lower voltage than the $\sim$2 kV required by a PMT. It was therefore necessary to determine the differences between each technology and how these would impact later designs.

Both digital and analogue processing methods were investigated, with digital methods expressed as discrete values processed using high speed digitisers, and analogue methods consisting of continuous voltage waveforms that would only be expressed digitally at a final output stage. The decision was made to attempt a comparative study, with the results recorded using digital

methods in combination with a PMT considered the benchmark. This was due to the greater signal stability presented by the PMT, whilst the SiPM and analogue methods presented more opportunities for noise or faults to enter the system. Unfortunately each of three SiPM arrays used at various points during this investigation failed for separate reasons, and it was not possible to take sufficient SiPM results to determine a clear comparison between the technologies.

Each detector material was investigated and characterised to determine which material would make for the most effective prototype. Key results such as the detector energy resolution and gamma efficiency were also calculated. For CLLBC, CLYC, EJ-276 and EJ-299-50 the energy resolution at 662 keV was determined as $5.6\% \pm 7.6 \times 10^{-3}\%$, $9.3\% \pm 0.04\%$, $20\% \pm 0.26\%$ and $22.2\% \pm 0.21\%$ respectively. The intrinsic gamma efficiency, also at 662 keV, was determined to be $17.6\% \pm 8.8\%$ and $13.6\% \pm 6.8\%$, for CLLBC and CLYC respectively. The use of a time-of-flight measurement allowed for the determination of neutron efficiency for the CLLBC, CLYC and EJ-276 materials, as EJ-299-50 was not available at the time of this measurement, with neutron efficiencies of $0.22\% \pm 0.05\%$, $0.31\% \pm 0.07\%$ and $0.53\% \pm 0.12\%$ determined respectively. This efficiency was calculated across the entire available neutron energy range which would affect each efficiency, due to the speciality of each material at detecting different neutron energies. The neutron efficiency of EJ-299-50 was unable to be calculated as there was not a characterised neutron source of known neutron emission rate available when this material was available, and as such would be an area of future interest.

The digital methods were used as a benchmark, with traditional figure-of-merit (FOM) analysis, which calculates the value of separation between the respective neutron energy regime and gamma species for each material, determining a FOM of 3.69 ± 0.029 for CLLBC, 1.82 ± 0.096 for EJ-276, 2.02 ± 0.025 for EJ-299-50 and 2.5 ± 0.1 for CLYC. However, the decision was made during this work to focus upon the analogue electronic methods, as it was believed the less intensive computing demands would decrease the power requirements, and allow for a better continuous passive interrogation prototype.

Electronic simulation results demonstrated that each of the chosen analogue PSD methods functioned as intended. These methods were the time-over-threshold method, which records the time a waveform is above a specified level, the zero-crossing method, which compares the time at which different waveforms cross a zero point, and the charge comparison method, which compares the amount of charge contained within predetermined time intervals. However due to manufacture delays and unforeseen noise contributions, the constructed prototypes did not produce results that matched the simulated outcomes. This meant that the current prototypes needed an additional round of redesign to prioritise noise suppression and signal amplification.

Overall, each of the available scintillation materials have been characterised to a greater extent which can be applied to later analogue PSD designs. This can be seen in combination with the

electronic simulations that demonstrate the efficacy of each method, meaning that the choice of detector material and analogue PSD method can be made based on the user requirements. The designed analogue solution in this case did not operate as intended, but each method showed great promise for future development and investigation of low power analogue PSD solutions.

Contents

List of Tables

List of Figures

Acknowledgements

There are many people I have worked with and met over the previous years who deserve thanks for their support, and so I apologise if I have missed anyone. Firstly I would like to thank my supervisors Dr. Bjoern Seitz and Dr. Frank Thomson, without their knowledge, insight and endless patience, this work would not have been possible. Their advice and technical support has been unrivalled, and have helped create a passion for research that I did not think I was capable of. I would like to thank our collaborators at AWE for their sponsorship, continual support, and overall guidance throughout this entire process, as well as the NuSec organisation for their support and funding throughout this PhD.

I would also like to thank Prof. Igor Jovanovic and his group at the University of Michigan, as well as Dr. Valentin Fondement, for welcoming me with open arms and allowing me to perform work there that was key to this research. The same thanks can be extended to Dr. Steven Dazeley and his colleagues at Lawrence Livermore National Laboratory, for making me feel at ease so quickly in the short time I was there, alongside the work that was extremely helpful to this PhD.

I would like to thank my fellow PhD students in the NHP group for making a very stressful final period of this work as relaxing as possible, mostly due to the many lunchtime card games. My 414 office mates, both past and present, also deserve thanks for making many frustrating hours in front of a computer far easier than they should have been. I would also like to thank the wider NHP group at Glasgow, it has been a tremendous pleasure to work within this group and it is something that I will always value.

I would like to thank Nonie, Shelagh and Erin for making me feel extremely welcome, and for making me feel at home when I was far away from mine, their kindness, jokes, love, excellent conversations (and wine) have always helped me to relax after too many long days in the lab. My family, who have played an enormous part in my academic life, including the kindness and wisdom of my Grandparents Jo and Pete, whose company never fails to brighten my day, and Cath and Alan, who are sorely missed, but whose impact upon my life will never be forgotten. To my Dad, I thank you for the many shared sports games and constant discussions of many varied topics that have inspired a lifelong curiosity. To my Mum, I thank you for always being there to support and listen, even if I still cause you stress to this day! To my brother, whose

passion for science inspired my own, and who continues to be an inspiration to me to this day, alongside my sister-in-law, nephew and niece, with whom I enjoy and savour every conversation and playtime, even if I was asked recently 'when is my Uncle leaving?'. And to my sister, who has been my closest confidant since we were teenagers, who has always been available for a rant, or to talk some sense into me, I cannot wait to welcome her and her partner back after their adventure.

And lastly, to my soon-to-be-wife Eilidh, without whose love and support none of this would have been possible. I owe you more than I could possibly explain in one paragraph but I'll try my best. You have helped me grow in such a profound way through your love, kindness and relentless passion for life, and you have helped me understand how to enjoy the little things, and to not fear the big things. Your energy is infectious, and has always made everything easier and brighter, even if I never get your leftover ramen anymore due to the ridiculous spice levels! This PhD has been one of the hardest things I've ever done, but I would do it again in a heartbeat if it meant doing it with you by my side again, although I'm certain you would be less than pleased if I suggested that and didn't finally get an adult job.

Declaration

I hereby declare that the composition of this thesis, along with the work contained and described within it are my own unless explicitly stated. Where input/results from others have been given or collaboration with others has been made this is stated or referenced appropriately throughout the thesis, and any images contained within have been granted permission to publish from the respective institutions. This work has not previously been submitted for any other degree to the University of Glasgow or any other institution.

David Matthew Alan Bennett

List of Common Abbreviations In Alphabetical Order

AI	Active Interrogation
ADC	Analog to Digital Converter
ASIC	Application Specific Integrated Circuit
APD	Avalanche Photodiode
BGA	Ball Grid Array
CLLBC	Caesium Lanthanum Lithium BromoChloride
CLYC	Caesium Lithium Yttrium Chloride
CFD	Constant Fraction Discriminator
CC	Charge Comparison
QDC	Charge to Digital Converter
CVL	Core Valence Luminescence
DAQ	Data Acquisition
DCR	Dark Count Rate
DDL	Double Delay Line
DPP	Digital Pulse Processing
FPGA	Field Programmable Gate Array
FOM	Figure of Merit
FWHM	Full Width Half Maximum
GBWP	Gain-Bandwidth Product
GEE	Gamma Equivalent Energy
HDPE	High Density Polyethylene
IAEA	International Atomic Energy Agency
IC	Integrated Circuit
MOSFET	Metal-Oxide-Semiconductor Field-Effect-Transistor

μC	Microcontroller
NORM	Naturally Occurring Radioactive Material
Op-amp	Operational Amplifier
OV	Overvoltage
PI	Passive Interrogation
PMT	Photomultiplier Tube
PDE	Photon Detection Efficiency
PVT	Polyvinyl Toluene
PCB	Printed Circuit Board
PSD	Pulse Shape Discrimination
QE	Quantum Efficiency
SCA	Single Channel Analyser
SiPM	Silicon Photomultiplier
SPAD	Single-Photon Avalanche Diode
SNR	Signal-To-Noise Ratio
SNM	Special Nuclear Material
SMD	Surface Mounted Device
TDC	Time to Digital Converter
TIA	Transimpedance Amplifier
TOF	Time-of-Flight
ToT	Time-over-Threshold
ZC	Zero Crossing

Chapter 1

Introduction

The proliferation of Special Nuclear Material (SNM) is an important risk facing the modern world, and as such its detection is a priority. The International Atomic Energy Agency (IAEA) was founded in 1957 in the wake of the international concern created by the increasingly nuclear outlook of major powers, and detecting and reducing the risk of nuclear material is one of the three main missions of the IAEA, with the other two being that of peaceful nuclear energy and nuclear safety.

It is necessary to be able to detect and characterise distinctive signatures, such as neutron or gamma radiation, that SNMs emit to prevent danger to human life, as many states or groups could cause harm if they possessed SNM [1][2]. There have been a number of nuclear material incidents in recent years alongside well categorised historical events, demonstrating that this is an issue that presents many challenges [3][4]. This is a pressing matter, especially as the world moves towards an increasingly nuclear future in order to meet the many varied challenges of a changing climate [5][6][7].

In order to understand what makes SNM unique, it is important to describe naturally occurring radioactive material (NORM). NORM consists of the radioactive isotopes present and are unavoidable throughout daily life, including those found in food or certain geological materials, as well as cosmic radiation [8]. This form of radiation exposure is unavoidable, with exposure rates varying due to many factors, such as altitude or occupation [9]. This is shown in figure 1.1, with the contributions in background radiation to US populations.

It is therefore important to understand that this work is not designed to investigate and determine civilian exposure to NORM, but to investigate and locate potentially harmful sources of anthropogenic (man-made) radiation that could be harmful to said civilians.

There are two forms of interrogation that can be undertaken to locate and evaluate SNM. The first is active interrogation (AI), which interacts with the material under investigation, causing it

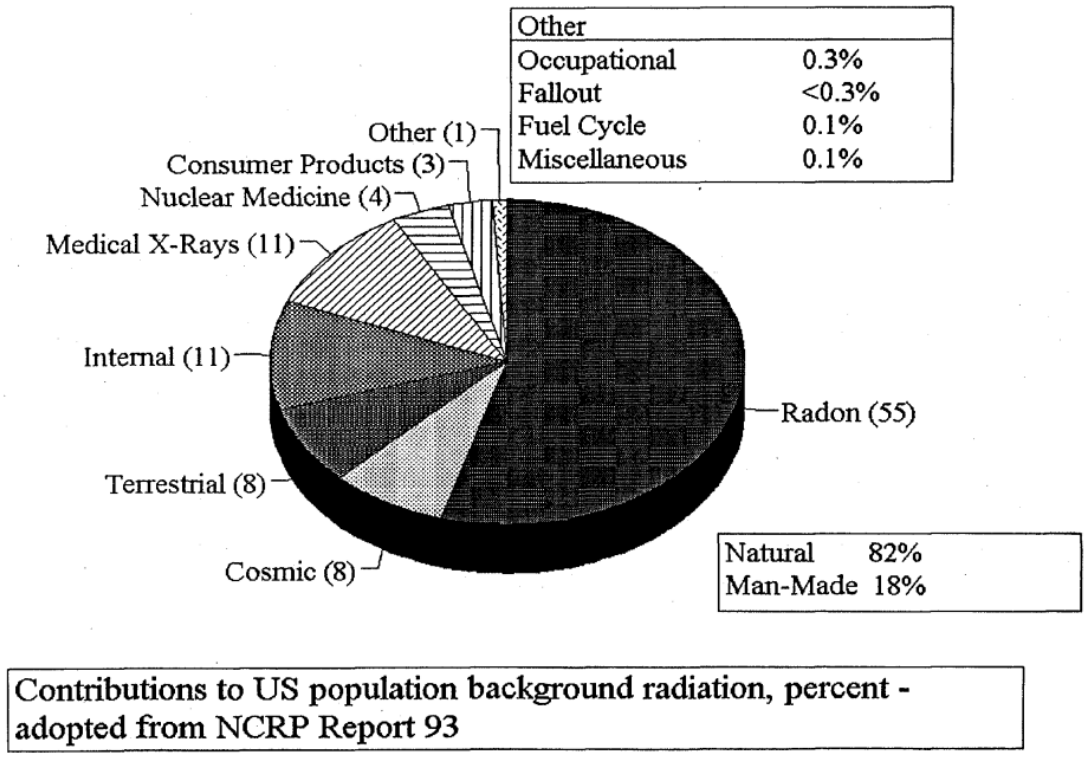

Figure 1.1: An illustration of the common background radiation contributions that affect the US population, further illustrating the inescapable nature of NORM exposure, adapted from [8].

to emit detectable particles. This is seen in techniques such as neutron activation which can be used to locate explosive material [10]. This is being pursued as one of the key methods to locate SNM and to separate it from the NORM present in the environment [11].

The work performed throughout this investigation is more accurately described as passive interrogation (PI), as it does not actively influence the materials under investigation through techniques like neutron activation, but rather it aims to detect the signatures naturally given off by SNM. The signatures of interest in this case are gamma radiation (γ-rays) and neutrons. PI would be primarily employed in areas of high transit, be that of personal or goods in a location such as a train station, with the intention of processing input signals for any sign of SNM or any other potentially harmful ionising radiation.

It is then important to be able to quantify any future detector's performance, with a common industry standard being the sensitivity of a detector to record ^{252}Cf, more specifically the counts per second per nanogram (cps/ng) of ^{252}Cf at a distance of 2 metres [12]. This performance metric is used for ^{3}He proportional counters, but may not be appropriate for a modern scintillation detector. This is because ^{3}He detectors have a very low γ-ray detection efficiency, and as such any event over threshold is of interest, whilst in a scintillation detector, events over threshold could be due to a γ-ray interaction, especially if a scintillation detector is

being used in an area with a high γ-ray background. Therefore performance metrics other than the detectability of a nanogram of ^{252}Cf are necessary to more accurately describe the performance of scintillation based detectors.

There are many different ways of describing detector performance, so it is important to introduce certain concepts. The first concept is the detector energy resolution, which is a measure of how effectively a detector can separate non-correlated events. The lower the percentage resolution, the greater the ability of the detection material to resolve events of different energies. For inorganic scintillation materials this value is typically between 3-10% [13]. However, for organic scintillation materials the energy resolution is often significantly worse due to the lower density and fluctuations in photon production, and there are also some difficulties in calibrating organic scintillators, but this will be discussed in more detail in chapter 3. For an organic scintillator, a resolution of 8-25% and above is common [14][15].

Detector efficiency is also determined to be a key factor in evaluating detector performance within the scope of this investigation, with two forms of efficiency considered important. The first is that of absolute efficiency, seen in equation 1.1:

$$\varepsilon_{abs} = \frac{Pulses\,Recorded}{Total\,Amount\,of\,Radiation\,Emitted\,by\,Source}. \tag{1.1}$$

In practical analysis terms, this is seen in the form of equation 1.2:

$$\varepsilon = \frac{Total\,Counts}{Live\,Time \times Emission\,Probability \times Source\,Activity}. \tag{1.2}$$

This value is often extremely small, as it compares the total source emission to the number of recorded events, meaning that a small detector geometry will only be able to capture a tiny fraction of the total emitted source radiation. In order to convert this value to a more useful form, the intrinsic efficiency is calculated. This takes the amount of radiation incident on the detector into account, and is defined in equation 1.3. This value more accurately describes the efficiency of a detection material, due to the dΩ term representing the solid angle of the detector as seen from the source position, which is defined in equation 1.4:

$$\varepsilon_{int} = \varepsilon_{abs} \times \frac{4\pi}{d\Omega}, \tag{1.3}$$

$$d\Omega = 2\pi(1 - \frac{d}{\sqrt{d^2 + a^2}}), \tag{1.4}$$

where d is the distance from source to detector and a is the area of the detection material.

Current neutron and gamma detection techniques often rely on a combination of a ^{3}He proportional counter for neutron detection, as it has a low γ-ray detection efficiency [16], and a plastic scintillator or inorganic scintillator for γ-ray detection [17]. It is important to move away from this as ^{3}He is a rare material with dwindling global supply [18], and is therefore an expensive option, so an alternative lower cost option must be developed.

It is possible for a single detector material to achieve what a combination of ^{3}He and plastic scintillator can achieve. This is performed by a dual mode detector, which can differentiate between neutron and gamma species in a waveform by using pulse shape discrimination (PSD). PSD is the ability of certain materials to generate different timing outputs, based on the incident radiation. This is because γ-ray's, fast neutrons and thermal neutrons have different timing outputs when interacting with scintillation materials, with an example of this seen in figure 1.2, greater detail on these processes can be found in chapter 2.5.

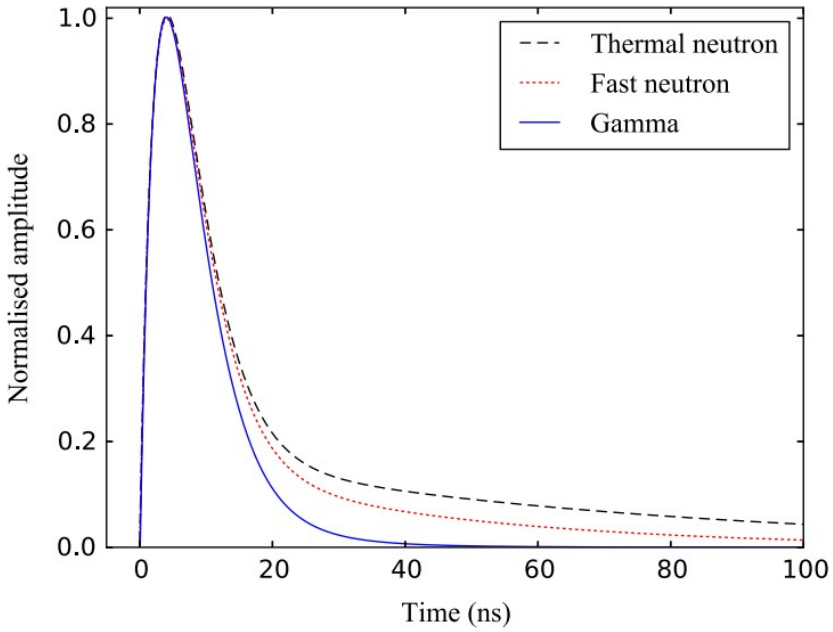

Figure 1.2: An illustration of the differences expected between γ-rays, fast and thermal neutrons in a ^{6}Li doped plastic scintillator, and their expected decay time profiles. The fastest decay is seen for γ-rays, a slower decay for fast neutrons and the slowest decay seen for thermal neutrons, an explanation for these differences can be found in chapter 2.3 [19].

The materials chosen to separate neutron and γ-ray species will have an effect on the detector output. Two detector materials have been chosen for primary investigation, the inorganic scintillator CLLBC ($Cs_2LiLa(Br_{4.8}Cl_{1.2})$:Ce) and the organic scintillator EJ-276 developed by Eljen Technology [20][21][22]. The primary differences in organic and inorganic scintillators,

and the reasons for these differences, can be found in chapter 2.3.

Two other scintillation materials have also been investigated to a lesser extent, with results being present in chapter 5. Another inorganic scintillator, CLYC (Cs_2LiYCl_6:Ce) [23], and the organic scintillator EJ-299-50, which has a similar light output to that of EJ-276, but is doped with ^{6}Li [24][25]. This means that it can act as a triple mode detector, which has the ability to not only separate γ-ray and neutron species, but it can separate between neutrons of different energies as well. The details of this can be found in chapter 2.2.1, and more specifically in table 2.3.

There are compromises to using either an organic or inorganic scintillator, but the primary benefit to using an inorganic scintillator is the higher density and light yield. For an organic scintillator the primary trade-off is the reduced light output, but with much faster decay times. A table of the properties of these materials can be seen in table 1.1, although the values for EJ-299-50 are best approximations from other studies, as this is a material still under development [24].

Table 1.1: The properties of the scintillation materials used throughout this investigation, with the material, light output, emission wavelength, material density and decays times all present. Further information regarding the properties of EJ-299-50 can be found in [24], CLLBC can be found in [26], EJ-276 in [27] and CLYC in [28].

Material	**Scintillation Efficiency (photons/MeV)**	**Emission Wavelength (nm)**	**Density (g/cm^3)**	**Decay Times (ns)**
CLLBC ($Cs_2LiLa(Br_{4.8}Cl_{1.2})$:Ce)	40×10^3	420	4.08	115, 500, 1500
EJ-276	8.6×10^3	425	1.099	13, 35, 270 (γ-ray excitation) and 13, 59, 460 (neutron excitation)
CLYC (Cs_2LiYCl_6:Ce)	20×10^3	370	3.31	1, 50, 1000
EJ-299-50	7×10^3	Unknown	1.095	6

Scintillation is the process of light emission when a highly charged particle is incident on a material, and has existed since it's discovery in the early 20th century. However, it is only with the invention of the photomultiplier tube (PMT) in the 1940's that it begins to become of serious interest [29]. This allowed for development to begin on both organic and inorganic scintillation over the coming years [30][31][32].

Plastic scintillators were proposed as far back as 1960 [33], although this could not be replicated at the time due to their instability, leading to the opinion that plastic scintillators

could not replicate the performance of organic liquid scintillators [34]. Plastic scintillators became of greater interest again in 2012, when it was proven that they could perform effective PSD separation [35], leading to much research and development of plastic scintillators over the following years, which can be seen in figure 1.3.

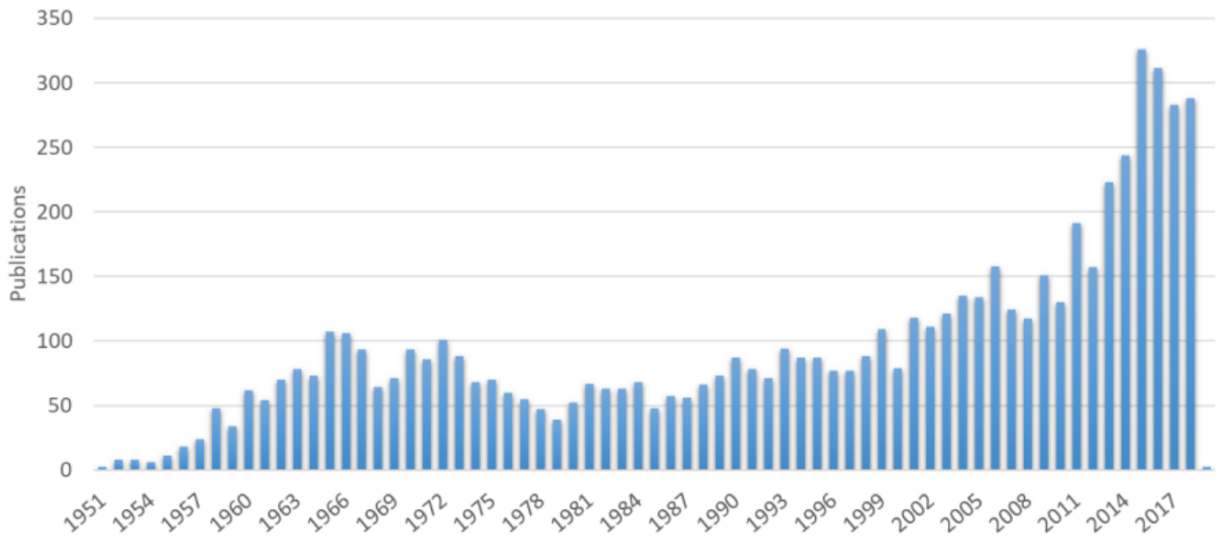

Figure 1.3: A chart demonstrating the number of publications referring to chemical modifications of plastic scintillators, with the increasing number of publications post 2012 seen due to renewed interest in plastic scintillators, adapted from [17].

The development of inorganic scintillators has also proceeded similarly to that of organic scintillation, with discoveries taking place throughout the decades following the 1940's. Many different scintillation materials were discovered, such as BGO in 1973 [36] or NaI(Ti) in 1949 [37], which remains a key inorganic scintillation material in current research, with these materials highlighting the first of the three phases of modern inorganic scintillator development. This first phase was discovery, which consisted of the development of crystal growing methods, as well as a greater understanding of the scintillation processes in inorganic materials. The second phase came when there was a greater need for inorganic scintillators in the medical and engineering fields, with the final phase currently being driven by the desire for high light yield scintillators in nuclear security and detection. This overall progress can be seen in figure 1.4.

Both inorganic and organic scintillation produce scintillation light through two processes, although these processes are different for each scintillator type. Each of these two processes have different timing characteristics, depending on whether a neutron or a γ-ray was incident on the scintillator, meaning that is possible to perform the aforementioned PSD. The full explanation of the reason for these timing differences can be found in chapters 2.3.1 and 2.3.2.

PSD as a concept is something that has been explored since the 1960's, with the most common

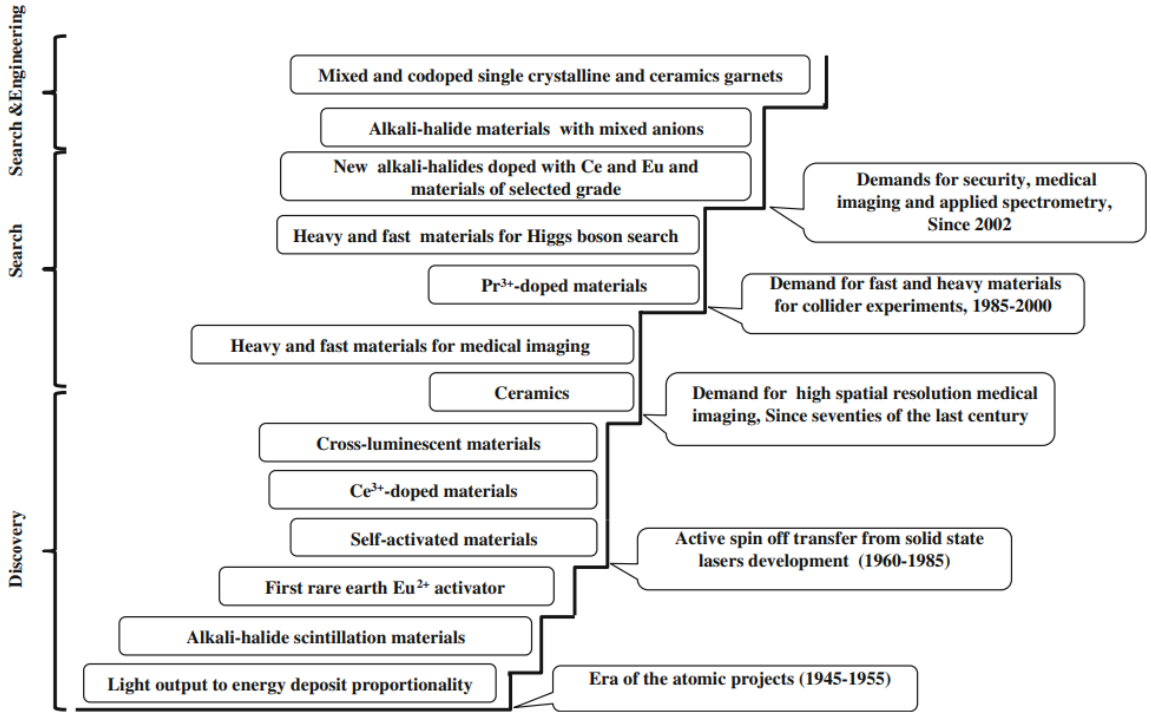

Figure 1.4: An illustration of the development of inorganic scintillators, with each of the three phases of development. This figure, as well as the information regarding the three phase history of inorganic scintillators was adapted from [38].

form of this time being that of a zero-crossing (ZC) detector, the theory of which will be given in chapter 2.5.3, and the operation of which will be given in chapter 4.1 [39]. This means that analogue PSD has been explored as a method to separate neutron and γ-ray signals for some time, and has shown promise [40]. In fact the analogue PSD comparison of inorganic and organic scintillation has occurred as far back as 1971 [41], with the first digital PSD methods being discussed in 1976 [42].

For the most part, comparisons of analogue and digital PSD methods have accelerated in recent years due to the availability of fast, high speed digitisers that can fully digitise a waveform [43][44]. This means that there is an interest within the field to investigate both analogue and digital solutions to PSD, with each option having its own benefits and drawbacks. The full details of this are discussed throughout chapter 4. The primary benefit of digital PSD is its real time display and ease of use. This is because in a digital scope, it is very easy to manipulate and alter the method of PSD being performed by editing a few commands or inputs. Analogue PSD must be done primarily in hardware, and so is affected by the components used and their drawbacks [43].

Whilst it may seem that digital PSD is superior due to its ease of use and flexibility, it still has its own drawbacks. Multichannel digital PSD requires the use of a field programmable gate array

(FPGA), or the development of an application specific integrated circuit (ASIC). An FPGA is an integrated circuit (IC), that can be programmed to serve a variety of needs, whilst an ASIC, as the name suggests, is an IC that has been developed with a specific use in mind. This means that FPGA's are often preferred to ASIC's, due to their greater flexibility of use and reduced cost. However, whilst being considerably more expensive to develop, an ASIC usually performs better than an FPGA, with an FPGA requiring a larger physical area, much more power, and will still run three times slower than an ASIC [45], although ASICs are often readout by FPGAs [46]. Due to the need for flexibility, modern digitisers will most commonly use FPGAs.

The need for these digital components mean that there is often a greater power requirement for digital PSD, as well as longer processing times. Before high speed digitisers were more readily available, the sampling speed of a digitiser could cause an analogue method to perform better than that of digital [43]. Although with the introduction of higher speed digitisers that can process 3 Gigasamples per second (GS/s) or more, this result has flipped and digital techniques using traditional figure-of-merit analysis can outperform analogue techniques by 10% or more, resulting in a better separation between species [44]. These drawbacks, the processing time and power requirement, as well as the cost of a high speed digitiser, mean that analogue techniques are still being investigated, despite the greater ease of digital methods. The reliance on the physical interactions between components in the analogue method mean that there are much lower power requirements but also less processing requirements, meaning that there are still benefits to using analogue PSD. However, analogue solutions are much harder to construct due to the many difficulties arising throughout the development process, including such issues as electrical component failure or poor design choices, meaning that despite the greater simplicity of analogue methods, the development issues result in digital methods being much more appealing.

Regardless of the digital/analogue PSD decision, it is necessary to convert the light output from the scintillator into a measurable electrical signal. The two primary ways to do this are to use either a PMT or a silicon photomultiplier (SiPM), both of which make use of the photoelectric effect. As previously mentioned, PMTs were originally developed between the 1930's and 1940's, with the specifics of their operation described in chapter 2.4.1. PMTs then became significant and almost ubiquitous in nuclear physics, with their high gain (order of 10^6) and lower room temperature noise (in comparison to SiPMs and other detectors of the time) making them a strong choice for pairing with scintillation materials. PMTs are usually contained within a vacuum tube in a glass housing, making them fragile, a major drawback of the PMT and a primary motivator of this research as described below. PMTs are also affected by magnetic fields, as they use accelerating dynodes for photoelectron multiplication, whereas magnetic fields do not impact SiPMs in the same way.

A SiPM is a solid state device focused on single photon avalanche diodes (SPADs) that can create self sustaining avalanches of photoelectrons from a single photon interaction (unless quenched). This is an oversimplification but greater detail will be given in chapter 2.4.2. SiPMs are much smaller than PMTs, with the SiPM used in this research being 4mm by 4mm, compared to the 2 inch diameter of the PMT used, an example of these can be seen in figures 3.1 and 3.4. They also require a much lower operating voltage, with PMTs requiring anywhere from 800 V to 2500 V but a SiPM requiring 30 to 60 V. These differences have resulted in the greater adoption of SiPMs in recent years, starting primarily in 2006, with SiPMs becoming more dominant in nuclear physics research in the following years [47]. However SiPMs have much greater dark counts at room temperature, with this dark count rate (DCR) being temperature dependent, which is the primary compromise in SiPM usage, as well as radiation damage over time that can also increase the DCR.

The fragile nature of PMTs, as well as the large power requirements, mean that they are not suited for long term PI. This is where a SiPM would be a much wiser choice, due to the lower power requirements, and as it is a solid state device, it is much studier than a PMT. When these benefits are combined with the lower power requirements and faster processing times of an analogue based PSD approach, it is believed that long term PI could be performed in areas of high goods and pedestrian traffic. The ideal criteria for an analogue SiPM detector are fast processing times, low power, compact and resistant to damage.

To investigate these criteria, it is important to understand the theory and operation of each scintillation material, from their interaction mechanisms and individual methods of scintillation photon production, to the electrical systems that allow for this photon detection and PSD processing, in both analogue and digital regimes. Once this is fully understood the method of investigation, alongside the data acquisition process, can be detailed, before the initial analogue design, simulation and manufacture processes can be understood. All of this will culminate in the comparison and evaluation of the current digital PSD methods to several novel analogue PSD designs, with the intention of determining if these analogue methods perform at a similar level to that of contemporary digital methods.

That is the primary motivator behind this research, a desire to create a low power, sturdy analogue based PSD detector, that can perform similarly to modern laboratory standard setups that use a PMT with a digital based PSD approach, but at a fraction of the power requirements with little to no performance reduction observed. This low power analogue approach, combined with a passive interrogation method, means that this detector prototype would be useful in an area of high transit, such as a train or bus station, and allow for fast real time evaluation of any SNM concerns. It was determined necessary to investigate both organic and inorganic scintillation materials for this reason, with each material form having benefits and

compromises that made them an intriguing option to achieve this final aim of a low power analogue PSD detector.

Chapter 2

Theory

In order to design and evaluate a novel detector prototype, it is important to understand the processes that allow for a scintillation detector to function. This includes the physical processes that allow for the detection of ionising radiation, as well as the photon detection technologies and the associated electronics that accompany them. As noted, the primary species of interest to this work are that of neutrons and γ-rays, with γ-rays being present to an extent in NORM backgrounds, and thus it is important to understand the detector principles that allow for the separation of these background and naturally occurring sources from radioactive sources of interest.

2.1 Charged Particle Interaction

Charged particles interact very differently to neutral particles as a result of their charged nature. It is important to understand these processes, as whilst this investigation is primarily interested in the detection of neutrons and γ-rays, these charged particles allow for their detection in each form of scintillation material. Therefore it is necessary to understand these differences and how they in turn affect neutron and γ-ray detection.

2.1.1 Heavy Charged Particles

Heavy charged particles, such as protons, lose energy primarily via inelastic Coulomb collisions, where the particle will interact with the electrons in the outer-most shell of the material and lose energy, gradually slowing down until it is stopped. When these heavy charged particles interact with the outermost electrons, the energy transferred can cause the electron to be excited to a higher energy state, or to be ionisied from the interacting medium. This allows the electron to interact with other materials in a similar manner to that of heavier charged particles. The energy loss per unit length is given by the Bethe-Bloch equation, seen in equation 2.1.

$$-\left\langle \frac{dE}{dx} \right\rangle = \frac{4\pi}{m_e c^2} \cdot \frac{nZ^2}{\beta^2} \cdot \left(\frac{e^2}{4\pi\varepsilon_0^2} \right)^2 \cdot \left[\ln\left(\frac{2m_e c^2 \beta^2}{I \cdot (1-\beta^2)} \right) - \beta^2 \right], \tag{2.1}$$

where m_e is the mass of the electron, c is the speed of light, Z is the atomic number of the material, β is the particle velocity, defined as $\beta = \frac{v}{c}$, with v being the speed of the particle, e is the electron charge, ε_0 is the vacuum permeability and I is the mean excitation potential, which varies by material. The remaining value n, is the electron density, which can be calculated using equation 2.2:

$$n = \frac{N_A Z \rho}{A m_u}, \tag{2.2}$$

where N_A is Avogadro's constant, A is the relative atomic mass and m_u is the molar mass constant [48]. As an interacting particle slows down, it will have a maximum energy deposition that is dependent on the material and the particle energy [49][50]. This can be seen in the Bragg curve in figure 2.1 [48].

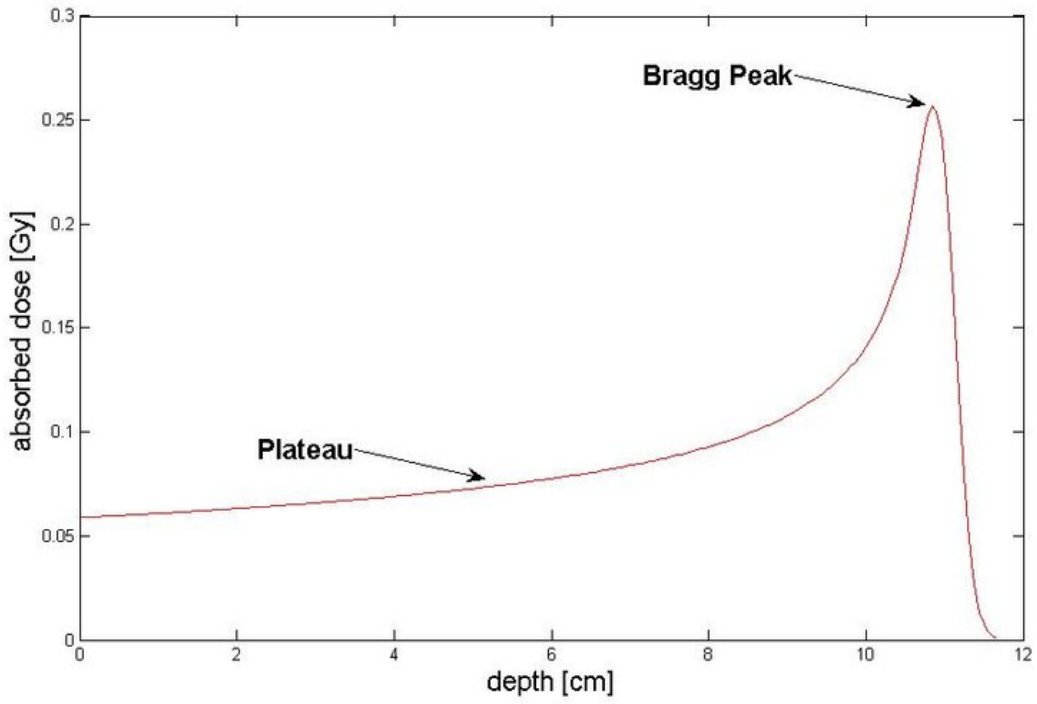

Figure 2.1: The absorbed dose, which is the specific energy deposited per unit mass, of a monoenergetic proton pencil beam in tissue as a function of the penetration depth, demonstrating that a charged particle has a characteristic radiation length, and does not deposit its full energy until it has interacted many times within the material, adapted from [51].

Scattering processes are not as significant for heavier particles due to their increased mass, meaning that these scattering processes occur over smaller angles during interactions with

atomic nuclei [52]. A summary table of the primary proton interaction processes can be seen in table 2.1.

Table 2.1: A table that highlights the primary interaction processes for protons, with v defined as the velocity of the proton. This table has been adapted from [53].

Interaction	Interaction Type	Target	Summary
Stopping	Inelastic	Atomic electrons	Frequent inelastic Coulomb interactions with electrons cause protons to continuously lose energy. The rate of energy loss increases dramatically towards the end of the range as the proton slows down (proportional to $1/v^2$).
Scattering	Elastic	Atomic nucleus	Protons passing close to a nucleus are repelled and scattered through small angles.
Nuclear Interactions	Inelastic	Atomic nucleus	If the proton has enough energy to enter the nucleus it causes an irreversible nuclear reaction. The nucleus then emits nucleons and/or ions.

2.1.2 Electrons

Electrons are charged, so they also interact through Coulomb interactions the same as protons. However, as electrons have a significantly smaller (approximately $\frac{1}{1836}$) mass than that of the proton, they scatter over greater angles [54]. This results in three electron interaction processes of interest to this investigation, these being excitation, ionisation and Bremsstrahlung.

Excitation is the process where an electron interacts with a particle, and is excited into a higher energy state. This electron then de-excites back to the ground state, emitting a photon of energy equivalent to the difference between the excited state and the ground state. Ionisation is the process whereupon an electron receives enough energy to be excited fully out of the shell, with

the initial atom then becoming an ion. This electron can then in turn cause further excitations or ionisations, depending on the emitted electron energy, with the vacancy left behind being filled by an outer electron or an Auger electron, which is a low energy electron that is emitted due to a higher energy electron filling a vacancy in a lower energy level [55].

The third and final interaction process of interest is Bremsstrahlung, which means 'braking radiation', and this occurs when an electron passes close enough to a nucleus for both Coulomb fields to interact, altering the electrons path and causing it to decelerate. A photon is emitted in this process which can be up to the kinetic energy of the incident electron. The energy of the electron determines which of these processes are dominant, with ionisation being the primary interaction process of 'slow' electrons, but after $\sim$50 MeV, Bremsstrahlung becomes the main interaction process. A summary of these 3 processes, can be seen in table 2.2, with the energy regions they become dominant seen in figure 2.2.

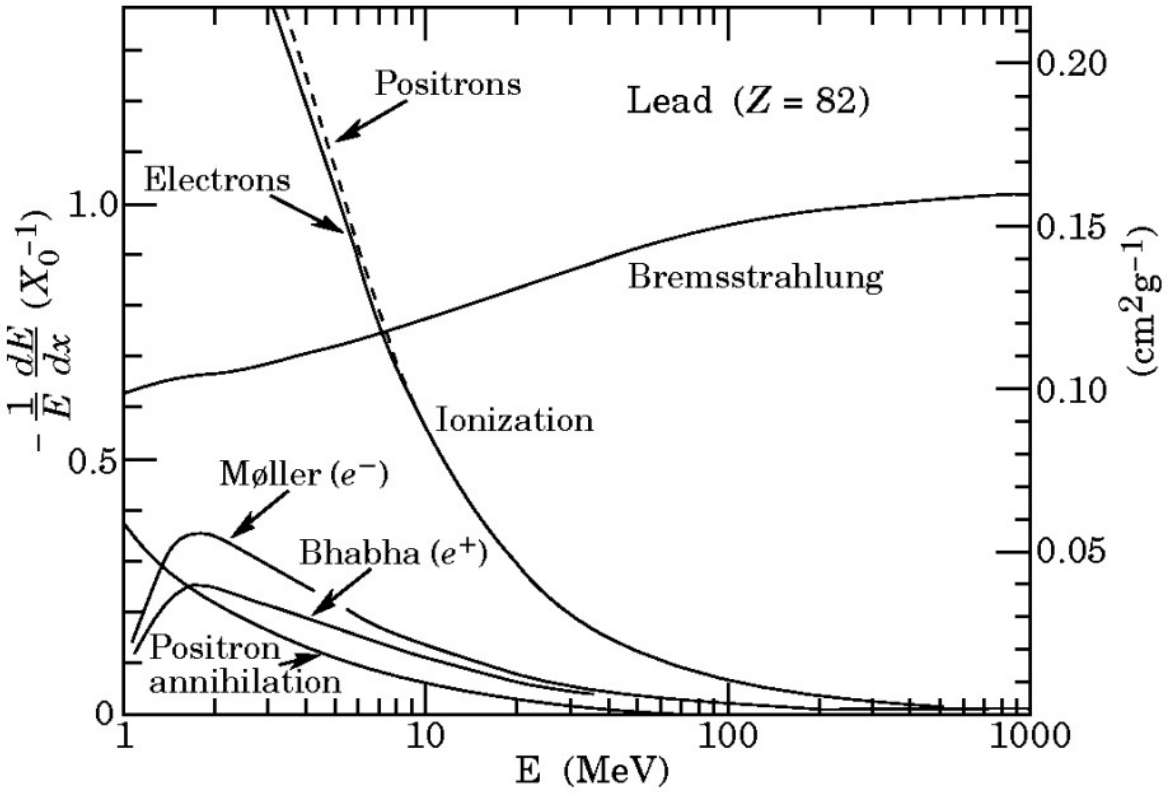

Figure 2.2: The energy loss in lead (Z=82), as a function of the incident electron energy, demonstrating the energy regions where each of the processes described in 2.2 are dominant [56].

Table 2.2: The primary electron interactions of interest are highlighted here, with their interaction type and distance of interaction also described. This table was adapted from [53].

Interaction	Interaction Type	Distance of e- from atom	Z and E dependence	Summary
Excitation	Collisional	>atomic radius	Complex with Z and E	Incident electron excites atomic electron to higher state, which then returns to ground state with the emission of a photon.
Ionisation	Collisional	$\sim$atomic radius	Complex with Z and E	Incident electron ejects orbital electron from shell. Both electrons can go on to deposit energy through further interactions.
Bremsstrahlung	Radiative	<atomic nucleus	Z^2, E	Incident electron interacts with field of nucleus; rapid deceleration causes emission of Bremsstrahlung photon.

2.2 Neutral Particle Interaction

Neutrons and photons do not have any charge, and as such they do not interact in the same manner as electrons and heavy charged particles. Uncharged interactions depend entirely upon the statistical likelihood of an interaction occurring. This is different for neutrons and photons, and is dependent on the incident particle energy. Neutral interactions are not directly detected in the material, but the emission of secondary charged particles that are detected allow for the inference of detected neutrons, with this also being true for γ-ray interactions.

2.2.1 Neutron Interactions

Heavy charged particles, electrons and photons are readily detectable by scintillators but neutrons require specialised materials. As a neutron is uncharged it cannot interact with the electric field of a particle, and as such it must interact directly with the nucleus. Due to this, neutrons interact primarily through scattering processes and neutron capture, both of which are dependent on the neutron kinetic energy, with the full range of neutron energies seen in table 2.3. As briefly discussed in chapter 1, the neutron energy will affect which scintillator is best for use, as organic scintillators are best for fast neutrons, and inorganic scintillators for thermal neutrons.

Table 2.3: A summary of the neutron energy regimes, this is important to understand as the primary regimes of interest for this work are the thermal and fast energy regimes. This can be seen throughout sections 2.3.1 and 2.3.2. This table was adapted from [57].

Energy Range	**Name**
0 - 0.025 eV	Cold
0.025 eV	Thermal
0.025 - 0.4 eV	Epithermal
0.4 - 0.6 eV	Cadmium
0.6 - 1.0 eV	Epicadmium
1 - 10 eV	Slow
10 - 300 eV	Resonance
300 eV - 1 MeV	Intermediate
1 - 20 MeV	Fast
>20 MeV	Relativistic

Fast neutrons interact primarily through scattering reactions, as the probability of neutron interaction is inversely proportional to the neutron energy, as can be seen in figure 2.3. This comes in two forms, elastic and inelastic scattering. Elastic scattering is when a neutron is incident on a nuclei and kinetic energy and momentum are conserved. This occurs when enough energy is transferred from an incident neutron to create a directly detectable ion, whilst inelastic scattering occurs when the incident neutron has an energy in excess of 1 MeV, with some of the neutrons kinetic energy being absorbed by the nuclei.

This is because the first excited state of most nuclei are typically <1 MeV, meaning that fast neutrons have enough energy to cause the nucleus to be in an excited state and undergo γ-ray emission, which can also be directly detected. Elastic scatter is more effective when the interacting nuclei have a mass similar to that of the neutron, as light nuclei often have higher first excited states. This is one of the reasons why high hydrogen content makes organic scintillators effective fast neutron detectors, and allows for neutron thermalisation.

Thermal neutrons interact primarily through neutron capture events, which occur when the incident neutron is captured by the nucleus to form an excited isotope that will either de-excite with the emission of γ-ray's or split into other daughter nuclei. The probability of this interaction taking place is not only dependent on the incident neutron energy, but also on the nuclei involved as the neutron capture cross section varies by element, also demonstrated in figure 2.3. The high neutron cross section of ^{157}Gd demonstrates why it is a material commonly used within the nuclear industry to control the reactivity of nuclear reactors, as well as its use in liquid scintillators for reactor antineutrino detection [58][59].

Other common nuclei used for thermal neutron interactions include ^{3}He, hence it's widespread use as a neutron proportional counter, or ^{10}B, as also shown by its common use in the nuclear industry [60]. However, the capture reaction of most interest to this investigation is the ^{6}Li capture reaction, which is used in inorganic and some novel organic scintillators to capture thermal neutrons, with the capture reaction seen in equation 2.3. The secondary particles produced in these reactions allow for thermal neutron detection:

$$^{6}\mathrm{Li} + \mathrm{n} \longrightarrow {}^{3}\mathrm{H} + {}^{4}\mathrm{He} + 4.78\ \mathrm{MeV}, \tag{2.3}$$

Neutron Thermalisation

All neutrons produced by a source or generator are created as fast neutrons [17], and as such in order to reach thermal energies, the neutrons must be thermalised. As stated above, lighter nuclei are best for this, with hydrogen being ideal. This is because hydrogen has the closest mass to a neutron, removing the maximum possible energy through elastic collisions. This is done in practice by using a neutron moderator, such as high density polyethylene (HDPE) or paraffin wax, which moderates these fast neutrons down to thermal energies through elastic scatter collisions:

$$v_{mp} = \sqrt{\frac{2k_B T}{m}}, \tag{2.4}$$

where v_{mp} is the most probable velocity of a particle with mass m, T = 298K as approximately room temperature, k_B is Boltzmann's constant given as $1.381 \times 10^{-23}\,\frac{J}{K}$, and m is the mass of the neutron and given as 1.675×10^{-27} kg.

The kinetic energy of this neutron would be:

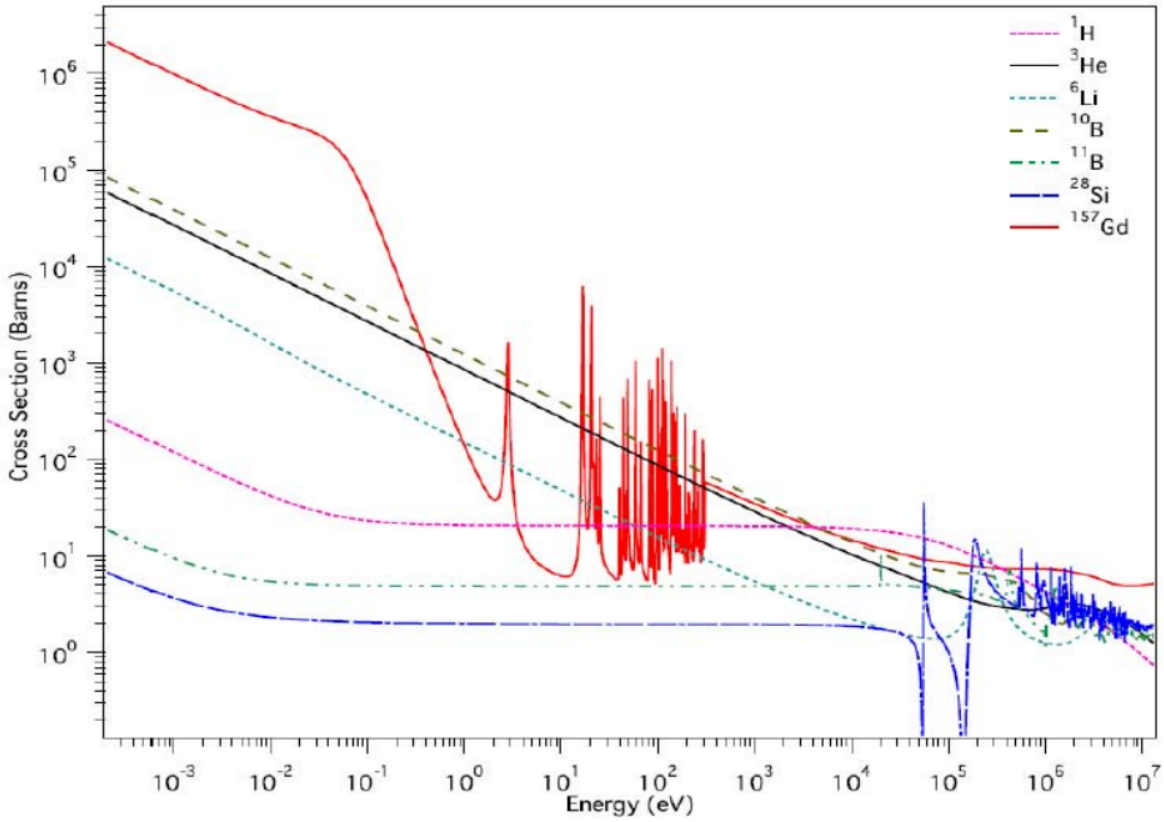

Figure 2.3: The neutron absorption cross section of various materials, demonstrating that the probability of neutron absorption varies according to $1/v$, meaning that it increases as neutron energy decreases. Inelastic scattering becoming dominant at higher energies can be also be seen. There are higher energy resonances present, but these are specific to the nuclei, adapted from [61].

$$E = \frac{1}{2}mv_{mp}^2 = 0.025\,eV. \tag{2.5}$$

Table 2.4: This table demonstrates why elements with a mass similar to that of the neutron are best for thermalisation, requiring fewer collisions and therefore a smaller amount of material is required, an illustration of this point can be seen in figure 3.9. This table was adapted from [62], where further information on this process is available.

Element	Mass A	β	Collisions to thermalisation
H	1	1	21
D	2	0.8888	25
He	4	0.64	38
Be	9	0.36	73
C	12	0.284	95
O	16	0.2215	124

Where β is defined as:

$$\beta = \frac{4mM}{(m+M)^2}, \tag{2.6}$$

with m being the mass of the neutron and M being the mass of the interacting particle, with this β term representing the average fractional loss of kinetic energy per collision, demonstrating why light nuclei are ideal for moderation. There is another term ζ, which is the mean logarithmic energy loss per collision, that is used in combination with the atomic mass number A to calculate the number of collisions required to reach thermalisation.

The equations present in 2.4, 2.5 and 2.6 illustrate why thermalised neutrons have a corresponding energy of 0.025 eV at room temperature, and why it is important to reach this energy for inorganic scintillation detectors. Table 2.4 further demonstrates why low mass materials are most effective at neutron thermalisation, which is simultaneously why organic scintillators excel at fast neutron detection due to their high interaction probability.

2.2.2 Photon Interactions

The Photoelectric Effect

Photons react differently to neutrons, as when a neutron interacts, it will interact with the atomic nucleus, whereas a photon will interact with the electrons of the element. Photons interact in three primary ways, the photoelectric effect, Compton scattering and pair production. The first of these, the photoelectric electric, occurs when a photon is absorbed by an atomic electron, usually in the K-shell, causing this atom to be ionised and eject an electron, leaving a vacancy in the shell. This vacancy is then filled by the capture of a free electron or an Auger electron, resulting in the emission of characteristic x-rays, with the energy of this process defined as:

$$E = h\nu - \delta, \tag{2.7}$$

where E is the energy of the electron, h is Planck's constant, ν is the frequency of the photon and δ is the binding energy of the atomic electron. This process is most significant at energies up to $\sim$100 keV. This process also varies with atomic number, as seen in equation 2.8 [48], this Z dependence is why high Z materials, such as lead, are chosen for γ-ray shielding.

$$\tau \propto \frac{Z^n}{E_\gamma^{3.5}}, \tag{2.8}$$

where, τ is the interaction probability, Z is atomic number and E is energy of the incoming photon, this is a best estimation of interaction probability as n varies between 4 and 5.

Compton Scattering

The second process is Compton scattering, which occurs when an incoming photon transfers some of its energy to an outer shell electron, which then becomes a recoil electron. This is possible up to a maximum scattering angle of 180°, which creates a sharp cutoff point known as the Compton edge, corresponding to the maximum possible energy transferred to the recoil electron. This process is inelastic, and is most significant above the photoelectric effect energy range, but below that where pair production becomes significant. The energy of this process is given in Equation 2.9:

$$E' = \frac{E}{1 + \frac{E}{m_e c^2}(1 - \cos\theta)} \quad , \tag{2.9}$$

where E' is the final energy of the electron, E is the initial energy, m_e is the mass of the electron, c is the speed of light and θ is the scattering angle of the recoil electron. An illustration of this process can be seen in figure 2.4.

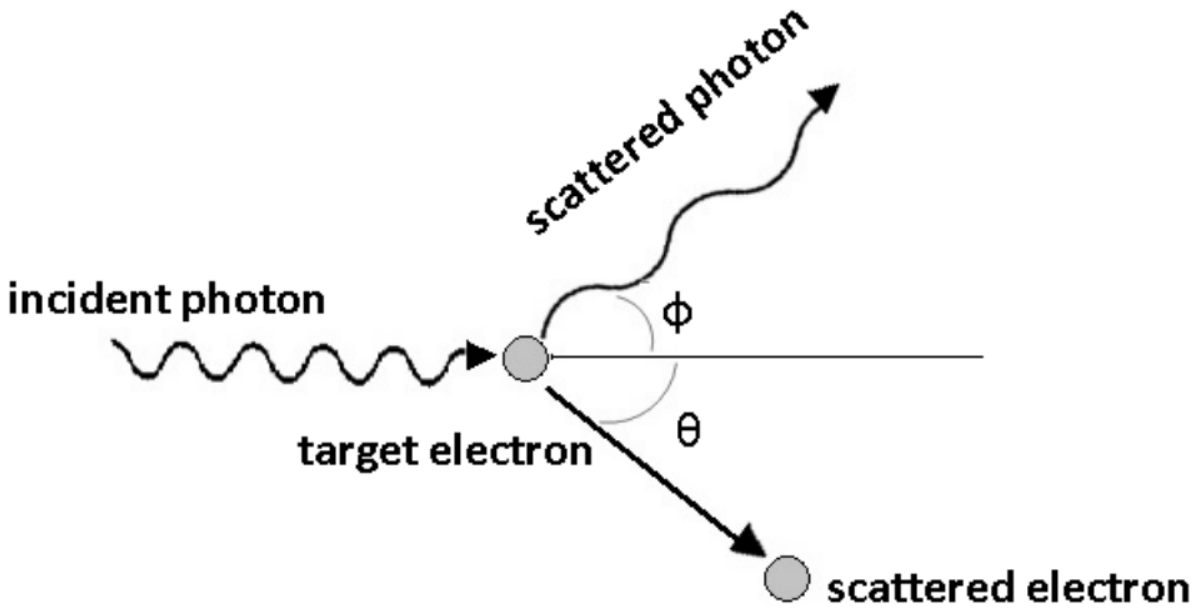

Figure 2.4: An illustration of the Compton scattering process, with the initial photon and scattered electron both present, adapted from [63].

Pair Production

The final primary process is pair production, which occurs at energies above 1.022 MeV. At this energy, a photon can interact with the electric field of a nucleus and produce an electron-positron pair. This is possible as the electron rest mass is 0.511 keV, so this incident photon will have an energy above the rest mass of the electron and positron pair. Any excess energy generated will

be shared between these two particles, with the electron interacting through any of its previously described processes, and the positron annihilating with an electron. The conservation of energy and momentum means that whilst pair production begins at energies above 1.022 MeV, it does not become dominant until higher energies. Each of these three processes and their dominant regions can be seen in figure 2.5.

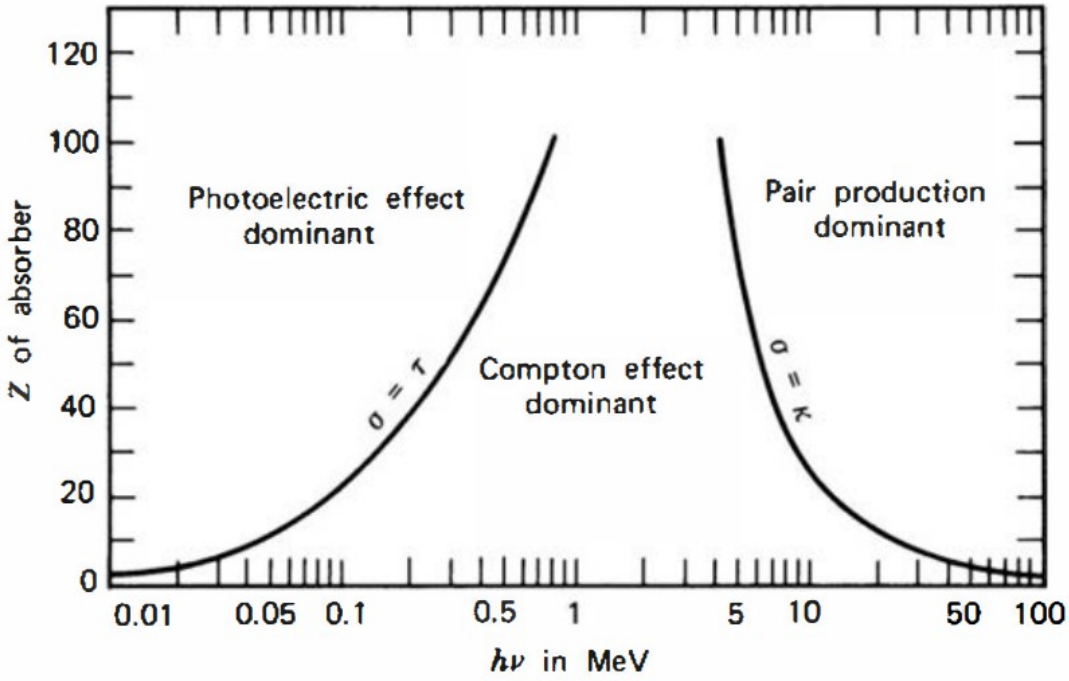

Figure 2.5: A comparison of the atomic number Z of the absorber material against the photon energy, demonstrating the Z dependence of each interaction process, as well as the energy regions where each process becomes dominant [64].

Photon Attenuation

As photons are uncharged, the photons created throughout these aforementioned processes will not lose energy steadily through Coulomb interactions with other atoms. Energy will be lost instead as the photons interact in a material, which is based upon the statistical likelihood of an interaction occurring. This is described by the Beer-Lambert Law, which can be seen in equation 2.10:

$$I(x) = I_0 e^{-\mu\rho x}, \tag{2.10}$$

where $I(x)$ is the intensity of the transmitted photons, I_0 is the initial photon intensity, μ is the linear absorption coefficient, ρ is the material density and x is the distance travelled through the material. In this case μ is the sum of the probabilities of interaction from all three of the

previously described photon interaction processes, giving a measure of how far into a material a photon is likely to pass.

2.3 Scintillation

Regardless of whether a neutron or γ-ray is incident on an inorganic or organic scintillation material, this incident energy will be converted into light by the material. The details of these processes vary for each scintillator form but there are some general similarities. There are many different forms of scintillator available for use, with different options available in solid, liquid and gas forms. Liquid scintillators have existed for many years, although a key drawback is that many liquid scintillators are highly toxic with the light yield dependent upon temperature [65], and as such would not be suitable for long term PI, so a solid scintillator would be more appropriate.

2.3.1 Inorganic Scintillators

Inorganic scintillation is possible due to the bandgap structure present in inorganic materials. This can be seen in figure 2.6. Lower energy electrons are present in the valence band, and when a particle is incident on the material it can excite an electron from the valence band into the conduction band, leaving behind an electron hole. This hole can then be filled by another electron, which emits a photon equivalent in energy to the transition, which can be directly detected. A γ-ray interaction will produce a large number of these electron-hole pairs (EH pairs), with the holes (areas of positive charge), drifting towards activator centres in order to ionise them. This emitted light can also be reabsorbed in the material through a process known as hole self-absorption, creating new EH pairs [66].

This is not an efficient process, and as such impurities are often added to the material, which create activator centres allowing for more efficient photon de-excitation. The de-excitation centres are also known as luminescence centres, and it is their structure which gives rise to the scintillation spectrum observed in inorganic scintillators. This process occurs on the order of nanoseconds, and is known as fluorescence. However, when an electron arrives at an activator site, it might create an electron configuration whose direct decay to the ground state is forbidden, meaning that it will need to absorb some energy to move to an energy state which can in turn decay to the ground state. This gives rise to a slower component known as phosphorescence, and is responsible for the delayed scintillation light that can be seen in inorganic scintillators. An additional problem seen in inorganic scintillators, is that this transition to the ground state can occur through a photon-less transition, which would quench

the signal and reduce overall light output.

There are also additional processes that can affect the timing profiles of each material, such as core valence luminescence (CVL), which is a phenomenon that effects certain scintillation crystals but not others. This is a process that is not quite fully understood, nor is why it affects certain crystals but not others [67]. However, what is known is that CLYC has CVL present, whilst CLLBC does not. What this means in practice is that CLYC has a very fast decay component which is reflected in the 1 ns decay component present seen in table 1.1, whilst the fastest decay for CLLBC is 115 ns, meaning that there is a significant timing difference in the fast decay components of each inorganic material. This decay time is defined as the time taken for the light intensity to reduce to $\frac{1}{e}$ of its maximum value, and is determined by analysing the scintillation pulse shape [68].

Both the fluorescence and phosphorescence processes occur on the order of 10-100ns, whereas the neutron capture process occurs on the order of ms, allowing for the necessary timing difference to perform PSD. This also means that the timing characteristics of an inorganic scintillator are quite long when compared to an organic scintillator. When discussing the thermal capture process, it is important to recognise that the 4.78 MeV emitted during the ^{6}Li capture reaction seen in equation 2.3 will not be directly observed. This energy will be seen as gamma equivalent energy (GEE), or electron energy equivalent, written in the form MeV_{ee}. This is required as the light output of neutron and gamma interactions can vary widely, and therefore it is necessary to calibrate a PSD detector (and any detector performing both γ-ray and neutron detection) using appropriate units. For CLLBC, the thermal peaks corresponds to a value of 3.1 MeV_{ee} [69], whilst for CLYC this corresponds to a value of 3.2 MeV_{ee} [70]. This means there is a unique neutron 'hotspot' present for inorganic scintillations which can aid in γ-ray and neutron separation.

2.3.2 Organic Scintillators

The process of organic scintillation is very different from that of inorganic scintillation. This is because whilst inorganic scintillation is caused by the overall crystal structure of the material, organic scintillation is caused by the properties of molecules within the scintillator. This allows for organic scintillators to be created in liquid, vapour or solid forms. Organic scintillators primarily rely on the symmetry created by two overlapping p atomic orbitals, which create a π orbital electron structure and allow for scintillation to occur. The π-electron structure creates two energy states that correspond to a state of spin = 0 and of spin = 1, which are the singlet and triplet state respectively. An example of this process can be seen in figure 2.7.

If a γ-ray or neutron is incident on an organic scintillator, it will impart some energy, via one of

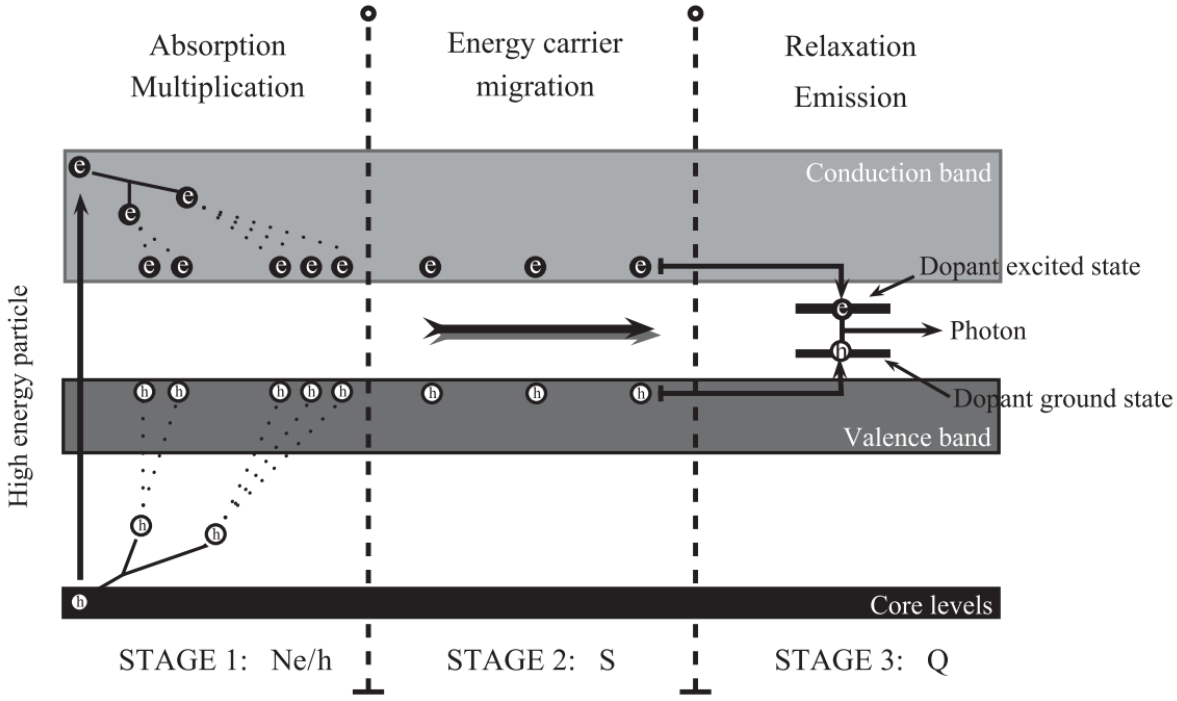

Figure 2.6: A diagram showcasing the various stages of inorganic scintillation, with an electron being excited up from the valence band into the conduction band, leaving a positively charged hole behind which is filled by a de-exciting electron, which subsequently emits a photon of equivalent energy to the change in energy state. Adapted from [71].

the aforementioned processes, to the scintillator and raise an electron from the ground state to a higher excited state. This will then promptly de-excite on the order of ns, emitting a photon of equivalent energy to that of the change in state, giving rise to the faster fluorescence component. However when a triplet state is formed through a process known as inter-state crossing, it cannot decay directly from the T1 state to the S0 state. It can undergo a process known as triplet-triplet annihilation (TTA), which causes two triplet states to decay, one going to the S1 state, and the other to the S0 state. This creates a fast and delayed component, as the S1 state will decay to S0 as normal. These triplet states are naturally longer lived than the singlet states, and give rise to the phosphorescence process observed in organic scintillators [17][73].

This timing difference between the fluorescence and phosphorescence processes allows for PSD to be performed in organic scintillators. When a fast neutron is incident on an organic scintillator, the recoil from an elastic scattering interaction will result in a proton which, due to its charge and mass, means that it has a much shorter range in the material than that of a γ-ray interaction. This yields a higher concentration of triplet states, meaning that there is a larger delayed component present, allowing for PSD to be performed in an organic scintillator.

The PSD ability of a plastic scintillator is also dependent on the amount of polyvinyl toluene (PVT) present within the material, as a larger proportion of PVT within the plastic increases

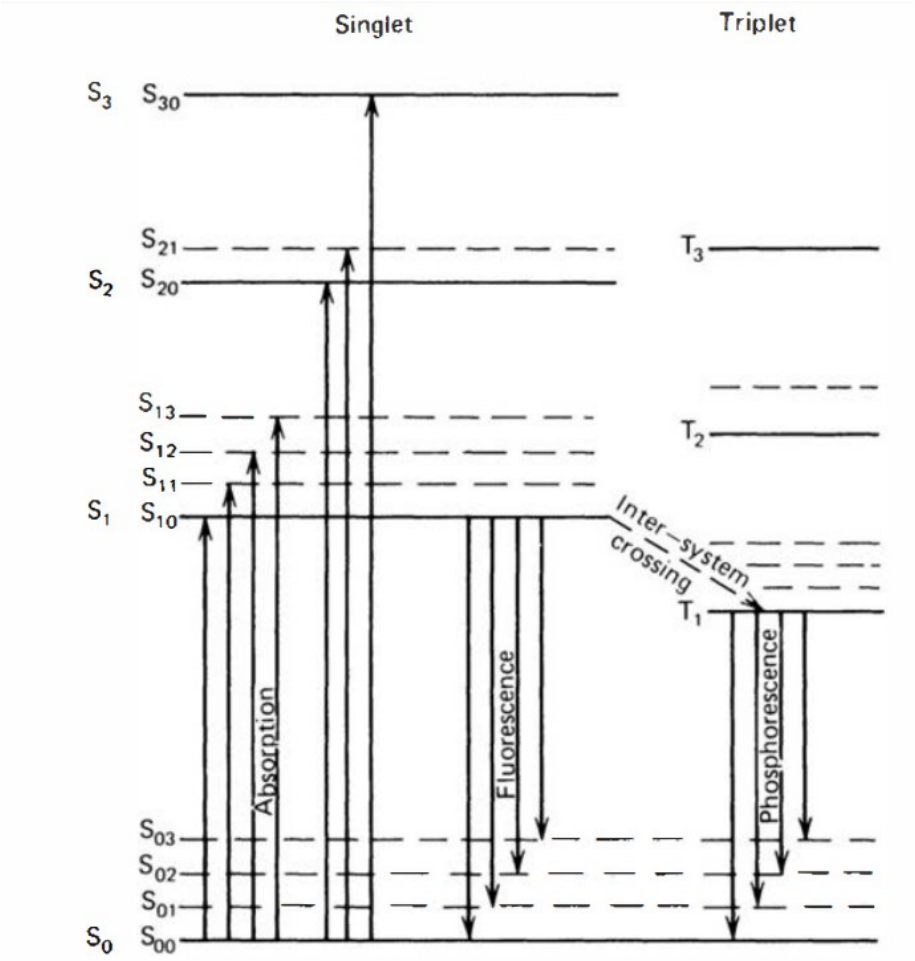

Figure 2.7: An illustration of organic scintillation, with the prompt electrons de-exciting to form the fluorescence component, whilst the slower phosphorescence component needs to absorb some energy to de-excite to the ground state as it cannot proceed directly from a triplet state to the ground state [72].

the PSD capability of the material, but at the cost of decreasing light yield, as the addition of PVT quenches some of the plastic scintillators light output [35]. There have also been many attempts to combine the fast timing characteristics of a plastic scintillator with the thermal neutron detection ability of an inorganic scintillator, primarily performed by adding a material with a high neutron capture cross section to an organic scintillator. The material most commonly chosen is ^{6}Li, which has a lower neutron capture cross section than that of ^{10}B (942 barns vs 3840 barns), but most importantly, as seen in equation 2.3, there is a higher final energy released and an absence of γ-rays in final products containing charged particles [17], hence making it a more appealing choice for addition to plastic scintillators.

2.4 Photon Detection Solutions

Whichever form of scintillation is utilised, the photons produced need to be converted into a measurable electrical signal for further analysis. There are many ways of doing this, through devices such as gaseous detectors, which rely on the ionisation of the contained gas to create a current flow that can be measured. However these detectors have their own drawbacks, such as influence from the environment through moisture [74], and as such were not considered for this investigation, although a detector that could deal with either single photon counting, or with a high photon flux environment would be key to the outcome of this investigation, due to the possible variation of input neutron flux. This means that a different detector type was required, with the primary forms of interest being the vacuum tube and solid state classes. This can be seen through two different photon detector technologies, the PMT (vacuum tube) or the SiPM (solid state semiconductor).

Both forms follow the same stages, which are photon conversion, charge collection, charge multiplication and finally signal readout. Photon conversion occurs through the photoelectric effect, meaning that the correct design material must be chosen, in order to maximise the electrical signal produced at the signal readout stage. It is also important to consider the cases of internal and external photon conversion, as they relate to SiPMs and PMTs respectively. Charge collection is performed when emitted photoelectrons are directed to a specific site, commonly where the next stage of charge multiplication can occur so the charge can be multiplied into a measurable signal. This then leads to the final stage where this measurable signal is fed into readout electronics, although it is key to state that each of these stages will have their own varied noise contributions, which will be covered in chapter 2.7. Both PMTs and SiPMs have similar gains, which is the ratio of input signal intensity to output intensity, but they vary quite broadly beyond this, with different noise contributions and bias voltages causing each to have useful positives and important drawbacks.

It is important at this point to define two key values used when analysing photodetectors, which are the quantum efficiency (QE) and photon detection efficiency (PDE). Quantum efficiency is the ratio of emitted photoelectrons to incident photons, which varies from material to material due to their response to different wavelengths [75]. Vacuum tube devices usually have lower QEs than semiconductors, $\sim$30% compared to $\sim$70% [76][77], so it is more informative to use the PDE to describe photon detection technologies, which accounts for the QE, the charge collection of the detector, the geometry and the interaction probability [78].

2.4.1 Photomultiplier Tubes

PMTs have been used in nuclear physics and radiation detection almost ubiquitously since their inception in the mid 20th century, and this popularity is due to their fast timing characteristics, their low room temperature noise and their high gain (typically $\sim 10^6$) [79]. This has allowed their use in a wide variety of different experiments such as Time-of-Flight experiments [80], a use that also benefitted this investigation. These characteristics made PMTs very appealing for the initial stages of this investigation. PMTs operate using external photon conversion, where a photon is incident on the photocathode material, which should have a low work function (the energy required to cause an electron to be emitted from a material) to maximise the number of photoelectrons produced by an incident photon. This causes an electron to be emitted, which is then accelerated through a series of dynodes, with each dynode multiplying the amount of produced photoelectrons into a measurable signal that is collected at the anode. An illustration of this process can be seen in figure 2.8, with more detail on their operation found in [81]. However this glass vacuum tube design meant that they did not suit the initial design conditions, due to the potential of damage to the vacuum tube and therefore loss of detector use.

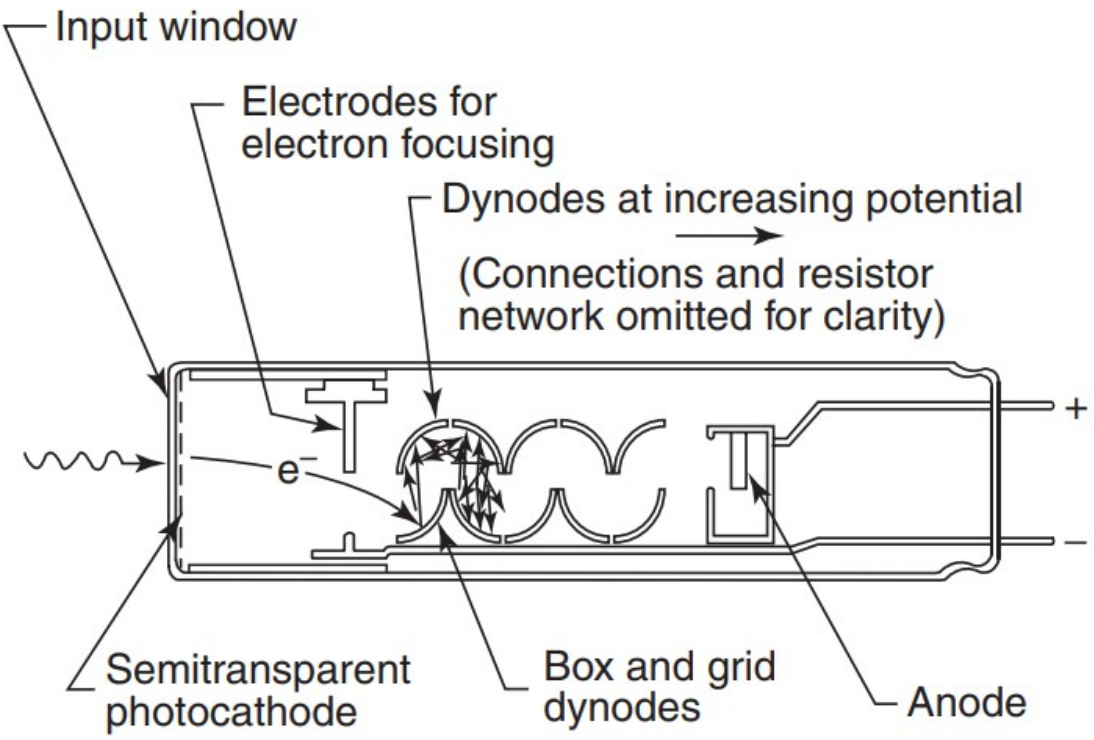

Figure 2.8: An illustration of PMT operation, with the semitransparent photocathode allowing for a greater number of initial photoelectrons to be emitted, then passed through the accelerating dynode stages that increase the number of photoelectrons, hence increasing the magnitude of the output signal that is collected at the anode, adapted from [79]

2.4.2 Silicon Photomultipliers

SiPMs are solid state, single photon sensitive devices that are commonly constructed in large arrays, which utilise a PN junction. This is when a p-type semiconductor (which has an excess of holes) is combined with an n-type semiconductor (which has an excess of electrons) to form a boundary where electrons from the n-type region diffuse into the p-type region and create what is known as a depletion zone. There is much more detail to this process which can be found in [82], although the key result is that it forms the basis of a diode, which means that when a positive (or forward) bias is applied, the depletion zone is decreased as the applied electric field opposes the built-in field. When a negative (or reverse) bias is applied, the depletion zone increases as the applied electric field increases the built-in field. This means that current can primarily flow in the forward direction when a positive bias is applied between the anode and cathode, which will have significant applications in chapter 2.6.

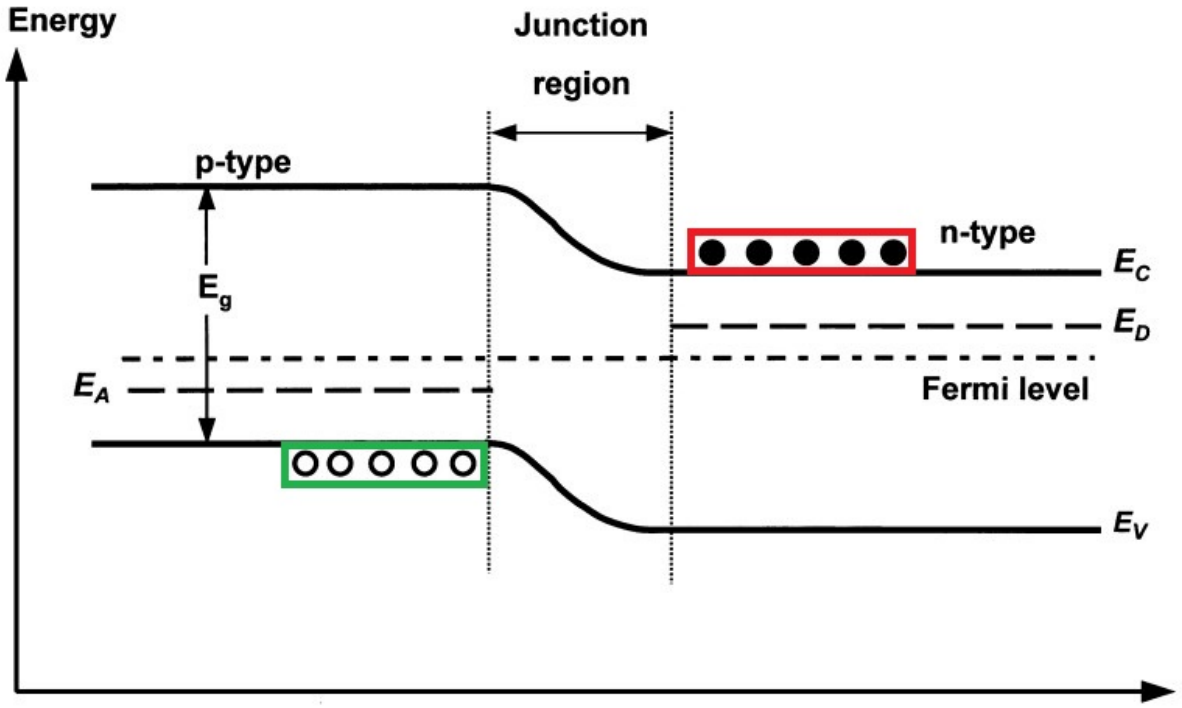

Figure 2.9: An illustration of a PN junction, with the p-type and n-type regions present, along with the junction region (depletion zone) that either decreases or increases dependent on the applied electric field. This forms a crucial part of semiconductor operation, such as SiPMs, and also forms the basis of transistors which are key to the later electronics designs of this investigation. The holes are seen in the green highlighted area, with the electrons seen in the red highlighted area, adapted from [83].

SiPMs operate using internal photon conversion, where the incident photon causes electrons to be excited from the valence band into the conduction band, creating an EH pair. This means that the material should have a low band gap energy to ensure that photoelectrons are produced

more easily, as well as a high proportion of activator sites to improve the overall efficiency of the emission process. SiPMs consist of Geiger mode avalanche photodiodes, termed as microcells, that are similar in operation to avalanche photodiodes (APDs), but are biased to operate in the Geiger region above the standard linear region that most APDs operate within. This means that the SiPM will initially be operating above its rated reverse breakdown voltage.

In Geiger mode, an avalanche is self-sustaining and needs to be quenched, either actively or passively. This is most often achieved using a high value resistor in series with the Geiger APDs, which pulls the SiPM back into the linear region where it will recharge back to the Geiger region. An illustration of this circuit can be seen in figure 2.11, with the series resistors present in order to pull the SiPM back into the linear region.

Due to this method of quenching and recharging, each microcell operates in a binary mode, indicating if there was photon absorption or not. This naturally introduces time dead time into the system as the SiPM returns to the Geiger region, with values of $\sim$25 ns to 50 ns reported for different manufacturers [84]. An SiPM array will contain thousands of these microcells connected in parallel, allowing for a combined analogue signal, proportional to the light incident on the SiPM. This setup allows SiPMs to have single photon sensitivity and high gain, achieved with a low bias voltage (V_{bias}) of $\sim$30V to 60 V. Additionally, SiPMs are more robust than PMTs, due to the solid state design versus the glass vacuum tube, meaning that they are ideal for meeting the initial design conditions. The dynode design of PMTs also mean that magnetic fields can distort the charge multiplication stage, which is not a concern for SiPMs.

SiPMs typically have high PDE, with values of $\sim$55% often reported [85], however their higher dark noise at room temperature are their primary drawback. This higher dark count rate (DCR) is directly proportional to both gain and temperature, with the DCR decreasing by a factor of 2-3 every 10°C [86]. Reducing the gain will also reduce this DCR, but this will decrease the output voltage as well, so a necessary balance must be struck. This DCR also follows Poisson statistics as a random source of noise, and as such it cannot be subtracted from any dataset.

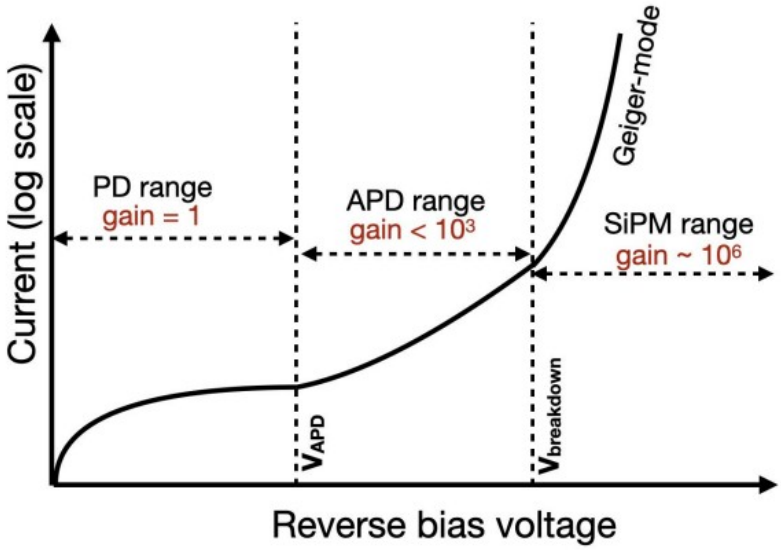

Figure 2.10: An illustration of the different SiPM photodetector regions, depending on the applied bias. The linear APD region can be seen, as well as the Geiger region where avalanches become self-sustaining [87].

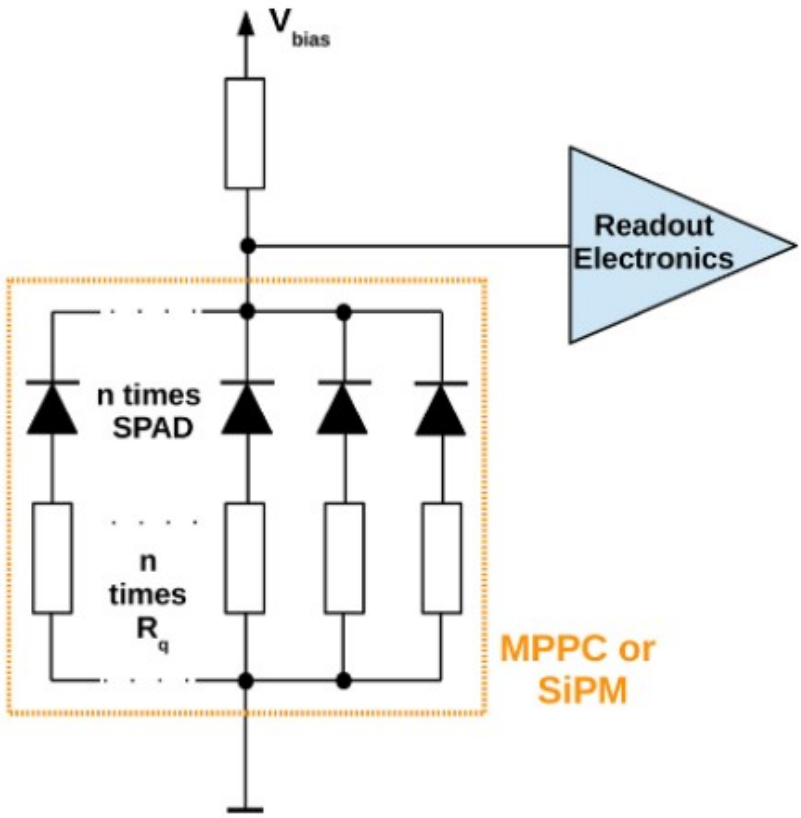

Figure 2.11: An illustration of a simplified SiPM circuit, with the series resistor included that is used to quench the SiPM, pulling it back into the linear region to recharge to the Geiger region, adapted from [88].

2.5 Pulse Shape Discrimination in the Time Domain

The analysis of the signals produced by either a PMT or SiPM, and the ability to discriminate between the γ-ray and neutron signals present are both crucial to this investigation. This is performed by the application of PSD which, as discussed in chapter 1, has a long history as a technique, with many different forms of application. Originally PSD was performed in analogue using the zero crossing (ZC) method as it was possible to achieve good time resolution without using expensive components, but the rise in fast digital pulse processing (DPP) has allowed for other methods to be investigated. It is also possible to perform PSD in the frequency domain rather than the time domain, with some investigations suggesting even greater values of separation [89]–[92]. This investigation prioritised time domain methods, as frequency domain based methods are better suited for high flux environments and for detecting lower energy pulses [93], both of which were not considered during the design of this detector, as the primary design aim of this investigation was passive neutron interrogation in transit environments.

Before defining any of the different time domain based PSD methods, it is first important to define the key values used to describe the PSD performance of a detector. Firstly, the timing characteristics of a waveform need to be described, with three regions of interest present. These are the rising edge, the peak and the falling edge. Each are relatively self explanatory, as the rising edge is when the pulse is rising from its lower state to its higher state, the peak is the maximum value that the pulse reaches, with the falling edge being the pulse returning to its lower state. The relationship between these regions are the primary method of performing PSD in the timing domain. The overall PSD analysis value is the figure-of-merit (FOM), which is defined as the separation between two species, divided by the full width half maximum of each distribution, with an example of this calculation seen in figure 2.14. The FOM represents the effective separation of two peaks, with the greater the FOM, the greater the separation and therefore the more effective the PSD.

2.5.1 Rise and Fall Time Methods

The rise time PSD method evaluates the rise time of a pulse, and uses this value to determine whether a γ-ray or a neutron was the incident particle. This is possible as a neutron signal will have a slower rise time than the signal generated by a γ-ray interaction. This can be done either as a raw amplitude, or as the time taken for the pulse height or integral to reach a predefined fraction of the total pulse height or integral. This is useful in scintillators that have fast timing characteristics, such as organics, and is simpler to implement due to relying solely on one aspect of the input waveform. This can be further improved when deciding the fraction of the pulse

considered, as if the time for the pulse to rise from 20% to 80% is used (this is also often seen between 10% and 90%) then the method becomes insensitive to the peak height of the pulse, and is dependent only upon the shape of the pulse, which will vary between γ-ray and neutron species.

Whilst it is possible to separate γ-ray and neutron species using the rising edge of a pulse, it is also possible to do the same using the falling edge of the pulse. This method is often considered easier than that of the aforementioned rise time method, due to the greater differences in decay timings, as seen in figure 1.2. This is also seen in each scintillation material, as the decay time of each material is slower than that seen for the rise time. This method can also be improved by considering a predefined fraction of the pulse, often taken to be 90% in this case. There are some similarities between these methods, and that of the charge comparison method that is often employed for PSD in a digital scope. These methods determine what time period is required to contain a certain fraction of the total pulse, whilst the charge comparison method does the opposite and determines the charge contained within preset gates [11].

2.5.2 Charge Comparison Method

The charge comparison (CC) method, works primarily by creating two timing gates, which can be seen in figure 2.12, that contain some amount of charge of the total pulse, and comparing these two to evaluate whether a γ-ray or neutron was detected. There are several methods to achieve this, but one of the most common, and indeed the one used frequently throughout the early digital work of this investigation, is to set a short gate that encompasses the rising edge of the pulse, and a long gate that encompasses the remainder of the pulse, and compare the charge contained within both. This can be seen clearly in figure 2.12, but essentially by taking the two separate features evaluated in the rise and fall time methods, it should be easier to perform species separation. This is because by taking the slightly different rise times of a γ-ray and neutron, and then comparing them to the larger difference in fall times, the species can be separated with greater accuracy than relying solely on one feature of the waveform.

The tail-to-total method is the opposite approach to the CC method, as it uses the charge contained within the tail (falling edge) of a pulse, and divides it by the charge contained within the full pulse, an example of expected pulse shape can be seen in figures 1.2 and 2.12. By using the ratio of these charges, as seen in figure 2.13, for an organic scintillator, it is possible to separate the γ-ray and neutron species.

This can be used to determine the Figure-of-Merit (FOM), a key value in determining detector performance. This is done by plotting the PSD factor against the frequency in a separate plot. The PSD factor definition depends on the PSD method used, but for the CC method it is

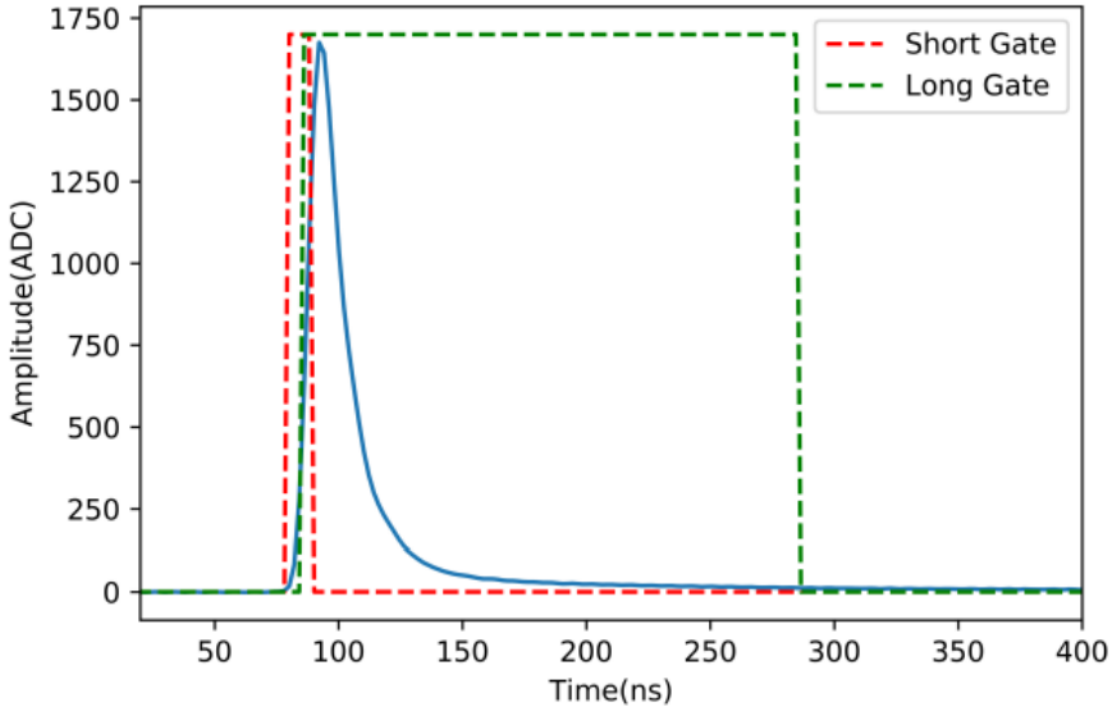

Figure 2.12: A pulse decay profile with the short (red) and long (green) timing gates required for the charge comparison PSD method seen. The rising edge of the pulse should be captured within the short gate, whilst the longer decay component should be captured within the long gate. A good balance between these gates is required, as the short gate needs to capture the rising edge but not be too long to infringe upon the long gate, whilst the long gate should not be too long as to be affected by the following pulse, distorting results [94].

calculated by using the ratio of the charges contained within the short and long gates. This can be seen in equation 2.11 with Q_{short} denoting the charge contained within the short gate and Q_{long} denoting the charge contained within the long gate. An example of these values plotted against each other can be seen in figure 2.13. This has been performed using an organic scintillator, hence the two continuous distributions, rather than the unique neutron energy signature present from inorganic scintillation.

$$PSD\ Factor = 1 - \frac{Q_{short}}{Q_{long}}. \tag{2.11}$$

This idea can then be taken a step further as seen in figure 2.14, where the 2 distributions are compared, with the separation between the 2 peaks being divided by the full width half maximum (FWHM) of each peak, with this value representing the FOM. If a FOM greater than 1.27 is calculated, it can be concluded that effective PSD has been performed. This can be seen in equation 2.12, where the standard definition that 2 peaks are well separated if S >

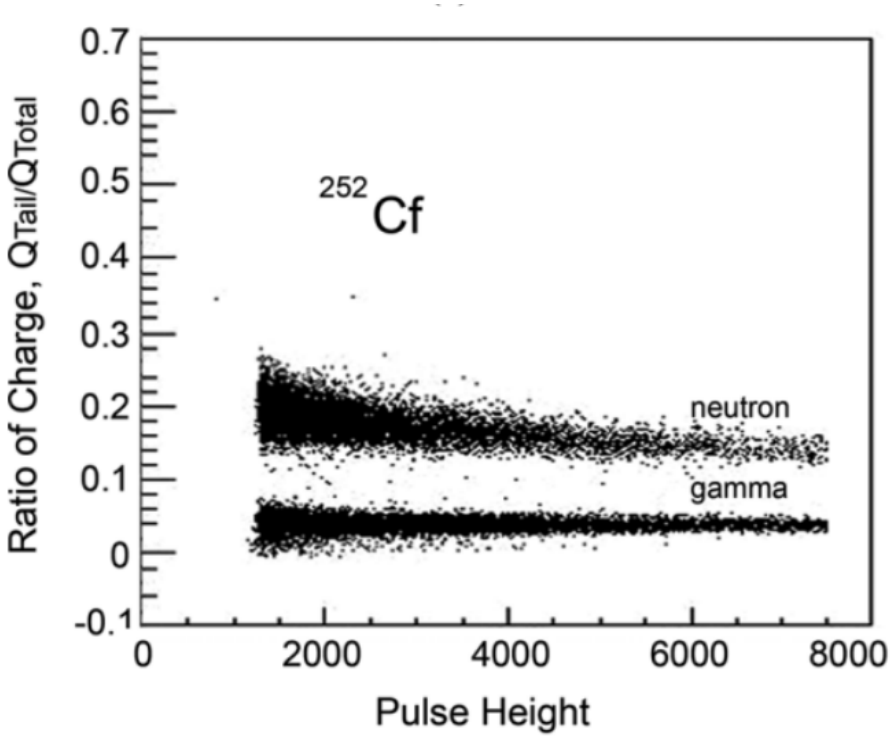

Figure 2.13: A plastic scintillator PSD factor vs amplitude plot, recorded using the organic scintillator stilbene. This highlights the expected separation between neutron and gamma species, with a lower energy pulse height cut present at ∼1500 to remove lower energy signals, adapted from [95].

$3(\sigma_\gamma + \sigma_{neutron})$, where σ is the standard deviation, and the FWHM for a Gaussian distribution is 2.36σ [96]:

$$FOM = \frac{3(\sigma_n + \sigma_\gamma)}{2.36(\sigma_n + \sigma_\gamma)}. \tag{2.12}$$

2.5.3 Zero Crossing Method

The CC method is one of the most common modern PSD methods, but as discussed other methods have been employed in the past, especially before the widespread accessibility of DPP. One of these methods is the zero crossing (ZC) method, which detects when a signal transitions from one state to another, traditionally from positive to negative, hence the name zero crossing, but this can be set to a reference voltage. As also discussed ZC has a long history in PSD, as far back as the 1960's, due to it's relative ease to implement using analogue electronics, the details of which will be discussed in chapter 4.1. Essentially, the pulse is passed through a shaping network (which will be explained in chapter 2.6) or a double delay line (DDL) shaper to convert the pulse into a bipolar pulse. The time at which this bipolar pulse will cross zero is not effected by the pulse shape or rise time, and so the comparison of these values would serve to

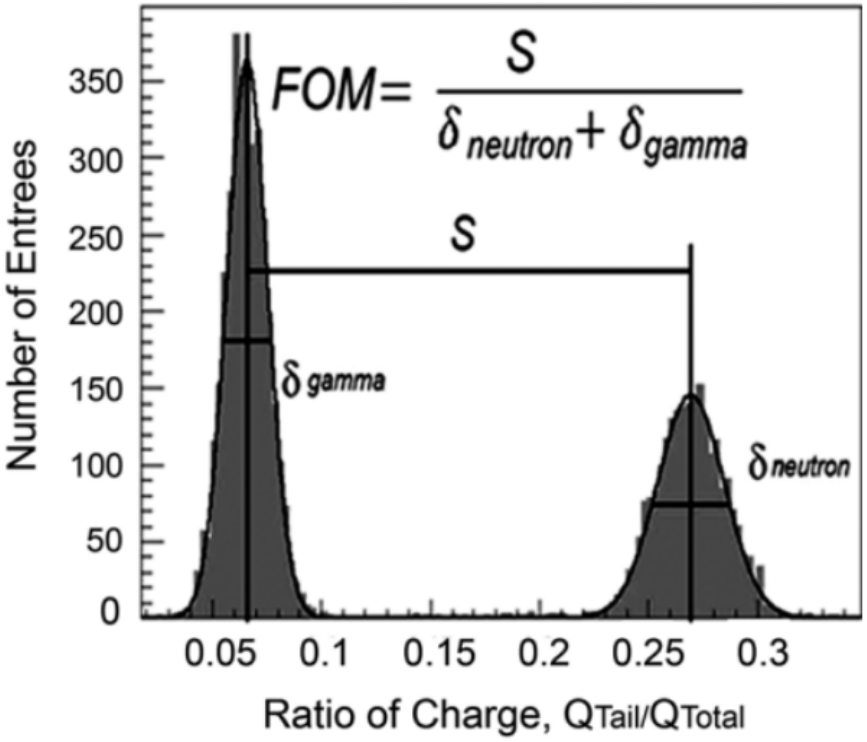

Figure 2.14: An illustration of a figure-of-merit calculation, with the separation of the peaks (S) divided by the full width half maximum (δ) of each respective peak. This allows for a measure of separation between these aforementioned peaks, with S being set to 3σ for ideal baseline separation of the species as seen in equation 2.12, adapted from [95].

separate γ-ray and neutron species [11][39][97].

2.5.4 Time-over-Threshold Method

Another method that has been used for PSD for many years similar to that of the ZC method, is the time-over-threshold (ToT) method. This method has several similarities to that of the rise and fall time methods, as the ToT method sets a predefined threshold and then evaluates the time above this threshold, an example of this can be seen in figure 2.16. This is a method that has found many uses in many different areas of physics due to its ease of implementation, with adaptions of this method, such as using a bipolar ToT method to improve accuracy in common use [98][99]. ToT is a popular choice for separating fast neutrons and γ-rays as the simple implementation means that many detection channels can be in use simultaneously [100][101].

2.5.5 Comparator Method

The CC, ZC and ToT PSD methods should allow for PSD to be performed with both organic and inorganic scintillation materials, as the pulses depend on the material decay times, rather than any specific feature of the scintillation material. These methods can also be more difficult to

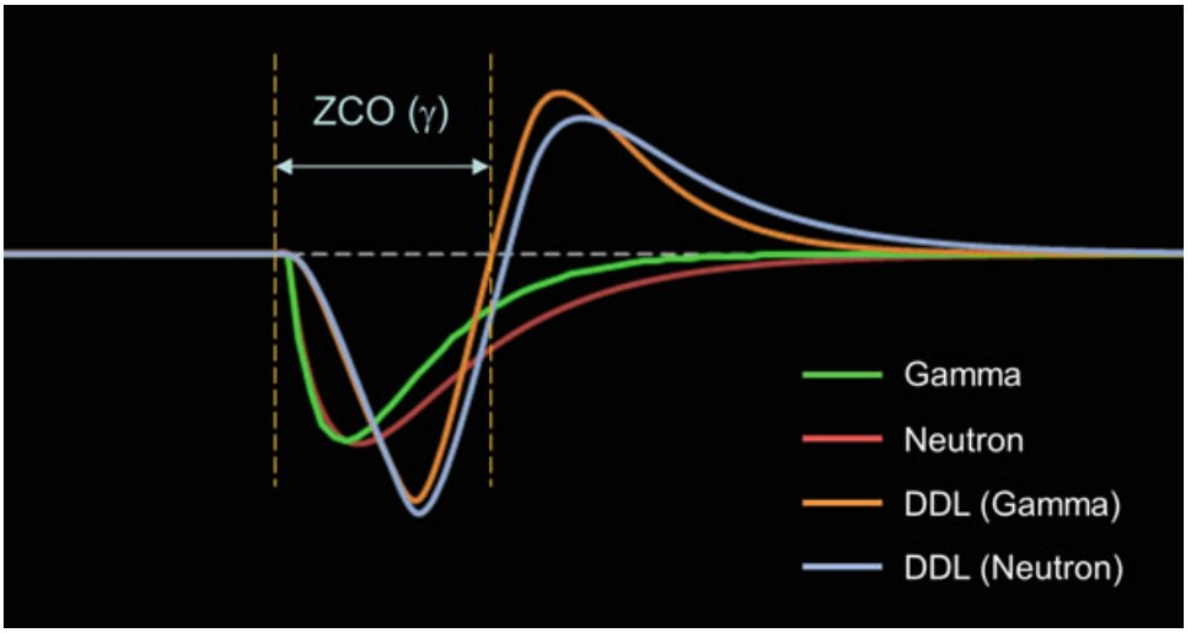

Figure 2.15: An example of the variation in zero crossing values for γ-rays and neutrons before and after they have been passed through a DDL shaper, further enhancing the timing differences between the two species, adapted from [11].

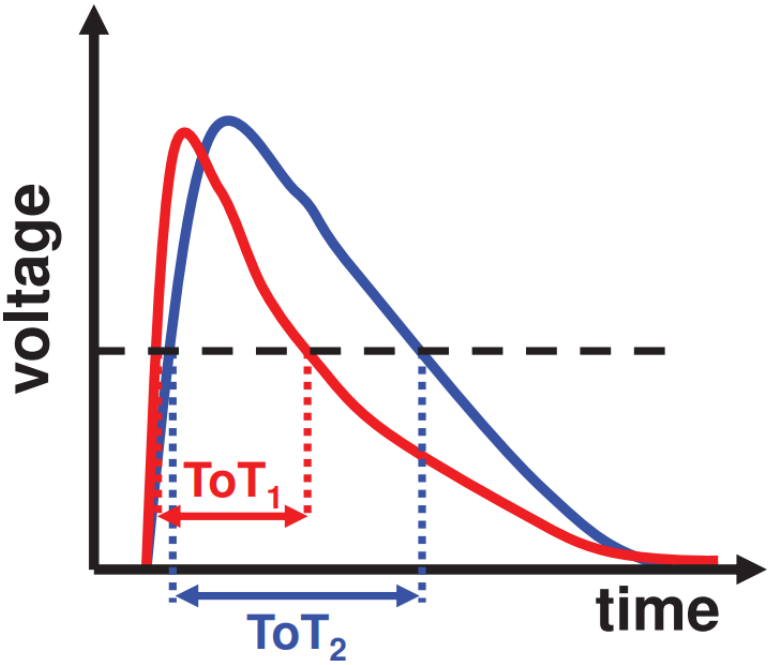

Figure 2.16: An example of the variation in ToT values for different species caused by their different timing profiles, with the dashed line set as the threshold value to be exceeded, adapted from [98].

implement electronically, as will be discussed in chapter 4.1. It is possible to separate γ-ray and neutron species in a simpler way, although this method would only work for inorganic materials.

By using the neutron hotspot described in chapter 2.3.1, an upper and lower level discriminator can be set to ignore all inputs below and above this 3.1 or 3.2 MeV_{ee} value and focus solely on the hotspot. This means that lower energy γ-rays can be ignored, and higher energy γ-rays such as the 4.4 MeV γ-ray expected from an AmBe source could also be ignored. Due to the continuous nature of an organic scintillator PSD result, such as EJ-276, (although this method would have some benefit for EJ-299-50 due to the ^{6}Li content) this method would not work for an organic scintillator. This method is named as such due to it's implementation using comparators to set the upper and lower limits for the neutron discrimination.

2.6 Electrical Components and Pulse Shaping

In order to transition from theoretical PSD methods to their application, it is required to use electronic methods, be they analogue or digital as briefly discussed in chapter 1. The primary difference between analogue and digital relate to the input signal. Analogue electronics consist of a continuous waveform, whilst digital signals use discrete values. This means that when PSD is performed in the analogue realm, it will be performed on a waveform, similar to the shape seen in figure 2.12. However analogue signals need to be converted into a digital form at some stage for modern analysis, so it is important to understand the conversion from one form to another.

2.6.1 Analogue Electronics

Analogue electronics rely solely on the electrical signals produced from the detector, which is passed through a series of electrical components that manipulate the original detector output into a waveform that is ready for PSD analysis. These stages follow on from the detector stages described in 2.4, where the detector output has been converted into a measurable signal for signal readout. Whilst this signal is technically measurable, it is often not large enough for direct use in the electronics, leading to the first (or amplification) stage. This is performed in order to boost the signal to a level that is readily measurable by the electronic systems, without having to use more complex components.

This amplified pulse will be of the same shape as the one produced by the detector, which will be that of an exponential decay, again similar to the shape seen in figure 2.12. This shape is not ideal for analysis, as the longer falling edge will mean that it is likely to interfere with the next waveform, and distort results. An example of this, known as pulse pile up, can be seen in figure 2.17. Once this pulse has been shaped into an appropriate form, it is then possible to perform analogue PSD. This is done using a series of analogue logic stages, where operations are performed on the waveform using the timing characteristics of the incident waveform, with

the intention of determining whether a γ-ray or a neutron was detected. This logic result can then be converted into a digital form for DPP, but this is the overall analogue process of amplification, shaping and finally logic.

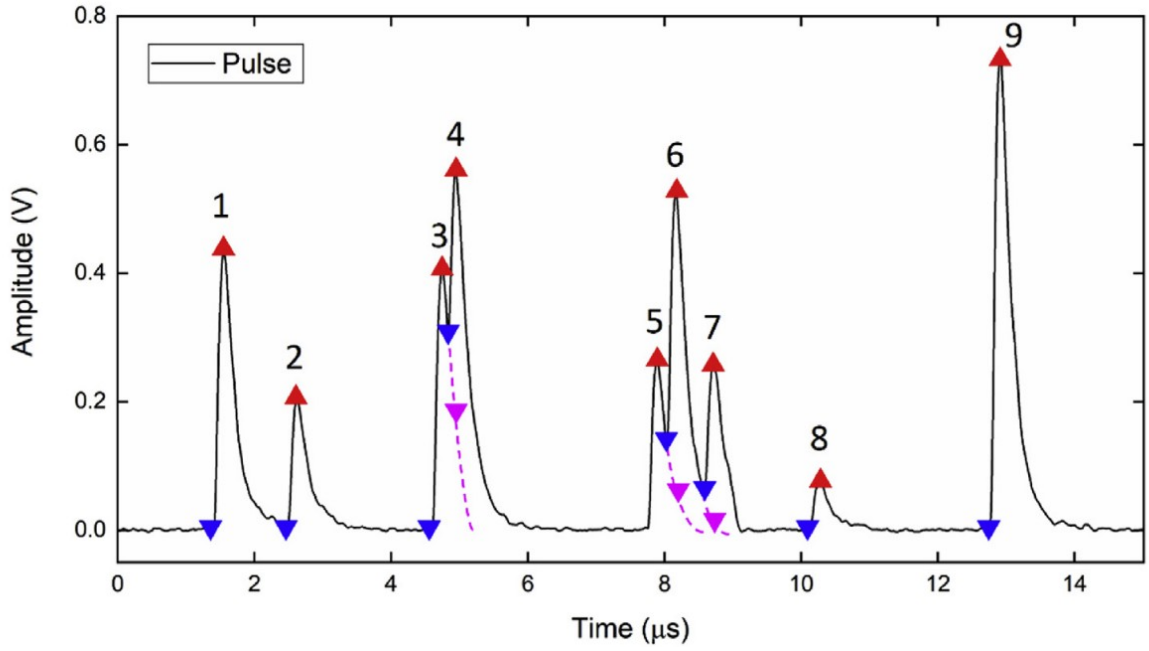

Figure 2.17: An illustration of pulse pile up caused by pulses with long tails, with the blue triangle denoting the start of each pulse, the red triangle the peak of each pulse and the purple triangle denoting the pulse profile that is lost to the pile up process. This demonstrates the need for pulse shaping to reduce the impact of multiple pulses interacting, adapted from [102].

Operational Amplifiers

One of the most important components in analogue and digital electronics is that of the operational amplifier (op-amp), which has a myriad of uses. These include, but are not limited to, buffers (or voltage followers), active filters, voltage amplifiers, transimpedance amplifiers and comparators, all of which have been utilised at some stage throughout this investigation. Op-amps are integrated circuits (ICs) that contain a series of components such as transistors, resistors and capacitors that are designed to perform operations on a waveform. Depending on the size and complexity of the IC, there can be a large number of components within the op-amp.

The primary building blocks of op-amps are transistors, which can be mainly operated in their linear region or operated as a switch. This is because a transistor uses a similar design to that of the PN junction described earlier, but it takes the concept further with an additional stage, meaning that transistors are found in PNP or NPN forms. This forms three terminals, the

emitter, which supplies charge carriers, the base, which controls the flow of these carriers, and the collector, which receives them. This form of transistor is known as a bipolar-junction transistor (BJT), but another form exists, known as a field-effect transistor (FET).

A FET uses an electric field to control the current flow, and operates in a similar manner to that of the BJT, but instead of being current driven as a BJT is, a FET is voltage driven. This means that a FET uses only one type of charge carriers, so is available in N or P types, rather than the NPN or PNP versions for BJTs. A common type of FET is the metal-oxide-semiconductor FET or MOSFET, which uses a semiconductor to isolate the gate part of the MOSFET. The three terminals of a MOSFET are different to that of a BJT, with these being the gate, which is where the voltage is applied to allow current to flow, and the source and drain, with the source acting as the input and the drain as the output. MOSFETs have low noise, high speeds and are low power, making them useful in this investigation.

By building an op-Amp IC out of many transistors, it is possible to form logic gates (which will become crucial in chapter 2.6.2) and to also amplify a waveform. This amplification is known as the op-amps gain, which is the value that the input signal is multiplied by to produce the output signal, and there are two primary ways of achieving gain. The first is open-loop gain, which occurs when the output of the op-amp has no (either positive or negative) feedback, causing an extremely high gain of $\sim$20,000 or more, although in reality this often saturates the op-Amp, which is when the output voltage reaches the maximum operating limit and cannot produce any greater signal.

The more common way of producing gain is to use closed-loop feedback, performed by feeding the output of the op-Amp back to the input. This gain is then dependant on the components used in the feedback loop, with an example of inverting and non-inverting op-Amps presented in figure 2.18. This allows for much more predictable operation, with the gain determined by the configuration and resistor values chosen, meaning that with good design choices, it is possible to achieve high stable gains in order to amplify input pulses to the desired output.

In terms of an SiPM output, the most commonly used op-amp design is that of a transimpedance amplifier (TIA), which converts a low level current output into a measurable voltage output. TIAs are extremely common for converting photodiode outputs because the resistor in the feedback path converts the output current into voltage using Ohm's law, the capacitor in the feedback loop is present to improve stability. A basic example of this can also be seen in figure 2.18.

It is possible to set an op-amps gain to 1, which is known as unity gain. However, guaranteed unity gain stability is not available for all op-amps, as some are not stable until higher gains,

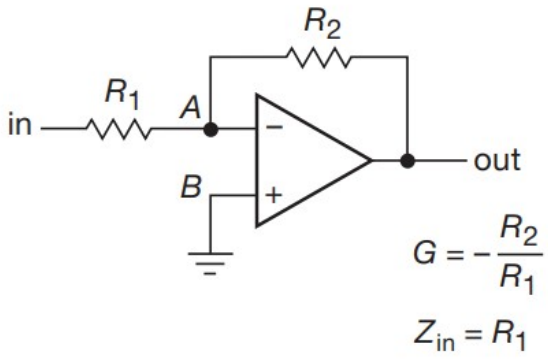

(a) Inverting Amplifier Topology

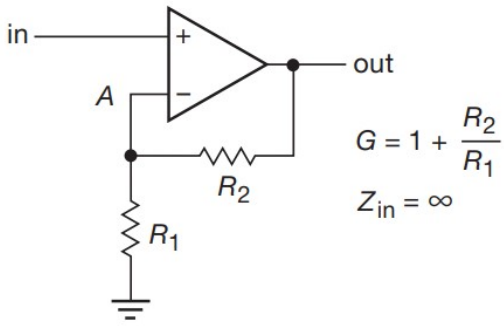

(b) Non-Inverting Amplifier topology

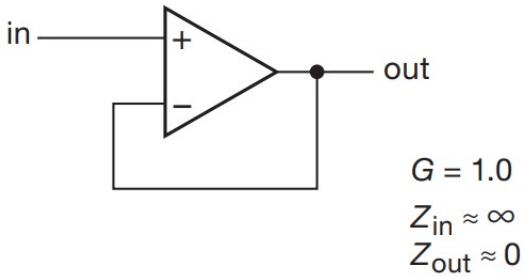

(c) Buffer Amplifier Topology

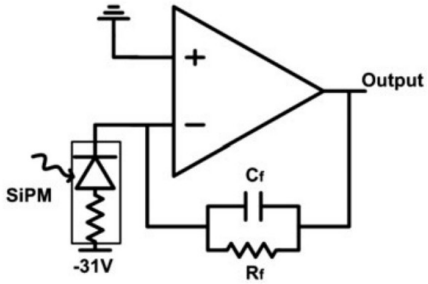

(d) Transimpedance Amplifier Topology

Figure 2.18: Four common op-amp topologies that perform specific operations on an input waveform, all of which are utilised at various points in the final electrical designs. Their respective gains (G), impedances (Z) and resistance (R) are also included. Figures a-c are adapted from [103], while d is adapted from [104].

but this is a key feature in the design of active filters. This is performed by taking the output of the op-amp and connecting it to the inverting input, which is done in order to have a high input impedance and a low output impedance. This means that the op-amp will act as a buffer (also known as a voltage follower, as the input and output voltage are the same) where the signal is unaffected by passing through the op-amp. This essentially forms a block in the circuit which effectively isolates the signal source from the load, ensuring the original signal source is minimally affected by the characteristics of the load.

Pulse Shaping

Op-amps have other uses than just amplification, as they can also affect the shape of the input pulse in different ways. At this point it is necessary to make a definition between active and passive components. A passive component is one that does not require an external power source to operate, and as such does not amplify the signal, whereas an active component is the inverse. To this point, a resistor or a capacitor is a passive component, whilst an op-amp is an active component. This is vital when designing a filter, which is used to allow certain

frequencies to pass, whilst attenuating others. There are many forms of filters, but key forms to consider are that of the highpass, lowpass and bandpass filters. The highpass (also known as a CR filter or differentiator) filter operates as the name implies, allowing frequencies above the cutoff frequency (defined in equation 2.13) to pass. The time constant τ of the filter is given by the product of the capacitance C and the resistance R:

$$f_c = \frac{1}{2\pi RC}. \tag{2.13}$$

Conversely, a lowpass (also known as an RC filter or integrator) filter allows frequencies below the cutoff frequency to pass and attenuates others. These can be combined to form a CR-RC filter which is also a bandpass filter, allowing a specific range of frequencies to pass whilst attenuating lower and higher frequencies. As a CR filter differentiates the input pulse, and an RC filter integrates the pulse, it is possible to shape an exponential input into a Gaussian form using a series of CR-RC^n filters, with $n = 4$ being enough that difference between the resulting waveform and a true Gaussian is negligible [48]. An example of this is seen in figure 2.19. Pulse shaping can be done with either passive or active filters, with active filters varying from passive due to the use of one or more op-amps in the design (the number of filter stages describes the filter's order). This adds amplification to the design but also complexity as active filters are harder to design, meaning that there is a trade-off between filter design choice. An additional differentiation stage can be very useful in pulse shaping, in the form of a CR-RC-CR filter. This additional stage converts the pulse into a bipolar pulse, and is useful at high counting rates. It is key in performing the ZC PSD method described in chapter 2.5.3, as this allows the pulse to cross zero as seen in figure 2.15.

2.6.2 Logic

Once the pulse has been amplified into a measurable voltage and shaped into a Gaussian to reduce pulse pileup, it is then ready for PSD analysis. There are many ways of doing this which can be replicated in analogue electronics, with the output of these stages then needing to be converted to a digital form for final processing and presentation.

Converters

It is often necessary to use the output of one stage to influence the next, and this is possible using a form of converter, which takes the form of the output and converts it into an alternate required form. There are three primary converters that are of interest to this investigation, which are

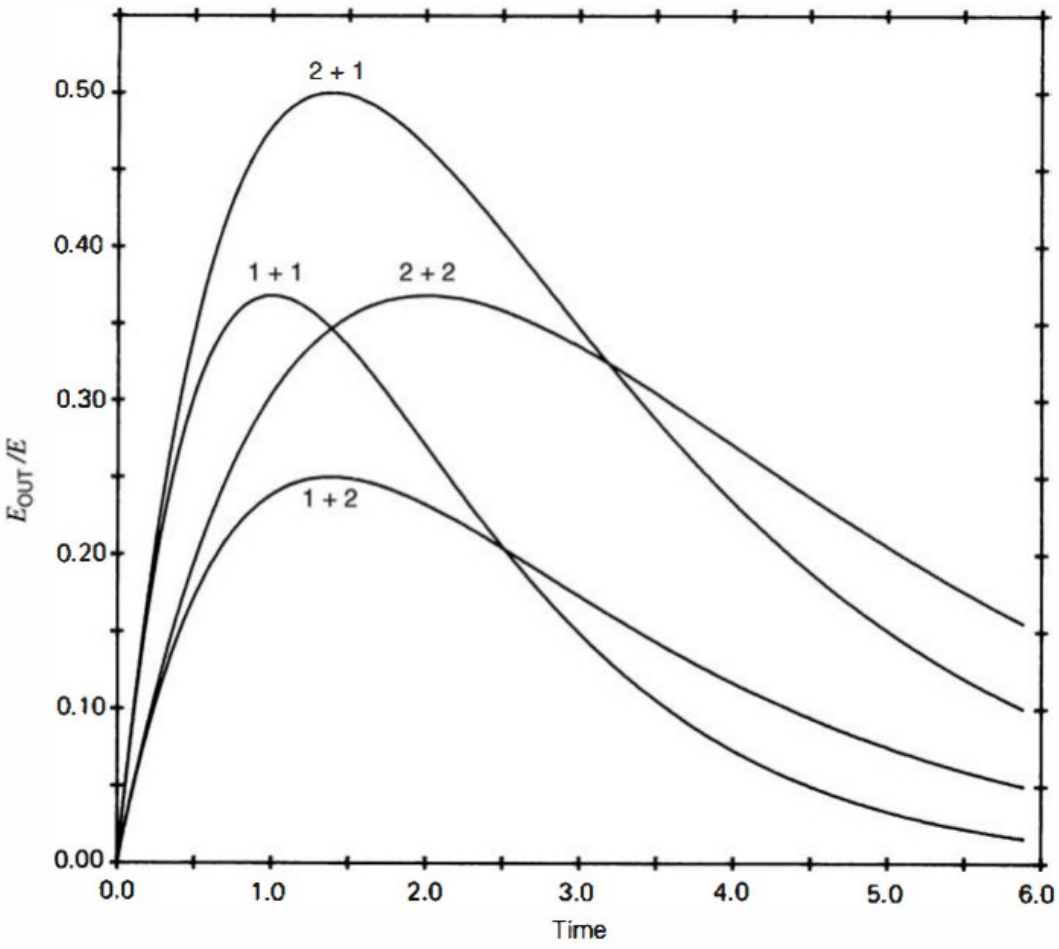

Figure 2.19: A CR-RC filter network with the effect of each stage shown. The E_{out}/E axis title is the final amplitude of the waveform divided by the initial amplitude. The number of CR differentiation stages is shown, represented as the first value, compared to the number of RC integration stages, represented as the second value, and their respective impacts on the output waveform demonstrated. A CR stage shortens the pulse length and forms a sharper peak, which can be seen in the (2+1) stage. However, the integration performed by additional RC stages causes the waveform to broaden, as can be seen in the (2+2) stage. This figure was adapted from [48].

time-to-digital converters (TDCs), charge-to-digital converters (QDCs) and analogue-to-digital converters (ADCs).

TDCs

A TDC commonly uses two input signals, a start and a stop signal. When the TDC receives the start signal, it begins a delay and then upon receiving the stop signal, the corresponding time interval is converted into a voltage output. This allows the timing between two events to be known very well, which will be very useful for determining the timing between two PSD events, such as is the case with the ZC PSD method. These input signals are often generated by a constant fraction discriminator (CFD), which is crucial in these logic designs. A CFD operates

by only triggering when an input pulse reaches a certain percentage of its amplitude, typically 20%, the details of operation will be covered in chapter 4 [105].

ADCs

An ADC is key building block for many systems and is a necessary stage in order to convert analogue outputs, such as the voltage output of a detector electronics chain, into a output that can be read and processed by a digital system. Essentially, an ADC takes real world output data and converts it into a form required for digital logic processing. This is done by taking the analogue signal at the moment it enters the ADC, and using a comparator to output a high or low voltage depending on the input, in the binary form 0 for low (or false) and 1 for high (or true). This is a key design element when using comparators, which are similar to op-amps (with the same electrical symbol), but with a reference and input voltage, comparing these two, and outputting a digital signal when the input voltage is higher than the reference voltage. This means that a basic comparator acts as a 1-bit analogue ADC, whilst modern ADC ICs will have a far higher number of bits.

There are many different forms of ADC, with one of the most common known as a flash ADC, named as such as they are the fastest way to convert from an analogue to a digital output in a data acquisition (DAQ) chain. A flash ADC is created by cascading many high speed comparators together, each of which will provide one quantisation level, meaning that for a modern 14-bit ADC, 2^{14} comparators will be contained within. This means that whilst the conversion speed is an advantage, a flash ADC will require greater power than other forms, and can be more expensive due to the large number of components required. An example of an ADC comparator chain can be seen in figure 2.20. An ADC is a key feature in modern DPP as it allows for the full pulse to be digitised and analysed, although this comes at the cost of increased processing time. Further detail on ADCs and their various forms can be found in [106].

QDCs

A QDC is similar in many ways to that of an ADC, and often uses an ADC during operation. A QDC will integrate charge over a given timing window, determining the amount of charge contained within. By using two of these with different integration windows it is possible to create a long and short integration window, which would then serve as the long and short gates necessary for the CC PSD method described in chapter 2.5.2. This result is then passed through an ADC for digital conversion, which as previously stated is a required stage regardless of the analogue logic that has been used to perform PSD on a waveform [108].

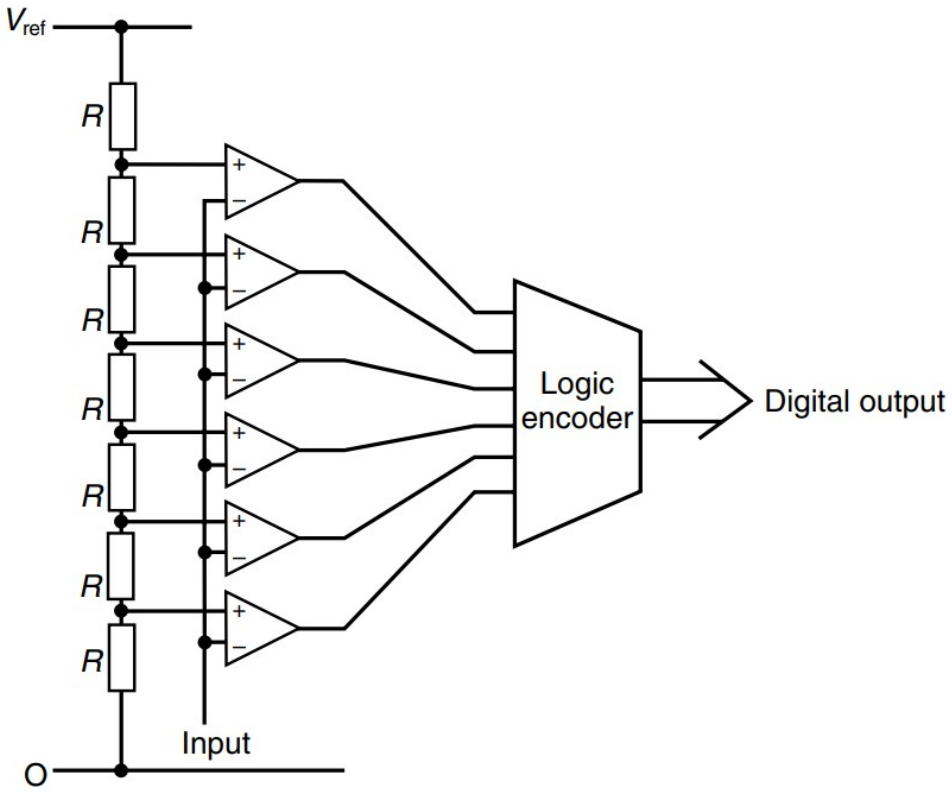

Figure 2.20: A flash ADC comparator chain, with a potential divider defining each quantisation level from the reference voltage for comparison by each comparator and the result being fed into a logic encoder for digital output, adapted from [107].

Flip-Flops

Once these analogue signals have been converted into a digital form, it is possible to pass these signals through logic gates. These come in several forms, such as the OR gate, which outputs 1 when either of its inputs are 1, or the AND gate, which outputs 1 when both of its inputs are 1. There are several different forms of logic gate, each giving a specific output depending on the state of the input signals.

It is possible to connect two NOR (Not OR) gates in such a way that the output of one gate is fed to another and vice-versa, resulting in an SR (set-reset) latch. An SR latch can be created using other gates, but this is a common version which is an asynchronous circuit (meaning that it does not require a clock signal), and can be used to store binary data, essentially the building blocks of memory. This is in contrast to the D (data) flip-flop, which requires a clock signal. An example of a combination of an SR latch and a D flip-flop can be seen in figure 2.21. A D flip-flop captures the value of the input at a certain portion of the clock cycle, meaning that it can capture the rising edge of a pulse for example. By using the outputs of two D flip-flops, it is possible to separate different parts of a waveform, which will be key in designing the charge comparison analogue design, further detail on latches and flip-flops can be found in [109].

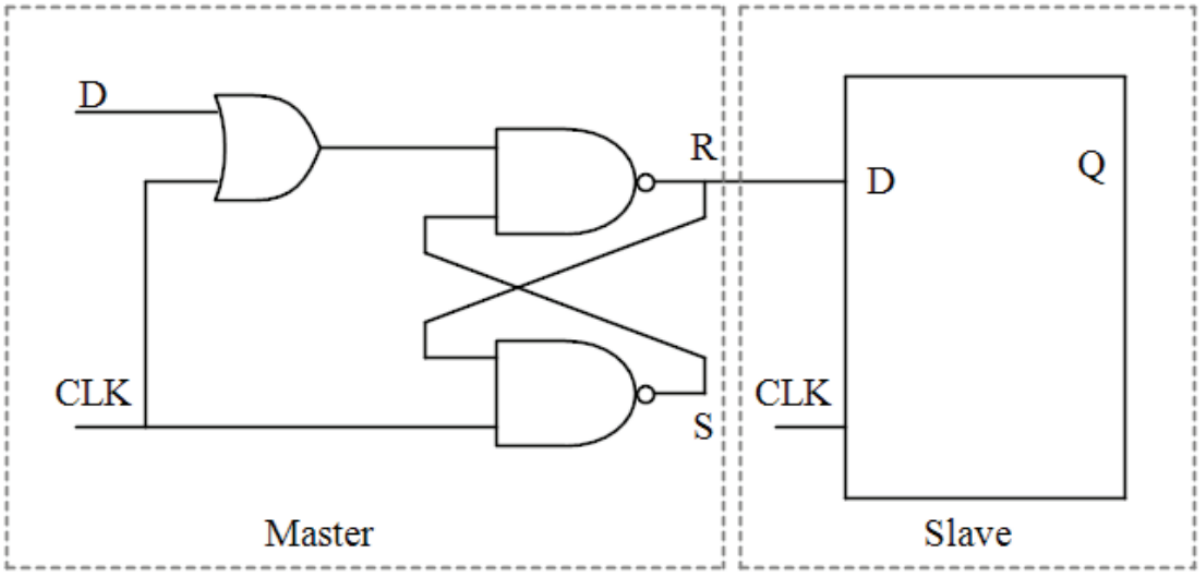

Figure 2.21: An example of an SR latch and a D flip-flop, with input data D, being fed into an OR gate, then into two NAND (Not AND) gates, creating the SR latch. CLK is the clock input signal, with Q being the flip-flop output, adapted from [110]

Microcontrollers

Despite the overall aim of an analogue system, in modern analysis DAQ chains, a point will be reached where digitisation is unavoidable. By doing this as late as possible in the chain, the result can be fed into a microcontroller or μC. These have existed in some form since the 1970's, but modern advancements have allowed for the development of small, high-bit and low power μC's with a wide variety of potential applications. μC's are essentially a small computer contained within a single IC, that has all the features that could be expected from a computer such as memory, a CPU and I/O terminals. This means that the digital outputs of each DAQ chain can be processed in an environment that allows for better visualisation and analysis of results for later presentation [111].

2.7 Noise

When designing and fabricating any electronic circuit, noise is something that must be considered, as it will impact upon the desired output to some extent. This is often expressed as the signal-to-noise ratio (SNR), as there will always be some level of noise present in the system. There are many different forms of noise that need to be considered, each of which comes from different sources within the system. As stated this is unavoidable to some extent but there ways to reduce noise to a degree. There are four primary noise sources that need to be considered in detector systems and electrical design, all with their own contributions, which are Johnson noise, Shot noise, Flicker noise and Burst noise. Each of these noise sources will be

present in each system to some extent, and are described here for completeness.

Johnson (Nyquist) Noise

The first noise source that must be understood is one that is found regardless of any voltage present in a system, which is Johnson (Nyquist) noise. This is the electronic noise created by the random thermal agitation of electrons inside a resistor, and is unavoidable at room temperature uses, as this is dependent on the temperature of the material. This can be seen in equation 2.14:

$$e_n = \sqrt{4kTR} \qquad V/Hz^{\frac{1}{2}}, \tag{2.14}$$

where e_n is the noise voltage-density, k is Boltzmann's constant, T is the absolute temperature, and R is the resistance. This can be reduced by reducing the temperature of circuit but there will always be some attributable noise contributions from Johnson noise throughout the system.

Shot Noise

The second noise source is known as Shot (sometimes called Poisson) noise, and this arises from the discrete nature of electric charge. The finite nature of the charge results in statistical fluctuations of the current, and if these charges act independently of each other then the fluctuating current noise density is given as:

$$i_n = \sqrt{2qI_{dc}} \qquad A/Hz^{\frac{1}{2}}, \tag{2.15}$$

where q is the electric charge, and I_{dc} is the direct current. This is similar to Johnson noise in that it is 'white noise' which means that it has a flat frequency spectrum, or that there is the same amount of noise power in each Hz of frequency [103]. For both Johnson and Shot noise their noise distributions are Gaussian, although the reason that Shot noise is sometimes known as Poisson noise is that it follows Poisson statistics, meaning that as the number of events increases it approaches a Gaussian distribution [103][112].

Flicker Noise

Johnson and Shot noise are both unique as they will exist in all electronics to some extent regardless of the actions taken to reduce them. In reality, components will have additional sources of noise, known as excess noise, that depend on external factors such as the construction material and potential component defects. Flicker (or $1/f$) noise is one such excess noise source, which is directly affected by the construction material. This noise has a $\sim 1/f$ power spectrum, which when plotted against voltage or current falls as $1/\sqrt{f}$, meaning that it is more significant at lower frequencies, as white noise sources are more prevalent at higher frequencies [113].

Burst Noise

Burst noise is the final noise source that needs to be understood within the context of this investigation, and is similar to Flicker noise in that it is dependent upon the material rather than a physical process. Burst noise then differs further from the three aforementioned noise sources, as it cannot be described by a distribution and is instead a random noise signal, best demonstrated by some of the other common names for Burst noise, such as 'random telegraph signal'. Burst noise occurs in semiconductors, and consists of random jumps between two voltage levels on the order of milliseconds. This noise comes most often from defects caused by the manufacturing process, even such problems as surface contamination, and can be seen in many op-amps, each of which will have its own independent burst noise contribution [114].

Chapter 3

Experimental Methodology

Several different avenues of investigation were required throughout this work, as whilst the physical processes were analysed using the described scintillation materials paired to photon detection technologies, these results needed to first be processed digitally to determine performance, before the eventual planned transition to an analogue design. This meant that the experimental work comprised of the investigative process and the data acquisition process before this information could be used to later simulate and design the analogue solution.

This analogue solution also required testing and analysis, but this process varied from that of the digital investigation. This is because of the lack of high speed digitisers in the analogue solution, meaning that the full waveform cannot be recorded and analysed in the same manner. Some understanding of the behaviour of the analogue methods can be determined by taking the initial analogue result and processing it using a digitiser, but in the final analogue solution this would not be possible.

The performance criteria of the digital investigation included some of the key detector terms introduced in chapter 1, such as the energy resolution and efficiency, which could be evaluated in both digital and analogue regimes through digitiser use. However these will not function as final performance metrics that can accurately compare both the current digital operation with a proposed analogue solution. To this end, the traditional figure-of-merit (FOM) analysis can be utilised to produce these parameters. The first is that of the FOM itself, as this will give a separation between the γ-ray and neutron species present. However, this can be taken a step further by evaluating the Gaussian fits, as seen in figure 2.14, used to determine the FOM. The overlap of one Gaussian's falling edge to the others rising edge can be used to create a true positive rate (TPR) and a false positive rate (FPR). These values can be used to create a receiver operator characteristic (ROC) curve, which will be explained in greater detail in chapter 5. A ROC curve can be used to evaluate how often one species will be mis-identified as another, therefore giving a value for how often a γ-ray is incorrectly classified as a neutron, and thus a

measure of accuracy for overall detector performance.

3.1 Investigation Process

The original motivations for this work required a low power, small and sturdy detector, both to enable field deployment and extend detector lifetime. To this end, SiPMs with an analogue PCB design were always considered to be the final step, but to proceed immediately to this point presented many challenges. Firstly, as also discussed in chapter 2.7, SiPMs are known to have a temperature dependent dark count greater than that of PMTs, so it was decided to begin this investigation with PMTs due to their reduced dark count at room temperature and greater overall stability. Secondly, analogue electronics are more difficult to develop and implement than digital solutions, as whilst the reliance on physical processes increases the processing speed, it means there are more opportunities for noise and disruption (such as a damaged component) to enter the system.

Therefore, using a PMT with a digital process in combination with CLLBC and EJ-276 (as the best available inorganic and organic scintillators at that point of investigation) would be the ideal setup for early stage results. The very first γ-ray spectra were recorded using a 2 inch Photonis XP2262 PMT [115]. This was powered by a high voltage (HV) power supply, with the results being fed into a high speed digitiser, although this PMT was later replaced with a Hamamatsu R1828-01 due to ageing concerns [116], with an example of this setup seen in figure 3.1. Data recorded at the University of Michigan used a 2 inch Hamamatsu R7724 [117], contained within a M510-20x20 aluminium casing, and data recorded at the Lawrence Livermore National Laboratory (LLNL) used a 1 inch Hamamatsu R1924A [118]. An additional μ-metal shield is often placed around a PMT to further reduce the noise present in the system, a picture of this can be seen in figure 3.1, with the black material around the body of the PMT being the μ-metal shield.

A Broadcom 4x4 array (AFBR-S4N44P164M [119]) was chosen and ordered for the SiPM array, due to its high photon detection efficiency (PDE) of 68% [120]. A previous SiPM model (ARRAYJ-60035-64P-PCB developed by SensL [121]) was also used in the early stages of this investigation. This SiPM was used for some early γ-ray and neutron results, but damage to the board this component was housed on, resulted in this component being unusable. Due to the increased photon detection efficiency of the Broadcom SiPM, it was decided to prioritise constructing a board to pair with this SiPM to provide the results desired for this investigation. The higher DCR at room temperature of SiPMs was a primary factor in their later adoption in this project, but their sturdiness and low operating voltage of 30 V to 60 V made them key to the eventual development stages of this investigation.

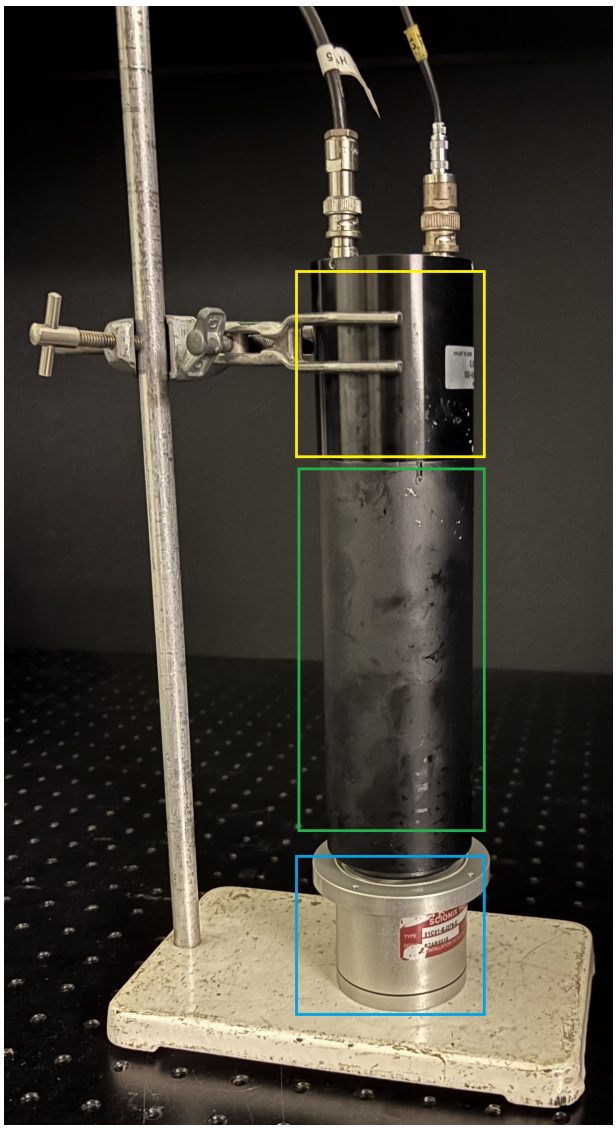

Figure 3.1: A picture of a R1828-01 PMT combined with the EJ-276 scintillation material, with the base containing the electrical components present in the yellow highlighted area. The vacuum tube covered by the μ-metal shield is seen in the green highlighted area and EJ-276 is seen in the blue highlighted area, there is also EJ-552 optical grease between the scintillator and the PMT. For results, a γ-ray source would be placed within 2-5 cm of the crystal base seen in the blue area, most often for a 10 minute time interval.

In order to use a SiPM array, it must be connected to a PCB which required design and manufacture. Further detail on this process is presented in chapter 4.3, but as a brief overview, a printed circuit board (PCB) is a bespoke electrical board with components soldered onto it and designed to carry out a specific purpose, often similar to an ASIC. They are made of non-conducting material such as fiberglass or FR4 (a composite fiberglass and epoxy resin material), with conducting tracks (known as traces), connecting the components. More detail of this process is presented in section 4.3.

Each scintillator material had a 2 inch diameter, with a transparent window to allow emitted

photons to escape, this window was constructed of perspex for EJ-276 [122], and quartz for CLLBC and CLYC [123][124]. Due to the hygroscopic nature of each material, this window is required to create a hermetically sealed environment essential to prevent water from damaging the scintillation material. The entire crystal was housed in an aluminium shell, an example of this for both CLLBC and EJ-276 can be seen in figure 3.2. This was the same for CLYC but not for EJ-299-50, which was constructed as a single crystal element of dimensions 6.7 cm x 3.5 cm x 3.4 cm. The EJ-276 material has had issues with degradation, caused by oxygen exposure and known as yellowing, in the past [25], which meant that the material performance has decreased over time, although this has not been seen presently in this EJ-276 sample, due to the sealed casing. This was part of the motivation for the development of EJ-299-50, as seen in other literature [24][92][125][126].

Figure 3.2: The aluminium housing for each scintillator material with the EJ-276 2 inch diameter perspex window and the CLLBC 2 inch diameter quartz window both visible. EJ-276 is the material on the left and CLLBC is on the right, with CLYC housed in the same setup.

An image of the EJ-299-50 element can be seen in figure 3.3, with the scintillator material being wrapped in several layers of different reflective material. Firstly, a layer of highly reflective foil is placed around the scintillator, with a reflectively of approximately 98%. This was then wrapped in 2 layers of teflon tape, and finally sealed with a layer of black tape that had a reflective inner layer. All of this was done in order to maximise light collection efficiency, and provide the best possible results for the detector.

Each scintillator material was bonded to the PMT using EJ-552, a silicone based optical grease.

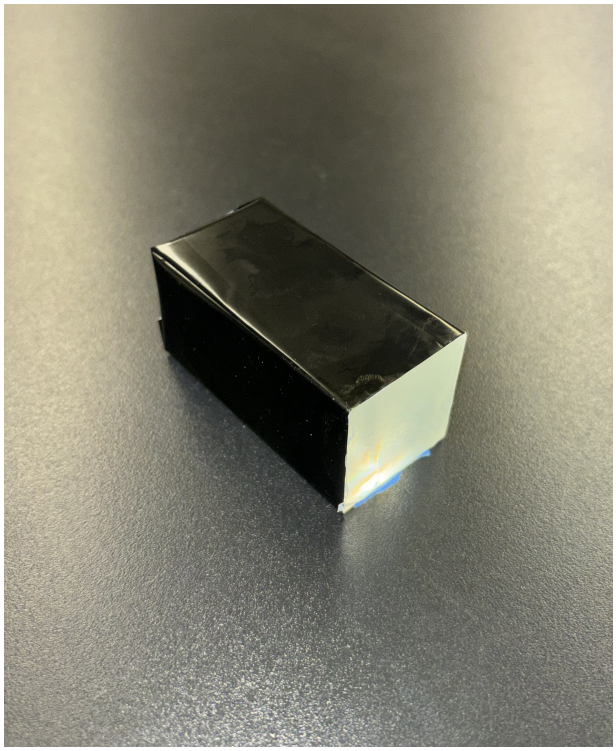

Figure 3.3: A picture of the smaller EJ-299-50 element, with the high reflectivity wrapping seen on the outside with the open surface to be mounted to a PMT or SiPM.

Data taken during this investigation demonstrated an approximately 40% decrease in light collection when the grease was not used. So optical grease was used to increase bonding of the scintillator to the PMT and to reduce the presence of air gaps between the PMT and the crystal. It is important to reduce the presence of air gaps in order to reduce the Fresnel losses, which are the losses incurred due to light reflecting off the end of one medium as the light travels between mediums of different refractive indexes. The refractive index of perspex is $\sim$1.5, whilst the refractive index of glass is also $\sim$1.5, meaning that there would be little issue from detector material to PMT. The Broadcom SiPM is also covered in a layer of transparent epoxy which has a similar refractive index of $\sim$1.5 [127]. However air has a refractive index of $\sim$1, so this is where the Fresnel losses are introduced to the system. The EJ-552 has a refractive index of 1.47, which is closer to the desired 1.5 refractive index, helping to reduce overall light losses.

As a result of the 2 inch PMTs chosen for the early stage of this investigation, there was no major concern of light loss, as the active area of the PMT matched that of the detection material. This however presented a challenge when transitioning to SiPMs, as the 16 mm^2 active area of the SiPM did not match the 2026 mm^2 area of the scintillator, this can be seen for the different scintillation material geometries in figure 3.4. There are a number of ways to mitigate this issue, with one example consisting of using a strip of reflective material surrounding the scintillator and leaving a gap for the SiPM. This reflected the emitted light back into the crystal causing it to reflect until it was incident upon the SiPM. This will affect the timing characteristics of the

detector, but as light travels 1 m in 3.3 ns, it is likely to add a ns or fewer onto the falling edge of a pulse, and as such it was not considered to be a serious concern for the PSD results. This was the method performed at LLNL, as the 1 inch PMT did not match the 2 inch scintillation materials.

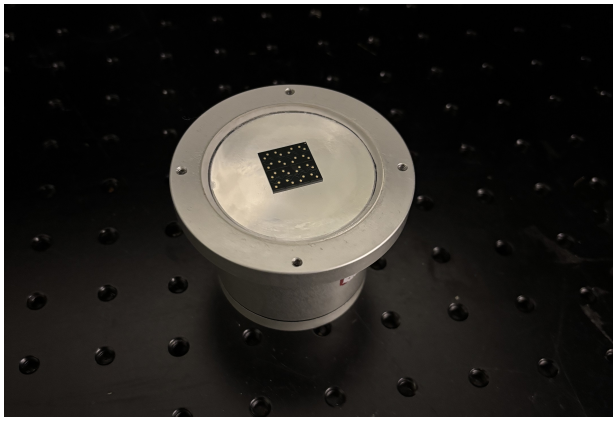

(a) SiPM size compared to 2 inch detector material.

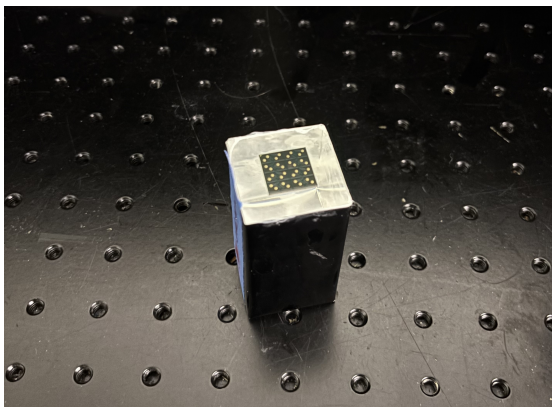

(b) SiPM size compared to EJ-299-50 material.

Figure 3.4: Pictures of the SiPM on one of the detector materials, demonstrating the difference in active area between the 2 inch scintillation material and the 16 mm^2 SiPM, as well as the smaller difference seen with the EJ-299-50 material.

Other methods of accounting for this size disparity involve using either a light guide or a Winston cone. Both can be expensive and difficult to manufacture, but a light guide can increase the energy and spatial resolution of the detector [128], whilst a Winston cone can increase photodetector efficiency [129]. A light guide does as its name suggests and directs the light from a source to a location, by passing light through the material via total internal reflection until it reaches the intended location, reducing the amount of light lost to the environment. A Winston cone on the other hand, concentrates light from a large area into a smaller area, with the light reflecting off the internal surfaces until it reaches this smaller area. These devices operate in a similar manner to each other but the primary difference is that a light guide is transparent, whilst a Winston Cone is not. Initial designs have not included either of these methods, but it is certainly an area that could be explored in future to fully maximise the light collection efficiency.

The initial phase of this investigation used several γ-ray sources of known energy, including ^{137}Cs, ^{60}Co and ^{22}Na, which have photopeaks of 662 keV, 1173 keV and 1332 keV respectively, with ^{22}Na having a 511 keV annihilation and 1275 keV peak. These peaks can be used for detector calibration, which converts raw digital amplitude pulses into a gamma equivalent energy (GEE) scale. Other known energy γ-ray sources have been used at irregular intervals, such as ^{152}Eu (which has many photopeaks) and ^{54}Mn, which has a 835 keV photopeak. The aforementioned 3 sources provide the clearest results due to good separation between peaks

and relatively long half-lives, with each source starting with an activity of ∼300 kBq. This does mean that there is some variation in overall activity, as ^{137}Cs has a half-life of ∼30 years, whilst ^{22}Na has a half-life of ∼2.6 years. The two ^{60}Co photopeaks can be an issue to resolve in a plastic scintillator due to their proximity, hence the use of other sources.

The primary reasons to collect this γ-ray data are that it is important to understand each materials ability to detect γ-rays, and to calibrate detector response. For inorganic spectra this is done using a calibration curve, where the known γ-ray photopeak energies are plotted against amplitudes recorded by the digitiser. This should form a linear relationship, allowing for spectra to be converted from amplitude into energy, with units of keV_{ee}, or keV electron equivalent. An example of a calibration curve can be seen in figure 5.1.

It is somewhat more difficult to calibrate an organic scintillator, as when a γ-ray scatters in a scintillator and escapes, only some of the energy is deposited. The greater atomic number of inorganic scintillators mean that this energy can be fully absorbed, creating a clearly defined photopeak, but this is not the case in an organic scintillator. The lack of clear photopeaks to fit a Gaussian distribution make finding correct comparison values challenging. The Compton edge, described in chapter 2.2.2, is often used instead, although there are some disagreements where this is located, with values ranging from 66% to 89% [130]. A commonly used value is 80%, and as such this was chosen as the value to calibrate the organic data present in this investigation, with a Gaussian fit applied to the falling edge of the organic scintillator spectra. This disparity is because this lack of clear photopeak means that the Compton edge is broad, and as such different conditions give slightly different edge positions.

Once these γ-ray energies were acquired, neutron data was required. There are a variety of methods possible to acquire neutron data, many of which have been applied at various stages throughout this investigation. The first of these methods is to use a spontaneous fission source, such as ^{252}Cf, which is a common analogous source for plutonium, and is often used to start up nuclear reactors. This spontaneous fission creates an average of 3.7 neutrons per fission [131], with an energy range up to 13 MeV, but a mean energy of 2.3 MeV [132]. This makes ^{252}Cf a useful source for neutrons, as it will most likely be present as a small solid source, able to be transported relatively easily, allowing for fast and thermal neutron energy regimes to be investigated. Its primary drawback is that it has a comparatively short half-life of 2.6 years [133], meaning that sources will need to be replaced more often than others, as after 10 years only 25% of the isotope will be remaining. The University of Michigan had a well categorised ^{252}Cf source, meaning that it was possible to perform a time-of-flight (ToF) experiment to determine the neutron energies present, greater details of an experiment of this kind can be found in [134].

A different option is to use an α emitter in combination with a low Z element such as Beryllium. This can present itself in different forms such as an AmBe or a PuBe source. At Glasgow there is an available AmBe neutron source, which produces neutrons when ^{241}Am, which is an α emitter, is mixed with ^{9}Be. The full equation can be seen in Equation 3.1.

$$^{9}\mathrm{Be} + \alpha \rightarrow ^{12}\mathrm{C} + n + 4.44\,MeV\,\gamma \tag{3.1}$$

An AmBe source has the same benefits as a ^{252}Cf, in that it is mobile and can be moved in order to suit the needs of the current work. It is also a passive spontaneous source, meaning that the neutrons will be generated regardless of human input, which is not always the case as will be discussed when describing the generator sources. An AmBe source has an energy spectrum up to 11 MeV, with a mean energy of 4.2 MeV, meaning that an AmBe source has a greater mean average than a ^{252}Cf source. An AmBe source also has a significantly longer half-life than a ^{252}Cf source, as the half-life of ^{241}Am is 432 years.

An alternate way of producing neutrons is to use an active method such as a neutron generator, using either the deuterium-deuterium (D-D) or deuterium-tritium (D-T) reaction. Both of these were utilised for the digital PSD investigation undertaken at the University of Michigan. A neutron generator operates by accelerating deuterium ions into a metal hydride target, commonly titanium, that is loaded with either deuterium or tritium depending on the required generator type. The D-D generator in use was a ThermoFisher Scientific MP320, which had a neutron flux of $\sim 2 \times 10^{6}$ neutrons per second [135]. The neutrons produced in the D-D reaction are monoenergetic 2.45 MeV neutrons, as seen in figure 3.5, allowing for a known incident neutron, although this can vary depending on the specific generator [136].

Whilst the neutrons produced by a D-D generator give a lower energy source of neutrons, a D-T generator produces higher energy monoenergetic neutrons, as seen in figure 3.6, with 14.1 MeV neutrons produced. The D-T generator used in this case was a ThermoFisher Scientific P211, which produced a neutron flux of $\sim 1 \times 10^{6}$ neutrons per pulse [137]. The generator was set to a pulse rate of 100 Hz, meaning that a total flux of $\sim 1 \times 10^{8}$ neutrons per second was emitted, although this generator had issues with stability, meaning that runs would often end prematurely due to generator fault, and this neutron flux was also dependent on the specific generator, as with the D-T generator [138]. This neutron energy allowed for the detection and analysis of high energy neutrons that would otherwise not be accessible from passive sources. A picture of the two generator setups used at the University of Michigan can be seen in figure 3.7.

As discussed in section 2.2.1, there are different energy values of neutrons that are of interest to this investigation. The moderator primarily used throughout this work was paraffin wax, an

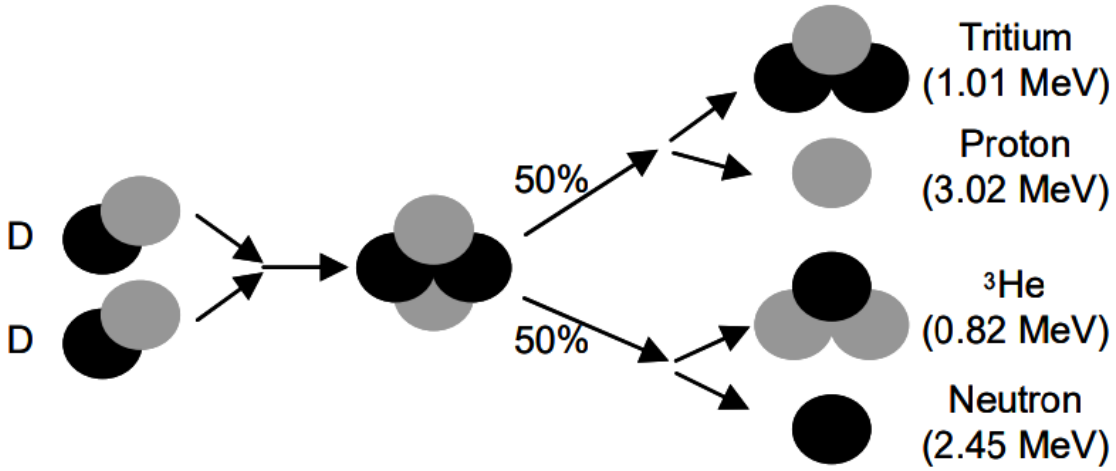

Figure 3.5: An illustration of the D-D fusion reaction, with the 2.45 MeV neutron seen, lower than that of the D-T reaction, adapted from [139].

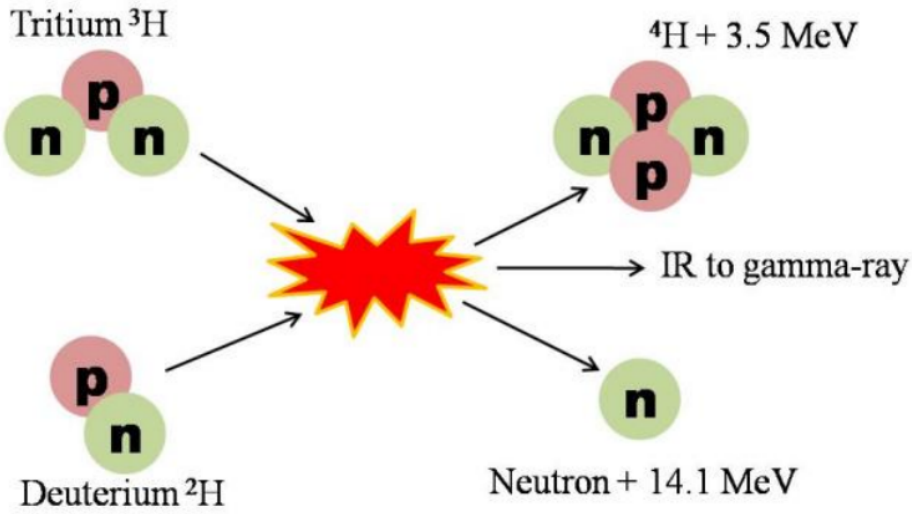

Figure 3.6: An illustration explaining the D-T fusion reaction, showing the higher energy 14.1 MeV neutron produced as well as other electromagnetic radiation such as infrared shown by the IR term, adapted from [140].

example of this can be seen in figure 3.8. It is also necessary, when using an AmBe or ^{252}Cf source in combination with an inorganic scintillator, to place some high Z material shielding (the most common being lead), to reduce γ-rays present that can be overwhelming to the detector, and can hinder the acquisition of the thermal neutron peak.

When using an inorganic scintillator, it is important to use enough moderation material to thermalise fast neutrons to thermal energies, allowing for more effective thermal neutron detection. Whilst the most often used moderator throughout this work was paraffin wax, other suitable materials exist, such as high density polyethylene (HDPE). The amount of these materials required for effective moderation varies, as seen in figure 3.9, which suggests that

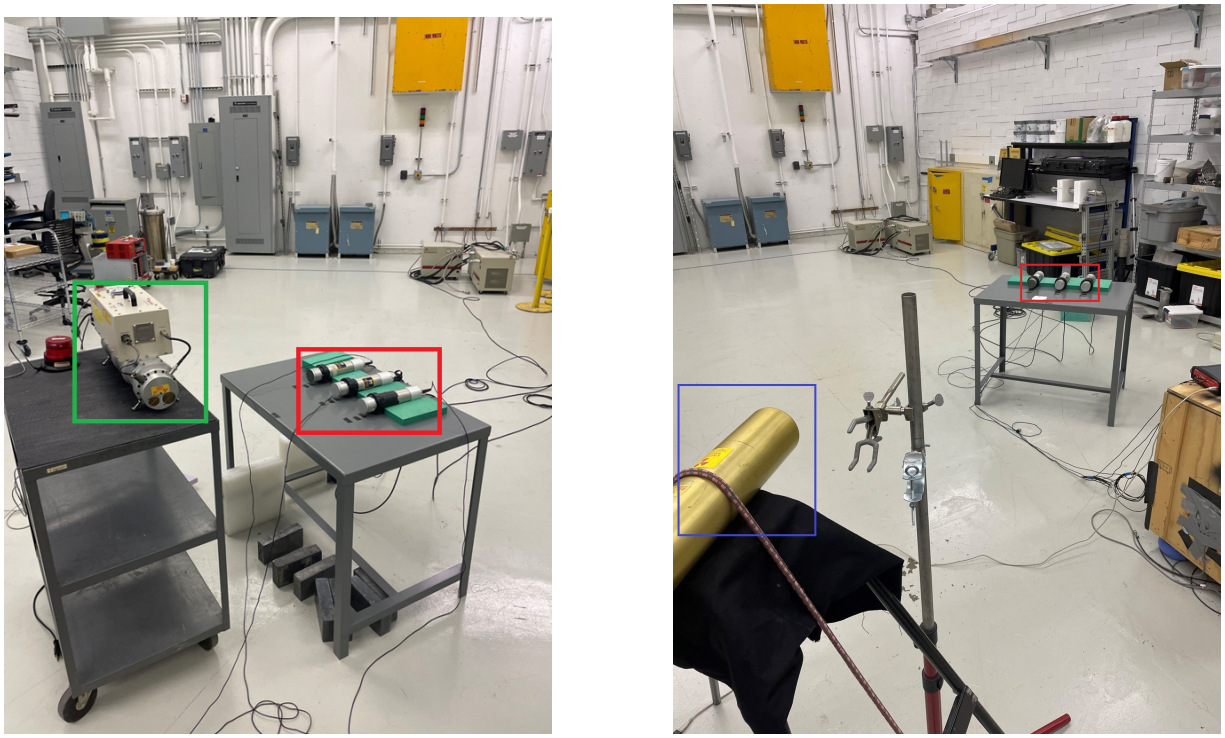

(a) D-D generator experimental setup.

(b) D-T generator experimental setup.

Figure 3.7: A picture of the ThermoFisher Scientific MP320 D-D and the ThermoFisher Scientific P211 D-T generators setup used at the University of Michigan, with a greater distance seen for the D-T than that of the D-D generator due to the higher energies and neutron flux rates. The neutron flux rate for the D-D generator was $\sim 2 \times 10^6$ neutrons per second, whilst the D-T generator had a neutron flux rate of $\sim 1 \times 10^8$ neutrons per second. The scintillators attached to PMTs can be seen in the red highlighted area, whilst the D-D generator is shown in the green highlighted area and the D-T in the blue highlighted area.

6 cm is the ideal thickness of paraffin wax for thermal moderation. This was considered for the AmBe source present, but due to the large activity of this source, it was decided to use a greater proportion of paraffin wax, as there needs to be sufficient moderator to cause a significant proportion of fast neutrons to thermalise, but to not be fully absorbed within the moderator as this would create additional γ-ray contributions [141]. The initial activity of this AmBe source was known, but the specific activity was not, as there was no accurately known age of the source.

Overall, this meant that there was a good range of γ-rays sources present, as well as two passive neutron sources, in the form of a ^{252}Cf or AmBe source, with two active neutron sources in D-D and D-T generators, present at various stages throughout this investigation. As a result the experimental work from these sources could be paired with the scintillation materials and photon detection technologies to high speed digitisers, allowing for the full waveforms to be recorded and processed for analysis. This granted the information desired to begin the design of the eventual analogue solution.

Figure 3.8: A picture of an example setup used for an AmBe source with CLLBC. The AmBe source is contained within the lead blocks which are placed to shield the emitted γ-rays with the paraffin wax used to thermalise the emitted fast neutrons. The detector setup seen in figure 3.1 is approximately 2 metres away, but due to the strength of the AmBe source, this was not considered to be a concern. In a standard shielding setup, the moderator would be placed first then the lead, but this is not the case here. This is because of the high but unknown specific activity of the source, which, when unshielded, produced too many γ-rays and impacted the detector and digitiser performance. The decision was made to shield the initially created γ-rays, but still allow some to be produced by the moderation process so that PSD could be performed without the detector being overwhelmed.

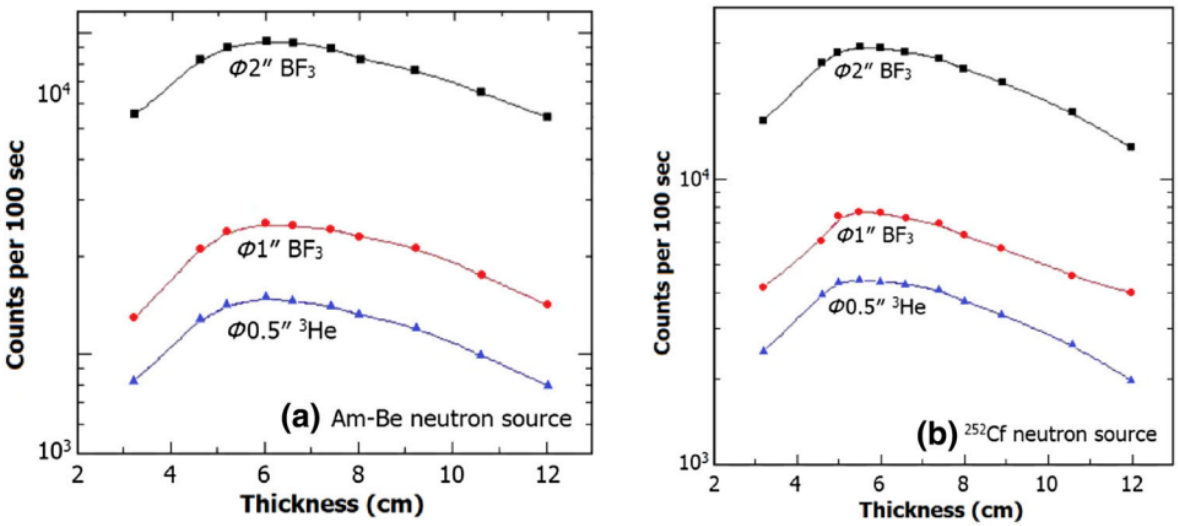

Figure 3.9: A result of a study that compared the necessary thermalisation thickness of paraffin wax when using an AmBe or a ^{252}Cf source, with a thickness of 6cm determined to be the most beneficial to neutron thermalisation with the least rate reduction, the black line represents a 2 inch diameter BF3 neutron detector, the red line a 1 inch diameter BF3 neutron detector and the blue line a 0.5 inch ^{3}He neutron detector, adapted from [142].

3.2 Data Acquisition Process

Whilst these datasets were gathered from the various available sources, it is important to understand the different methods of digital data acquisition required to record these datasets for analysis. Data acquisition (DAQ) was a crucial part of this work, with the outputs of both the digital and analogue setups requiring readout methods. The digital aspect required a combination of a high speed digitiser, and the necessary DAQ readout software to record the output. The raw data outputs would be saved separately allowing for later DPP, but the initial acquisition required specific software packages. The analogue outputs were read from the PCBs directly into a microcontroller (μC), and could be directly processed on a computer readout without the need for predeveloped DAQ software.

The CAEN DT57xx digitiser family was used extensively throughout this work for the capture of the digital pulses, with initial work recorded using the DT5720 [143]. The DT5730 later became the preferred digitiser [144], whilst the DT5742 was also used intermittently, although the DT5742 also has a DRS-4 chip that allows for a higher sampling speed that requires calibration [145]. Each of these digitisers incorporate FPGA technology, allowing for a greater level of flexibility than that would be allowed by an ASIC. The DT5730 was the most commonly used as it had a high sampling rate of 500 MS/s (MegaSamples per second), as well as having a 14-bit resolution ADC in comparison to the 12 bit-ADC of both the 5720 and 5742 [146]. The higher sampling rate of the 5742 (5GS/s) was considered, but it was decided that the higher 14-bit resolution and lack of required calibration was preferable. The 5730 uses a flash analogue-to-digital (ADC) converter, allowing for the high sampling speeds discussed in chapter 2.6.2. A physical example of the DT5730 can be seen in figure 3.10. The PMT was powered by an N1470 CAEN HV power supply, with a bias voltage of between 1.5kV and 2kV required. This additionally highlights the desire to transition to the lower power SiPM due to these high voltage requirements.

The software packages used throughout this investigation for data acquisition were the CAEN softwares WaveDump and CoMPASS [147][148]. These software packages were required by CAEN to operate their digitisers, and had both advantages and disadvantages. WaveDump was the first software used in this investigation in combination with the DT5720 digitiser. WaveDump was an older software, and presented as a basic waveform acquisition console, but with more flexibility, as commands were given in a text file that was applied to the digitiser for each run, allowing for more advanced functions to be called if required. This allowed for greater control of the settings before each data run, but had a steeper learning curve than CoMPASS.

CoMPASS, on the other hand, was a newer software that was used with the DT5730 digitiser.

Figure 3.10: A picture of a CAEN DT5730 digitiser with the smaller number of available channels seen on the front, as compared to other available CAEN digitisers. Also the USB output is clearly seen, allowing for high speed digital outputs.

CoMPASS was designed as a software package for digital pulse processing and acquisition from multiple boards at the same time. This allowed for easier integration with varied detector systems, with the options previously required to be programmed in WaveDump available in graphical menus. This allowed for easier operation, but at the cost of the flexibility afforded by the WaveDump package. CoMPASS also allowed for easy settings control, such as the threshold represented by least significant bit or lsb, which is the smallest change in the input signal that the ADC can convert.

Figures 3.11, 3.12 and 3.13 demonstrate the real time information that is available to the user, indicating almost immediately if a desired γ-ray photopeak is present, as seen in figure 3.11. This real time use also extends to the PSD, as CoMPASS allows for the inclusion of timing gates, meaning that the CC method can be implemented in CoMPASS by setting a short and long gate that then generates a PSD value. This can then be plotted against the ADC channel number, as seen in figure 3.12, with the spread of γ-ray energies present, as well as the separate thermal neutron hotspot. This can also be performed for a plastic scintillator, as seen in figure 3.13, which has the two γ-ray and fast neutron species present as the two higher energy continuous regions.

This is in contrast to WaveDump, which instead of producing a cumulative histogram of all the results with each value present, produces a singular waveform of each input. This is also a feature of CoMPASS, but the real time histogram display of CoMPASS allows for adjustment of detector and digitiser settings without the need for any post processing.

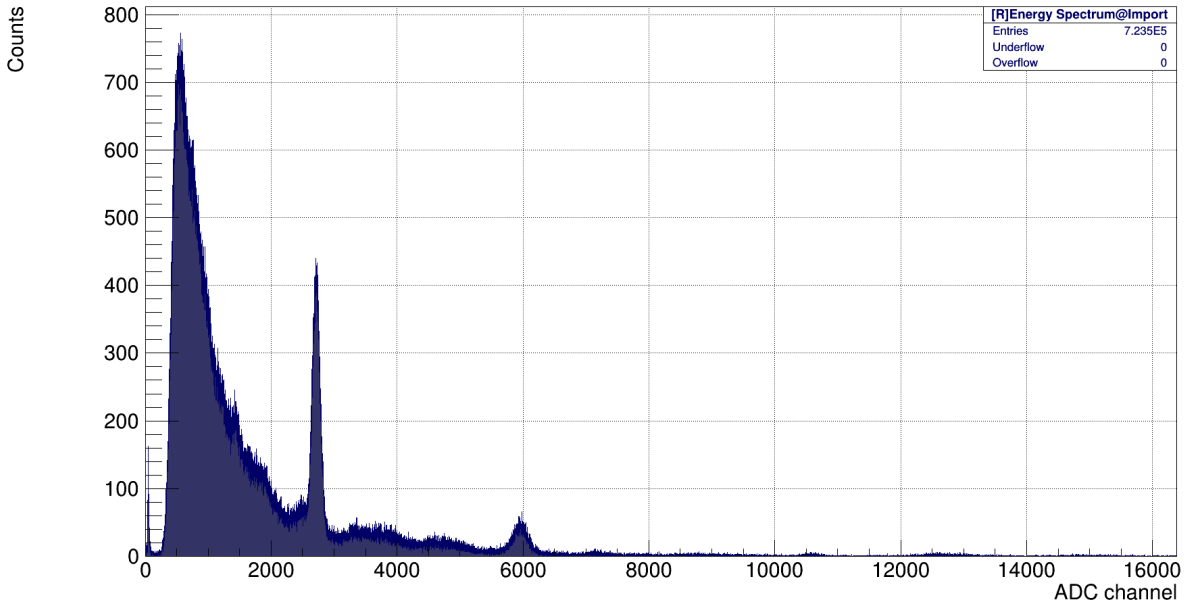

Figure 3.11: A raw CoMPASS ^{137}Cs plot taken using the inorganic scintillator CLLBC, with the 662 keV photopeak present at ∼2500 channels. The 1.49 MeV potassium line can also be seen at 6000 channels. This demonstrates the ability of CoMPASS to provide real time data and analysis for γ-ray detection. This spectra was taken with using the R7724 PMT at the University of Michigan at a bias of 1.3 kV for 5 minutes using a CoMPASS threshold of 130 lsb.

The DAQ is a key feature in the experimental work performed throughout this investigation, as it is the results recorded by the DAQ software that allow for current digital PSD methods to be performed. This means that this digital results will form the benchmark results that the analogue results will be compared to.

Once this design stage was completed, the proposed analogue solutions required testing. As stated at the beginning of this chapter, the performance metrics would be different to those of the digital process, although the overall process of investigation would be very similar. The alternate neutron sources used throughout this investigation, such as the neutron generators and ^{252}Cf sources, were not available for later analogue results, but the range of γ-ray sources and the AmBe neutron source were still available.

This meant that there was a consistent investigation process for both analogue and digital results, with the use of γ-ray sources for initial SiPM testing, before the AmBe source could be used to evaluate the PSD performance of each planned method. As each method would be designed to operate almost entirely analogue, the analogue DAQ process would be different to that of the digital results.

This is because the lack of digitiser in the analogue solution makes recording the full waveform impossible. However, as the SiPM could be used in combination with the digitiser, it was

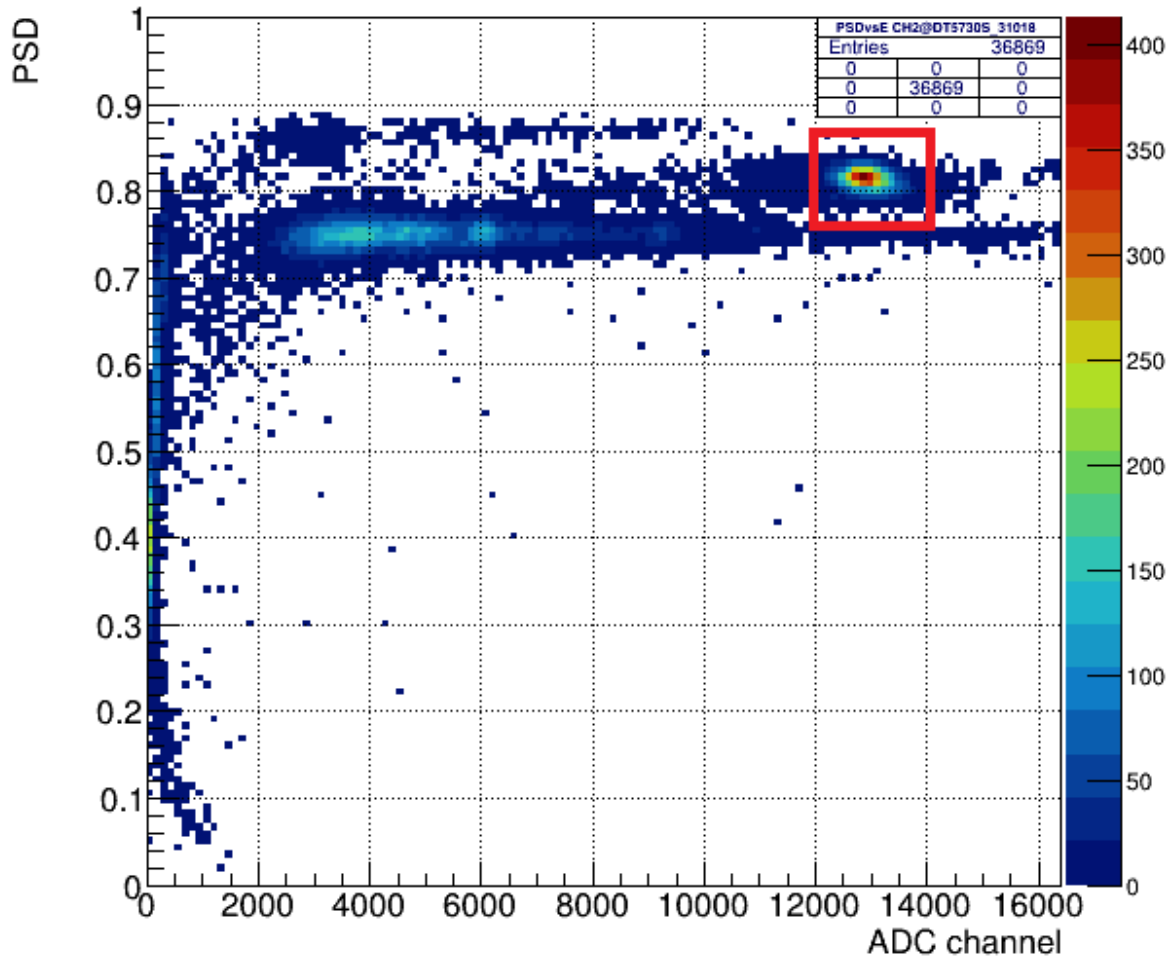

Figure 3.12: A raw PSD vs ADC Channel CoMPASS plot using CLYC and a ^{252}Cf source, with the expected neutron hotspot highlighted in the red box (added post data recording) when compared to the spectrum of γ-ray energies seen below, this further demonstrates the ability of CoMPASS to provide fast and real time PSD results for neutron and γ-ray separation. The Z axis represents counts, with this being the case for all following similar figures.

possible to understand a portion of the overall analogue process using a similar DAQ approach.

Once the full analogue solution was designed and constructed, the output format would be different to that of the digital output. This is because whilst CoMPASS allows for real time presentation of results, this is not possible with this current stage of analogue development. To resolve this, a microcontroller was determined to be the most effective method of providing a digital output for later analysis. As the method of investigation and data acquisition was decided, the next stage of progression was the electrical design, simulation and fabrication of an analogue solution in an attempt to match the digital PSD performance.

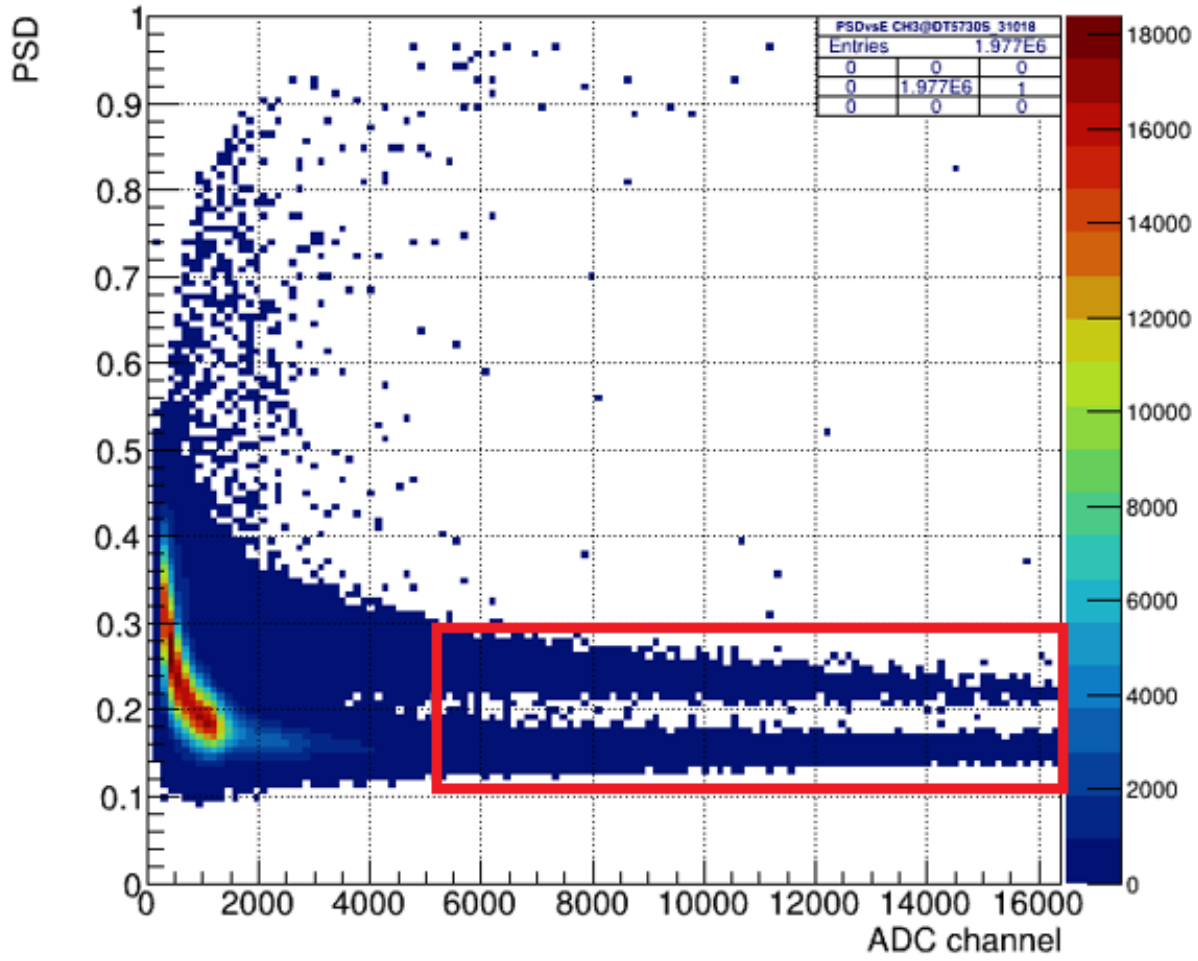

Figure 3.13: A final raw CoMPASS plot recorded using EJ-276. This spectrum has the expected separation between fast neutrons and γ-rays present, seen in the red highlighted area (added post data recording). This result is similar to the expected result shown in figure 2.13, although without the lower energy cut present. This demonstrates CoMPASS's ability to provide results for both organic and inorganic materials. Both this figure and figure 3.12 were recorded using the R7724 PMT at the University of Michigan, with a bias of 1.3 kV and a threshold of 130lsb for 30 minutes.

Chapter 4

Design

The design and manufacture of the required analogue hardware was a multifaceted process, that needed to be planned with components and theory in mind, then tested using the electronic simulation software LTSpice to ensure the effectiveness of the design, before being assembled in design software for manufacture. Each of these stages had its own challenges that were unique to that design phase, but that all contributed towards the final design.

4.1 Electrical Design

The first step in analogue electronics development is creating a functional model of each section of the required final system, in this case a printed circuit board (PCB). To this end, a modular design was chosen for each section of the resulting analogue PCB, as this would allow for any issues to be identified and resolved much easier than for one large PCB. The three planned modules were, an input bias and amplification module, a filter module and a logic module, with the logic module the stage at which the PSD method would be locked into the hardware. The output of this logic module would be read into a microcontroller (μC), as this would be the latest stage an analogue result could be converted into a digital result for analysis. In the final design, the desired filter result simulation was achieved using passive filters and several op-amps. Therefore it was decided to incorporate the filter module into that of the logic module to reduce costs from PCB manufacture, meaning that two modules were sent for manufacture rather than the initially planned three. The eventual goal was to create a single PCB that had the best performing PSD method integrated, but due to reasons that will be discussed in chapters 5 and 6, this was not achieved throughout the course of this investigation, but is something that could be resolved in future.

Upon deciding on the modular design, it was necessary to determine which method of PSD would be feasible in analogue electronics. The zero crossing (ZC) method was chosen due to its history as a commonly used form of analogue PSD, meaning that this method had provided good

results in the past, and so this novel design could be compared to detector outputs of the past. The time-over-threshold (ToT) method was chosen due to the simplicity of application, meaning that the results could be evaluated with fewer components required, therefore determining if the greater simplicity resulted in a poorer final detector performance. The charge comparison (CC) method was chosen as this is the most common method of modern PSD, with it being the PSD method automatically included in the CoMPASS DAQ software, ensuring that a direct analogue to digital comparison would be possible. The comparator method was considered, but the reduced application potential of this method caused it to be considered the weakest candidate for investigation, and so the other three PSD methods were investigated instead. This is because the comparator method focused on the neutron hotspot generated by an inorganic scintillator, therefore it was not able to function for the continuous distribution created by an organic scintillator. The block diagram for the process undertaken for the ZC module can be seen in figure 4.1.

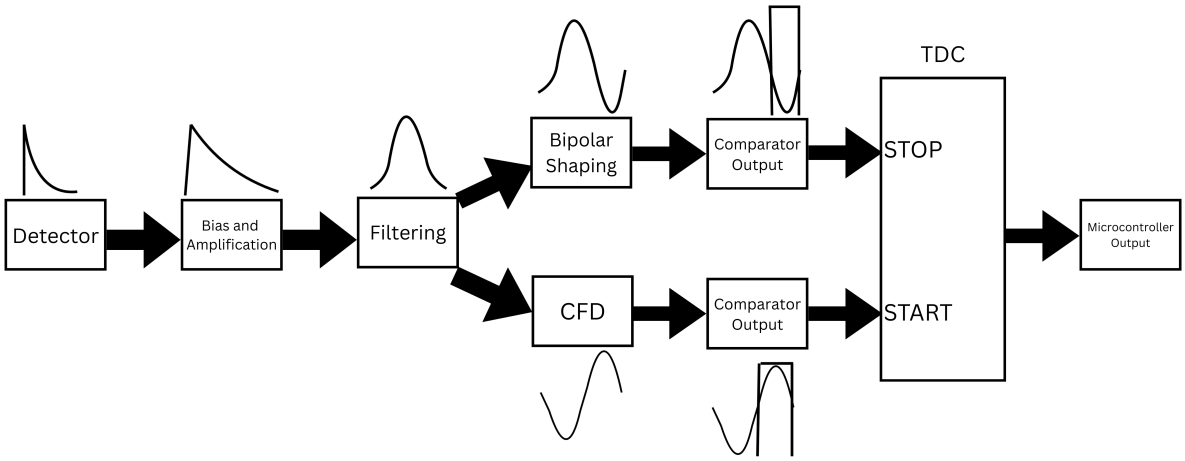

Figure 4.1: A functional block diagram of each of the necessary operations required to perform a zero crossing measurement. The initial SiPM output pulse is amplified during the bias and amplification stage, before being shaped into a Gaussian pulse shape during the filtering stage. This signal is then split, with a bipolar shaping stage and a CFD stage present. The bipolar shaping stage will create the ZC measurement time, whilst the CFD will generate the start signal for the TDC. It is the output of this TDC that will be evaluated by the μC.

Once this design stage was complete, it was necessary to choose the components that could achieve the design aims, with certain component types requiring much more consideration than others. The passive components, such as the resistors and capacitors, were chosen by evaluating the required component values, and combining this with their cost and availability. This was an easier process than later component evaluation as it is possible to find many small surface mount devices (SMDs) that have the desired component values, with 1% tolerance, at an extremely low cost. This was not always the case however, as certain ICs recommended specific component types, such as a high capacitance electrolytic capacitor close to a specific pin. Where evaluation

was vital was the choice of active components. This can be seen in the first module that was designed, the bias and amplification board.

This first module was intended to provide a bias voltage to the SiPM, and to then take the current output pulse produced by a photodiode, convert it into a voltage, and then amplify this voltage into a useful signal value. This module presented the first of many challenges experienced throughout the design phase of this investigation, as this Broadcom SiPM had a unique ball grid array (BGA) pattern that made designing and adding a footprint in PCB software extremely challenging. This required several redesigns to resolve, and exemplified why careful component choice and PCB design is important in analogue electronic design, as the design choices become locked into place once manufactured, and cannot be resolved through iteration such as in a digital environment.

The first component of importance following the SiPM was the choice of op-amp, as with the correct choice it was possible to both convert the SiPM current output and apply a large amount of gain to the signal to amplify it. This is possible using a transimpedance amplifier or TIA, introduced in chapter 2.6.1, as a common method of converting a photodiode current output into a voltage. For this reason a TIA was used, with the Texas Instruments LMH6629 chosen as a strong candidate [149], as it is an ultra-low noise, high speed op-amp, which was desired due to the fast decay times of the plastic scintillation materials.

The second active component of choice was the op-amp for the filter stage, because whilst the shaping could be achieved through passive components, several op-amps were required that were unity gain stable. This was not possible with the LMH6629 as it only became stable at a gain between 4 and 10, depending on the setting of the compensation pin. To this point, the Texas Instruments OPA820 was chosen [150], as it is another low noise op-amp, but unity gain stable, with recommended functions including ADC preamplifiers and filters, both designs that would be important in the eventual desired analogue solution.

The final component choice to be considered that would affect all three PSD board designs, was the comparator. Each of these designs would require a comparator during the logic module, meaning that this was an important choice. The component chosen to fulfill this role was the Analog Devices LTC6752 [151], as it had a fast switching time between states of 2.9 ns, with recommended uses including high speed data acquisition systems and window comparators, two more uses that are vital in this design. The ToT module required the most comparators of any module with four, the reason for this number of comparators can be seen in the ToT block diagram in figure 4.2.

The logic stage of each board has slight variations, with the CC board having two additional

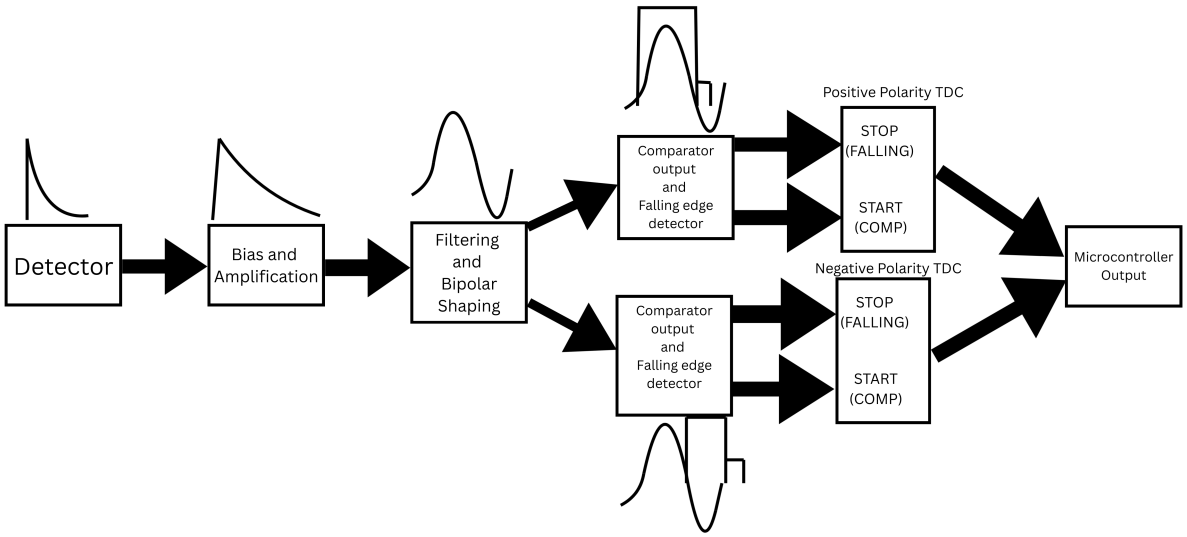

Figure 4.2: A functional block diagram of each of the necessary operations required to perform a bipolar time-over-threshold measurement. The initial SiPM output pulse is amplified during the bias and amplification stage, before being shaped into a bipolar pulse during the filtering stage. This bipolar waveform is then split, with the positive polarity comparator creating a start signal for a TDC, and a logic stage creating a falling edge detector that will generate the stop signal for the TDC. The same is true for the negative polarity waveform, with the output of each TDC being passed to a μC, where each result can be taken independently or in comparison with the other.

components that were not part of the other boards, these being the D-flipflop, and MOSFETs. The D flip-flops (Texas Instruments SN74LVC2G74DCUR [152]) are used to separate the combined output of the comparators, which comprise of the short and long gate, creating a single separate output for both gates. These gates are then sent to the gate of an N type MOSFET (Onsemi 2N7002ET1G [153]), causing it to open and allow current to flow when the comparator state is high, charging a capacitor, with the voltage discharge across this capacitor equal to the charge contained within the respective gate. The block diagram for this process can be seen in figure 4.3. The ToT board used three additional unique components, in the form of an inverter (Texas Instruments SN74LVC1G14DCKR [154]), which inverts the output state, an AND gate (Texas Instruments SN74LVC1G08DBVR [155]), which outputs high when both inputs are in a high state, and a time-to-digital converter (Texas Instruments TDC7200PWR [156]). The inverter and AND gate were necessary to create a falling edge detector that could generate a stop signal for the output TDC. The ZC board also uses a TDC to evaluate the ZC time, with the outputs of all three boards being fed into a μC. The TDC required a clock input, which was an external 16 MHz crystal oscillator (Vishay Dale XO57CRECNA16M [157]), with 16 MHz chosen as it gave the best timing standard deviation for the TDC of $\sim$40 ps [158].

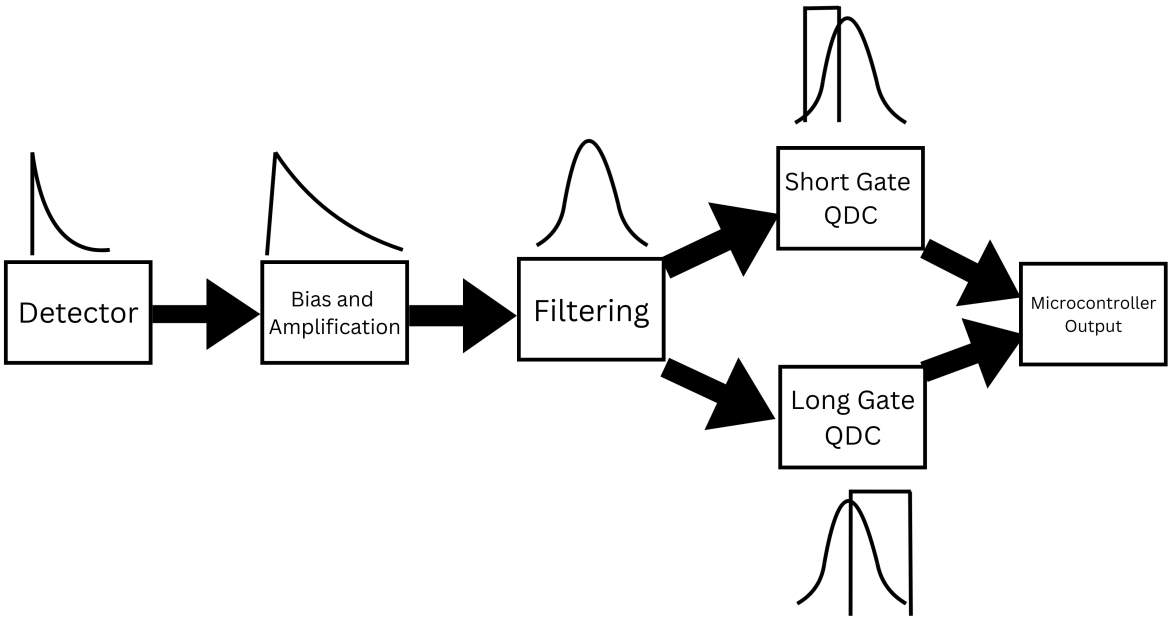

Figure 4.3: A functional block diagram of each of the necessary operations required to perform a charge comparison measurement, with the QDC outputs that record the short and long gate charges for the μC output. The initial SiPM output pulse is amplified during the bias and amplification stage, before being shaped into a Gaussian during the filtering stage. The charge contained within each preset gate is recorded by each QDC stage, before sent to a μC for evaluation.

4.2 Electronic Simulation

The electrical simulation undertaken throughout this investigation was performed using LTSpice, which is a program that builds upon the electrical simulation program SPICE (Simulation Program with Integrated Circuit Emphasis) from Linear Technology [159], which has existed since the 1970's. This is because it is not usually possible or practical to breadboard and test a full IC before manufacture, so LTSpice allows for the simulation and testing of different aspects of an IC throughout each stage of operation to ensure accurate performance. However the simulation does not always behave the same as the real PCB, as will be discussed later.

The first stage of design was to chose an input current pulse similar to that of a SiPM. It was not necessary to simulate a full SiPM, as characterising a SiPM in LTSpice was not a primary aim of this investigation, but creating effective analogue PSD from an output pulse was. Further details of SPICE simulations of SiPMs can be found in [160]. To this end, an exponential pulse with an initial current of 0 rising to 1 μA, a rise delay of 100 ns, a rise time constant (or τ as seen in the simulation software), defined as the time taken until the pulse reaches 63% of its total value, of 1.3 ns, a fall delay of 0 and a fall time constant, defined as the time taken for the pulse to reach

37% of its final value, of 400 ns. This can be seen as the input pulse in figure 4.4 and as the input values in figure 4.5 shown by the red highlighted area.

Also present in figure 4.5 is the timescale, set to 3 μs, as this was the likely timescale that most pulses would be fully resolved within, as seen in table 1.1 with the longest decay time of 1500 ns for CLLBC. There are also two step functions present for both the input current and fall time constant values, meaning that these values could be iterated over, determining if larger input currents or much longer decay times were present, they could be tested effectively, similar to those expected from long neutron decays.

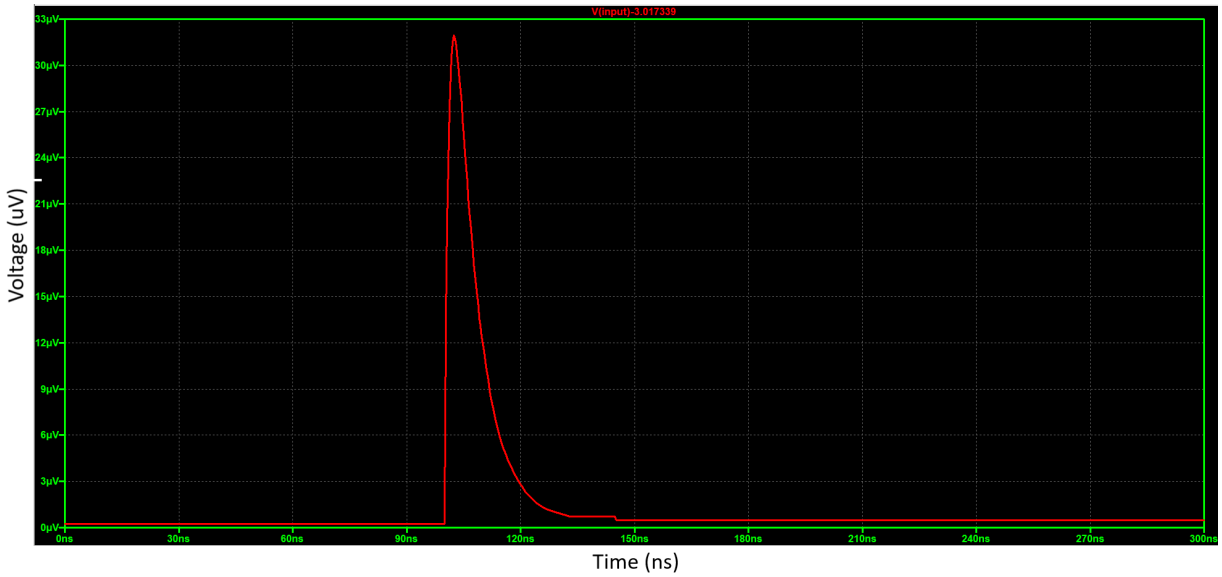

Figure 4.4: The input pulse used to determine the output of the following modules. This is a similar pulse to that of which should be produced by a SiPM, with a sharp exponential shape, a rise delay of 100 ns, a rise time constant of 1.3 ns, a fall time constant of 400 ns and a starting current of 0 A pulsed to a value of 1 μA. A $\sim$3 V offset was added to the pulse by the TIA, this has been removed in LTSpice to demonstrate the expected voltage amplitude.

In figure 4.5, the TIA setup can be seen from the LMH6629 op-amp, with the feedback capacitor and resistor present in the green highlighted area. The feedback resistor in a TIA topology decides the gain, meaning that this has a high gain of -10 $\times$ 10^3 as it is in the inverting configuration, with the feedback capacitor present to increase signal stability.

The output of this board is then passed to the configuration seen in figure 4.6, which makes up the second part of the bias and amplification module. This second part takes the output of the TIA and applies a further gain of 10 to the system, calculated from the 5 kΩ and 500 Ω resistor negative feedback network. An additional voltage amplifier was chosen for two reasons. Firstly, it was decided that some additional gain was required from the output of the TIA, but increasing the gain of the TIA, or using a second TIA stage, could create instability. Secondly, in this

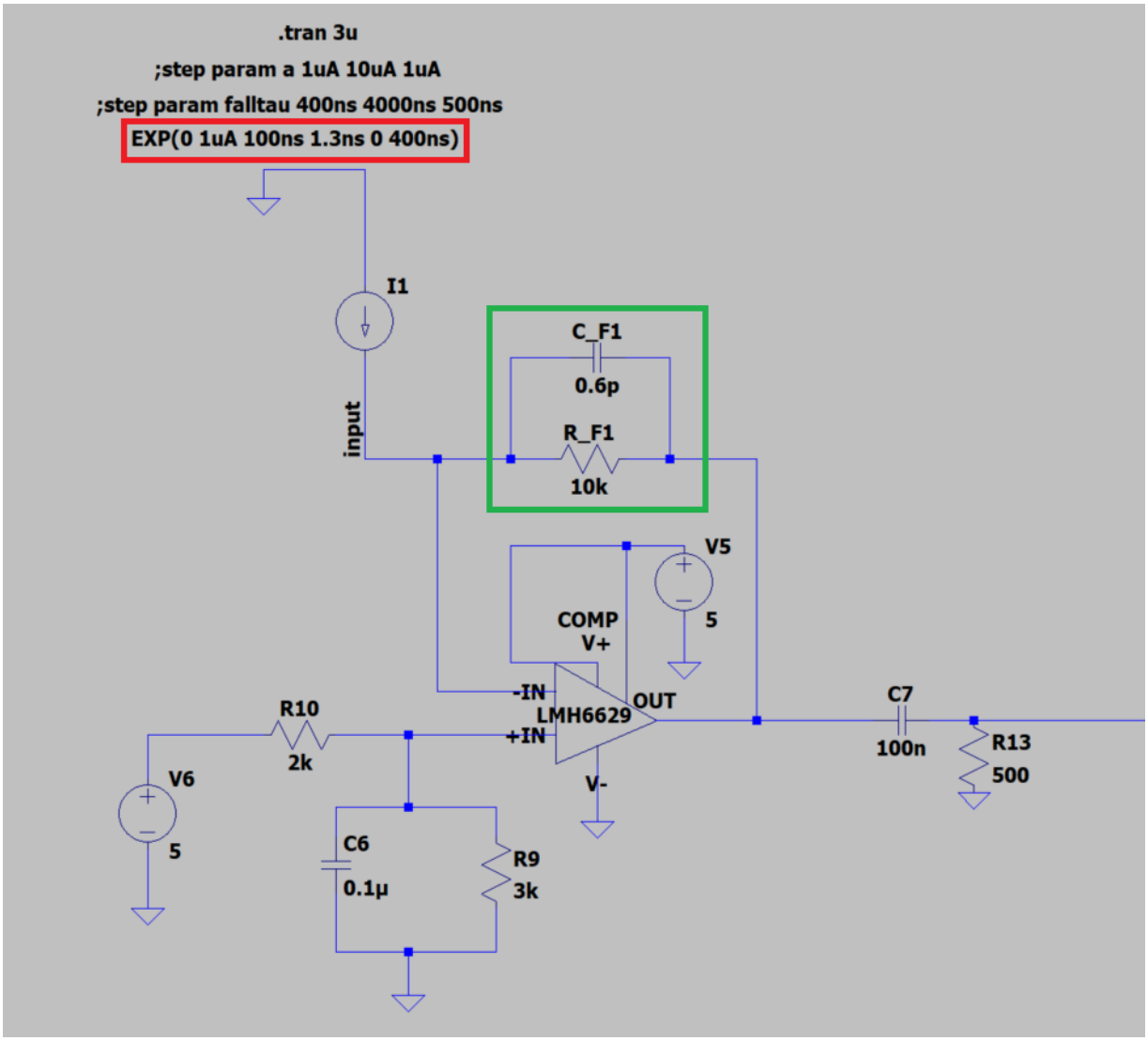

Figure 4.5: The LTSpice simulation schematic, with the current input described in figure 4.4 fed into a TIA amplifier with a gain of -10 $\times$ 10^3. There are also a series of stepping parameters present to vary the input current from 1 μA to 10 μA, to test the circuit at higher inputs. The fall time constant was also varied from 400 ns to 4000 ns in 500 ns steps to test that the circuit functioned as expected with longer pulses, such as those expected for a neutron interaction.

configuration the SiPM produces a positive polarity pulse, whilst the TIA is set in an inverting configuration, so by using an additional inverting amplifier configuration the waveform could be inverted a second time and set to a form similar to that of the input pulse.

At this point it is also important to define a feature of op-amps known as the Gain-Bandwidth product (GBWP). The GBWP is essentially a trade-off between the open-loop gain of an amplifier and its bandwidth, which is the range of frequencies where the component can operate effectively. This means that an amplifier with a high GBWP would provide high gain at low frequencies, but would have lower gain at high frequencies, and vice-versa. This meant that the GBWP of the op-amp needed to be considered in the design phase for each

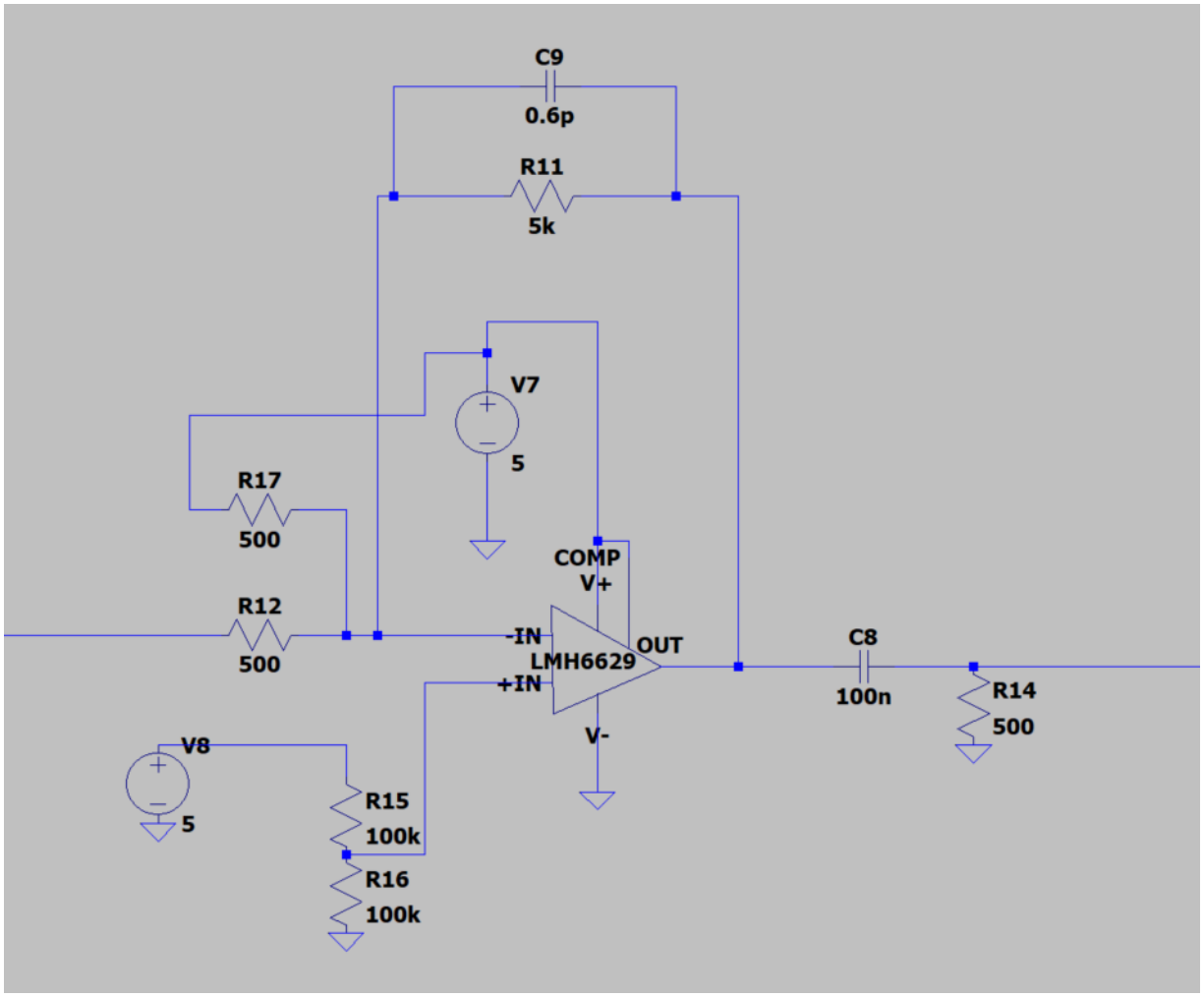

Figure 4.6: The LTSpice simulation schematic of the voltage amplifier, with a lower gain of 10 from the feedback resistors, as the output from the TIA required slightly more gain, but with greater stability than that of the TIA.

independent stage, with the expected signal frequency a major part of this design choice.

The expected output of the bias and amplification module can be seen in figure 4.7, where the small input pulse seen in figure 4.4 is amplified from a value of $\sim 33\,\mu$V to $\sim 80\,$mV, which is suitable for shaping and readout by further electronics. The Bode plot of the magnitude and phase response seen in figure 4.8 demonstrates the effective frequency range of this board, highlighting the regions where the boards output will begin to be become unstable.

The pulse produced by the bias and amplification module has the same exponential shape as that of the initial input, but as highlighted in figure 2.17, keeping this shape would introduce pulse pile up to the system. This would affect the output as the information contained within the falling edge, which is where the primary difference between neutron and γ-ray species are expected, as it would interact with the rising edge of another pulse.

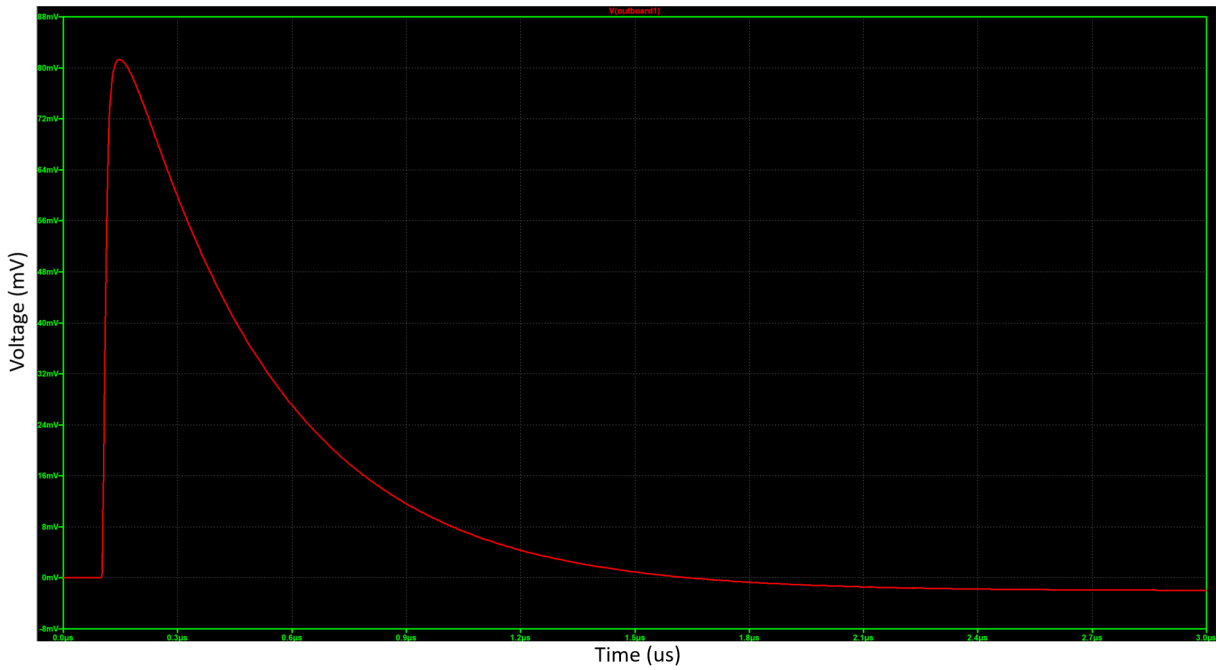

Figure 4.7: A simulated voltage output of the first board module, shown as the red trace, and an output gain of 80, shown by the voltage increase from 0 to ∼80mV. This was created from the exponential input pulse seen in figure 4.4.

This means that the shape of this pulse should be conditioned, with a Gaussian shape being the most appropriate, as the Gaussian pulse shape causes the effects of pile up to be reduced 2.17. Attempts were made to create an active filter using op-amps, but the simulations suggested that this would reduce the pulse amplitude significantly whilst not shaping the pulse as expected. The reasons for this were unclear, however when a passive CR-RC network was designed instead, it shaped the pulse in the desired manner. The planned circuit can be seen in figure 4.9 with the resulting waveform seen in figure 4.10.

This passive filtering was tested with different fall time constant values, up to 4 μs, to simulate the longer neutron decays expected in inorganic scintillators, ensuring that this filtering would behave as expected in longer pulses. However, this filtering had the unintended effect of creating undershoot, where the waveform drops below 0 before slowly recovering. This would create similar problems to the exponential decay of the original pulse, so it was necessary to remove this undershoot.

A pole-zero (PZ) correction circuit was considered, with efforts made using simulation to find an appropriate PZ value that improved overall system stability. However, many combinations were trialled, none of which affected the undershoot in a manner significant enough to remove it and restore the pulse to baseline. A second method was trialled, which involved passing the filtered waveform through a non-inverting amplifier that had a variable resistor, allowing for easily controllable gain, and a diode. This can be seen in figure 4.12.

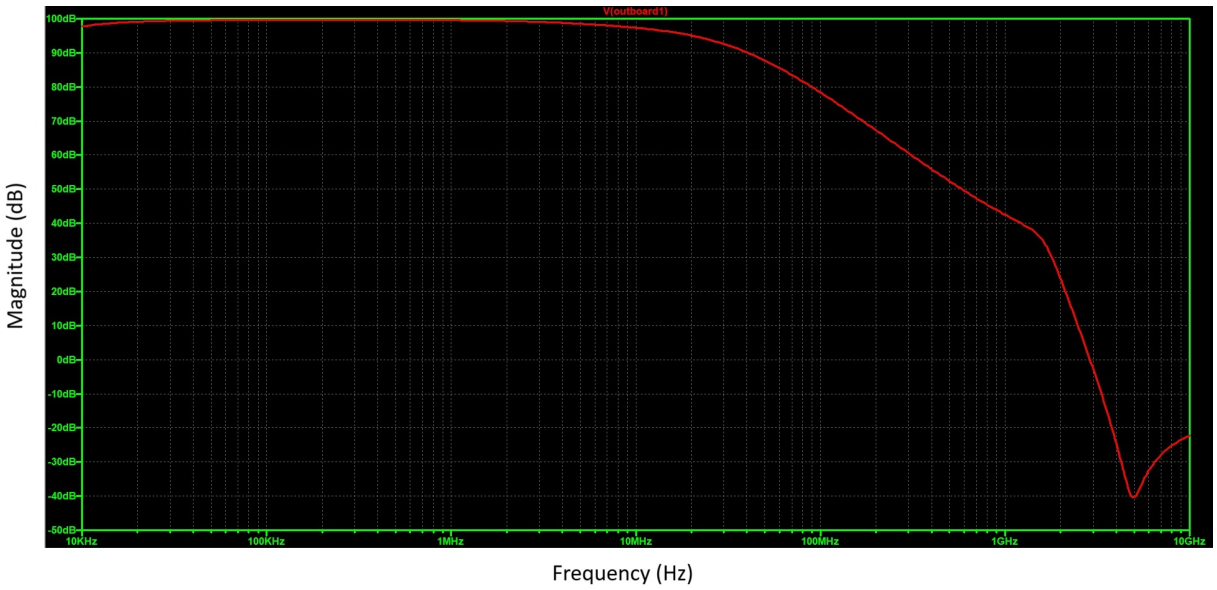

(a) Magnitude section of the Bode Plot.

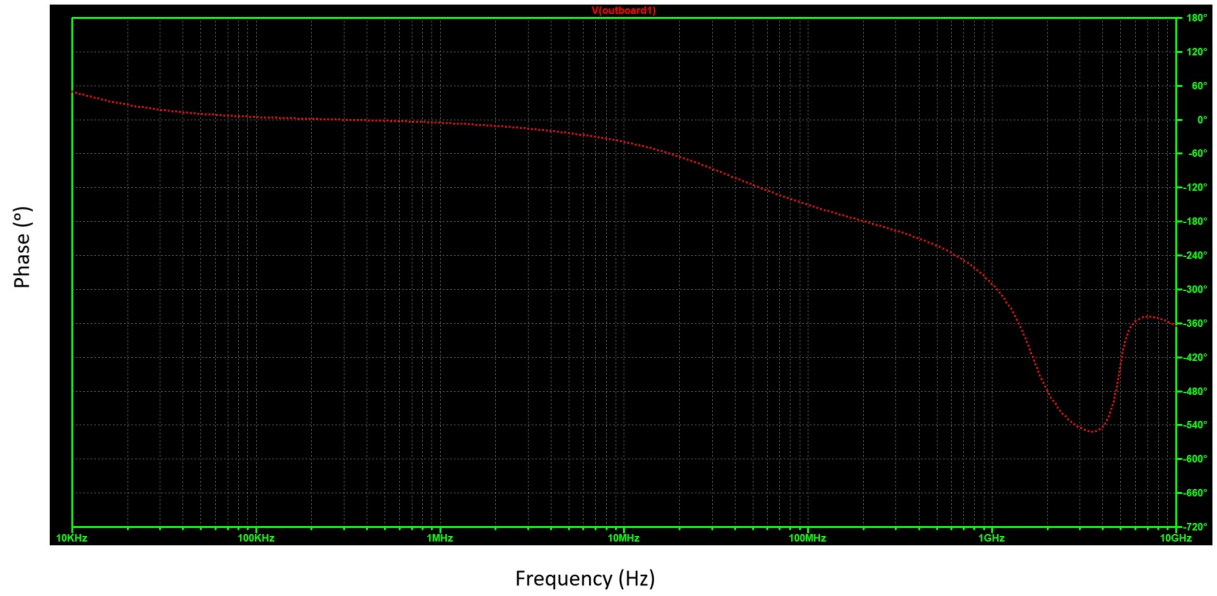

(b) Phase response section of the Bode Plot.

Figure 4.8: The magnitude of the Bode plot for the output of the amplification and bias board is seen in a) with the phase response seen in b). The magnitude and phase response both decrease as the frequency increases, with the corner frequency, the point at which the frequency rolls off and the system response changes, beginning at $\sim$10 MHz. This decrease is linear, with the sharp roll off occurring once the frequency reaches approximately 1 GHz.

The diode present should allow positive values to pass but block any negative values from passing through. The output of this stage is passed into the circuit seen in figure 4.13, which consists of a non-inverting amplifier with a CR network to remove voltage offset from the previous stage, then passed into a buffer to ensure that a stable signal is passed to the logic stages. This final shaping stage, shown as the red highlighted area, is the end of the shaping stage, which is mostly identical for each module. The shaped output pulse can be seen in figure

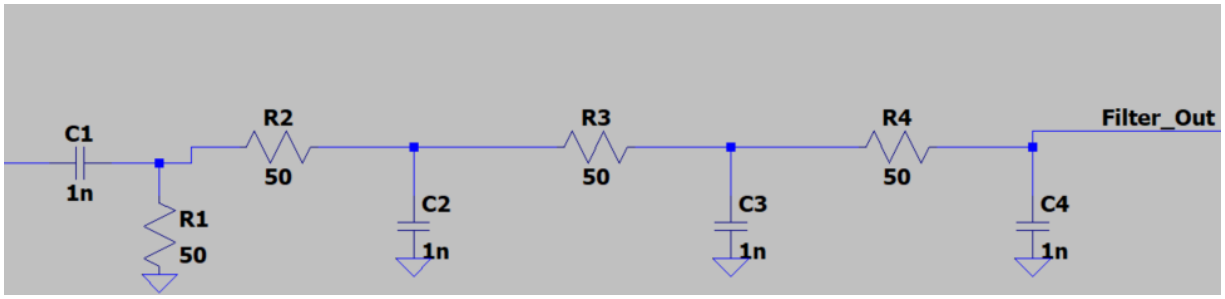

Figure 4.9: The passive CR-RC filter shaping network schematic, that shapes the exponential output pulse seen in figure 4.7 into a more Gaussian shape.

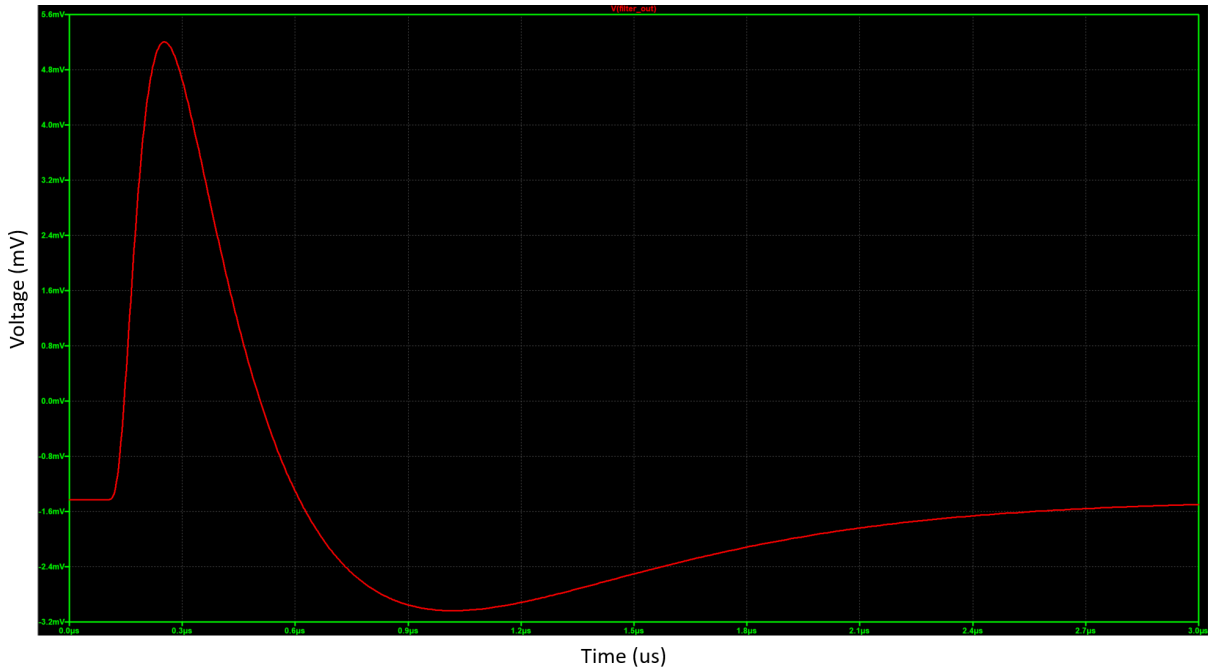

Figure 4.10: This is the output of the filter board module, that shapes the output seen in figure 4.7, and forms it into a more Gaussian shape as seen here, the undershoot can also be seen with the long decay back to baseline clearly visible.

4.14. Similar to the bias and amplification module, there is some offset applied to the pulse, which has been removed in LTSpice. This is resolved using either a capacitor, or a capacitor with a resistor to ground, before the pulse is processed in the logic hardware.

This shaped pulse was then ready for analysis, with the first board designed being the ZC board. The three stages that allow for this board to function are presented in figures 4.15, 4.16 and 4.17. The first of these, figure 4.15, generates the stop signal that is passed to the TDC, which consists of a buffer, then an additional CR network that operates as the final stage of a CR-RC-CR network. This converts the Gaussian pulse into a bipolar pulse, creating a ZC time that is then passed to a comparator to create a digital output. The reference voltage was chosen as a low non-zero value, as it is close to 0, being that ground is a noisy reference point, so it was best to use a low voltage to reduce noise in the system.

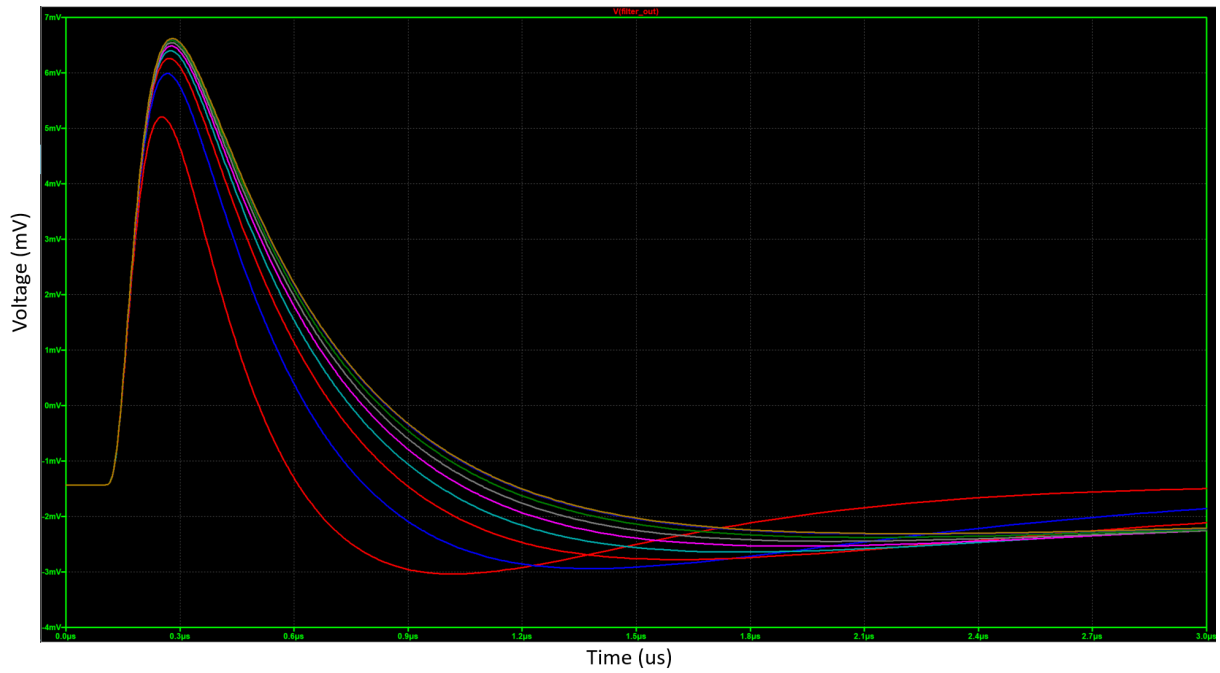

Figure 4.11: By passing pulses of different fall times through the filter design, it can be seen that the timing information of pulses with longer tails will be preserved, and can be separated later on, with the intention of allowing for analogue PSD operation. It can also be seen that pulses with longer fall times have less undershoot, but take longer to return to baseline.

The second ZC stage present in figure 4.16 is the first part of the processes required to create a constant fraction discriminator (CFD). This operates using another buffer stage followed by a long RC chain, that integrates the pulse in order to create a delayed waveform, seen in the red highlighted area. This delayed fraction needs to be compared to the original waveform, which can be seen in figure 4.17, which uses a summing amplifier with negative feedback in an inverting configuration to combine the two input signals. This is then shaped similarly to figure 4.15 with an additional CR stage, creating a delayed inverted waveform that will operate as the start signal for the TDC stage.

The two outputs of the ZC logic module, that operate as the TDC start and stop signals, can be seen in figure 4.18, with the start signal from figures 4.16 and 4.17 present as the light blue waveform. The stop signal generated by figure 4.15 is present as the red waveform, with the yellow highlighted area demonstrating the difference in zero crossing times of the waveforms.

These output signals are passed to separate comparators that generate the digital signals seen in 4.19 as the pink and light blue square waveforms. The start signal comparator goes high when the waveform is above 5 mV, meaning that when the signal goes high, it will create a start signal for the TDC. The stop signal comparator then goes high when the bipolar pulse is below -5 mV, with the rising edge of the comparator output generating a stop signal for the TDC. In the real circuit, hysteresis would be applied to the comparator, which involves large positive feedback,

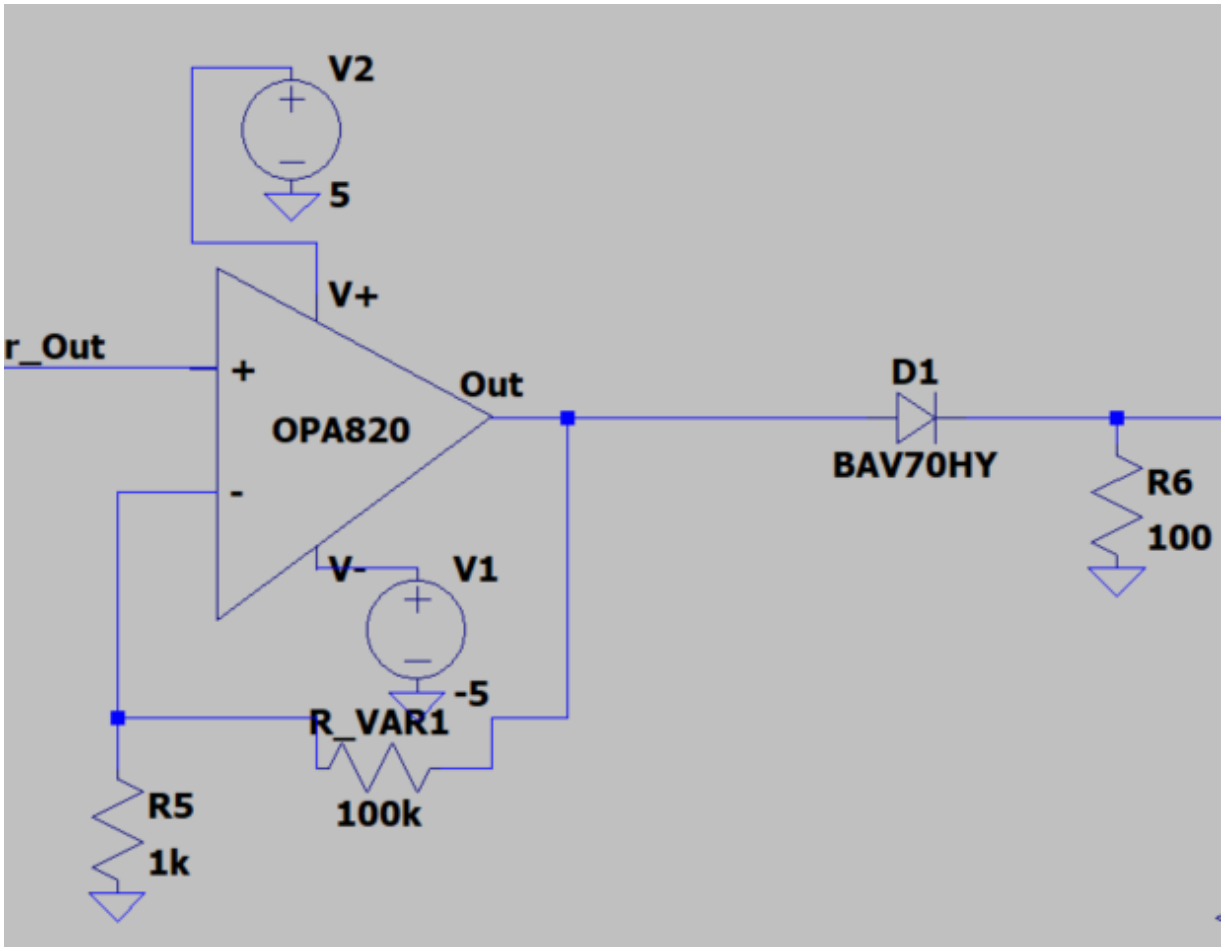

Figure 4.12: The stage following the passive filtering, that uses a 100 kΩ variable resistor to set the gain of the signal, with a diode and resistor present to reduce signal undershoot and approach a Gaussian pulse shape.

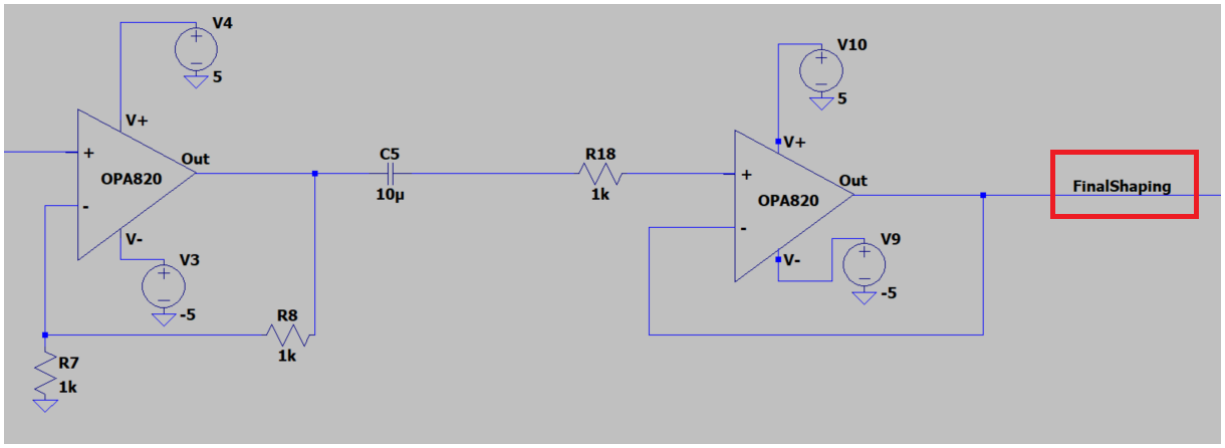

Figure 4.13: Two buffer amplifiers that are designed to reduce impedance effects and perform final pulse shaping on the filtered pulse shape.

but this did not function effectively in simulation.

As previously stated, these simulations were designed with a fall time constant of 400 ns, but

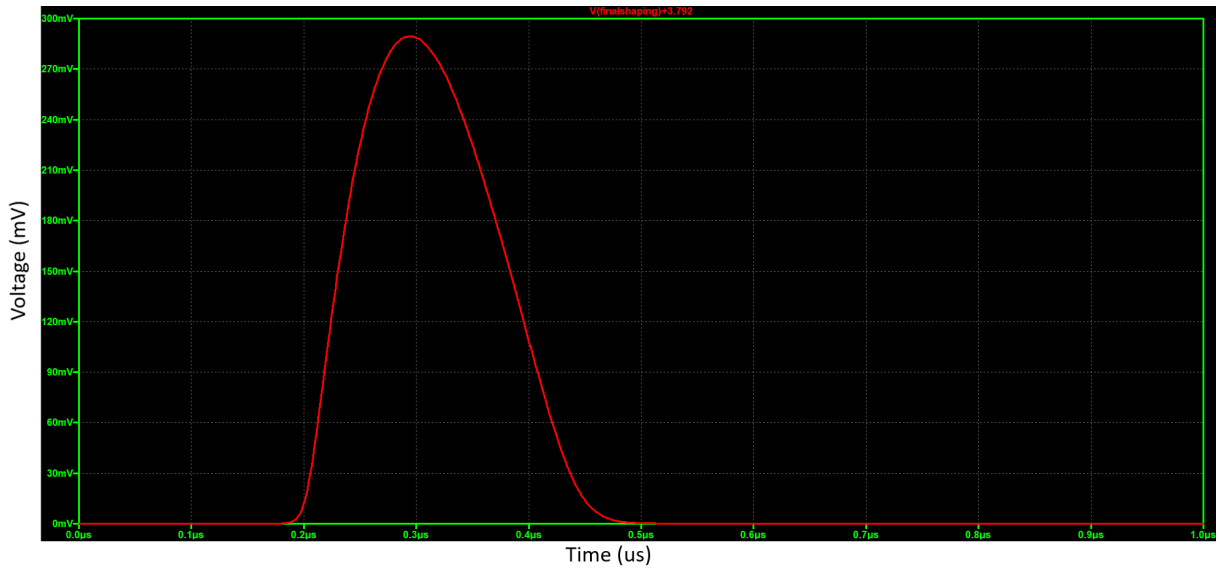

Figure 4.14: The final Gaussian pulse shape that is passed to the logic stages, there is a significant negative offset that has been introduced from the buffer amplifiers, this is resolved after the logic stages to bring the pulse back to baseline, the pulse here is shown with the offset removed.

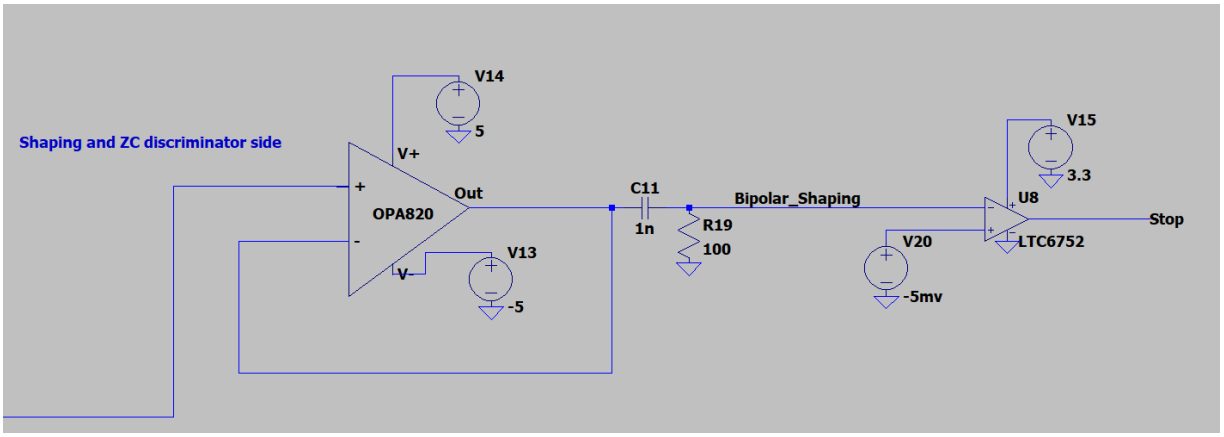

Figure 4.15: This is the first part of the ZC logic simulation that makes up the stop signal that is passed to the TDC. It consists of a buffer stage to separate the signal from any other effects, followed by a capacitor and resistor that acts as an additional CR stage to convert the Gaussian pulse into a bipolar pulse. This is then sent to the comparator with a -5 mV reference voltage, which is set as essentially ground, but ground is a noisy reference, so a small reference voltage was used instead.

a range of values were expected in reality. When the fall time constant is changed to 4 μs the time between the start and stop signals increases, also seen in figure 4.19. This means that this method can, in simulation, separate species of different timing characteristics, and can therefore be applied for neutron and γ-ray separation. A fall of time of 400 ns and 4000 ns were chosen to represent a γ-ray and neutron respectively, due to their expected timing differences, hence why these values for chosen for simulation comparison.

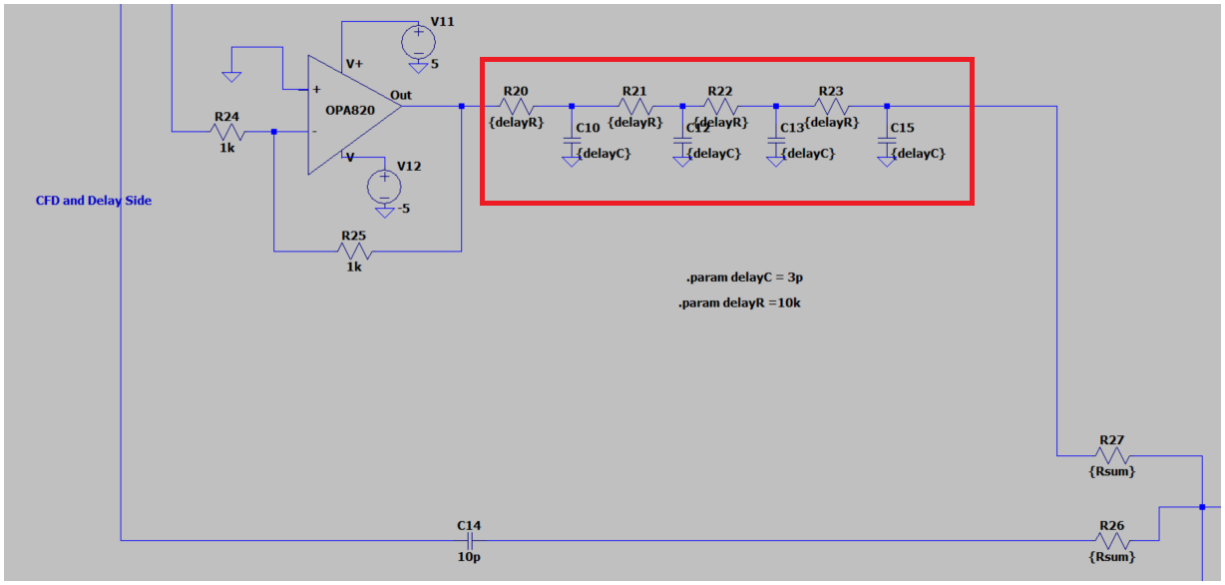

Figure 4.16: The second stage of the ZC detector, which creates a delayed fraction of the original waveform using the RC network present in the red highlighted area. This is then combined with the original waveform.

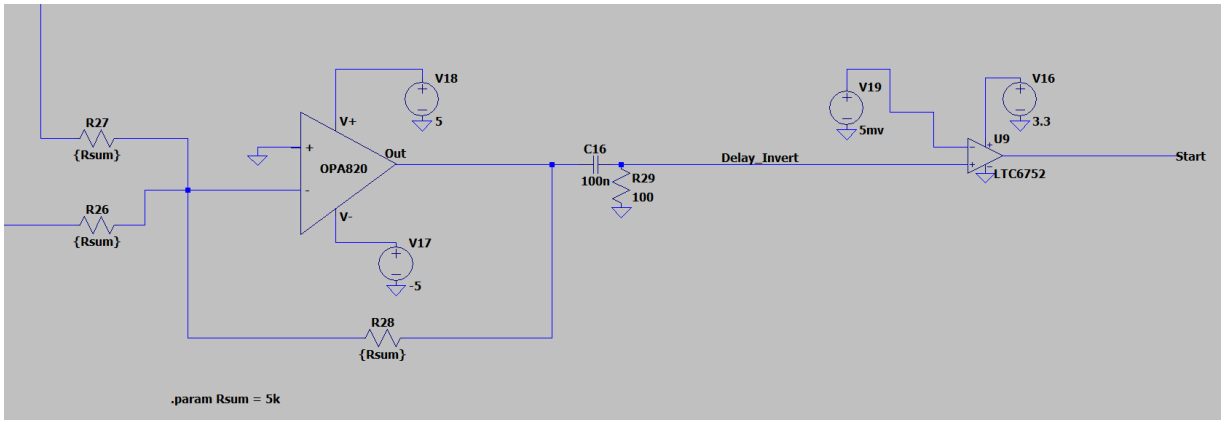

Figure 4.17: The delayed and original waveforms are combined using an inverting summing amplifier, which is then converted into a bipolar pulse using a CR stage that is then ready to operate as the TDC start signal.

This encompassed the simulations performed for the ZC PSD method, but the ToT and CC methods still needed to be simulated. The ToT method was investigated next, with a slight modification made to the standard method. Improvements to the ToT method have been performed by different investigations, with a bipolar ToT method appearing promising [99]. This allowed for a standard ToT measurement to recorded, whilst also creating a second ToT measurement that could be used independently, or as a comparative value to the standard ToT value.

The full ToT circuit can be seen in figures 4.20 and 4.21, with figure 4.20 illustrating the first ToT measurement, and therefore the start and stop signals for the first TDC, and figure 4.21

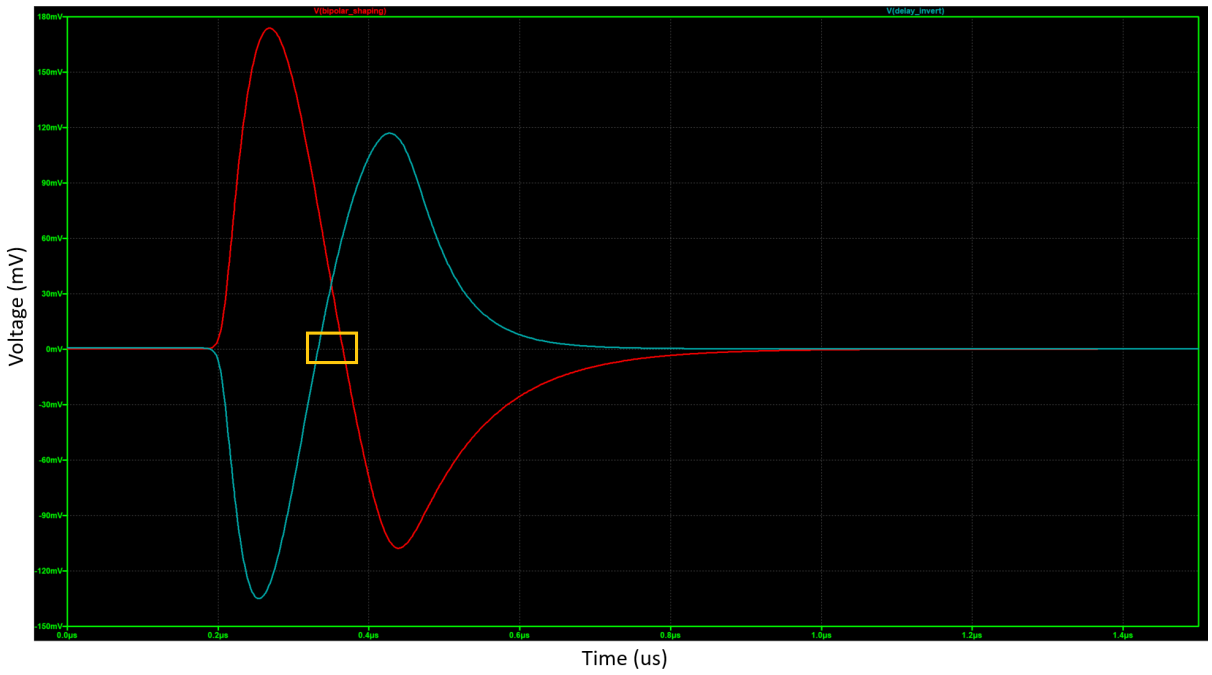

Figure 4.18: The start and stop signals required for a ZC detector, with the light blue waveform being the CFD start signal, and the red waveform being the inverted stop signal. The yellow highlighted area illustrates the difference in zero crossing times that will be passed to the TDC.

representing the second. The key parts of this circuit can be seen in 4.20, highlighted in the red and green areas. The red area represents the additional CR stage that differentiates the pulse and converts it into a bipolar pulse to allow for the second ToT measurement, performed before the signal is split so that it affects both measurements. The green area consists of an RC stage, an inverter and an AND gate, all of which come together to form a falling edge detector that will act as a stop signal for the TDC.

The only difference between figures 4.20 and 4.21 is the negative comparator reference voltage present in figure 4.21, which is required due to the negative polarity of the second ToT measurement. This reference voltage of 160 mV was chosen as it was the largest voltage amplitude achievable using a 1 μA pulse with the gain setting variable resistor set to 100 kΩ. This voltage was also likely to be above the background noise present in the system, so the system should not trigger on noise. The primary difference between the ZC and ToT simulations, beyond the additional components required for the CFD, is that hysteresis is present for the ToT comparators. It was determined that the hysteresis present for the ToT simulations did not affect the outputs, as it did in the ZC simulations, which would be expected in reality.

The ToT input pulse can be seen in figure 4.22, with the positive and negative areas present. This creates the two ToT measurements, which can be seen in figure 4.23, with the positive ToT measurement shown as the blue square wave, and the falling edge necessary for the stop signal

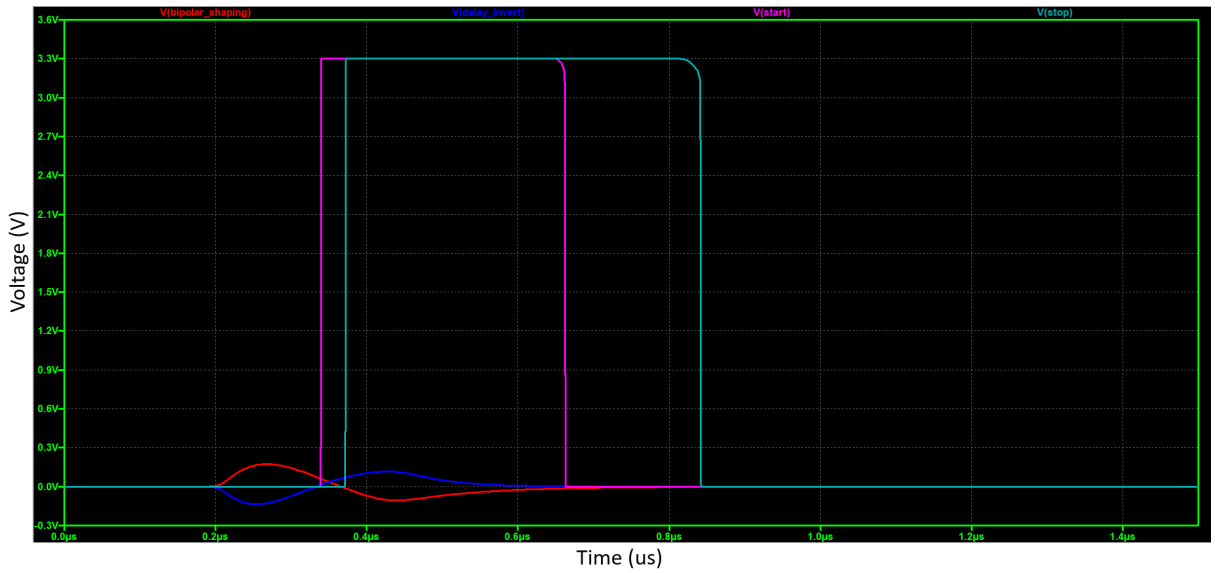

(a) A 400 ns fall time constant ZC simulation result with start and stop signals present.

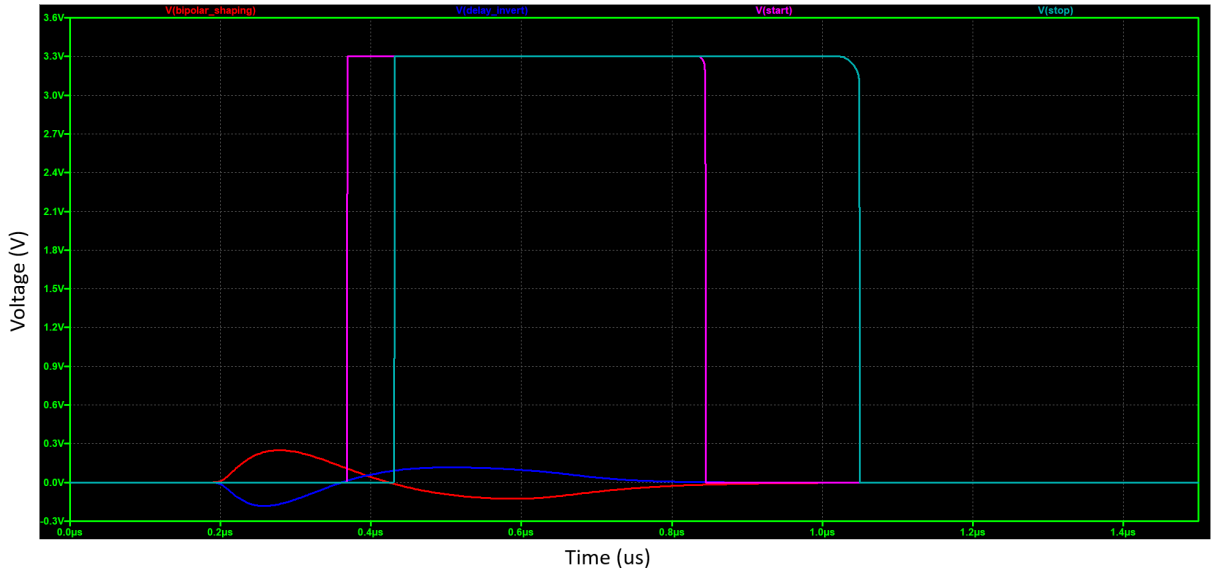

(b) A longer fall time constant input of 4000 ns ZC simulation result with start and stop signals present.

Figure 4.19: The output of the ZC simulations with varying fall time constants, with the two input signals present as the dark blue and red traces, with their comparator outputs seen as the pink and light blue square waveforms respectively. Figure a) was designed using the shorter 400 ns fall time constant, whilst figure b) was designed using the 4000 ns fall time constant. The timing difference between the start and stop signals of each figure is 35 ns, which should be easily resolved by the TDC and allow for effective species separation.

seen in the small white square wave. The same can be seen in the light blue and pink square waves for the negative ToT measurement.

As with the ZC PSD method, the ToT method was designed using the same input pulse. This would need to be tested with waveforms of different timing characteristics, and so a waveform with a fall time constant of 4 μs was input. The larger ToT values can also be seen in figure

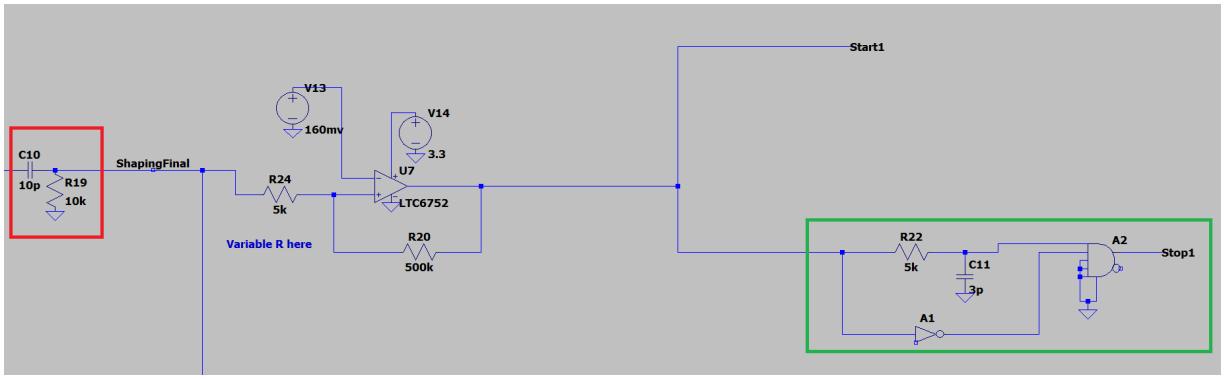

Figure 4.20: The first stage of the time-over-threshold PSD method, with the CR stage that converts the unipolar pulse into a bipolar pulse to allow for both ToT measurements highlighted in red. The comparator output is split into a start signal for the TDC, and an additional stage that creates a stop signal from the falling edge of the comparator output signal, this falling edge detector can be seen in the green highlighted area.

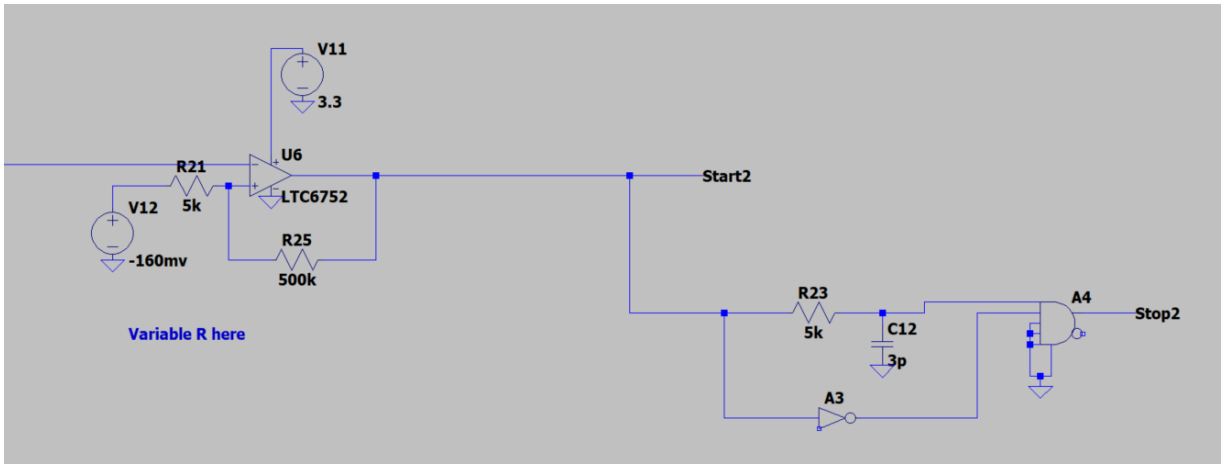

Figure 4.21: The second stage of time-over-threshold PSD method, this is identical to the first stage, apart from the negative reference voltage which is used to determine the ToT for the negative part of the input pulse.

4.23, as when compared to the square waveforms present in figure b), it is observed that there is a greater ToT value. This means that, according to the simulation results, the ToT method should be able to separate species of different timing characteristics, and can therefore be considered for analogue PSD.

The third and final analogue PSD method planned for this investigation was the charge comparison method. This method was easy to implement in a digital environment as it involves using the digital hardware to record the charge contained within each timing gate. Performing this in an analogue environment would be more difficult, as it would involve creating two timing gates that encompassed the rising and falling edges of the the pulse, most likely using comparators similarly to digital gates, and then use a MOSFET that will allow voltage to pass when there is a high output from the comparator. This voltage will then be used to charge a

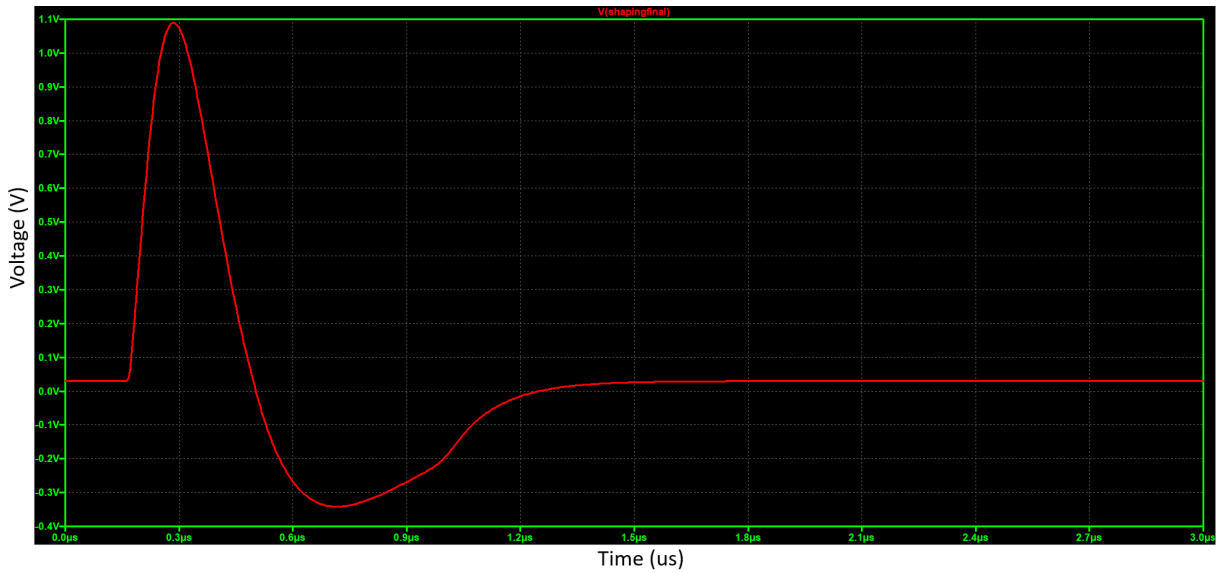

Figure 4.22: The time-over-threshold input pulse, with the positive and negative regions present that enable for both ToT measurements to be performed, the curve in the return to baseline is believed to be caused by the software, and was not considered a concern for results.

capacitor, with the voltage dissipated across this capacitor equivalent to the charge contained within the gate, allowing for the CC method to be performed.

The main difference in the early stages of this method involved the placement of the undershoot removing diode, which is placed later in the chain in the CC simulation as an early placement did not effectively remove the undershoot. This can be seen in figure 4.24, before the waveform is sent to the comparators that generate the short and long gate. This is done by giving a small reference voltage to one comparator which will be in a high state for the entirety of the pulse, and another comparator with a variable reference voltage that begins in a high state, and goes low when the pulse is above this reference voltage, an example of this can be seen in figure 4.25. This results in a subtraction of the comparator outputs, which can be seen along with the input waveform in figure 4.26.

The next stage of this process is to separate the short and long gates, as currently both gates are part of the same output, so any evaluation would result in both gates containing the exact same amount of charge. To separate these signals, a combination of two D flipflops were used. The output of the comparators are passed to the clock input of the first flipflop, causing the flipflop to begin in a high state, output low at the rising edge of the first gate and then return high at the rising edge of the second gate. By passing the value of the complimentary output $\overline{Q}$ to D, the clock signal is pushed through the channel Q, which is then passed through an inverter.

This signal is passed to the clock input of the second flipflop, with the same setup as the previous flipflop. This means that the output of the second flipflop goes low at the rising edge of the

second comparator. By passing this output to an AND gate, with the other input being the original comparator output, it causes the AND gate to output high only when the short gate is present, separating the short gate. For the long gate, the output of the first AND gate is passed through an inverter, which causes the signal to be low only when the short gate is present, and to be in a high state otherwise. Combining this with the original comparator output means that this gate will only be high when the long gate is present, thus creating the two separate timing gates. This circuit can be seen in figure 4.27, with the result of this separation seen in figure 4.28, with the short and long gate being separate outputs that can each be passed to a MOSFET.

The final stage of the charge comparison method involves passing the output seen in figure 4.28 into the gate of two N-MOSFETs, one for the short and long gate, with the original wave passed into the source terminal, and the output from the drain terminal being the charge that will be read into the μC. This arrangement means that the MOSFET allows a voltage to pass when the comparator is in a high state, and the capacitor charges proportionally to the amount of charge contained within the gate. This circuit design can be seen in figure 4.29, with the output capacitor and resistor values chosen to maximise the output charge.

The final output of this board can be seen in figure 4.30, with the larger light blue trace consisting of the charge contained within the long gate and the red trace being the charge contained within the short gate. A ratio of these charges can be determined in the μC to give a PSD factor, in the same way that is performed in a digital scope. As with the other simulations, it is necessary to determine whether pulses of different timing characteristics would give different end results, with the range of 400 ns to 4 μs chosen due to their large difference. This timing difference should serve as an analogy to the expected timing difference between a neutron and a γ-ray. A pulse of the same amplitude but with a larger 4 μs fall time constant was input, with the output of this also seen in figure 4.30. The different output voltages present mean that this method should be able to separate species of different timing profiles, and is therefore a candidate for neutron and γ-ray separation.

Despite the results presented throughout this chapter, the simulation work did not often proceed smoothly, with many setbacks occurring that required resolution. A primary example of this was the original idea for a filter and shaping module, which was designed in simulation, appeared to operate well and as such was manufactured. This filter module used an op-amp for active filtering, and suggested that open loop control was the most effective way to achieve this, as when negative feedback was added, the filter no longer functioned. When the board arrived and was tested, the open loop control meant that was far too much gain in the system, and the op-amp saturated, so despite the simulated output, this was not the correct approach. It is not currently understood why this was not seen in the simulated output. This module was redesigned into the filtering stage present in each logic board, so this setback was used to improve the design, but it

did cause timing delays.

This was not the only simulation issue, as at one stage the CC method was not approved for manufacture. This occurred as the simulation would function for a certain input waveform, and would then be altered to test the ability of the circuit to resolve input waveforms of different timing characteristics. Once this alteration was performed, the simulation would no longer function, and required several redesigns, with the old simulation present in figure 4.31, where the only significant difference is the use of NPN transistors rather than MOSFETs. The outputs of the flipflops operated as expected, with two separate gate outputs created, but when these gates were connected to the transistors, the short gate saw almost all of the charge, with the long gate collecting only a small fraction, this can be seen in figure 4.32. This resulted in an incorrect amount of charge being recorded by each gate, which can be seen in figure 4.33, and often with redesign, both gates would output the exact same charge. The use of MOSFETs allowed for the resolution of this issue, and demonstrated that methods derived in simulation are still liable to risk or unexpected fault and should only be trusted for design to an extent.

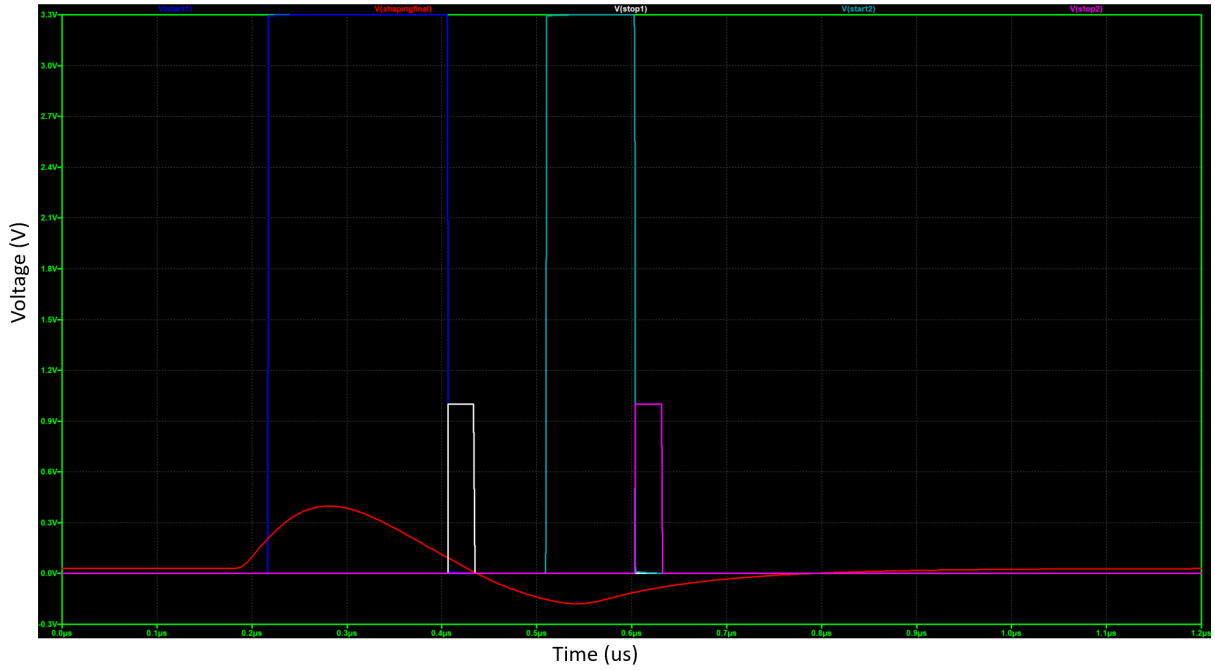

(a) A 400 ns fall time constant ToT simulation result with start and stop signals present.

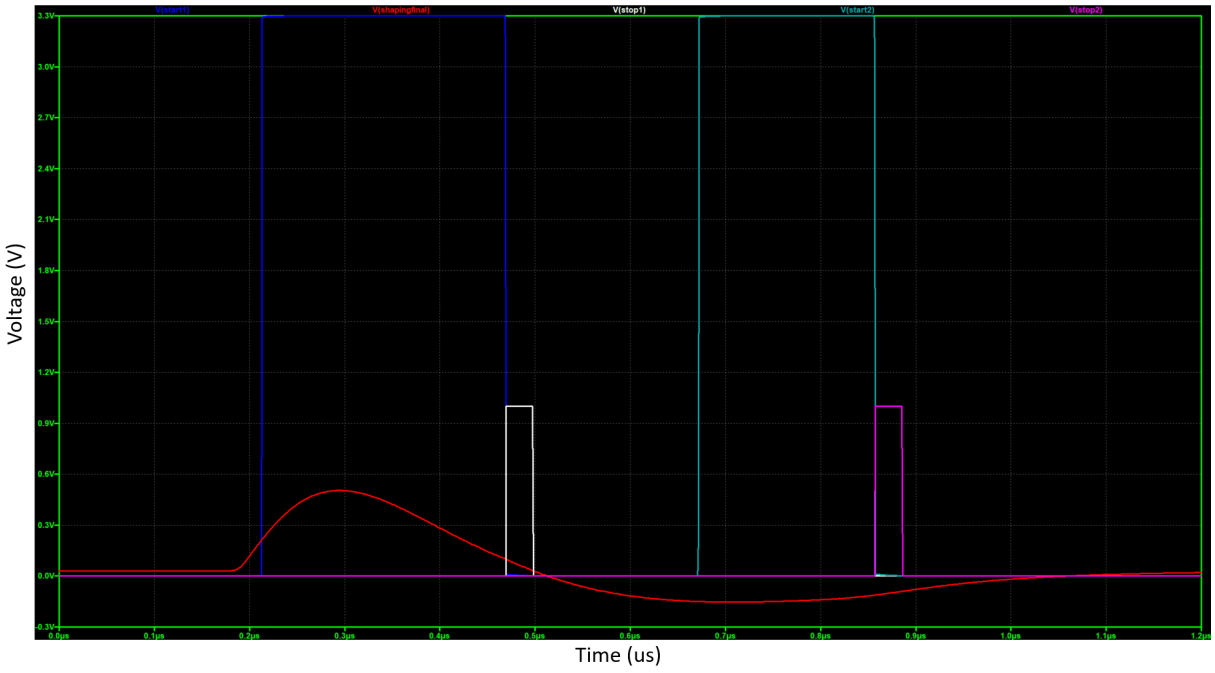

(b) A longer fall time constant input of 4000 ns ToT simulation result with start and stop signals present.

Figure 4.23: The time-over-threshold PSD method, with the first TDC start signal present as the blue comparator output, with the white square output acting as the stop signal. The negative polarity ToT measurement is seen with the light blue comparator output acting as the start signal for the second TDC, and the pink comparator output operating as the stop signal. Having two measurement values should allow for comparison to improve the effectiveness of the method. Figure a) was designed using the shorter 400 ns fall time constant, whilst figure b) was designed using the 4000 ns fall time constant. The timing difference between the start and stop signals of the positive ToT was 65 ns, whilst it was 90 ns for the negative ToT, meaning that both methods should effectively separate species.

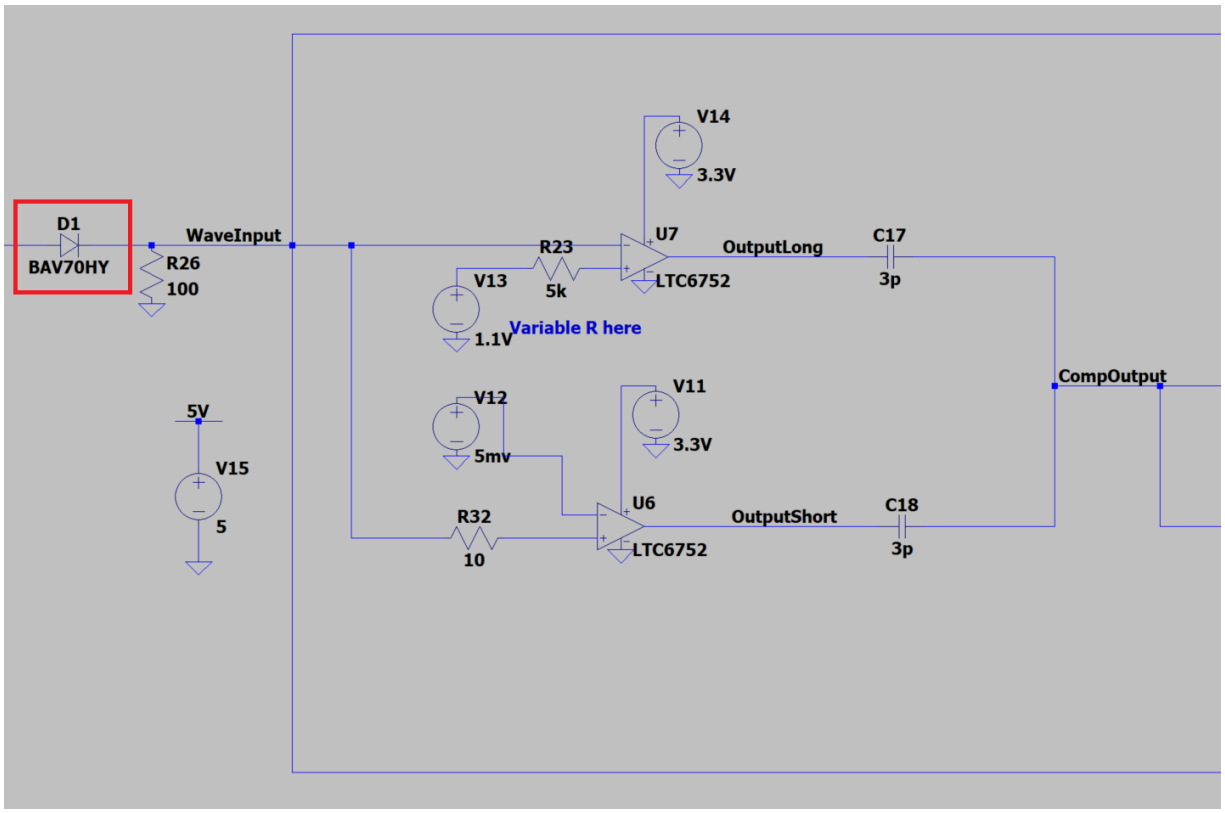

Figure 4.24: The first stage of the charge comparison analogue PSD method, with the diode removing undershoot present in the red highlighted area, that is then passed to two comparators that combine to create the long and short gates necessary for the CC method to be performed.

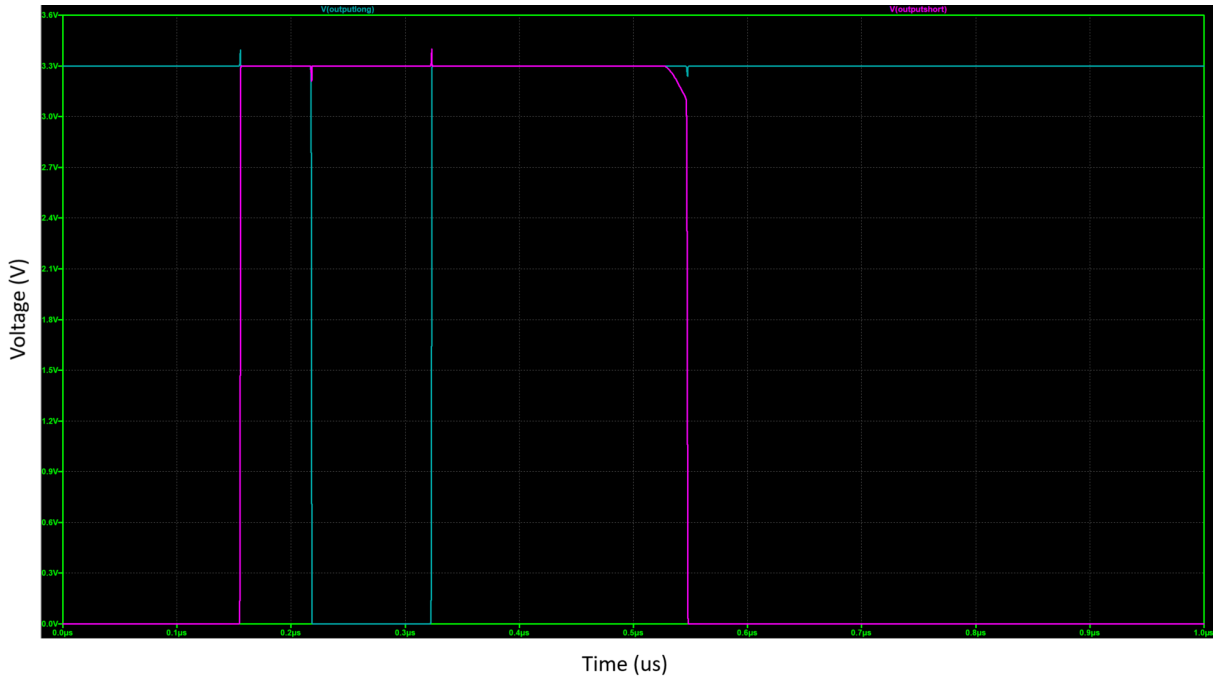

Figure 4.25: The comparator outputs that create both gates by performing a substitution of their outputs, with the pink output signal in a high state whilst the signal is in excess of 5 mV and the light blue output in a high state whilst the signal has an amplitude above 1.1 V, although in reality this will have a variable voltage to allow for a variable gate width. This results in a short and long gate present. The small shifts in both comparator outputs seen at 3.3 V are believed to be a noise contribution caused by the other comparator changing state and briefly impacting the other comparator as they are connected.

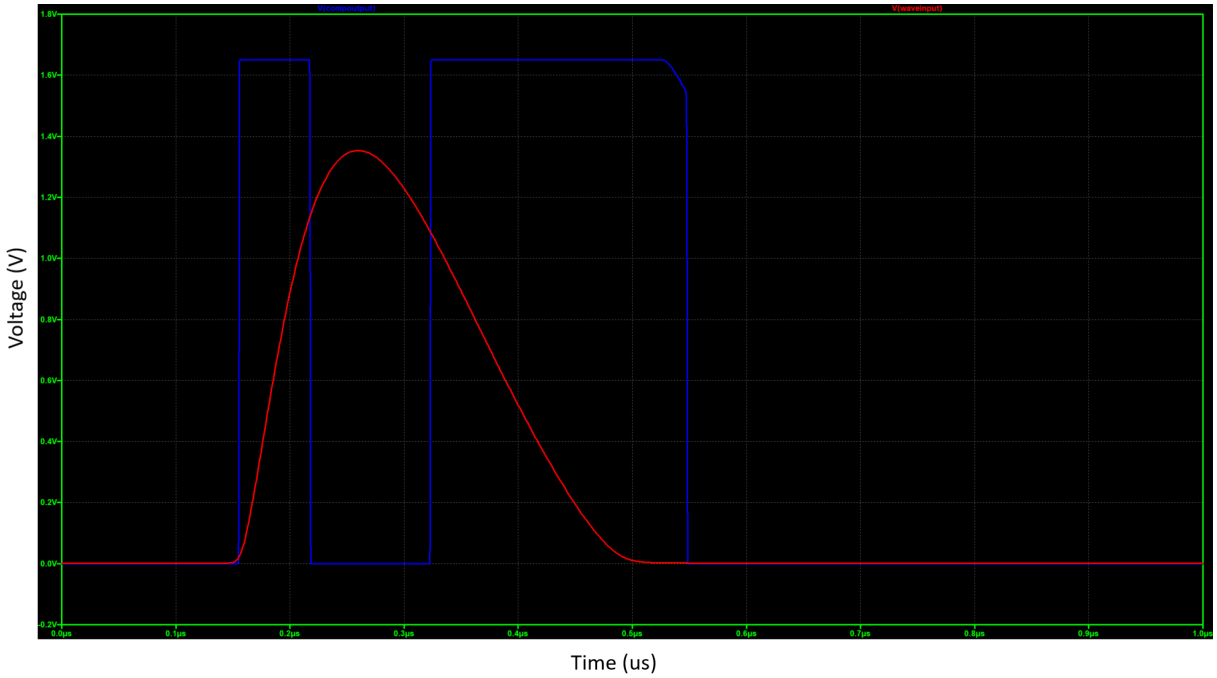

Figure 4.26: The output of the two comparators, alongside the original input waveform which demonstrates the short and long gates with the rising and falling edges contained within them, creating the first stage of the CC PSD method.

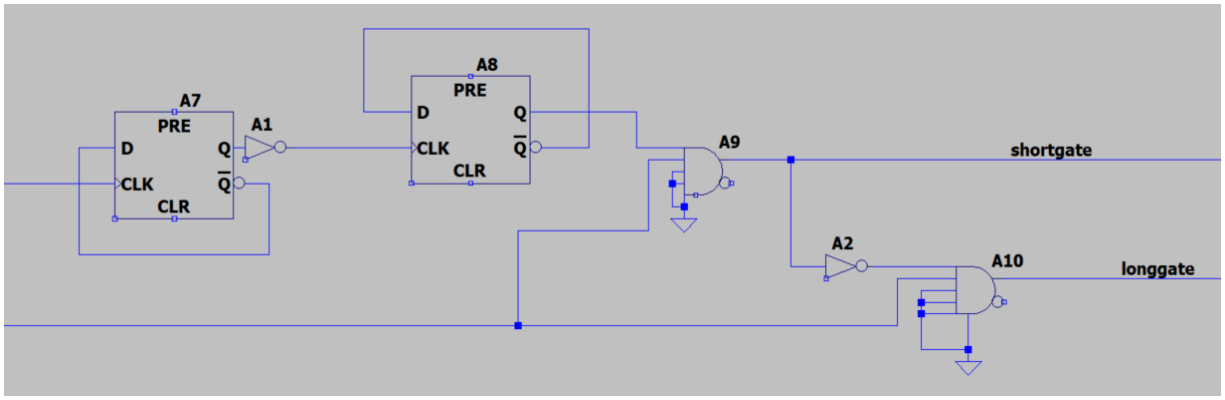

Figure 4.27: The 2nd stage of the charge comparison analogue PSD method, which uses the two D flipflops, AND gates and inverters to separate the timing gates into two separate outputs that can then be used to evaluate the charge contained within the respective gate.

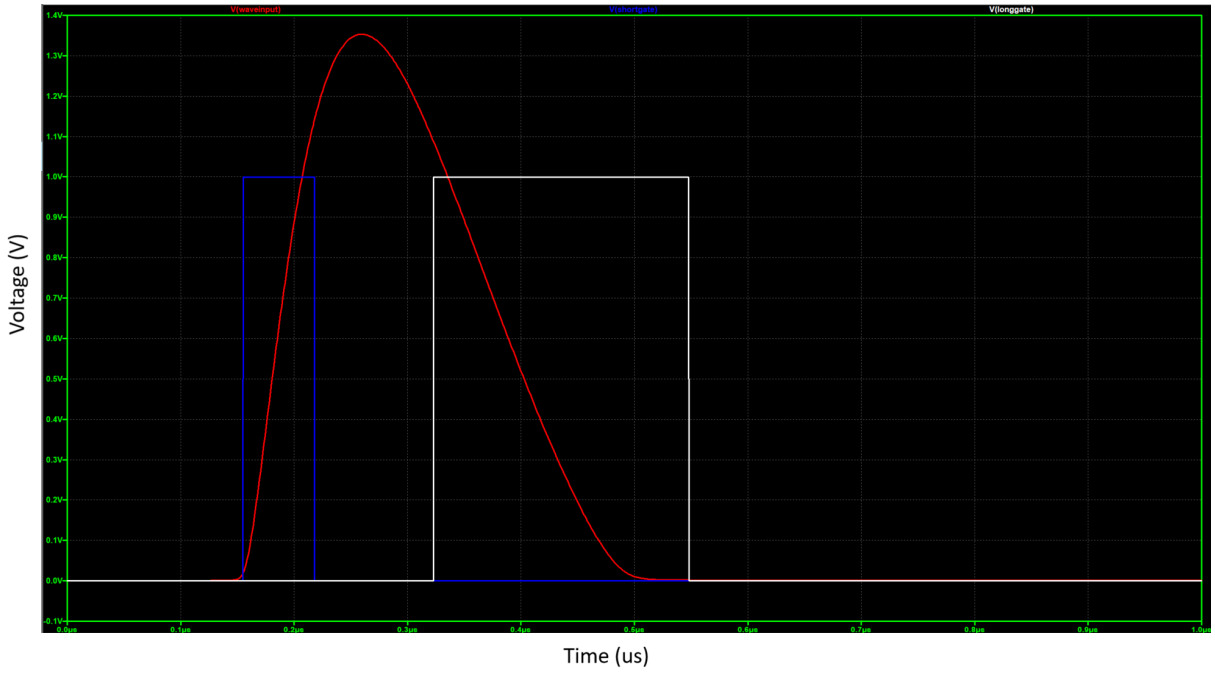

Figure 4.28: The result of the circuit seen in figure 4.27, where the timing gates are separated from a single output into two individual outputs that can be used for the CC method. The short gate is seen as the blue square wave, with the long gate being the white square wave output.

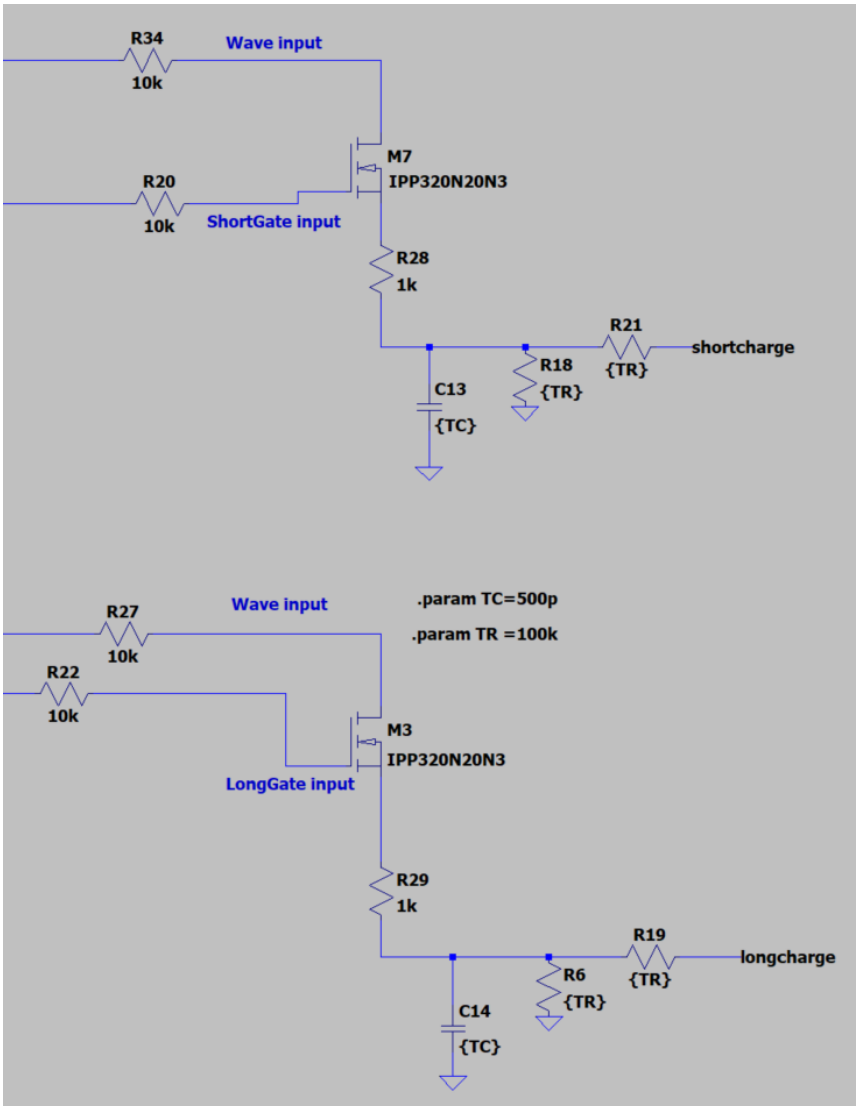

Figure 4.29: The 3rd and final stage of the charge comparison circuit, with the MOSFETs present that allow for the charge present in the timing gates to be passed to a capacitor and then to the output μC.

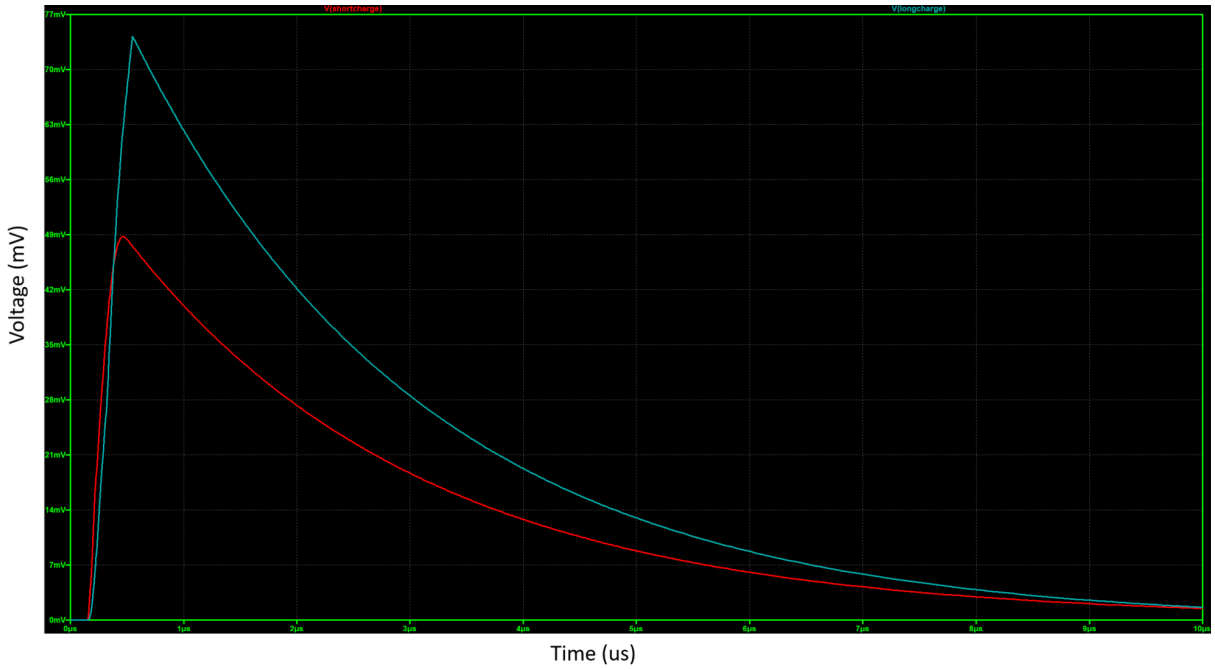

(a) A 400 ns fall time constant CC simulation result with start and stop signals present.

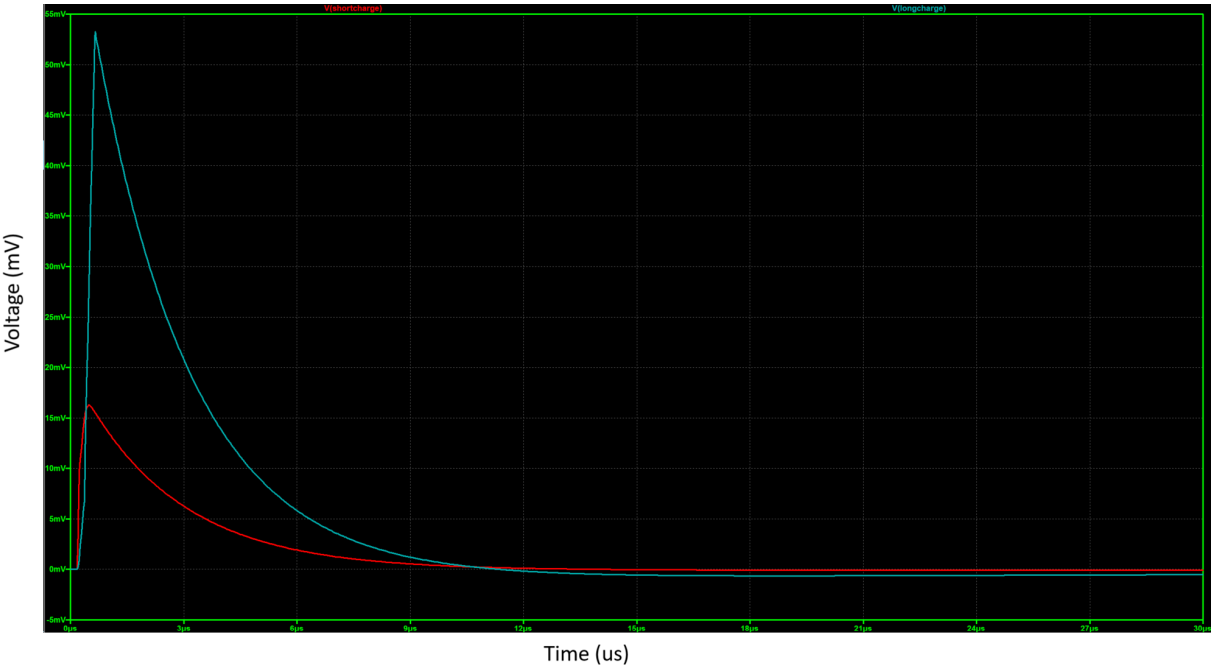

(b) A longer fall time constant input of 4000 ns CC simulation result with start and stop signals present.

Figure 4.30: The output of the simulation seen in figure 4.29, with the different voltages contained within both gates present, with the long gate having more charge as expected as it encompasses the longer falling edge of the pulse. Figure a) was designed using the shorter 400 ns fall time constant, whilst figure b) was designed using the 4000 ns fall time constant.

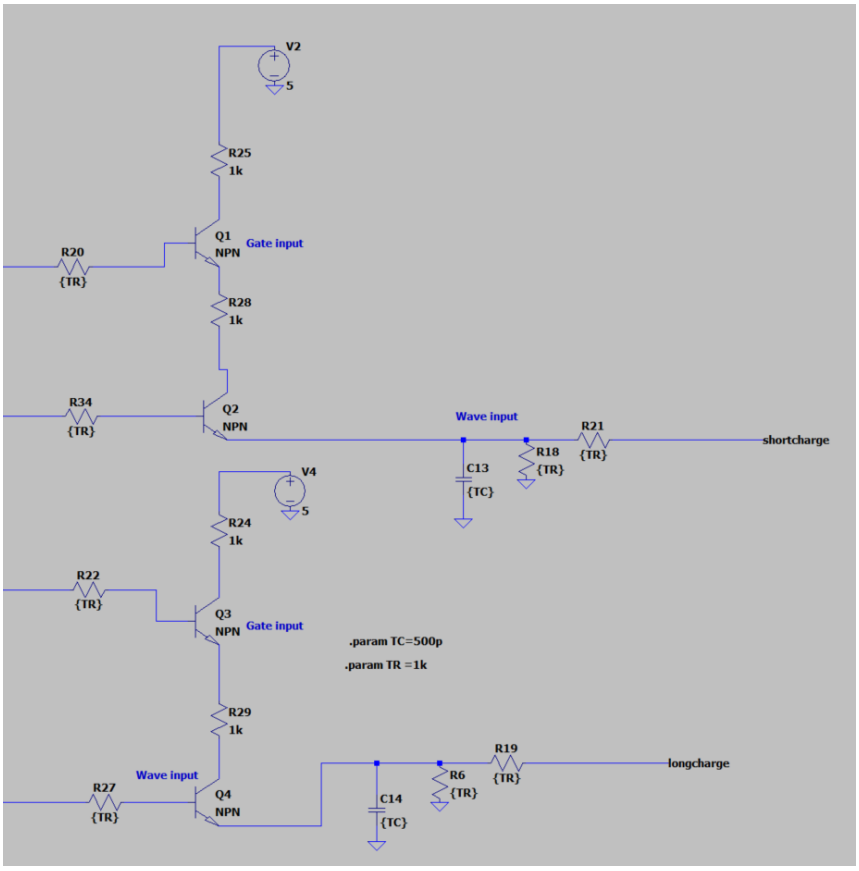

Figure 4.31: The old charge comparison simulation circuit with NPN transistors in place of N-MOSFETs, this did not operate as expected and required many redesigns for the eventual operating version present in figure 4.29.

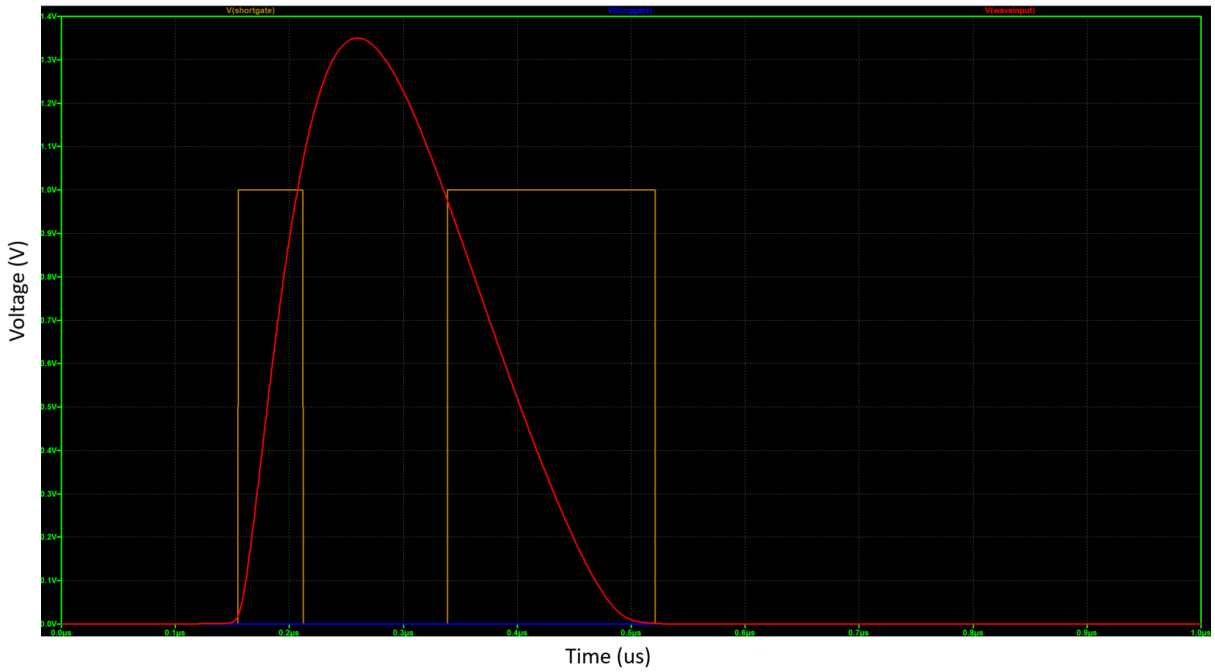

Figure 4.32: The charge comparison simulation with both gates present on a single output, meaning that both outputs would receive the incorrect amount of charge.

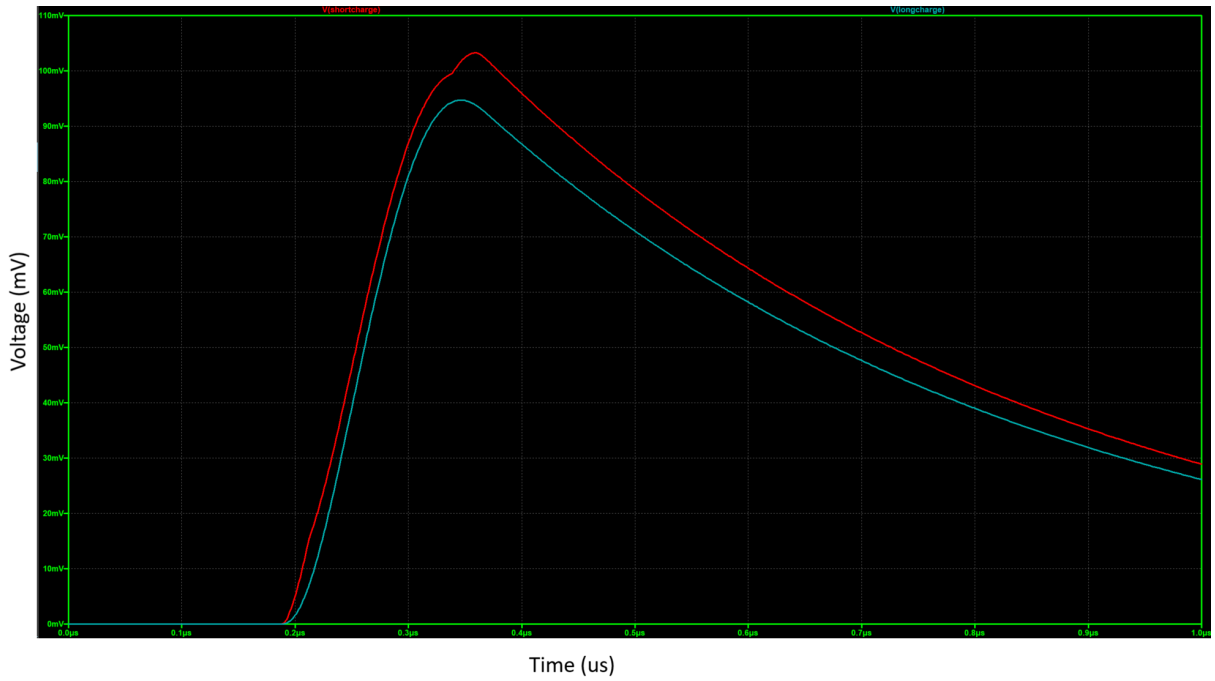

Figure 4.33: The previous charge comparison simulation outputs, with the short gate containing a larger amount of charge than that of the large gate, which is not expected as the long gate is collecting the charge over a longer time period.

4.3 Printed Circuit Board Design

Once the simulations were complete, the next stage of design was to assemble the circuit onto a printed circuit board (PCB) so that it could be used an analogue PSD method. There are many different parts to this process, with components necessary for accurate function that cannot be properly simulated, such as the decoupling capacitors, as they mostly relate to signal stability and correct operation of components. These components are vital for proper function, but do not impact directly on operations carried out throughout the board.

In order to understand the PCB design choices, it is first necessary to understand certain features of PCB design. It is not required to understand the full manufacture process, but certain aspects of the design will impact on this manufacture, such as the board thickness. As stated in chapter 3.1, PCBs are often made of layers of a dielectric fiberglass and epoxy resin known as FR4, with layers of metal between these layers, forming conducting and insulating layers. PCBs can have a variable quantity of these layers, with a 4 layer PCB chosen for these designs. This decision was made to allow for the top and bottom layers to operate as signal layers, where components can be placed and routed. The two layers between consisted of two solid metal layers, known as planes, with one being a ground plane, and the other being a power plane. This was chosen as a solid power plane allows for easier transfer of power to components, whilst a solid ground plane, preferably close to the signal layer with the most components, should reduce noise in the system.

Components can be connected to these planes and other layers using vias, which are small holes that connect between different layers, acting as a path between them. They have many uses and come in different forms, but connecting these different layers were their primary function in these designs. It is also important for these layers to have similar impedances, with $50\,\Omega$ the common value, used because it is a good compromise value that prevents signal reflections, whilst allowing for impedance matching. The trace width vs the plane thickness gives the overall trace impedance, resulting in trace thicknesses of 0.2 mm for signal traces, and 0.5 mm for power traces. These traces do not need to be impedance matched, but should be large enough for power to pass without causing any reflections and have as low an impedance as practical, with the via width set by the current. There are also no 90° corners in the traces to further reduce reflections.

All of these design choices can be seen in the PCB example in figure 4.34, which is the PCB design created to replicate the bias and amplification module designs present in figures 4.5 and 4.6. It should be noted that the components and traces on the top layer are red, the bottom layer components are blue, the ground plane is green and the power plane is a dark red. The additional feature not present in the simulations that are included in the PCB design are the bypass and decoupling capacitors, as well as hysteresis in the later comparator designs. A key design feature

that should be noted is that traces should not be routed underneath active components, as this can interfere with the signal trace and affect operation.

The bypass and decoupling capacitors can be seen as the blue components in figure 4.34, highlighted in green. These components shunt noise from a power supply to ground, therefore filtering unwanted signals, whilst also acting as local energy storage to smooth out any voltage fluctuations that could negatively affect another part of the circuit. The capacitors are placed close to the power supply pins, as well as the power pins of certain active components such as op-amps, to protect against these noise sources and voltage changes. The capacitor values are often suggested by the respective component datasheet, providing a guide for selection.

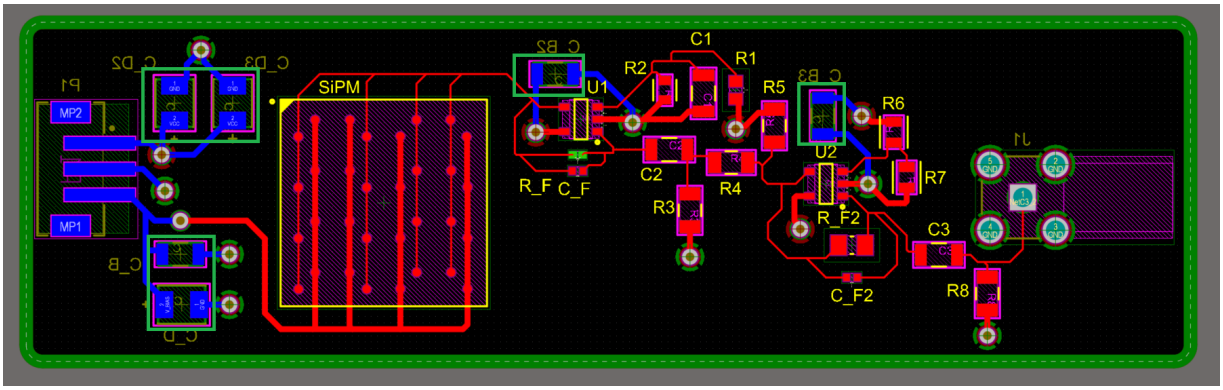

Figure 4.34: The bias and amplification module created in PCB design software, with the SiPM detector position present with the TIA seen as U1 and the voltage amplifier in U2 before sent to an SMA output at J1.

Whilst this board was the final design, several redesigns were required to reach this stage, due to issues with the SiPM footprint and spacial arrangements. The filter module that was described earlier arrived before this bias module was ready, but it still required testing. This was possible using a detector emulator, with the CAEN DT5810B module seen in figure 4.35. This operates by creating an example pulse, similar to the way that the initial pulse was designed for simulation, and it was this testing that identified the open loop feedback problem.

Due to the growing complexity of PCB design as components are placed and traces are added, it is best to look at a schematic, such as the simulation designs present in chapter 4.2, for a clear understanding of the motivations behind component choices. However, it is still important to understand the design and planning of each stage of the eventual PCB to understand the intended output. The first part of the ZC board can be seen in figure 4.36, with components P1 providing a +5 V, -5 V and ground (GND) connections, which were the required voltage differentials for components to function, and J1 representing an SMA input to be connected to the output of the bias and amplification module. This is the same for each of the three boards, due to the similarities in the filtering stages of each module. The full boards and simulations for

Figure 4.35: A picture of a CAEN DT5810B Detector Emulator used to simulate input SiPM pulses into the designed boards to ensure that the outcome is as expected.

each design are available in the appendix. The primary difference between the board in figure 4.34 and the following logic boards are that the early active components with the identifier U are changed from the LMH6629 to the OPA820.

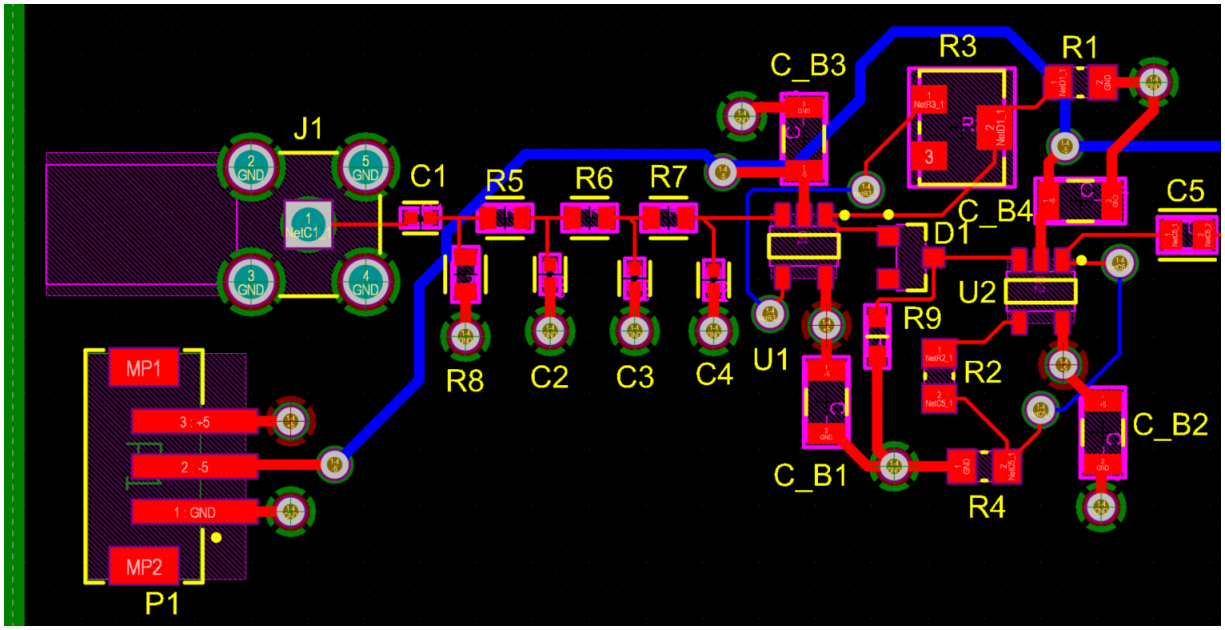

Figure 4.36: The first part of the zero crossing PSD module created in the PCB design software, the inputs can be seen as J1 and P1, with the passive filtering stage seen as the C and R network, before the active components, represented by U, the diode shown by the identifier D, with R3 being the gain setting variable resistor.

The second ZC module is where the differences begin to become apparent, with the hysteresis for one of the comparators (U11) present through R25 and R26, shown in the green highlighted areas of figure 4.37. Hysteresis is important for comparators, as it reduces the effects of small noise signals causing switching between high and low states. These resistor values were determined

as 5 kΩ and 500 kΩ, as this creates a hysteresis voltage of 100 mV, so any signals smaller than this should not cause switching to occur, therefore insulating the comparator from some of the noise present in the system.

There is an additional component required for the operation of the LTC6752 comparator, which can be seen with the identifier U12, and is a 5 V to 3.3 V (Texas Instruments LM3940IMP-3.3/NOPB) low dropout (LDO) voltage regulator. This is an essential addition as certain components will not be able to operate using a 5 V supply, and could be damaged. This lower voltage could be achieved using a voltage divider created using resistors, such as the reference voltages for the comparators, but this would be liable to fluctuations from the variation in true resistance values. A voltage regulator provides a very stable output voltage, and as such was necessary for powering certain components. The final region of interest in figure 4.37 can be seen in the yellow highlighted area, which corresponds to the delay network highlighted in figure 4.16.

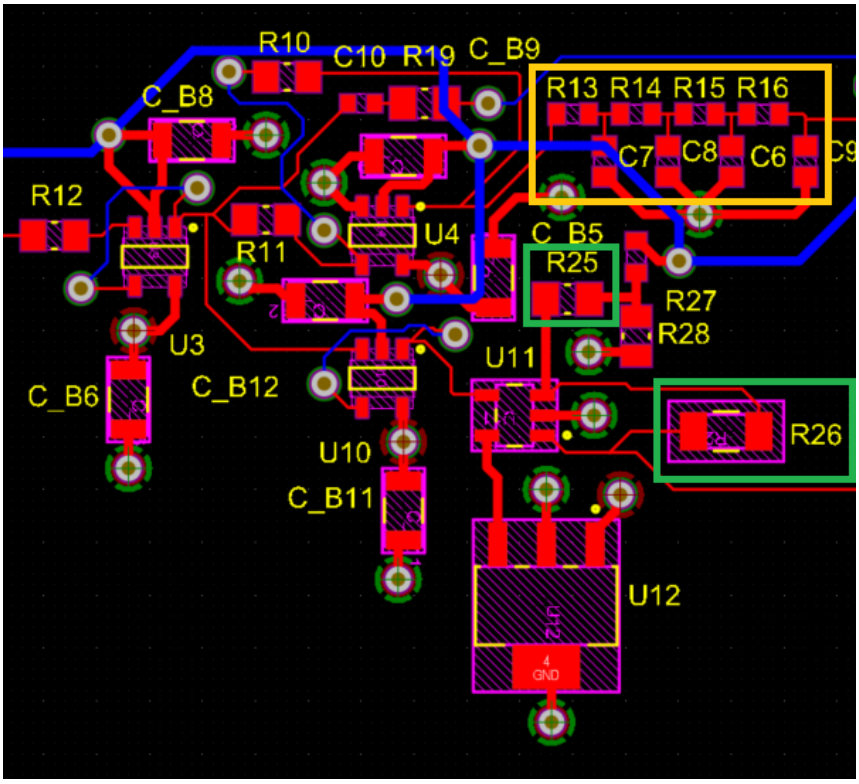

Figure 4.37: The second part of the zero crossing module created in the PCB design software, the first 5 V to 3.3 V regulator can seen in U12, with the first comparator also seen in U11.

The third and final part of the ZC board are where the key differences from simulation are clear, as the simulation present in 4.17 ends with the creation of the start and stop signal for the TDC. This is not the case in the actual design, as these start and stop signals are only two parts of the TDCs 14-pins, seen in figure 4.39 with the identifier J2. Another component required for the successful operation of a TDC is a crystal oscillator, which is an external clock signal that

creates an accurate timing input to the TDC, ensuring ensure it can produce accurate timing results. This can be seen as the Y1 component, with a crystal oscillator of 16 MHz chosen to provide the best results.

The TDC choice (Texas Instruments TDC7200PWR) was also key, as another version of this TDC that consists of a small BGA based component was considered, with initial designs using this version. However, it was impossible to route the traces of this component correctly with the current number of layers, so this 14-pin package was chosen instead. Of these 14-pins, 7 needed to be interfaced with the μC, with these being the ENABLE, TRIGG, SCLK, CSB, DIN, DOUT and INTB, all of which can be seen on the top silkscreen layer in figure 4.39. These are mostly self explanatory, with D representing data and TRIGG representing the trigger, except for SCLK which is the serial peripheral interface (SPI) clock, the CSB which is the SPI chip select, and the INTB, which is the interrupt signal to the TDC. The other TDC pins are related to the power supply and regulation of the TDC, with the remaining pins consisting of the external clock signal, and the start and stop inputs, all of these can be seen in figure 4.38. The start and stop inputs need to consist of very similar trace lengths, as the timing of these signals are crucial, so different trace lengths could cause different input signal timings.

The ToT board required a smaller number of overall components than the ZC board, and had a lower degree of overall complexity as the ZC performed several further operations to the incident waveform. Meanwhile, the ToT method simply sets a voltage threshold and evaluates the time above this threshold. However, the overall designs are similar due to the TDCs and their required components. The choice to use two ToT measurements from both the positive and negative aspects of the waveform was made to improve the accuracy of the method, and act as a comparative value, whilst not increasing the complexity in any major way.

The ToT module can be seen in figure 4.40, with the additional TDCs and their respective inputs and outputs also present. The additional output stage can be seen in J3, but as μC's often have a significant number of I/O pins, the further 7-pins were not considered to be a concern in the later results analysis. The threshold for the ToT board was set at 160 mV as discussed above, which was achieved using a voltage divider as seen in the components R20 and R21, with one connected to the +5 V power plane and the other connected to the -5 V power input pin for the positive and negative thresholds. The +5 V was attached to the power plane as more components required a +5 V input, so it simplified the design by connecting this power input to the power plane, therefore not requiring as many traces routed throughout the board.

The final PCB design was the CC board, which was the simplest in terms of component count, but the most difficult to develop due to the aforementioned simulation issues. The final design can be seen in figure 4.41, which begins the same as the ToT board, but differs as the output of

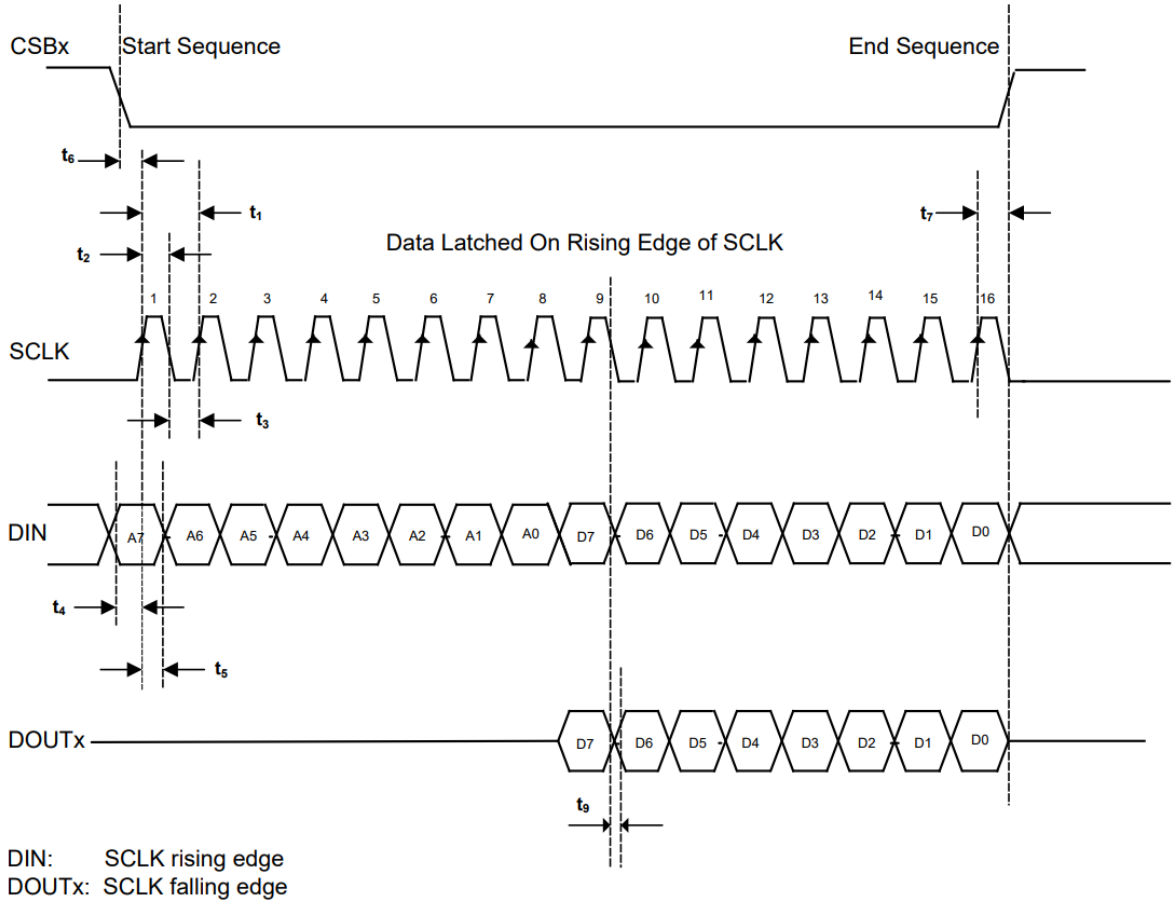

Figure 4.38: An illustration of the SPI register write using an 8 bit register example. This demonstrates the point at which each TDC signal goes high and impacts the other signals. Adapted from [161].

the comparators are combined rather than independently evaluated.

The D flipflop ICs can be seen with the identifiers U6 and U8 before the split gate results are passed into the two MOSFETs of Q1 and Q2. These MOSFET outputs are passed to the output connector P1 which will themselves be passed to the μC, where the pulse heights will be evaluated as the charge in each timing gate, therefore providing a charge comparison result.

As seen throughout all the PCB designs, the outputs of each board were to be connected to a μC that could be connected to a digital output for processing, but none of the designs have included a μC directly on the board. This was intentional as μC's are often bought with evaluation boards which they can be connected to for operation. This meant rather than purchasing a μC for each output, the output could be passed directly to this evaluation board without the need for an additional PCB board design. The overall aim of creating one single integrated board would then include a μC so that board could be processed directly without the need for additional module stages. There are still many different ways each of these boards could be refined and redesigned to improve predicted outcomes, such as reduction of component number or complexity, such as

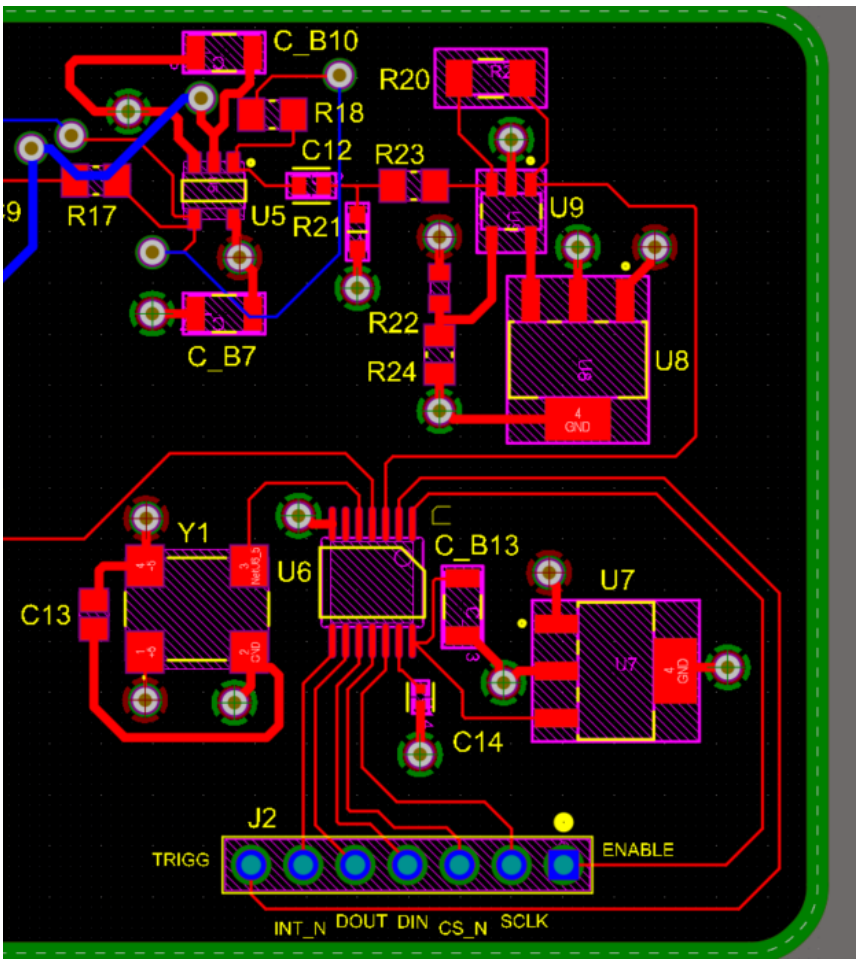

Figure 4.39: The third and final part of the zero crossing module created in PCB design software, with the TDC present as U6, also requiring a voltage regulator seen in U7, and the external clock input as Y1. The I/O signals from the μC will be routed through the connector of J2.

a smaller CFD in the ZC module design [162]. However, to make any redesigns effective, real world results that can be processed and analysed must be generated that can guide any redesign processes effectively.

As illustrated throughout this chapter, the design and simulation of a PCB is a process that involves many different aspects, beginning with an initial design plan that must be simulated to demonstrate feasibility, before being assembled in PCB design software and sent for manufacture. There was numerous delays during this process, with setbacks created from both simulation and manufacture, but these were resolved in order to create a series of boards that should form part of an analogue PSD solution. The next stage in the overall development of these solutions was the physical testing, to see the board outputs in the real world, and to then compare these analogue results to those provided by modern digital PSD methods.

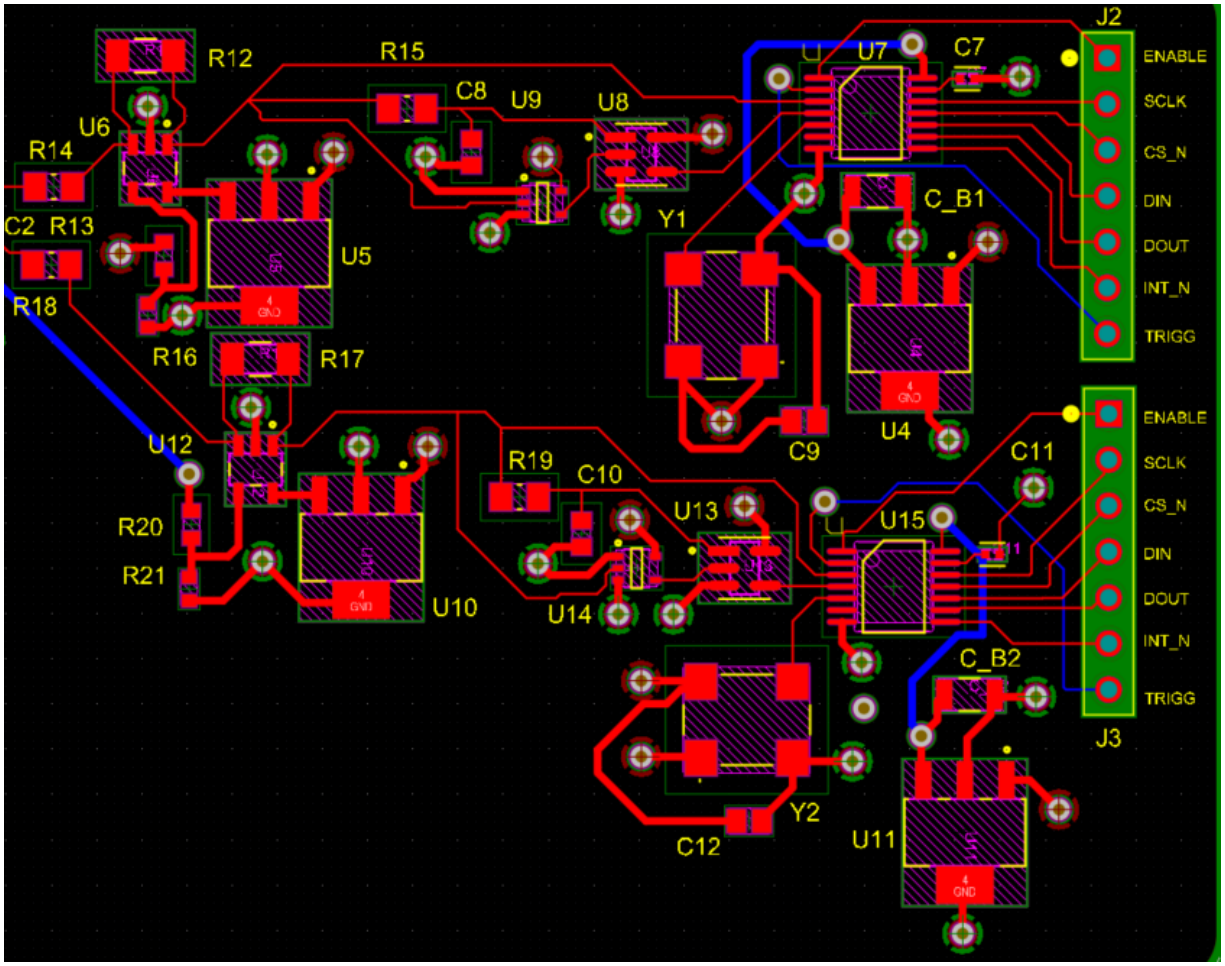

Figure 4.40: The logic stage of the time-over-threshold logic PSD module created in PCB design software. The overall smaller component count when compared to the zero crossing boards can be seen, with the two TDCs present in components U7 and U15 connected to outputs J2 and J3.

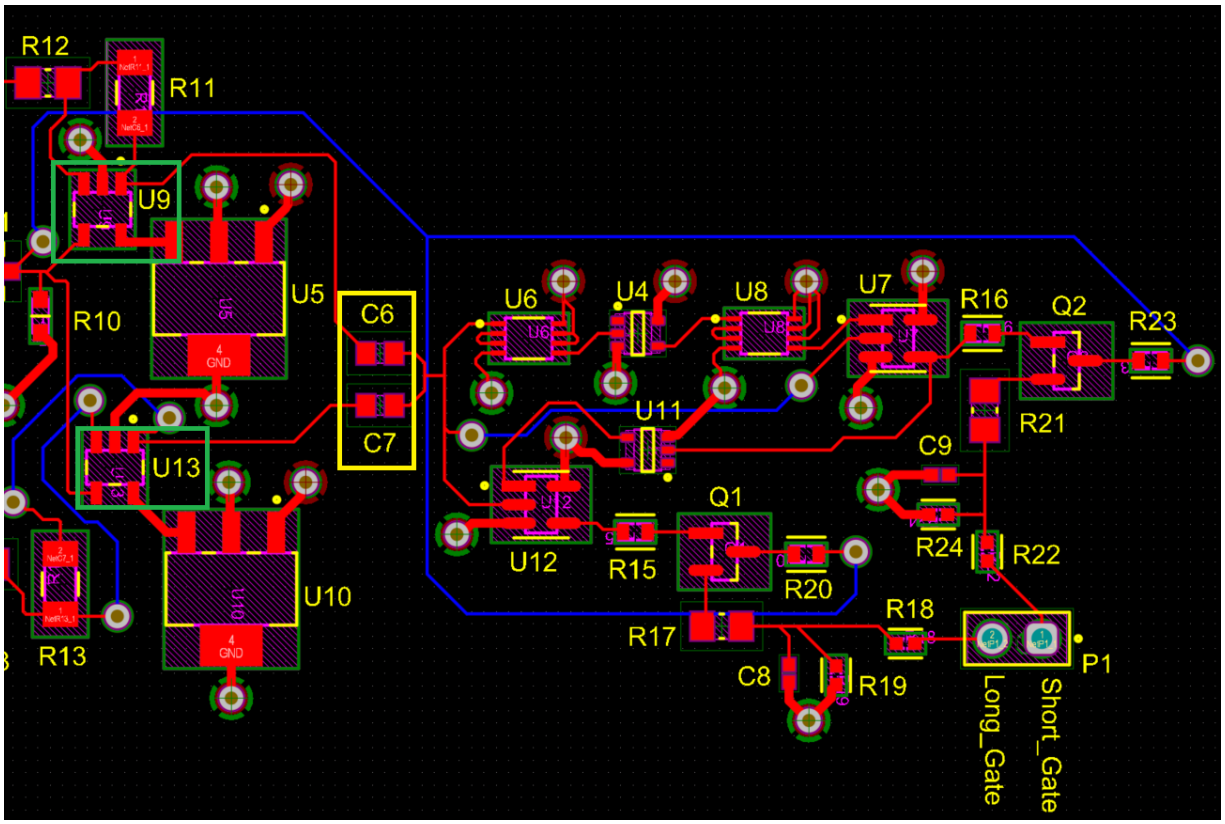

Figure 4.41: The logic stage of the charge comparison analogue PSD method created in PCB design software. The procession from the comparators (U9 and U13) in green, through their respective capacitors (C6 and C7) in yellow, are processed through the logic chains described in figures 4.27 and 4.29, with the two gate outputs passed directly to the μC, seen as the yellow markings short and long gate.

Chapter 5

Evaluation of Digital and Analogue PSD Solutions

Whilst the eventual analogue design was key to the goal of this work, the comparative digital results still required generation and evaluation. The work detailed in chapter 4 was a key factor in the design of this analogue solution, but this was not the only work undertaken throughout this investigation. A significant amount of early stage digital spectra were recorded and evaluated to form early analogue design choices, as well as allowing for benchmark comparison values to the eventual analogue outputs.

This then allowed for the next stage of investigation to begin, which involved separating each stage of the analogue process for a full comparison. The bias and amplification module was paired with a digitiser to fully understand the output of the SiPM module.

Due to the lack of digitiser for the analogue designs, the same outputs for digital and analogue results were not possible. However, it was possible in theory to perform FOM analysis for both the analogue and digital results, as the full digitisation of the waveform enabled the projection of neutron and γ-ray species onto a new plane that formed two Gaussian outputs. In the case of the analogue results, each logic board was designed to produce a varying output depending on the charge and timing characteristics of the input waveform. Over a time interval, these outputs should begin to form into two Gaussian distributions that should then allow for a FOM analysis. Having a consistent output form would allow for a better comparison between the digital and analogue outputs, with the aim of determining if the analogue PCB designs can match the performance output of a digital setup. This was unfortunately not the case, as will be explained throughout this chapter.

5.1 Digital PSD with Photomultiplier Tubes

As stated in chapter 3.1, initial results could be recorded and evaluated using a combination of a PMT and digitiser readout from an early stage. This began with γ-ray spectra in combination with an inorganic scintillator that could be used for detector calibration. This resulted in a linear calibration curve, such as the one seen in figure 5.1.

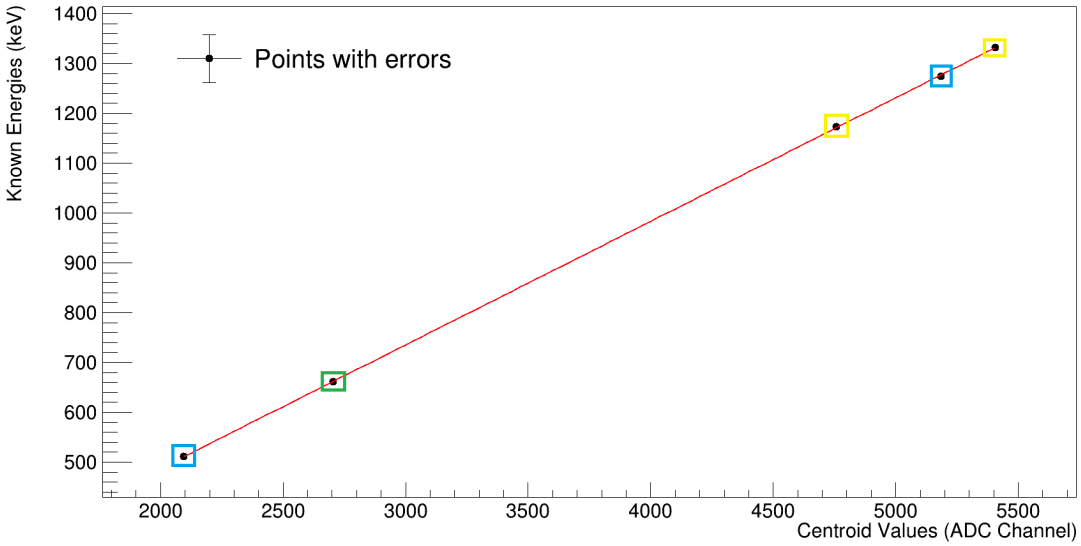

Figure 5.1: The calibration curve for the inorganic scintillation material CLLBC demonstrating that the scintillator responds linearly to increasing energy and can be used to calibrate other spectra, the ^{22}Na annihilation and photopeak are shown in the blue highlighted areas, as are the the ^{137}Cs photopeak in the green highlighted area, and the ^{60}Co high energy photopeaks in the yellow highlighted areas. All spectra were taken over 10 minute intervals at a bias of 1.3 kV, the errors included are smaller than the data points.

By applying the output of this fit to the original ^{137}Cs spectrum, it was possible to convert from amplitude to keV, which can be seen in figure 5.2, with the photopeak found at 662 kev$\pm$0.0254 keV as expected.

By plotting the FWHM of each photopeak against the known photopeak energy, similar to the method seen in figure 5.1, the detector energy resolution can be determined. This value is expected to be approximately 3.5% at 662 keV for CLLBC [123], although this value was not found in these results, with the resolution in figure 5.1 recorded as $5.6\% \pm 7.6 \times 10^{-3}\%$ at 662 keV. This is not significantly different to the industry standard, but this reduced resolution suggests that improvements can be made. An option could be the use of a light tight spring loaded mechanism to attach the PMT to the scintillator, as whilst the optical grease reduces air pockets and the PMT is kept in dark box conditions, it cannot be ruled out that some light could enter through this gap between the PMT and the scintillator.

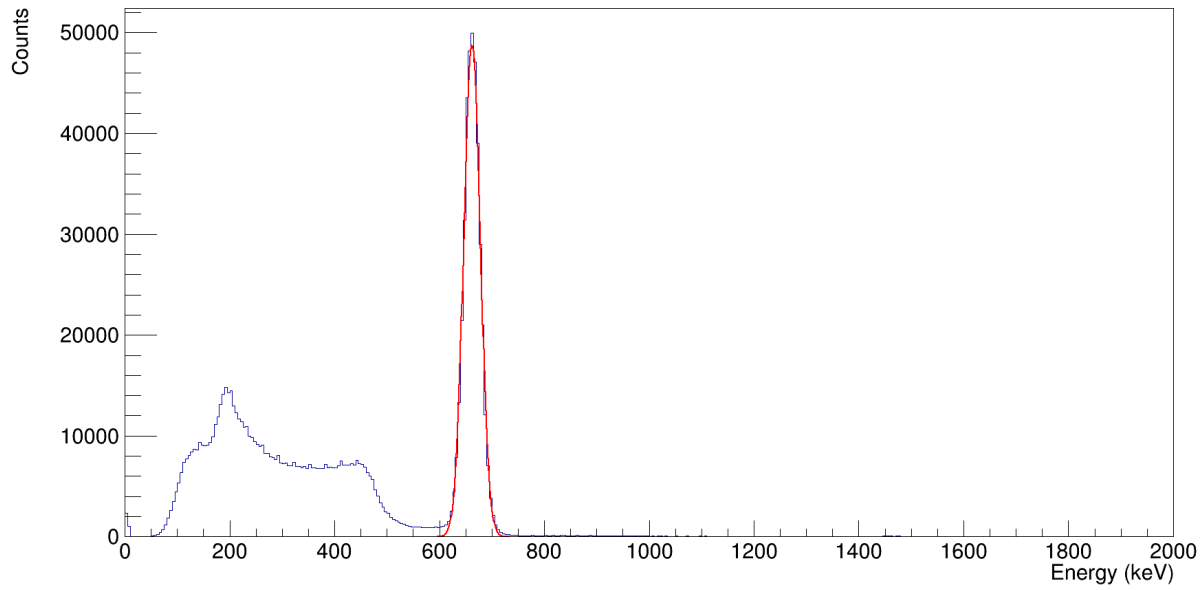

Figure 5.2: An energy calibrated event histogram ^{137}Cs spectrum recorded using the CLLBC scintillation material. The 662 keV photopeak can be clearly seen, as well as the lower energy Compton spectrum and backscatter peak, the red line is the included Gaussian fit.

When this process is repeated for CLYC, an energy resolution of $9.3\% \pm 0.04\%$ is determined, worse than that of CLLBC. This was expected as the CLYC sample available for use is old and has been damaged in the past, which is believed to have degraded the performance of this particular CLYC. The process of determining detector energy resolution at 662 keV is not the same for an organic scintillator, as discussed in chapter 3. However, upon using the method described in chapter 3, a resolution of $20\% \pm 0.26\%$ was determined for EJ-276, similar to that described in other literature, with one study also finding a 20% energy resolution [163]. When this same method was applied to EJ-299-50, a resolution of $22.2\% \pm 0.21\%$ was determined. As γ-ray energy increases the energy resolution also tends to improve, this is because higher energy signals are more likely to have different contributions that are not seen at higher energies. This is demonstrated by the energy resolution at 1275 keV for the CLLBC material, which was calculated to be $3.8\% \pm 0.062\%$.

Another key result first highlighted in chapter 1 is that of the intrinsic efficiency, which is the detector efficiency with the detector geometry accounted for in the calculation. For CLLBC at 662 keV, an intrinsic γ-ray efficiency of $17.6\% \pm 8.8\%$ was measured, with this value expected to decrease as energy increases. This is because higher energy photons are more likely to pass through the material without interaction, although the higher density of CLLBC would mitigate this to an extent. This can be seen when the intrinsic efficiency at 1275 keV was calculated as $8.2\% \pm 4.2\%$. For CLYC, a similar intrinsic γ-ray efficiency to that of CLLBC of $13.6\% \pm 6.8\%$ at 662 keV was determined. These large errors are likely caused by the solid angle, as a measurement distance of 5.08 cm was used, and as such extending the distance in a repeated

measurement should reduce this uncertainty.

For the EJ-276 and EJ-299-50 materials, the process of determining intrinsic γ-ray efficiency is similarly difficult to that of the detector resolution. This is also due to the lack of clear photopeaks which makes accurately determining the number of γ-rays seen by the detector difficult. This can be seen in figure 5.3. Because of this lack of photopeaks, the γ-ray efficiency cannot be determined in the same manner as an inorganic scintillator, with simulation often used to more accurately determine intrinsic γ-ray efficiency in plastic scintillators. Both the inorganic efficiencies were calculated using the setup at the University of Michigan, with all efficiencies calculated at a 5.08 cm distance with a 10 minute time interval of recording.

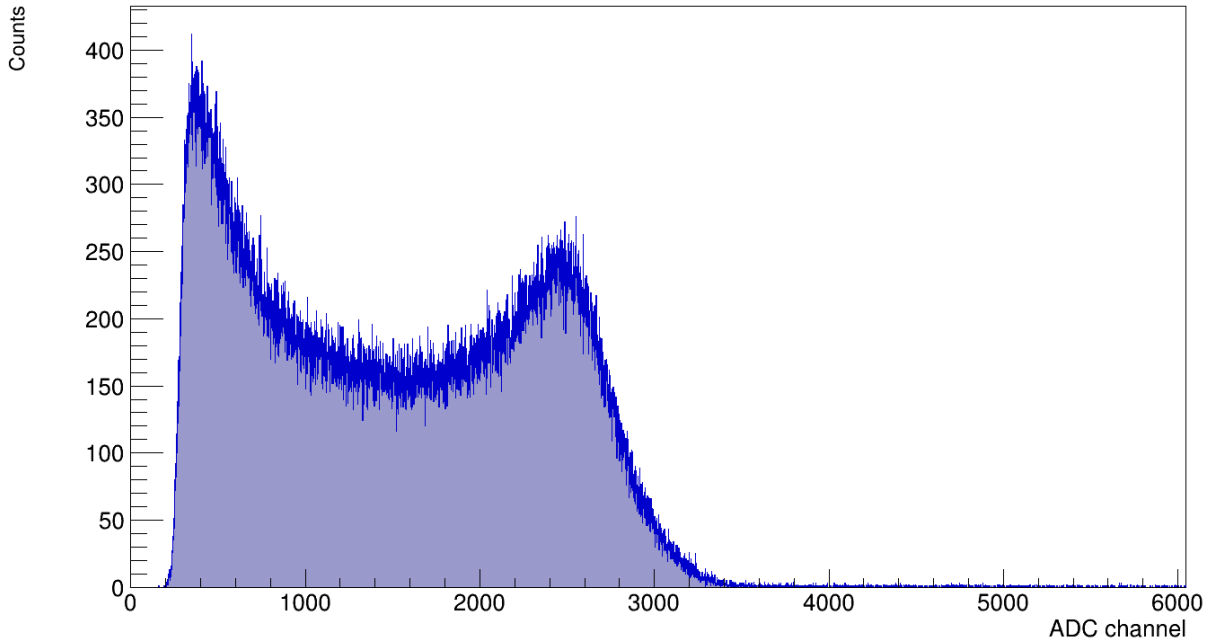

Figure 5.3: An event histogram ^{137}Cs spectrum recorded using the EJ-276 scintillation material. The lack of clear photopeak but Compton edge features are shown, therefore demonstrating why it is more difficult to determine the intrinsic efficiency of a plastic scintillator.

The histograms seen in figures 5.4 and 5.5 represent the expected energy histogram pattern for neutron spectra, but this is not the most effective form for neutron analysis. The thermal neutron peak can be seen in figure 5.5, but when the organic scintillator histogram is observed there is no discernible separation between fast neutrons and γ-rays. This is where the use of the PSD factor becomes crucial, as can be seen in chapter 3 in figures 3.12 and 3.13. These figures demonstrate the patterns that emerge from each scintillator form, with the thermal neutron hotspot present for inorganic scintillators, and the continuous distributions for the organic scintillators.

This pattern can be seen again in figure 5.6, which was generated using CLYC and an AmBe source, although the neutron hotspot in this case is less defined than expected. This is believed

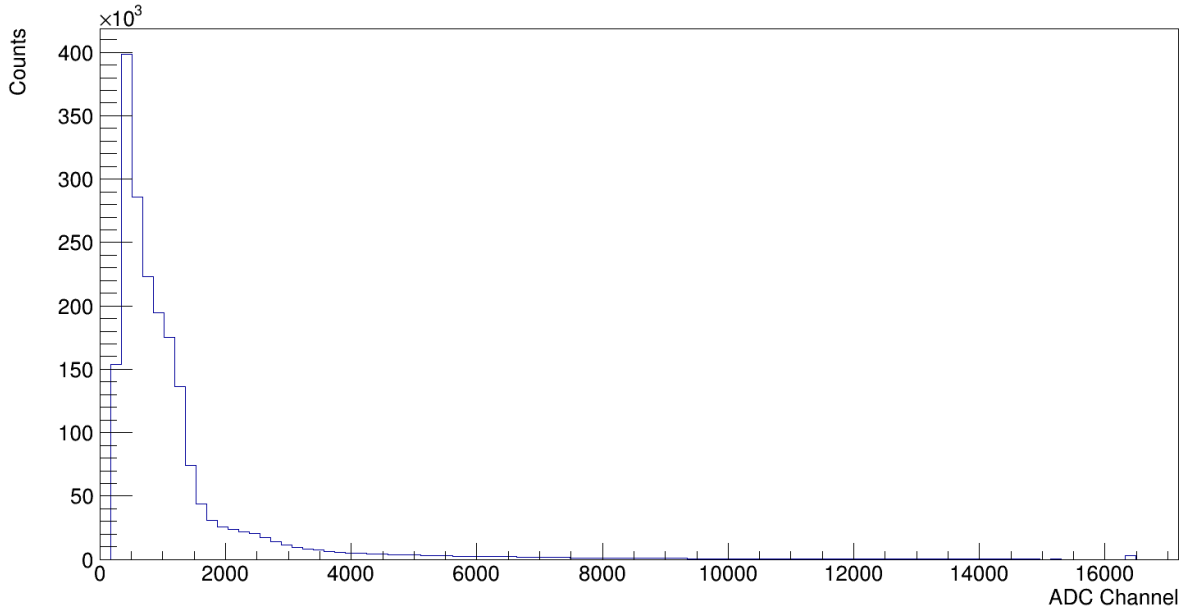

Figure 5.4: An ADC Channel histogram for a ^{252}Cf source using the EJ-276 material. There is no discernible pattern visible in the spectra, hence why the use of timing gates to separate the neutron and γ-ray species is crucial.

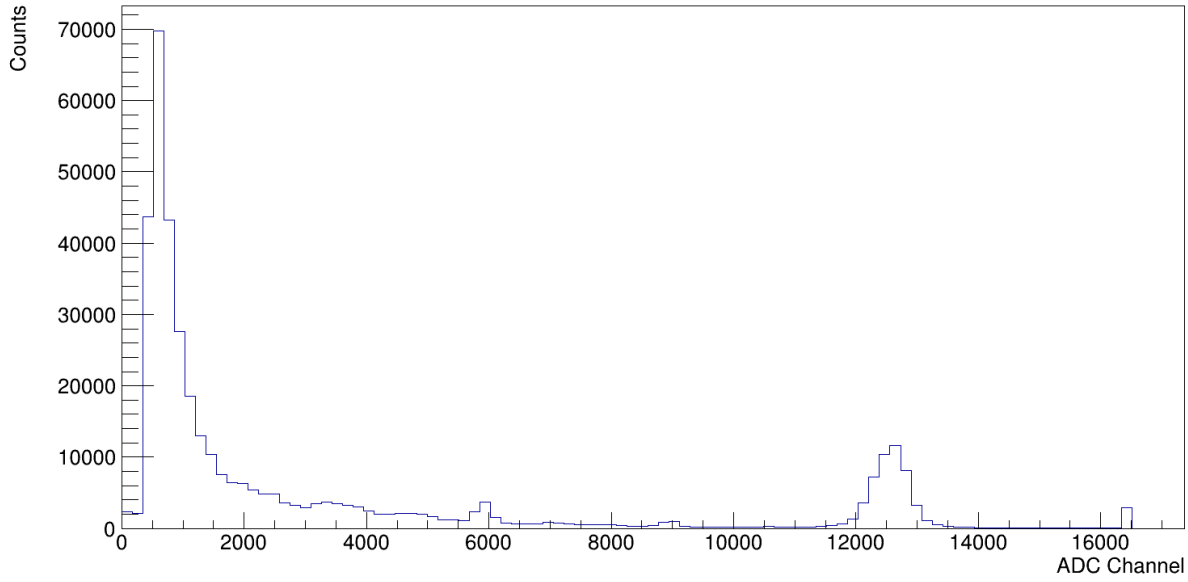

Figure 5.5: An ADC Channel histogram of a ^{252}Cf source using the CLLBC material. Some patterns can be seen for an inorganic scintillator, such as the thermal neutron peak towards the upper end of the energy range.

to be due to the ^{35}Cl present, which can cause some elastic scatter to occur, creating a small range of energy values through the neutron hotspot. These distributions are then projected in the y direction to form two Gaussian distributions, as seen in figure 5.7. When a traditional FOM analysis is performed for this CLYC spectra, a FOM of 2.5 ± 0.1 is determined, and when this method is repeated using CLLBC, a FOM of 3.69 ± 0.03 was determined, both far exceeding

the baseline 1.27 described in chapter 2. This means that CLLBC, using digital PSD methods, is capable of performing neutron and γ-ray species separation. Additional work using CLLBC was published here: [94].

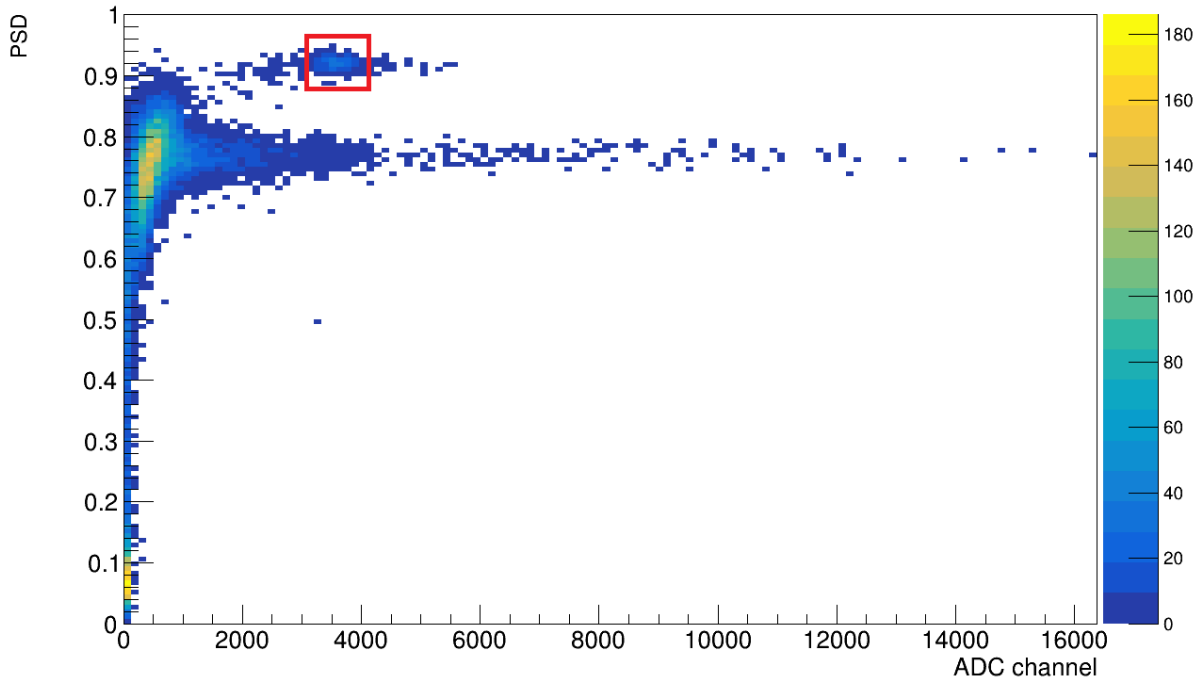

Figure 5.6: The PSD factor vs ADC Channel plot for CLYC, with the range of γ-ray energies seen as the continuous distribution. The thermal neutron peak can also be seen in the red highlighted area, with some spreading of the peak, believed to be due to elastic scatter from the ^{35}Cl.

When this same method of analysis is performed with EJ-276, a FOM of 1.82 ± 0.097 was determined. This is worse than that of CLLBC, but this is to be expected due to the decreased photon production and reduced density. This 1.82 value still exceeds the desired 1.27 baseline, meaning that EJ-276 is also capable of performing neutron and γ-ray species separation using digital PSD methods. As stated with CLYC a FOM of 2.5 was calculated. This was was closer to the value seen by CLLBC, but there are several mitigating factors. Firstly, as described before, this CLYC sample available has been damaged before due to the hermetic seal breaking and allowing water ingress. This has been repaired but it has affected performance, which was seen during experimental work as the trigger threshold for CLYC was significantly higher than that of other materials, due to an extremely large low energy peak that was believed to be noise from the crystal. This is believed to be a result of the specific crystal itself rather than the material due to the damage this crystal has received, regardless this suggested that this CLYC sample was also able to effectively separate neutron and γ-ray species.

The FOM analysis for the EJ-299-50 material was slightly different to that of the other materials,

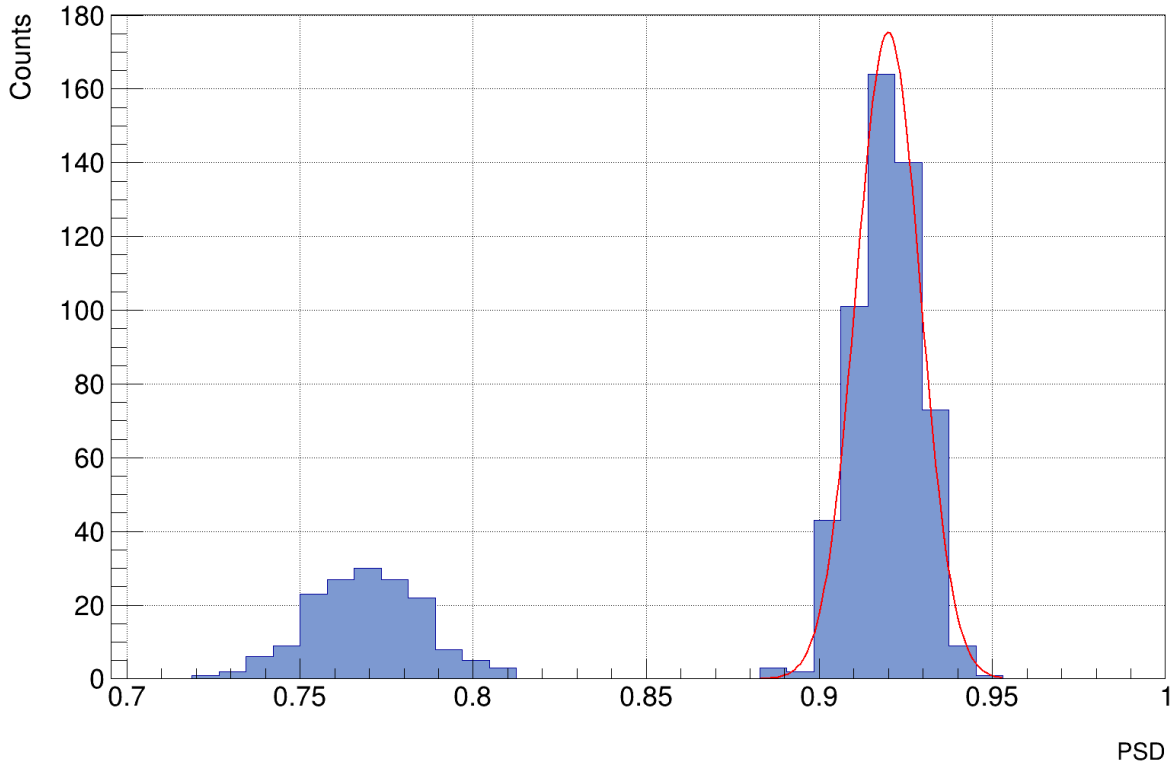

Figure 5.7: The Gaussian projection for CLYC, with the γ-ray and thermal neutron peaks present. The separation between these two peaks divided by the FWHM of each peak produces the FOM, which in this case is 2.5, the Gaussian fit included is an example of the fit used on both peaks.

as the triple mode nature of the material meant that it was possible to determine a difference between the γ-rays, thermal and fast neutrons. It is common when using a plastic scintillator to not use moderation, as fast neutrons are the most relevant neutron energy, and due to the amount of hydrogen contained with the EJ-299-50 material, it should self moderate to an extent. However when this was attempted, the neutron hotspot was mostly overwhelmed by the number of fast neutrons present from the AmBe source used at Glasgow. This can be seen in figure 5.8, where the beginning of the neutron hotspot can be seen in the red area, but it is not distinctive.

Once some additional moderation is added in the form of 4.4 cm blocks of paraffin wax, the neutron hotspot begins to become clearer, this is seen as the amount of moderation increases in figure 5.9, up to an extent. It can be seen when 26.4 cm of moderator is used in figure 5.10 that the neutron hotspot has a reduced number of counts despite equal time intervals, with the fast neutron species being significantly reduced, as would be expected.

Once a cut of a minimum cut of 20 is applied to figure 5.10, meaning any bin with less than 20 counts is removed, the thermal neutron hotspot and γ-ray species become the only two visible as seen in figure 5.11. When a FOM analysis is performed, a FOM of 2.02 ± 0.025 is calculated, demonstrating that EJ-299-50 can effectively separate thermal neutrons and γ-rays. When this

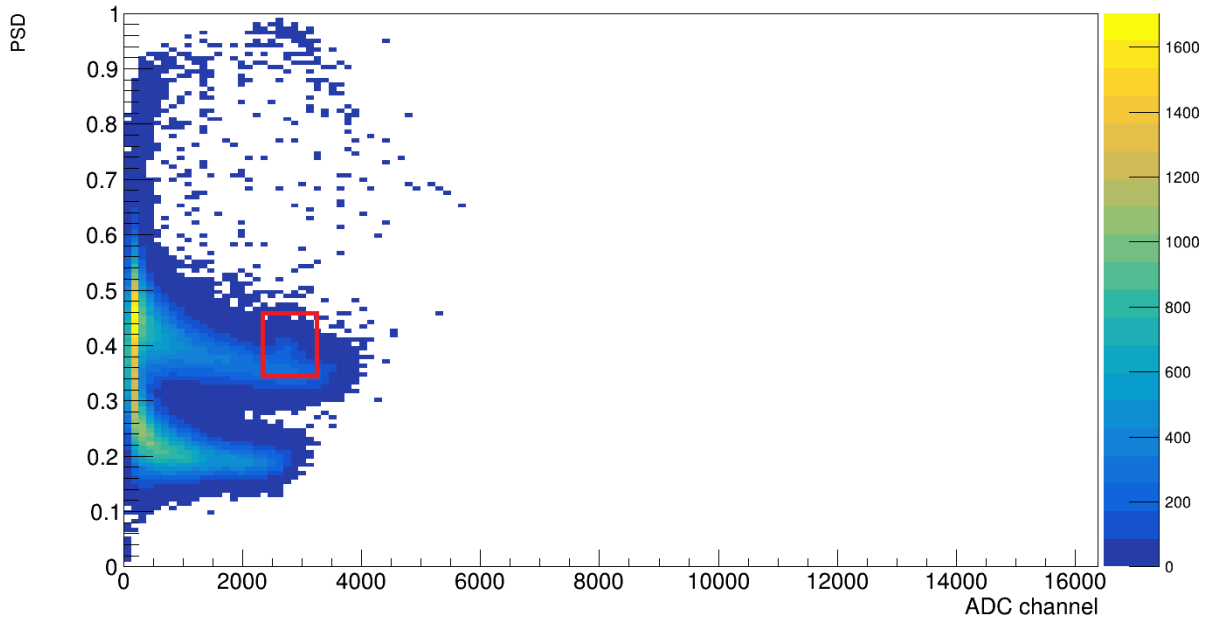

Figure 5.8: A PSD factor factor vs ADC channel plot for an AmBe source using the EJ-299-50 scintillation material with no moderation present. The formation of the fast neutron and γ-ray species can be seen, with the formation of the thermal neutron hotspot beginning, as seen in the red area, although this is almost entirely covered by the fast neutrons.

same analysis is applied to a spectra with no moderation present, such as the one in figure 5.8, a FOM between the entire neutron energy range and the γ-ray species is calculated to be 1.75 ± 0.014. A FOM analysis was performed on the thermal neutron and fast neutron energies, although this only yielded a FOM of 0.68 ± 0.1. Therefore whilst EJ-299-50 is effective at neutron and γ-ray separation, it is not able to separate between specific neutron energies.

When comparing these FOMs to literature results, the CLLBC FOM of 3.69 was found to slightly exceed that found elsewhere, with a range of 1.3 to 3.5 reported, as well as CLYC with a reported FOM of 2.2 [164][165]. This is also the case for EJ-276, which has been quoted as having a FOM of 1.15 [166], less than the value found during this investigation of 1.82. As a relatively new material, there was no widely reported FOM result for EJ-299-50 currently available, and as such it was not possible to determine how this 2.02 FOM compared to literature values.

When a neutron source of known activity is available, it is possible to perform a time-of-flight (TOF) measurement. This is useful as it allows for the determination of the neutron energy range emitted by a source, as well as a neutron efficiency calculation. The first stage of this measurement is to record the timing offset between the scintillators under investigation and a fast timing scintillator, in this case a EJ-309 organic scintillator. This is done using a ^{22}Na source, due to the two 511 keV annihilation photons, meaning that a coincidence measurement

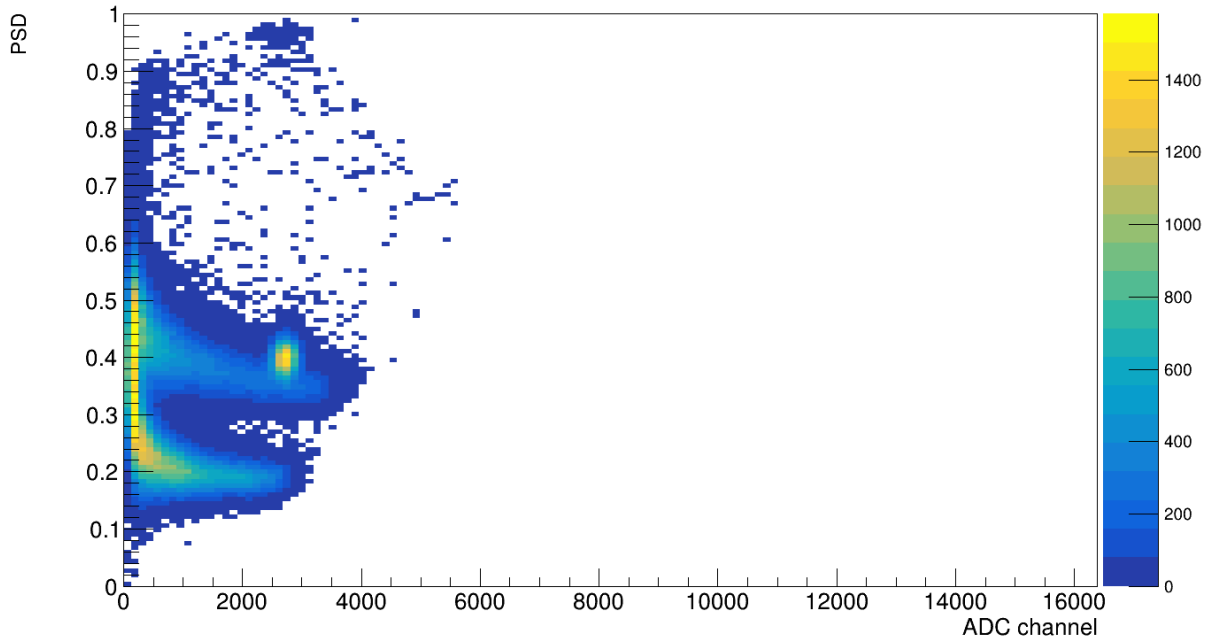

(a) An EJ-299-50 AmBe PSD factor vs ADC channel spectra with 4.4 cm of moderation.

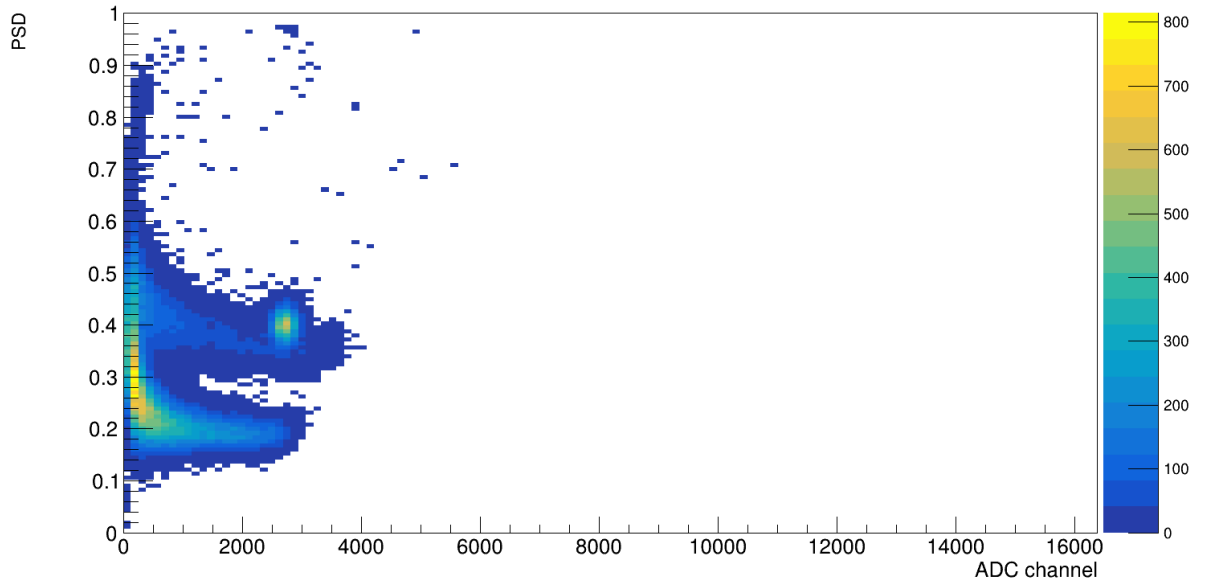

(b) An EJ-299-50 AmBe PSD factor vs ADC channel spectra with 13.2 cm of moderation.

Figure 5.9: Two EJ-299-50 AmBe spectra with 4.4 cm and 13.2 cm cm of paraffin wax moderator respectively. This was performed in order to demonstrate the reducing fast neutron species being replaced by the increasing thermal neutrons seen in the thermal neutron hotspot.

can be performed. An example of this setup can be seen in figure 5.12.

The reason for performing this offset measurement is to account for the physical variables that will affect the result, such as varying cable lengths, with each scintillation material having a

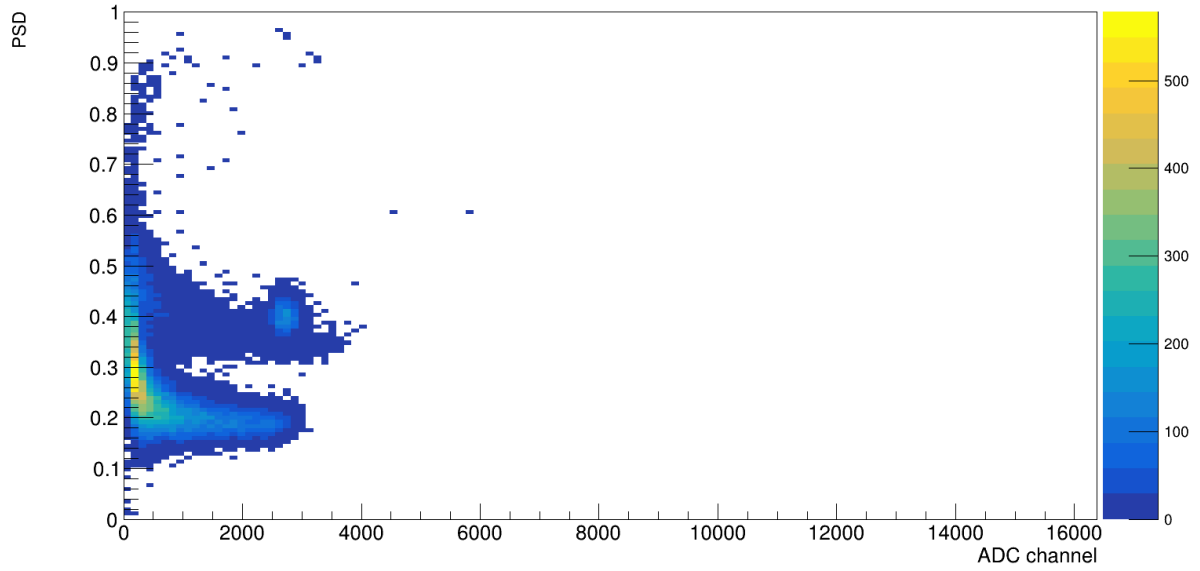

Figure 5.10: An EJ-299-50 PSD factor vs ADC channel spectra with 26.4 cm of moderation, demonstrating that increased moderation can also reduce the number of counts present in the results.

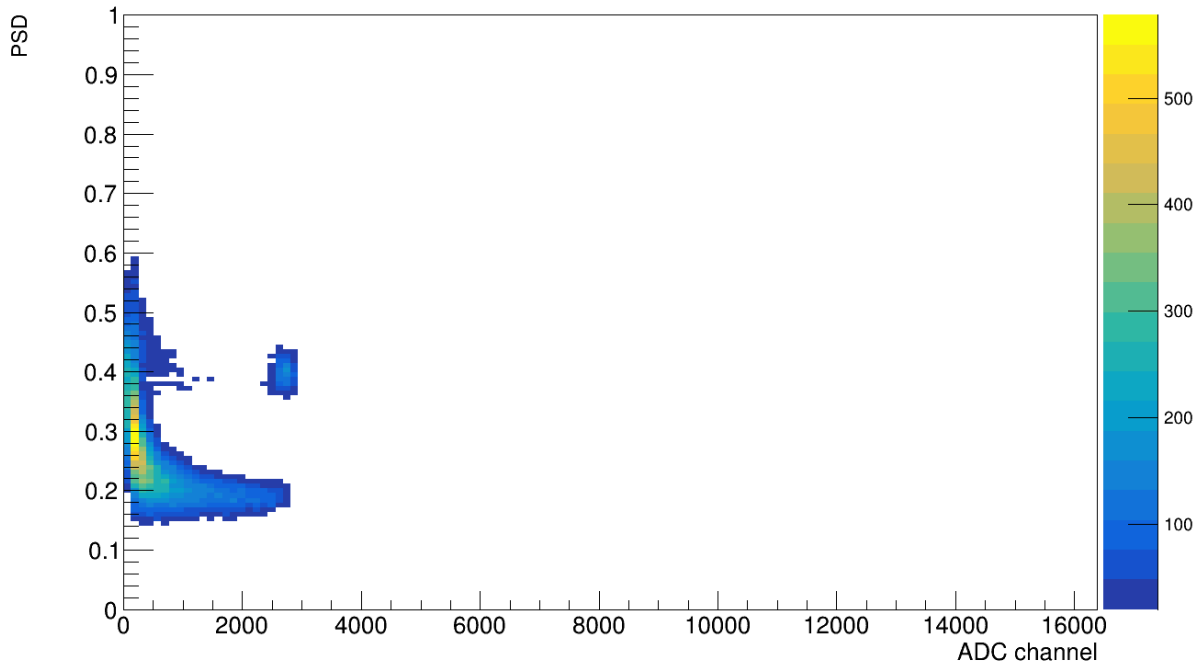

Figure 5.11: An AmBe PSD factor vs ADC channel spectrum with 26.4 cm of moderation, with a minimum frequency cut of 20 applied. This was performed to remove the fast neutron signal completely from this result, allowing for a FOM analysis entirely between the thermal neutron and the γ-ray species.

timing offset of approximately 60 ns. Once this offset was recorded for each scintillation material, it could be removed from the eventual TOF measurement. The ^{252}Cf source used for this TOF measurement was quite weak, and as such a 65 hour measurement was performed.

(a) Time-of-flight offset calculation demonstration.

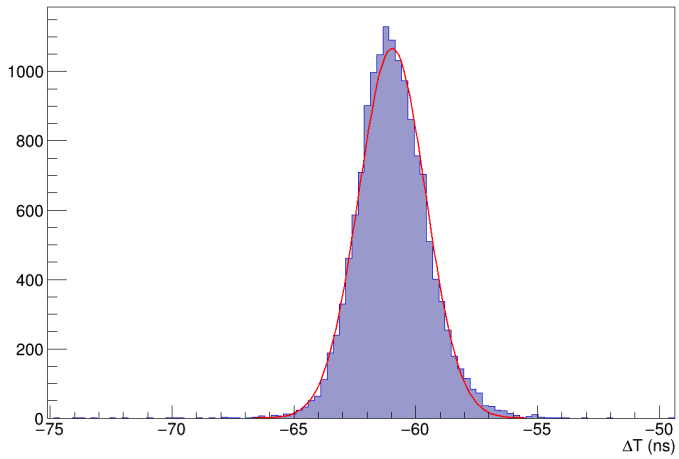

(b) Time-of-flight calibration result.

Figure 5.12: An example of the time-of-flight offset calculation performed for each material, with a ^{22}Na source, highlighted in red, placed between a EJ-309 organic scintillator and one of the scintillation materials under investigation to record a coincidence measurement. The result of this can be seen in b, with an offset of 61 ns determined using the Gaussian fit present.

An example of the TOF spectrum with the offset removed can be seen in figure 5.15, with the sharp central peak relating to the γ-ray species and the wider peak relating to the neutron species. One method of performing a TOF measurement is to force the γ-ray peak to 0, as it is presumed that over a short distance these γ-rays arrive almost instantaneously. This is not the case in this measurement, as can be seen by the γ-ray peak found at approximately 1 ns. This is believed to be a result of the setup seen in figure 5.13, where the distance from source to detector caused the γ-ray species to arrive at approximately 1 ns. This distance was chosen because, whilst the source was indeed weak as described above, if it was too close to the detector materials the digitiser would become overwhelmed. This would increase the detector dead time and reduce the available data, and as such a distance of 76.2 cm was used.

One of the primary results from each of the TOF spectra seen in figures 5.14, 5.15 and 5.16, are the large γ-ray signals present. This is why it is necessary to focus on the neutron timing values between 10 ns to 60 ns, as this is the region where the relevant TOF data will be found. The ^{252}Cf source used in this experiment was unshielded and also ran for 65 hours, meaning that a large proportion of the output being γ-rays is not unexpected. This also meant that EJ-276 would be the material expected to see the highest number of neutrons, due to its ability to detect fast neutrons more readily, which can be seen by the higher counts over the neutron timing range.

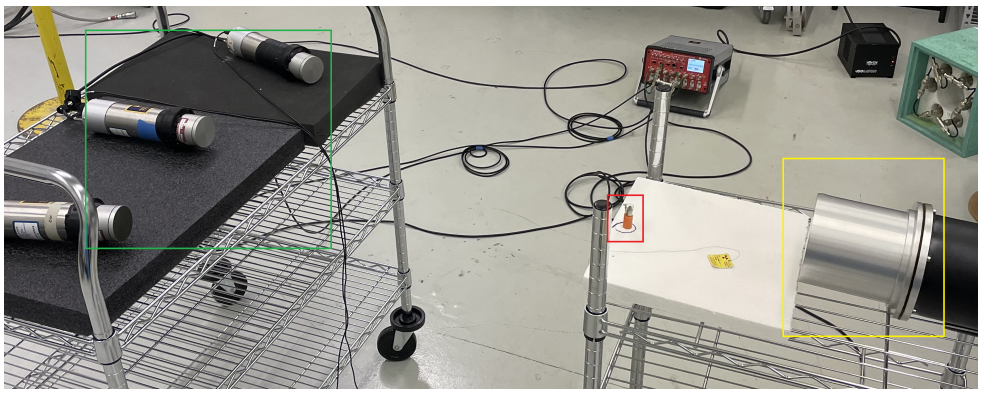

Figure 5.13: A picture of the time-of-flight experimental setup, with the trigger detector, highlighted in yellow, placed approximately 27 cm from the ^{252}Cf source, highlighted in red, and each detector material placed approximately 76.2 cm from the ^{252}Cf source, with each material highlighted in the green area, with CLYC at the top, EJ-276 in the middle and CLLBC at the bottom.

Overall the neutron timing for each material appear to match other conclusions made regarding the material. These include the prediction that EJ-276 would see more fast neutrons due to its high hydrogen content, and that CLLBC has some elastic scatter present due to the ^{35}Cl. When the CLYC material neutron timing is focused on in figure 5.16, the peak appears very different to that of EJ-276 and CLLBC, as there is no clear rising edge to the peak. This becomes clearer when the timings are converted into neutron energy spectra.

This was performed using the equation 5.1 to convert from neutron velocity to energy:

$$E_k = \frac{1}{2}mv^2. \tag{5.1}$$

It was possible to determine a neutron energy spectrum for CLLBC from this TOF data, as well as for CLYC and EJ-276, with the energy spectra seen in figures 5.17, 5.18 and 5.19. Each of these figures follow the expected distribution for a ^{252}Cf source, with a mean energy of in the 2 MeV to 2.8 MeV range, up to an energy of $\sim$8 MeV. The exception is that of CLYC in figure 5.18, which does not appear to see almost any of the fast neutrons, and instead only sees neutrons closer to thermal energies. These energy calculations were made without a relativistic correction as the mean energy corresponded to 0.07 c, with relativistic effects only coming into effect above 0.1 c or $\sim$6 MeV on this spectra, where only some neutrons were seen by the CLLBC material, as seen in figure 5.18.

It is also possible to determine the intrinsic fast neutron efficiency from this result through a similar procedure as the γ-ray efficiency. This procedure was different as the intrinsic γ-ray efficiency was determined at a specific energy, due to the nature of the γ-ray sources. When these efficiencies are determined, they are done so across the emitted neutron energy range. An intrinsic neutron efficiency of $0.53\% \pm 0.12\%$ was calculated for EJ-276, with values of

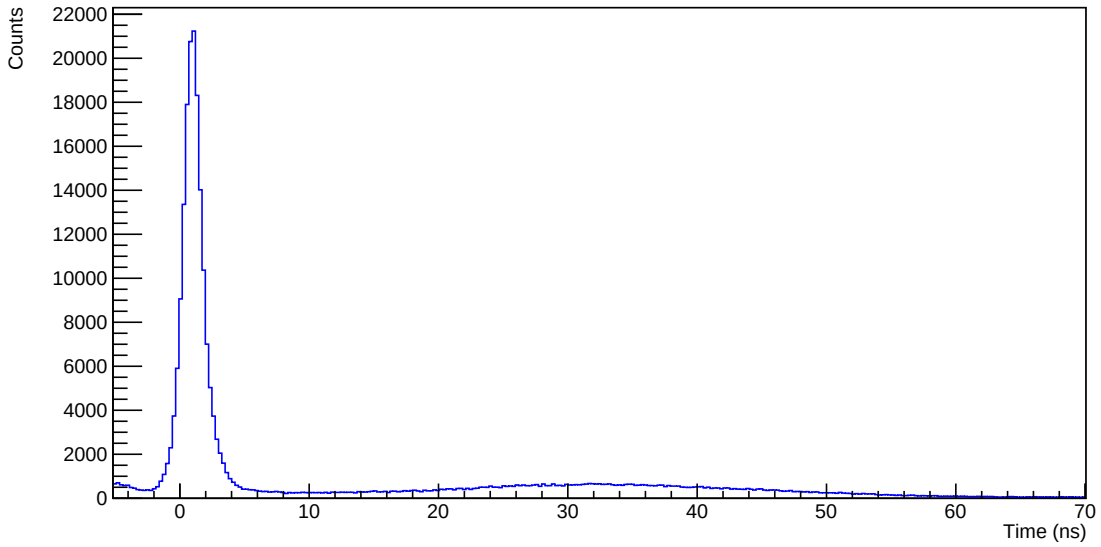

(a) The full time-of-flight spectrum for EJ-276.

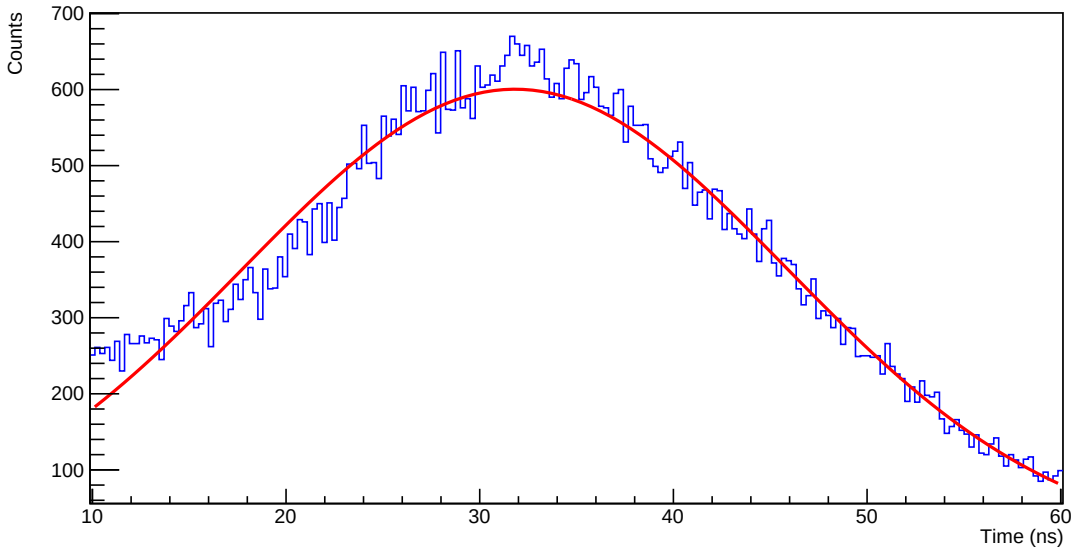

(b) The 10 ns to 60 ns range of the EJ-276 time-of-flight spectrum.

Figure 5.14: The full time-of-flight spectra for the EJ-276 material, along with a focus on the 10 ns to 60 ns range where the neutron energy peak was located. These spectra demonstrate the better timing characteristics of a plastic scintillator when compared to an inorganic, with the greater number of γ-rays and fast neutrons seen as compared to the other materials.

$0.22\% \pm 0.05\%$ and $0.31\% \pm 0.07\%$ recorded for CLLBC and CLYC respectively. It was not possible to perform a TOF measurement for the EJ-299-50 sample, as the material was not available at the time this measurement was performed. It was also not possible to retroactively perform this measurement, as the AmBe source available at Glasgow is of unknown activity, and therefore cannot be used for a neutron efficiency measurement.

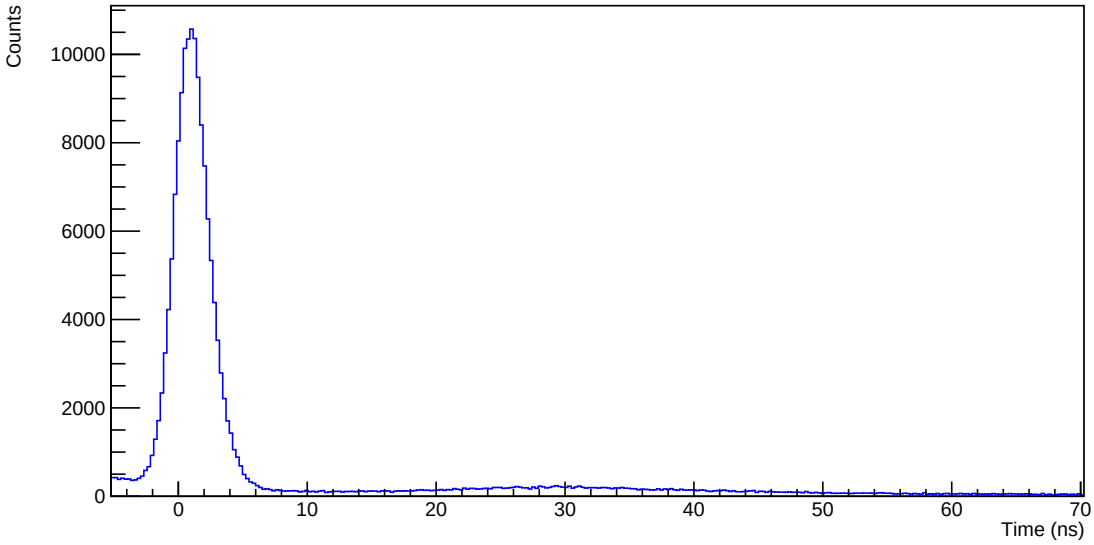

(a) The full time-of-flight spectrum for CLLBC.

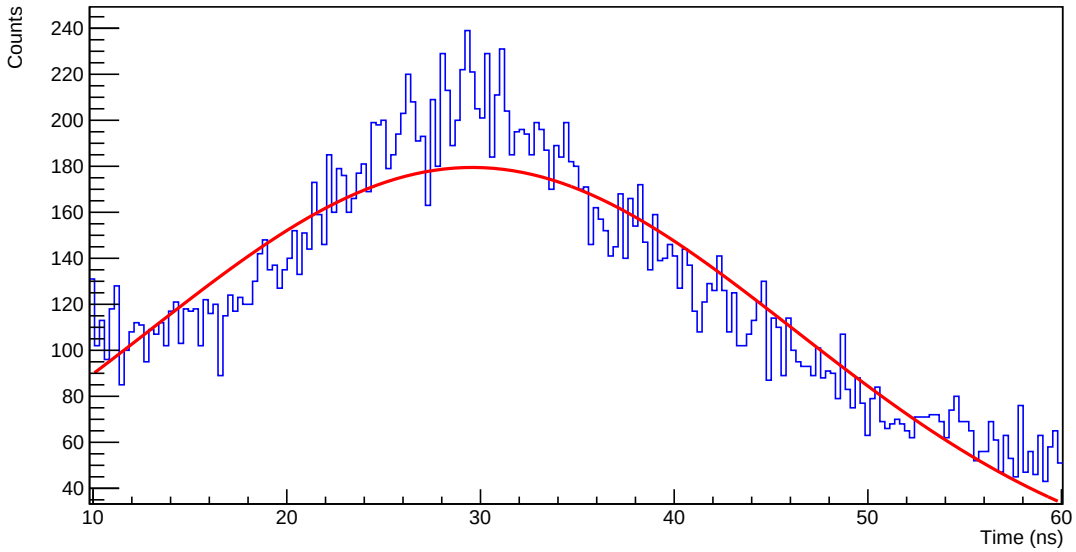

(b) The 10 ns to 60 ns range of the CLLBC time-of-flight spectrum.

Figure 5.15: The full time-of-flight spectra for the CLLBC material, along with a focus on the 10 ns to 60 ns range where the neutron energy peak was located. The slower timing of CLLBC can be seen by the smaller γ-ray peak than that seen in figure 5.14, but there is still some elastic scatter present seen by the neutron peak, although there are a much smaller number of counts. The Gaussian fit can also be seen that was used to determine the neutron energy range.

These low efficiencies are expected for inorganic materials due to their thermal neutron specialty and therefore these values are expected. However, CLYC recording a higher neutron efficiency than CLLBC was unexpected and may be due to CLYC only appearing to detect low energy neutrons. This could also be due to other factors, such as the aforementioned damage, or issues with the Gaussian fit as seen in figure 5.16. Organic scintillators have a typical fast neutron

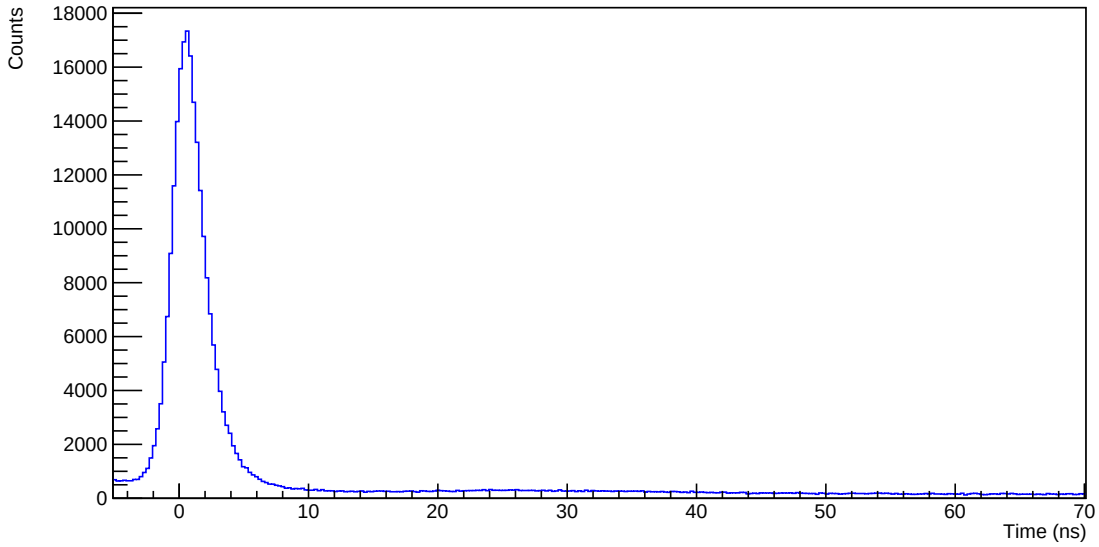

(a) The full time-of-flight spectrum for CLYC.

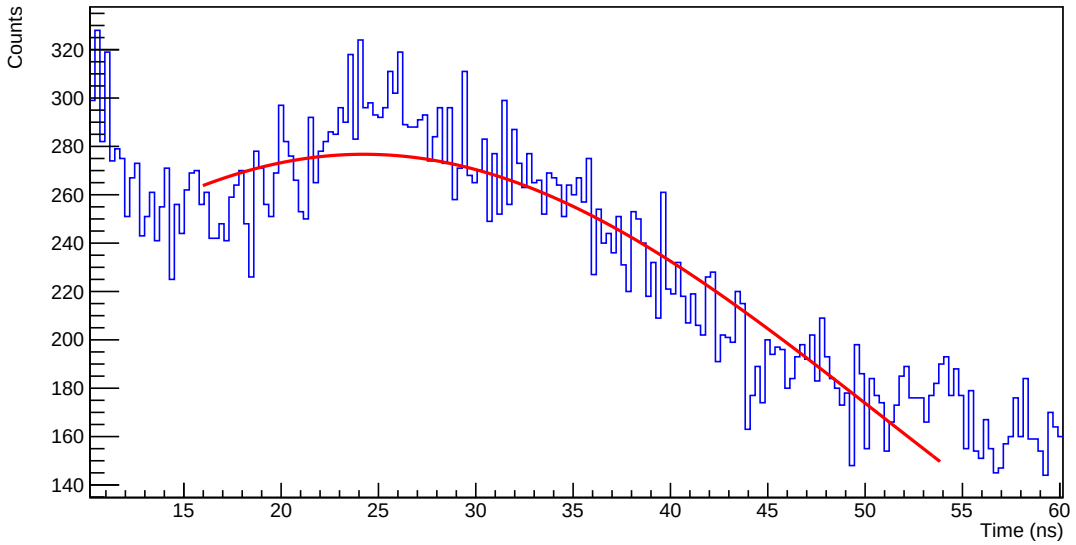

(b) The 10 ns to 60 ns range of the CLYC time-of-flight spectrum.

Figure 5.16: The full time-of-flight spectra for the CLYC material, along with a focus on the 10 ns to 60 ns range where the neutron energy peak was located. The neutron peak is not as clear here, with no clear rising edge, although this was expected based on previous findings of this material. This can also be seen by the Gaussian fit applied, which has been restricted to a 15 ns to 55 ns range in an attempt to improve the result, but still does not provide a clear result.

efficiency of between 1%-10% [167], so the calculated neutron efficiency is below expected for EJ-276, but not unreasonable.

Using the setup present in a) of figure 3.7, it was possible to perform a neutron measurement using a D-D generator for each of the three available scintillation materials. As seen in figure

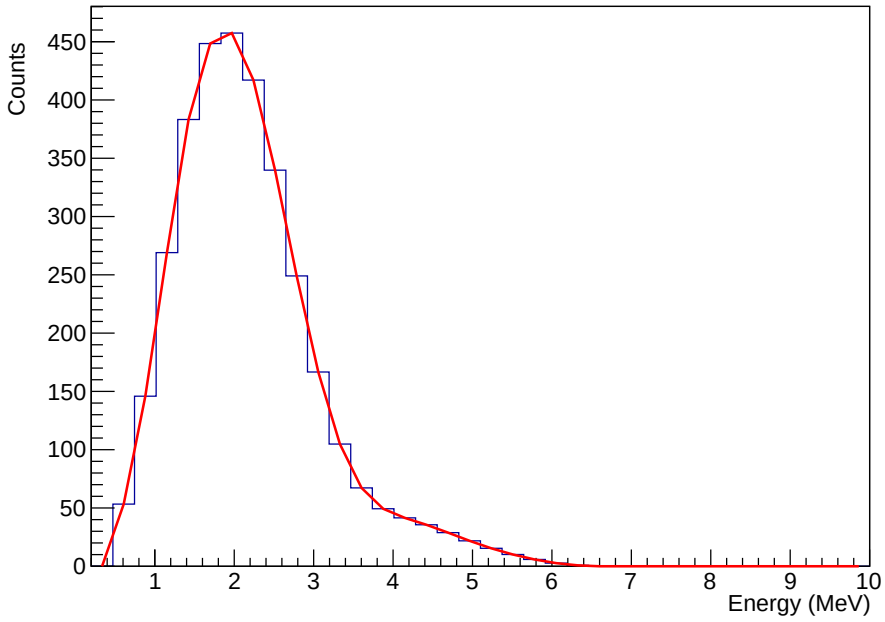

Figure 5.17: The ^{252}Cf neutron energy spectrum for the EJ-276 material, with the mean energy of 2.1 MeV and peak energy of 6 MeV present, the red distribution is a smoothing function intended to guide the eye and is not a fit, this is the same for figures 5.18 and 5.19.

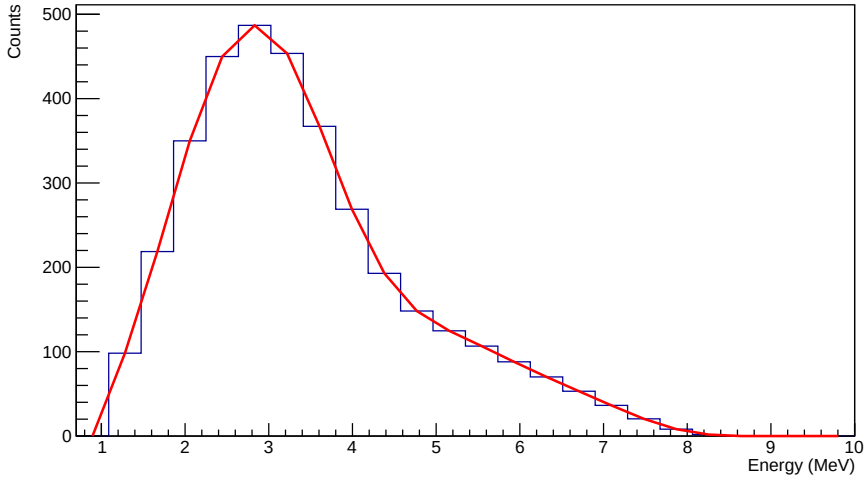

Figure 5.18: The ^{252}Cf neutron energy spectrum for the CLLBC material, with a mean energy of ∼2.8 MeV and peak energy of ∼8 MeV present. This demonstrates the elastic scatter present in CLLBC, and also seems to indicate that CLLBC was able to record a similar range of fast neutron energies to that of the EJ-276 material.

3.5, monoenergetic neutrons of 2.45 MeV are generated, allowing for a consistent source of low energy neutrons. As described in chapter 3, this neutron generator had a flux of $\sim 2 \times 10^6$ neutrons per second with each run taking place over 10 minutes.

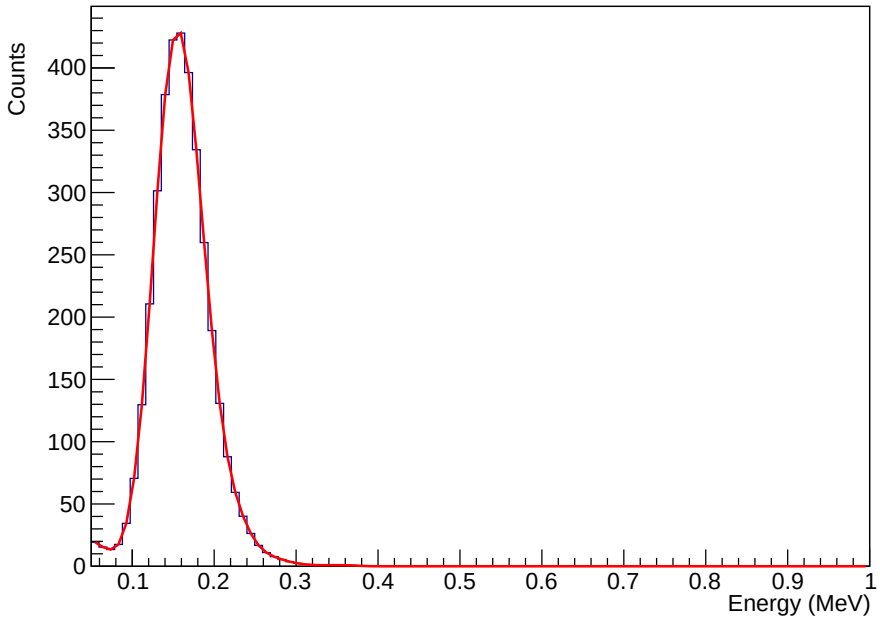

Figure 5.19: The ^{252}Cf neutron energy spectrum for the CLLBC material, with only lower energy neutrons detected by the material, demonstrating that CLYC is almost entirely blind to fast neutrons, only recording neutrons closer to the 0.025 eV thermal neutrons.

The energy spectra recorded can be seen in figure 5.20, which is similar to that seen in figure 5.4 and does not indicate much about the neutron beam. When the energy is plotted against the PSD factor, seen in figure 5.21, the formation of two species can be seen. This is interesting as a D-D generator should only emit the 2.45 MeV neutron beam, but this effect can also be noticed when looking at the CLLBC D-D spectra seen in figure 5.22. It can also be seen that a thermal neutron peak is recorded, so there are likely to be environmental thermalisations occurring due to the materials present in the room, most likely from reflections from physical materials, such as concrete.

The method of operation for the D-T generator was very similar to that of the D-D generator, with the setup itself seen in b) of figure 3.7. As seen in figure 3.6, monoenergetic neutrons of 14.1 MeV are generated, allowing for a consistent source of high energy neutrons. This neutron generator had a neutron flux of $\sim 1 \times 10^8$ neutrons per second, with runs of 10 minutes planned. This was not the case as the D-T generator had some issues with operation, and often cut off partway through a run. The high flux of this generator meant that this was not a significant issue, but it was not as consistent as the available D-D generator.

The same pattern as the EJ-276 D-D generator result seen in figure 5.20 can itself be seen in figure 5.23, although there is a key difference. The energy range drops off significantly in the D-D spectra, however in figure 5.23 the energy range is continuous until it reaches the top of

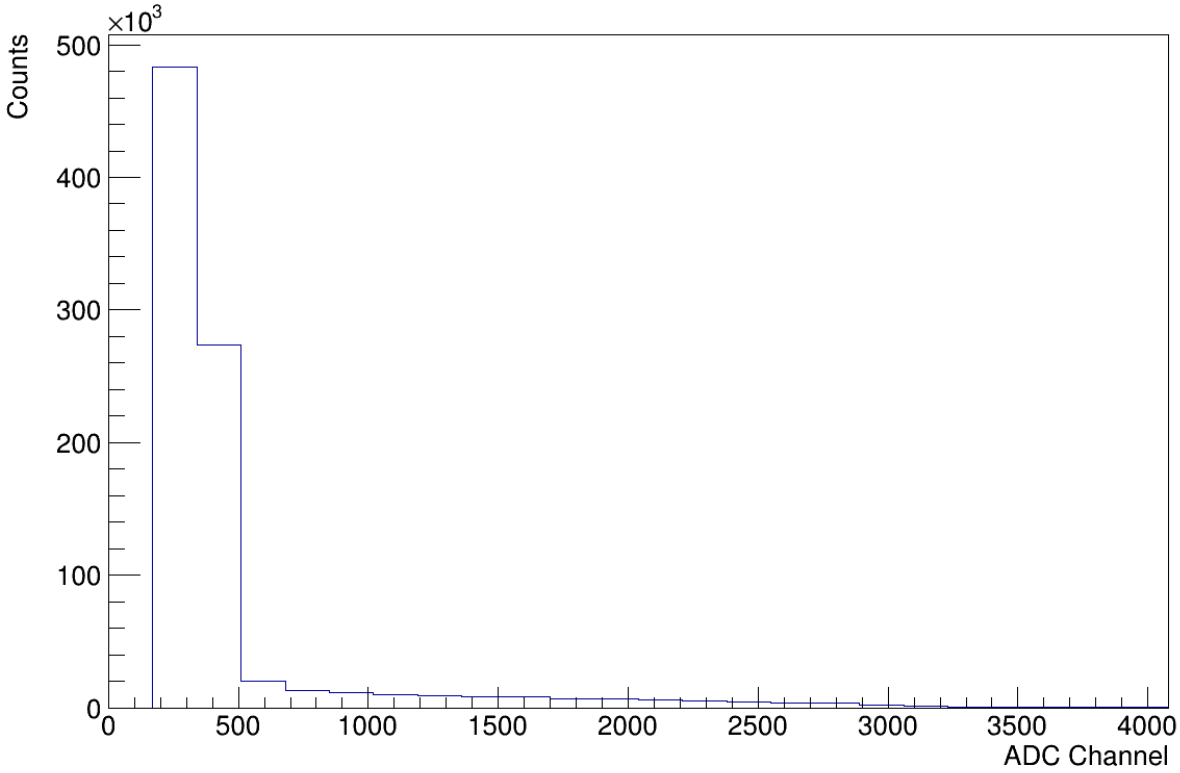

Figure 5.20: A D-D generator ADC channel spectrum recorded using the EJ-276 material. There is no clear discernible pattern seen from the energy spectra, but when the PSD factor is considered, as seen in figure 5.21, then two species begin to form.

the digitisers dynamic range, where it clips and forms the large peak seen at the far energy range. This means that the detectors gain was too high to see the full amount of the high energy neutrons emitted by the D-T generator. This is illustrated when the EJ-276 PSD vs energy spectra is analysed in figure 5.24 with the formation of two species seen again. However the higher neutron flux of the D-T generator in comparison to the D-D generator can be seen here, as the two species are heavily impacted by the other events present, and the curving effect initially seen in figure 5.21 is seen much more clearly in 5.24, with this believed to be caused by the digitiser struggling with the high count rate. This does not impact other neutron results significantly as results from the AmBe and ^{252}Cf sources are often shielded or moderated to an extent to avoid high count rates. This is also likely caused by incorrectly set timing gates, as a PSD factor approaching 1 suggests that the ratio of charges contained within both gates is negligible, as seen by the charge comparison ratio definition in equation 2.11.

The CLLBC thermal peak recorded in figure 5.22 is significantly larger in figure 5.25, suggesting a significant portion of the emitted neutrons are indeed thermalising in the environment. This peak is believed to be significant because of both the increased neutron flux and energy, causing more neutron reflections and there opportunities to be moderated to thermal energies. The clipping peak can also be clearly seen, meaning that the dynamic range

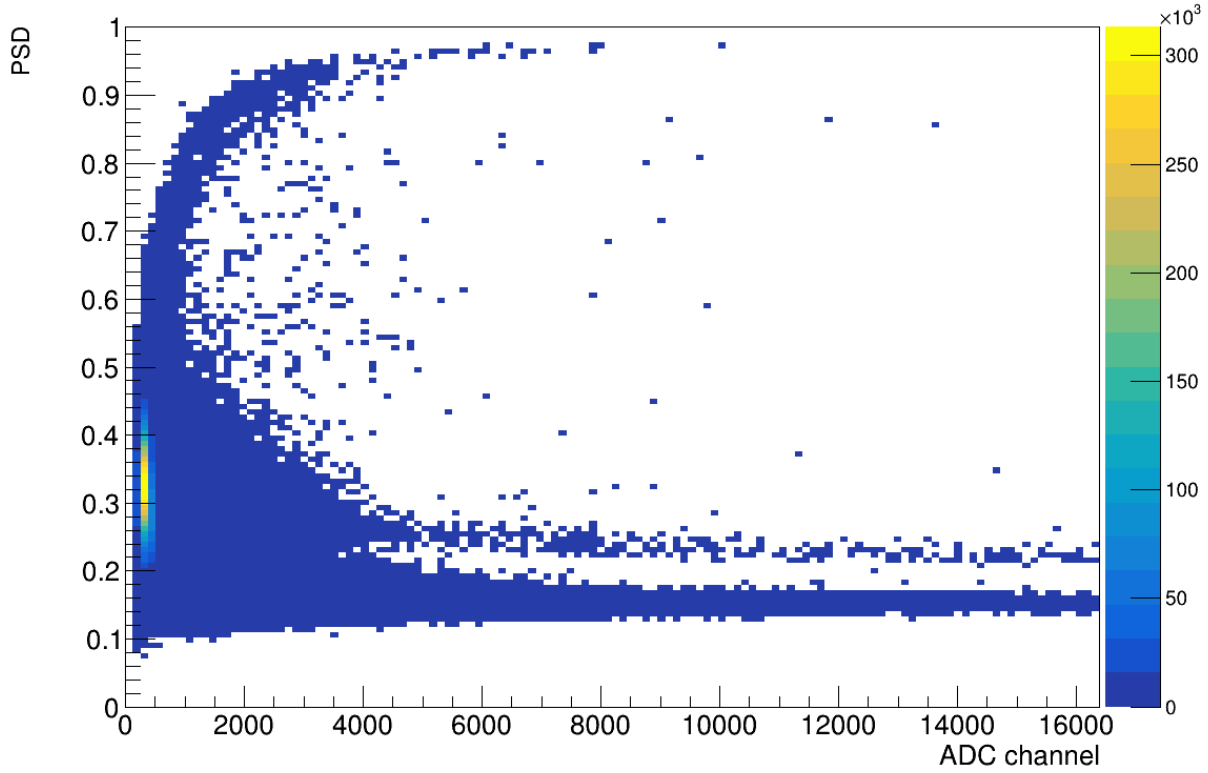

Figure 5.21: A D-D generator PSD factor vs ADC channel spectrum recorded using the EJ-276 material. The beginning formation of two species can be seen, indicating that an additional species is being generated by a process when the generator is in use. A curving effect at high PSD factors can be seen, with this believed to be caused by clipping in the digitiser.

needs to be carefully adjusted in order to not lose the 3.1 MeV thermal neutron peak, but to also keep the information from the 14.1 MeV D-T generator output.

When discussing these results, it is important to consider errors such as those seen on the efficiencies and FOMs. However, it is also important to consider the systematic errors present throughout the system, of which two sources would have an impact on this investigation. The first is that of electronic noise, such as those discussed in chapter 2.7, where random noise contributions will affect results to some extent, regardless of steps taken to mitigate them. The second contribution is that of the scintillation processes of both the organic and inorganic materials. Due to the methods of photon production for each material, there will be random fluctations in the photon production rate. Both of these noise sources should not contribute significantly to the results of the investigation, as the electronics were designed to function above low noise ranges, and there is significant photon production to reduce the impact of fluctations, but these sources should still both be considered.

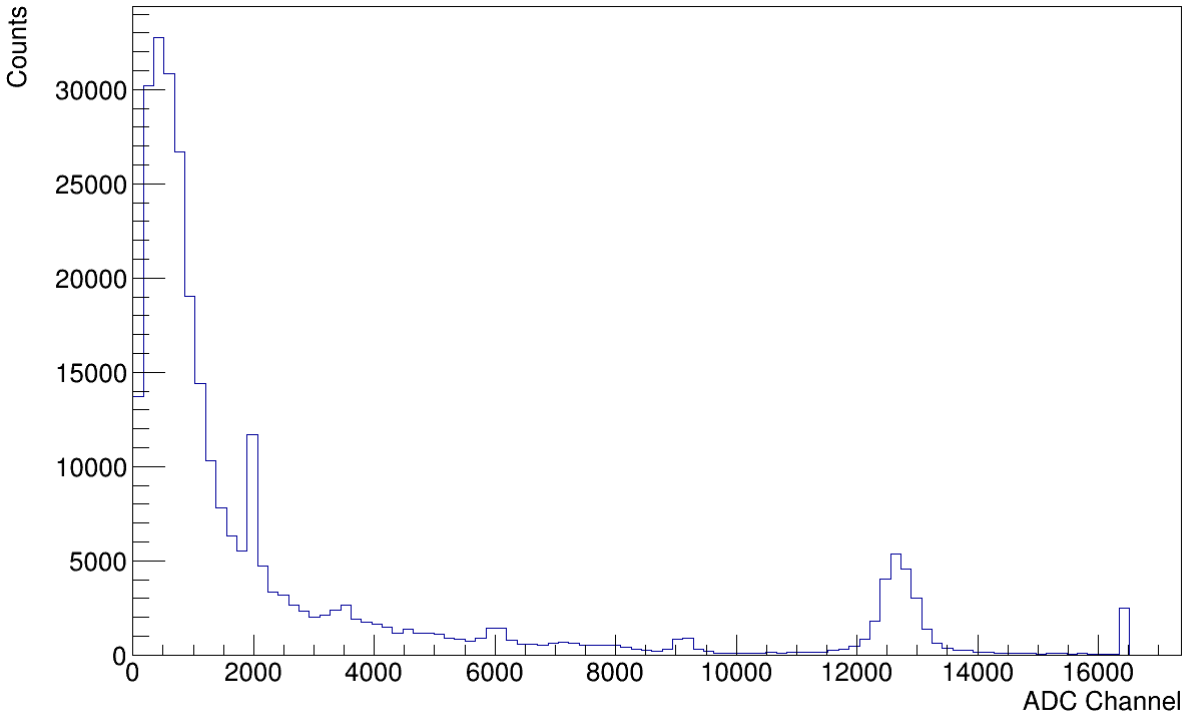

Figure 5.22: A D-D generator counts vs ADC channel spectrum recorded using the CLLBC material. The thermal neutron peak can be seen at ∼12500 ADC channels, meaning that there are likely to be environmental thermalisations causing neutron moderation. Some slight clipping can also be seen, meaning that even from a lower neutron flux and energy level the digitiser often struggled with the event rate.

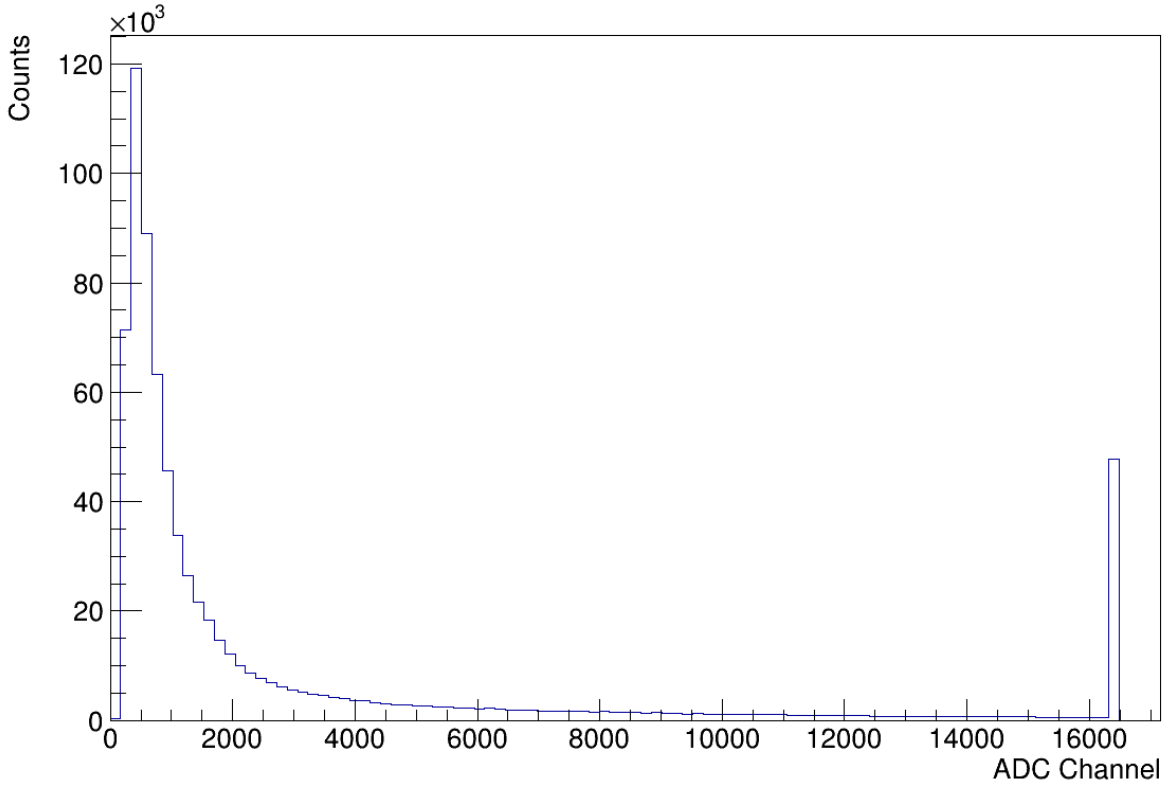

Figure 5.23: The ADC channel spectra for a D-T generator recorded using the EJ-276 material. The common pattern seen in other EJ-276 neutron spectra is also seen here, but the main exception is the amount of clipping seen at the top of the axis. The high event rate and neutron energy created by the D-T generator often overwhelmed the digitiser and would require reduced detector gain.

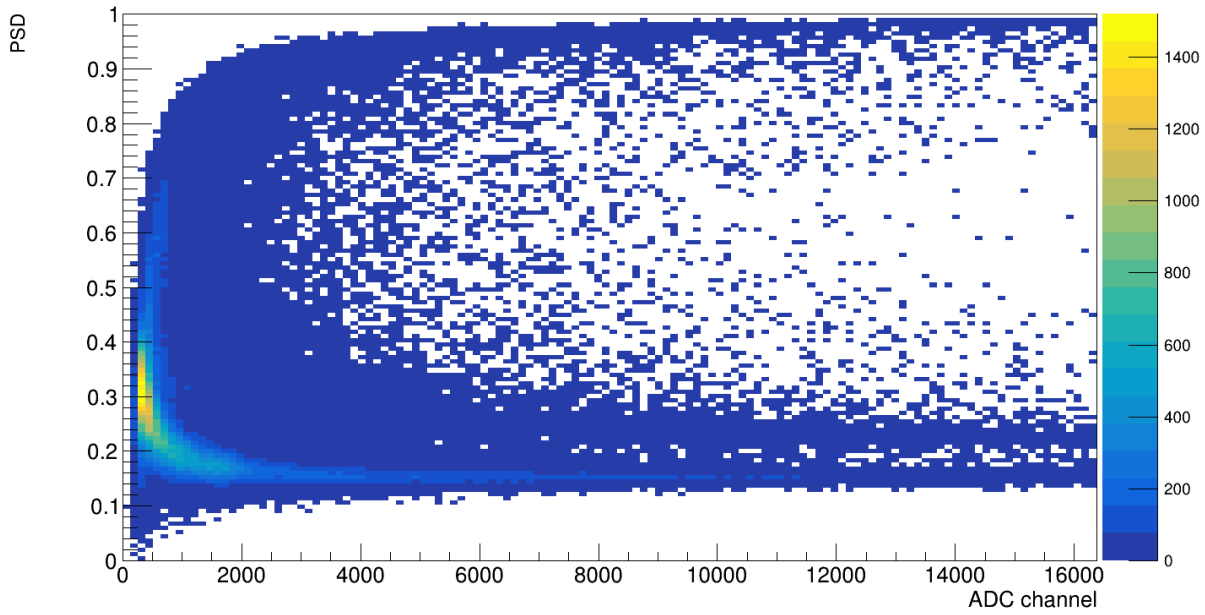

Figure 5.24: The PSD vs ADC channel spectrum for a D-T generator recorded using the EJ-276 material. The two species that formed in figure 5.21 can also be seen here, but the high event rate means that they can be more difficult to resolve. The curving effect can be also be seen here but to a greater extent than before.

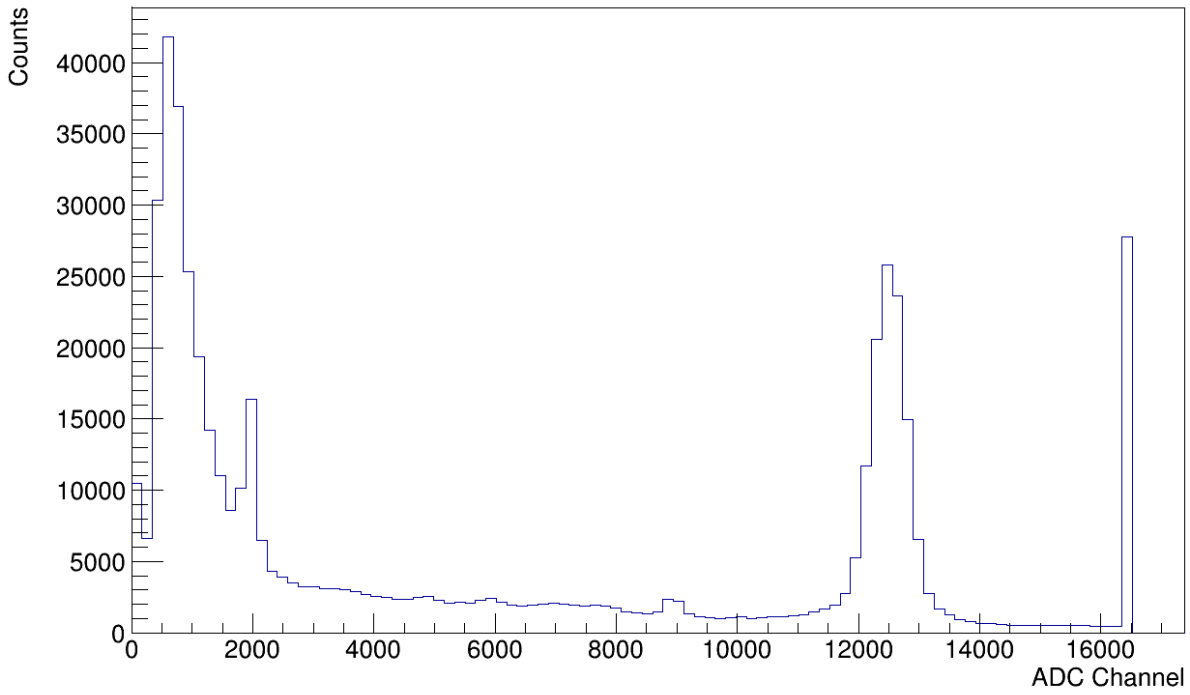

Figure 5.25: The ADC channel spectra for a D-T generator recorded using the CLLBC material. The thermal neutron peak seen in figure 5.22 is seen here at ∼12500 ADC channels, but at a much higher proportion. This is believed to be due to the higher neutron flux of the D-T generator, but also the higher energy, meaning that neutrons could undergo more reflections and be detected as thermal neutrons. The clipping of the digitiser can also be seen at a very high rate, this would especially difficult to resolve with the inorganic scintillation materials, as the dynamic range would need to be set carefully to capture the 3.1 MeV thermal neutron peak as well as the full data produced.

5.2 Digital and Analogue SiPM PSD investigation

When the bias and amplification module designed in chapter 4.2 was connected, there appeared to be some ripple on the SiPM output, this was believed to be caused by signal reflections from the op-amps on the board. There was also reduced capacitance on the bias input, meaning the signal was not as smooth as initially planned. This is because the TIA caused a 3 V offset to be applied to the SiPM, which already had a stated breakdown voltage of 32 V [119]. This meant that the discharge capacitor on the bias trace was carrying additional unplanned voltage, and the capacitor was rated for 16 V, when a standard 50 V version should have been used. This caused the capacitor to fail, and therefore the input bias signal would have less capacitance available to smooth out the bias.

Once this capacitor was removed and the connections repaired, the output of the board was first evaluated on an oscilloscope, before being connected to a CAEN DT5730 digitiser. When this board is paired with the CLLBC material, the resulting spectra with ^{137}Cs present can be seen in figure 5.26, with the digitiser's internal amplifier in use. As can be seen in the figure, there appears to be no discernible information present in the spectrum, with no clear Compton continuum or photopeak present. A ^{60}Co source was then trialled as it was hoped that higher energy photopeaks might be resolved easier, with the output seen in figure 5.27. It is unclear if the two ^{60}Co photopeaks are present, as the two central peaks could be the photopeaks, but the presence of a higher energy species indicates there could be high energy noise entering the board, with the noise source not currently identified.

Upon further investigation of the board, it seemed that when $\sim$1.89 V was passed to the op-amps on the bias and amplification board, any voltage above 2 V on the bias caused the op-amps to saturate and pass a large amount of noise to the system. It is currently unknown why this is the case, as the op-amps were chosen for their low noise, high speed properties, and should not begin operation until they have a 10 V differential passed from the +5 and -5 inputs.

Upon the determination that the bias and amplification board required further evaluation and future redesign, the SensL ARRAYJ-60035-64P-PCB board was repaired for use. Unfortunately upon testing, this SiPM array was only able to record low frequency signals, such as overhead lighting, and was therefore unable to record the high frequency signals emitted by each of the scintillation materials. The final option available was the use of a Broadcom AFBR-S4E001 evaluation kit that came with the purchase of the SiPM. The Broadcom AFBR-S4E001 was the same as the Broadcom AFBR-S4N44P164M, in that it had a breakdown voltage of $\sim$32 V, but could be overvoltaged (OV) significantly, with results present in [119] often recorded using an OV of 16 V. An OV of 10 V was applied to the AFBR-S4E001 board and there appeared to be a signal output recorded on the oscilloscope, at which point one of the power supplies being

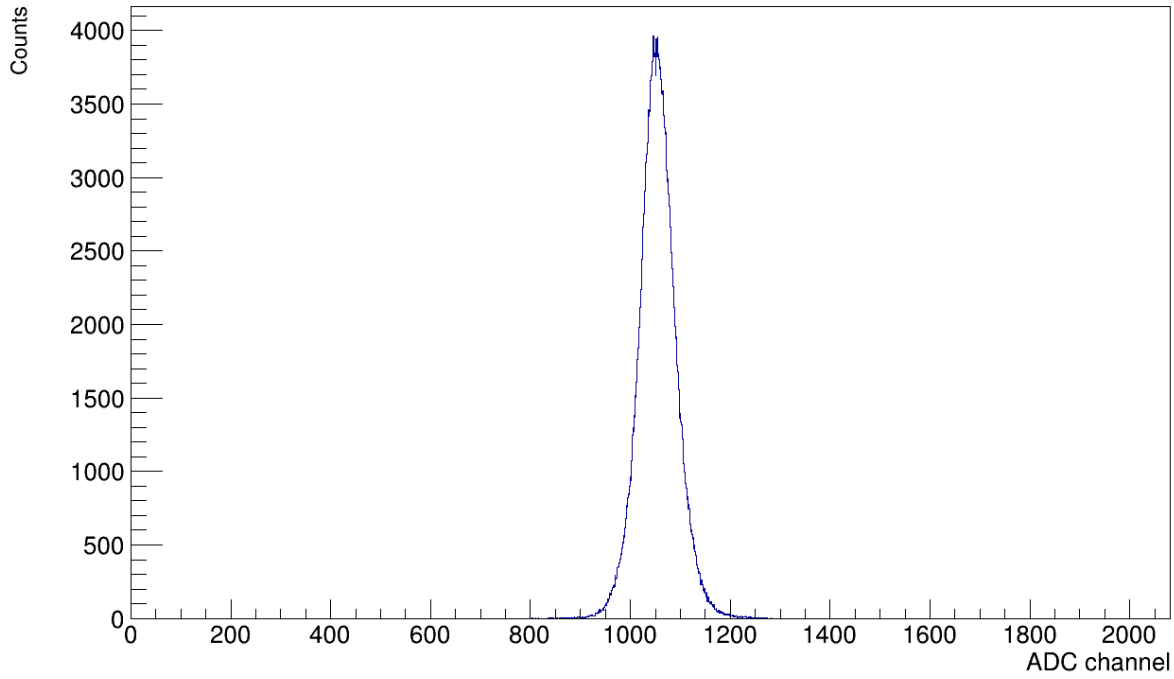

Figure 5.26: The bias and amplification board output using CLLBC and a ^{137}Cs source. It can be seen that there are no clear patterns visible, such as Compton energies or the 662 keV photopeak. These features are believed to be contained within the noise output from the board and cannot be resolved from this noise.

used appeared to surge, causing the SiPM to fail. The result of the SiPM can be seen in figure 5.28,with the board now unable to output a signal.

As a SiPM board was not available for digital or analogue PSD testing, it was decided to proceed with testing the analogue PSD boards with the detector emulator and PMT. A SiPM remains the ideal choice for a low power analogue PSD detector due to its low input voltage, but it was unable to be tested during this work.

It was decided to begin with the detector emulator seen in figure 4.35, as this could provide a continuous ^{60}Co spectrum to the boards. This would not be ideal for a full investigation as the boards were designed to separate neutrons and γ-ray species, and as such a ^{60}Co spectrum would not meet these requirements, but it was a good starting point as it would allow for a consistent input that the boards could be altered around. This first stage required the initialisation of each logic board with the +5, -5 and GND connections tested. The variable resistor on each board set the gain, and as such was set to a low value in order to not overwhelm the system, as if the diode was saturated it could become damaged. The resistance was evaluated using a multimeter and set using a twelve turn mechanism, chosen to increase the gain precision. When the charge comparison board was first powered, the charge did not appear to be reaching the two output pins, so the gain was increased, and when the μC was connected and a spectrum recorded, there

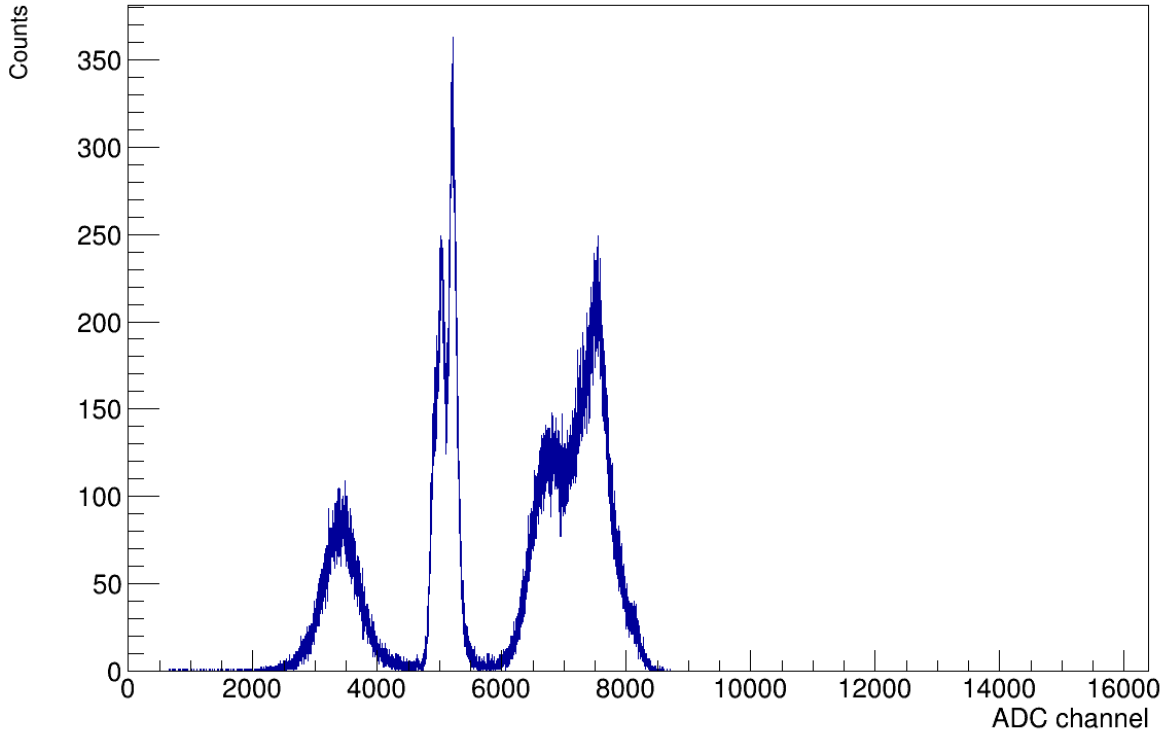

Figure 5.27: The bias and amplification board output using CLLBC and a ^{60}Co source. There appears to be more recognisable patterns present, but it is unclear what causes these peaks to arise and so it cannot be stated with confidence which species represent the ^{60}Co photopeaks.

appeared to be variation on the voltage outputs of each pin, although it was not clear if this was caused by noise.

The next stage of this investigation was to connect the PMT to the board and use the AmBe source. When the source was not present, the charge comparison board output pins varied the results produced when connected to the emulator and so the source was introduced. Upon introduction, the board recorded a ratio between each pin of either 1 V or 5 V, which means that both output pins are receiving the same voltage, or the μC is outputting the 5 V maximum respectively. This is because the μC in use was an ELEGOO Arduino Mega 2560 which is a 5 V μC board. The gain on the charge comparison was reduced using the variable resistor but the output was the same each time. It is unclear whether this is caused by the additional gain of a PMT, but even with the reduction of detector gain, the output did not change. This means that the charge comparison design did not operate as designed, and requires further investigation to understand why the output pins did not see different voltages.

The μC board being a 5 V board meant that it could not be connected to the ZC or ToT boards, as the TI TDC7200PWR was a 3.3 V component and could not be connected directly to the available μC due the 5 V logic level. This was acknowledged on the ZC and ToT boards, as seen

Figure 5.28: The damaged SiPM on the AFBR-S4E001 evaluation kit. The damage can be seen in the bottom right corner, there appeared to be no output from the board after this damage occurred.

in component U7 in figure 4.39, which is a 3.3 V LDO regulator to protect the TDC7200PWR from the +5 board input. However a 3.3 V logic level μC is required for accurate testing of these boards, and to ensure no damage to the TDC7200PWR, with the use of a 3.3 V μC planned for these boards.

5.3 Summary

Overall, the experimental output of this research has provided greater characterisation of each initially present detector material, as well as the novel EJ-299-50 scintillation material. A summary of the primary results can be found in table 5.1, including the figure-of-merit for each material, the energy resolution and intrinsic efficiency both at 662 keV and the neutron

efficiency. As described before, it was not possible to determine the EJ-299-50 neutron efficiency as it was not available when the time-of-flight measurement was performed.

.

Table 5.1: A summary table of the primary digital results of this investigation, with each material present alongside the best figure-of-merit determined for each, as well as the detector energy resolution and intrinsic gamma efficiency, both at 662 keV. The overall neutron efficiency for each is also included, apart from the EJ-299-50, which was not available when the time-of-flight measurement was performed.

Material	**Best FOM**	**Energy Res. @662 keV (%)**	**Intrinsic Eff. (%)**	**Neutron Eff. (%)**
CLLBC	3.69 ± 0.029	$5.6 \pm 7.6 \times 10^{-3}$	17.6 ± 8.8	0.22 ± 0.05
EJ-276	1.82 ± 0.096	20.0 ± 0.26	–	0.53 ± 0.12
CLYC	2.5 ± 0.1	9.3 ± 0.04	13.6 ± 6.8	0.31 ± 0.07
EJ-299-50	2.02 ± 0.025	22.2 ± 0.21	–	–

This enhanced understanding of each scintillation material means that future analogue designs can be tailored to specific design wishes. This is because from the FOM of each material, in combination with their timing characteristics, it can be understood that if accuracy is key to the initial design conditions but timing is not, then an inorganic scintillator is the ideal choice. If timing is crucial then an organic scintillator would be ideal, but this would come at the cost of reduced resolution between neutron and γ-ray species, although the EJ-299-50 material demonstrated a greater FOM than the EJ-276 material.

The next stage in the development of the generator results would be a physical simulation of the setup, using GEANT4, to fully understand the amount of neutron thermalisation occurring in the environment. This would allow for an understanding on the number of thermal neutrons produced, which would be a key step in approaching a thermal neutron efficiency calculation. This is a value that would further improve the understanding of the inorganic scintillation materials, and allow for an accurate comparison with other thermal neutron detection materials, such as a ^{3}He detector, often considered the most effective thermal neutron detection material, whose replacement was one of the inspirations of this work.

In terms of the analogue pulse shape discrimination work performed throughout this investigation, the results were not as planned and require future design considerations to match the simulation work produced in chapter 4. The small amount of SiPM results obviously present a challenge when a key part of the intended analogue solution involved low power design, and so the next stage of future investigation is to evaluate a working SiPM array for a PMT comparison. This remains key due to the reduced input voltage that automatically makes an SiPM the primary photon detection technology for an analogue PSD solution. To this end,

another key area to focus on would be extensive noise reduction considerations, as noise reduction was considered and accounted for during design, but it was clearly insufficient to account for the noise present in the system.

A final consideration would be the μC element, as integration into a full analogue PCB remains the final goal for this research, with each element from amplification to shaping to logic through to the μC processing all being self-contained. However the delays and unexpected noise interactions have meant that this planned combination was not possible, and each element needs further analysis to be ready for integration into a single detector prototype. Overall whilst the simulation outputs demonstrate the effectiveness of each analogue PSD method, combined with greater characterisation of each scintillation material demonstrating the long term feasibility of this process, it was not currently possible to provide a low power analogue PSD solution, albeit with the knowledge that future designs could remedy this.

Chapter 6

Conclusion and Future Work

As stated throughout this work, the detection of SNM is a necessary and important undertaking, due to an increasingly nuclear world, and as such neutron and γ-ray detection is an area of keen interest. This detection can be either active, where a sample is activated in order to determine the composition, or passive, where the sample is not directly affected but instead monitored for detectable radiative emissions. The primary motivation of this investigation involved creating a low power, compact, and robust analogue pulse shape discrimination detector that could act as a long term passive neutron detector. The decision to design primarily in an analogue scope rather than a digital one was inspired by the lower power requirement and faster processing speeds of an analogue system, creating the belief that it would be the stronger candidate for a passive detector.

To begin investigating this design, it was first necessary to understand the processes that allowed for a detector of this form to function, from both a physical and electrical perspective. This included the scintillation materials, both inorganic and organic, that would allow for the conversion of either a neutron or γ-ray species into a detectable photon, and the photon detection technologies that would convert this into a usable output. From this point it was important to define pulse shape discrimination and some of the different methods of application, before proceeding to understand the electronic methods, either analogue or digital, that enabled these methods to be recorded and processed, as well as an understanding of the physical processes that generate noise in these electrical systems.

Once these topics were understood, the experimental methods and design began in earnest. The use of both neutron and γ-ray sources allowed for a large variety of sources to be utilised, with their impacts being key to the development of this investigation. The inorganic scintillators CLLBC and CLYC, and the organic scintillators EJ-276 and EJ-299-50 were used at different points throughout this investigation. These scintillation materials were used in combination with these neutron and γ-ray sources, which were initially recorded through digital methods

using PMTs.

Once these initial digital results were recorded and processed, the following stage of investigation required the design of several planned analogue solutions, and three different designs were selected. Each of these designs were planned as independent modules to reduce manufacturing costs and enable easier fault detection, due to a smaller number of components. The zero crossing, time-over-threshold and charge comparison methods were selected due to historic use, ease of application and modern usage respectively. The first stage of this overall process involved planning the operations required to convert a signal from the intended SiPM output into a PSD variable. This varied according to each method, so a broad block diagram was created to plan out the necessary stages.

Once these broad plans were finalised, the following stage required the designs to be separated and replicated in the simulation software LTSpice, which allowed for each circuit to be modelled and tested. This stage caused several delays, with simulations not operating as expected, or simulated results not matching the physical outputs, with the reasons for this not currently well understood. However, these simulations were invaluable to the design of each module, and each of their outputs were tested with input waveforms of varying current magnitude and decay times, ensuring that each method varied linearly with the timing and magnitude of an input pulse. It was these outputs that demonstrated, at least in simulation, that each of these modules should be able to separate neutron and γ-ray species.

The final stage of design required the simulations to be recreated in printed circuit board design software, which presented its own challenges to the investigation. This stage caused many delays, from aspects such as manufacture delays, to issues caused by incorrect placement of decoupling capacitors or an incorrectly designed SiPM footprint. However, this stage also allowed for the physical construction of each PSD module that could then be presented as a possible fast, compact and low power alternative to a modern digital PSD method.

When considering the design aspect of this investigation, it is natural to review other avenues of investigation that were considered but not fully developed to the warranted extent. The primary area that should be revisited is the investigation of frequency domain based PSD methods, as whilst not considered in the scope of this investigation due to its greater suitability in high flux environments, could still potentially offer improvement and comparison to the results of this investigation. This could then allow for analogue PSD to be applied in a greater variety of situations, all of which would culminate in more effective neutron detection technologies.

The next problem worth investigating would be the addition of a light guide between the scintillation material output and the photon detection technology. This is not expected to

completely change the output of this investigation, but to design the best performing analogue solution, increases in efficiency should be sought wherever possible. Another another alteration would involve the evaluation of a portable battery supply, to allow this solution to run completely passively for an extended period.

A greater investigation into simulation would be beneficial to various aspects of this work, as whilst the electrical simulation was prioritised in an attempt to create the best analogue PSD prototype, this came at the cost of the physical simulation. This work would be useful to understand the amount of thermal neutrons created when fast neutrons were moderated, such as in the time-of-flight and neutron generator results. This would be done with the intention of determining a thermal neutron efficiency of each material, which would be especially useful for the inorganic scintillation materials. This would allow for a more direct comparison with ^{3}He detectors, often considered the best option for thermal neutron detection. This simulation work would also be useful for greater understanding of the plastic scintillators, with the determination of their intrinsic γ-ray efficiency.

A redesign of each module, with the aim of reducing general complexity would also be beneficial. This would be performed with the intention of either reducing component count, or trialling alternate components with a lower power consumption. All of this should culminate in a detector prototype that could perform effective PSD for longer time periods, further enhancing the passive interrogation ability of the analogue detector prototype. Other redesigns could also be considered, such as the compact analogue CFD suggested by other investigations. This would help to reduce the component count and complexity of the zero crossing module, as well as revisiting the planned comparator PSD method. This could be performed to determine whether this method was the most effective for inorganic scintillation materials. Overall these considerations could be investigated to potentially improve upon the analogue PSD methods presented throughout this work, with the aim of creating a more effective analogue PSD solution.

With the conclusion of the design aspect, the detector performance analysis could begin. The first element of this investigation involved the digital PMT results, with γ-ray results used to create a linear detector calibration for both CLLBC and CLYC. Energy resolutions of 5.1% and 8.8% were determined respectively, as well as intrinsic γ-ray efficiencies of 17.6% and 13.6%, alongside intrinsic neutron efficiencies of 0.22% and 0.31%. These digital methods provided a FOM of 3.69 and 2.51, meaning that both the CLLBC and CLYC materials exceeded the desired 1.27 FOM, determined by a 3σ separation divided by the FWHM of a Gaussian distribution of 2.355, and were able to effectively separate neutron and γ-ray species.

When this analysis was extended to the organic materials of EJ-276 and EJ-299-50, energy

resolutions of 20% and 25.7% were determined respectively, as well as EJ-276 having an intrinsic neutron efficiency of 0.53%. The FOM analysis of each material determined a 1.39 FOM for EJ-276 and 1.84 for EJ-299-50, meaning that both materials are capable of effectively separating neutron and γ-ray species. These digital results acted as the benchmark, with the intention to compare the analogue results to these.

To complete a full comparative study, the analogue SiPM bias and amplification module was connected to the CAEN DT5730 digitiser, with the same digital evaluation methods used. This led to the determination that high energy noise was being output by the bias and amplification board, with the board unable to resolve γ-ray photopeaks from noise contributions. As such a board used in the early stages of this work that had been damaged was repaired, but did not operate as previously, and only detected low frequency signals, making it unable to detect the high frequency signals output by the scintillation materials. This led to the use of an alternate SiPM evaluation board, but this was damaged by a power surge and rendered unusable as a result of this damage.

It was decided to operate without these SiPM results, and to attempt to directly investigate the logic modules themselves by combining the analogue PCB modules and a PMT, with the aim of providing a more stable photon detection technology. This was performed for the charge comparison logic module, with results not operating as expected and the μC outputting either equal voltages from both gates, or its maximum voltage logic level, meaning that even at low gain, the board was overwhelmed. It was decided to pause investigating the ZC and ToT boards currently, until the saturation issues seen by the CC module was better understood, as the TDC present on each of these boards were more sensitive to damage than the components on the CC board, which recorded the output voltages on each of its output pins.

Overall, the simulation outputs demonstrate the potential of each analogue PSD method, and their ability to separate between neutron and γ-ray species. Future investigations into the application of frequency based analogue PSD methods could open different avenues and allow for alternative solutions. These simulations, when combined with the characterisation of the scintillation materials, act as proof of concept that analogue methods still hold potential as a modern method of neutron and γ-ray separation, with the choice of the specific combination of PSD method and scintillation material dependent on the required design specifications. So, whilst the original aims of this investigation were not currently met, the work performed throughout suggests that future designs, with the issues of this work resolved, should operate effectively as low power analogue PSD solutions.

Appendix A

Printed Circuit Board Designs and Simulations

This chapter contains the full LTSpice and Altium PCB design outputs that were considered too large to include in one figure, and as such were split into several figures to improve clarity and readability, with these figures allowing for the full interaction process of each simulation and board to be understood.

Each of the three schematics present in figures A.1 A.2 and A.3 all demonstrate the predicted operation of each of these modules. The full schematic, simulation and breakdown of each is presented throughout chapter 4.

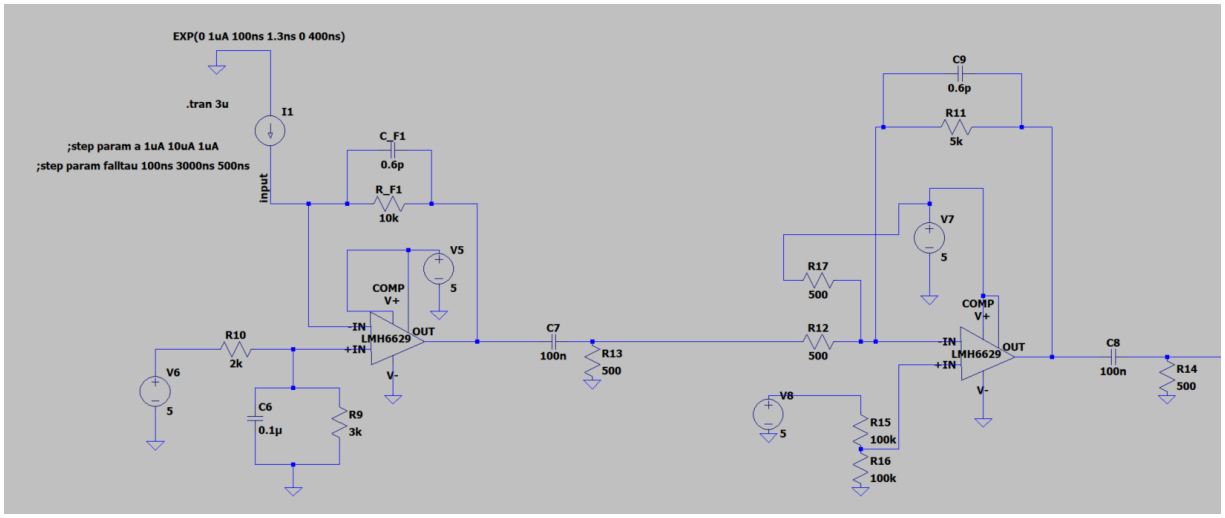

Figure A.1: The full LTSpice simulation of the bias and amplification module, with the SiPM input seen as the current source that proceeds to the TIA, before being fed into the voltage amplifier.

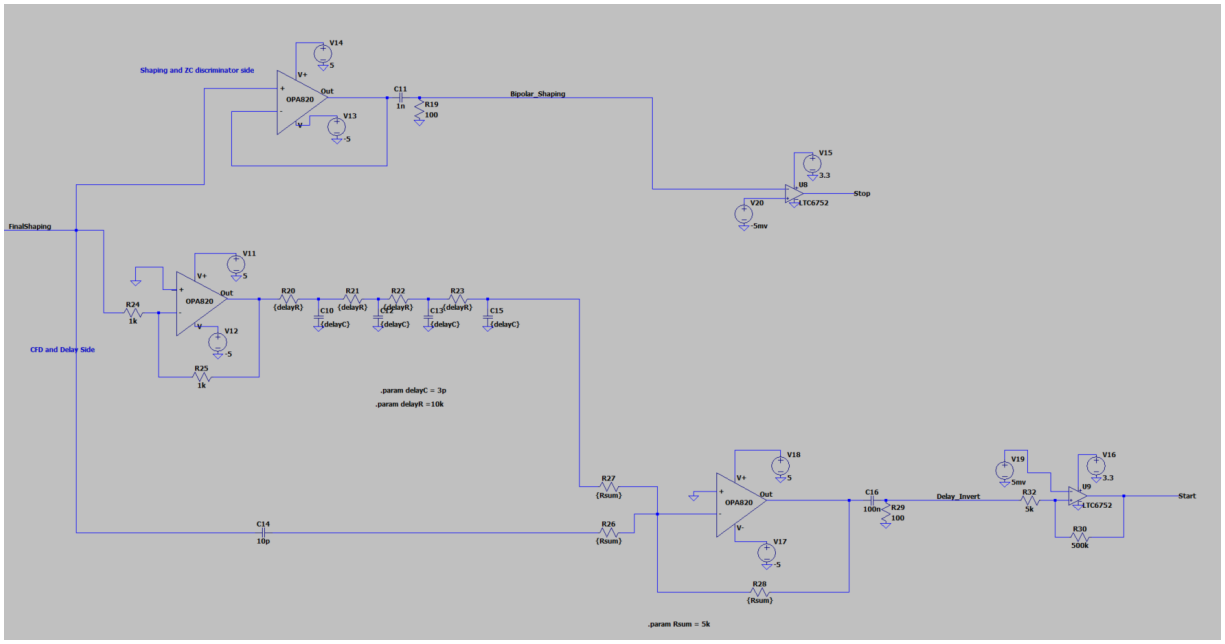

Figure A.2: The full LTSpice simulation of the zero crossing module, with the CFD start signal present with the summing amplifier, whilst the stop signal consisting of the delay module present.

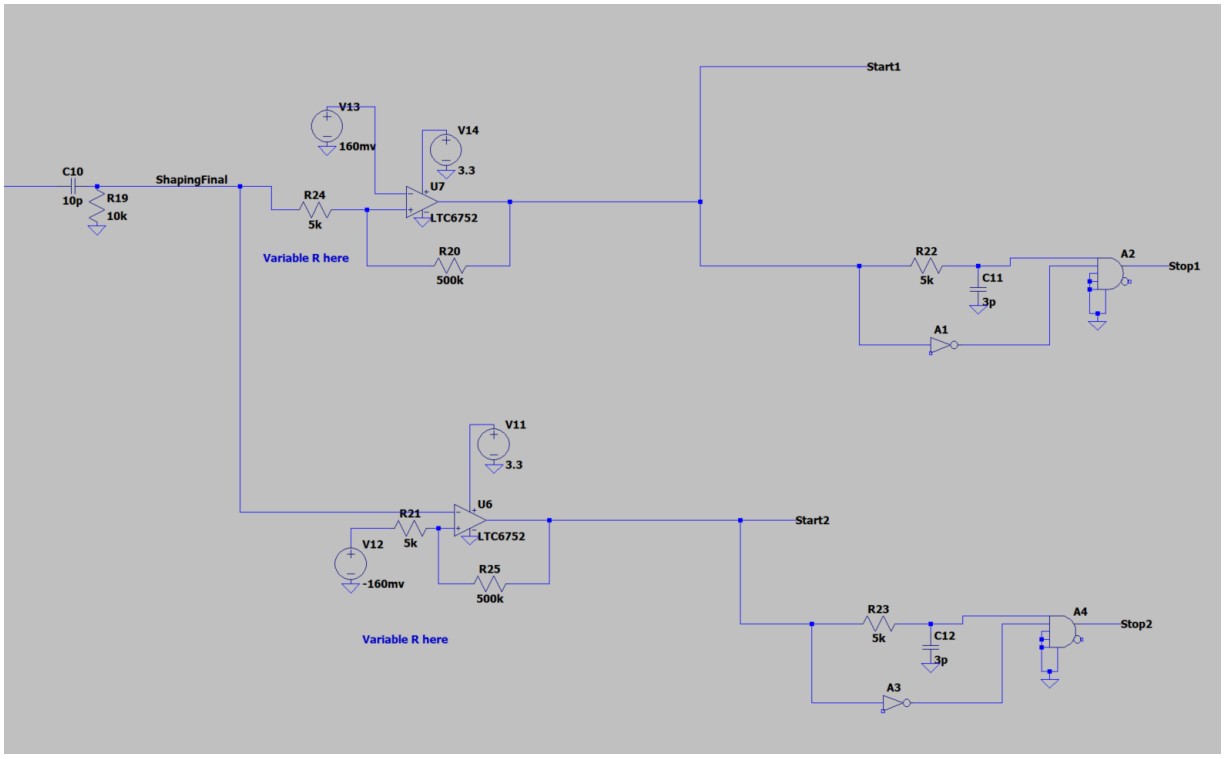

Figure A.3: The full LTSpice simulation of the time-over-threshold module, with the positive ToT module present at the top half of the schematic, seen with the positive comparator reference voltage, whilst the negative polarity section can be seen by the negative comparator reference voltage.

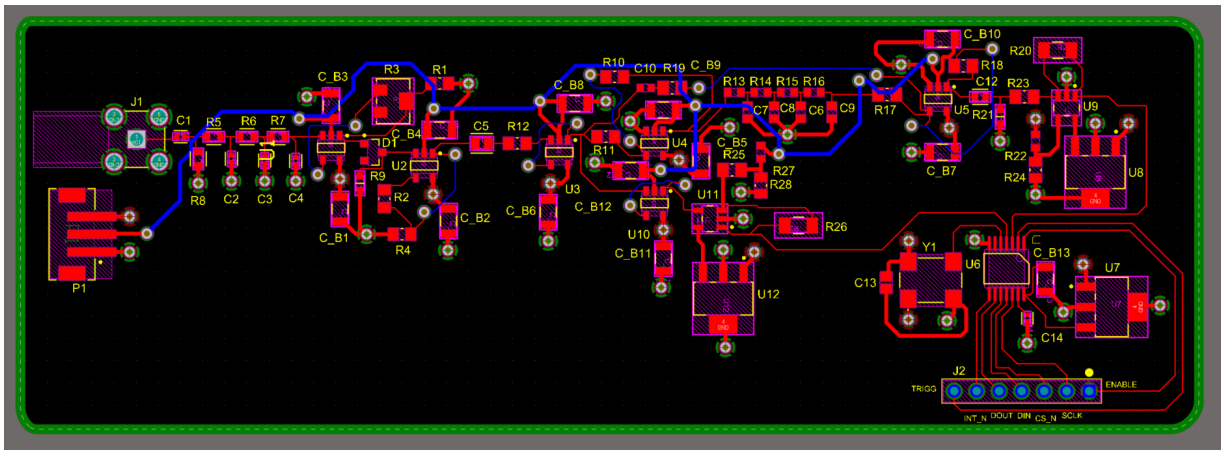

Figure A.4: The full zero crossing module that was created in PCB design software, each of the features described in figure A.1 are present, with the shaping and filtering present, before the ZC timings are created and fed into the TDC, with the required microcontroller pins present on the J2 component.

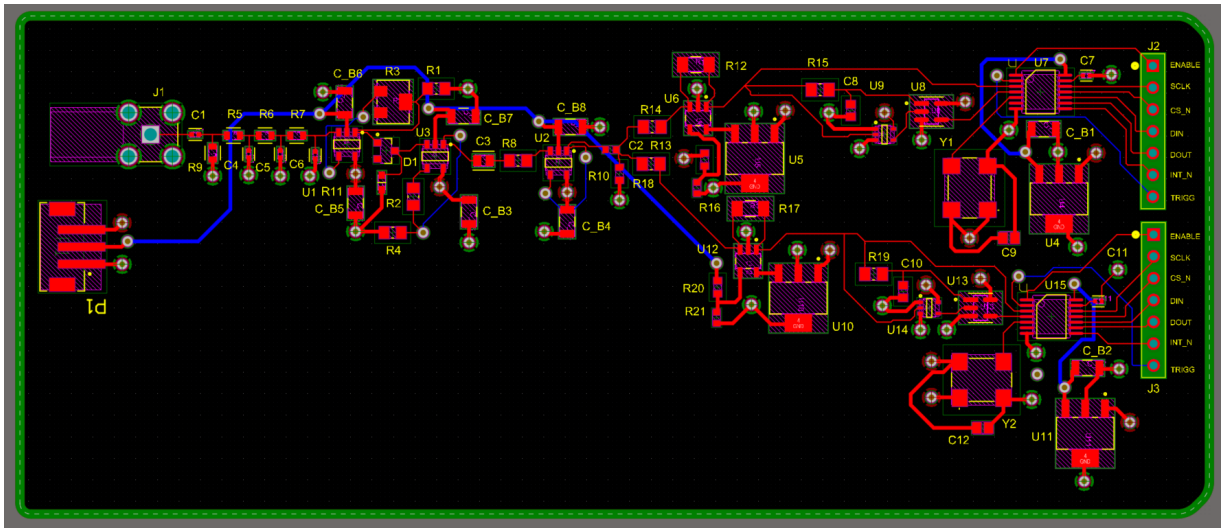

Figure A.5: The full time-over-threshold module that was created in PCB design software. The two TDCs are also seen, that should allow for the positive and negative ToT measurements.

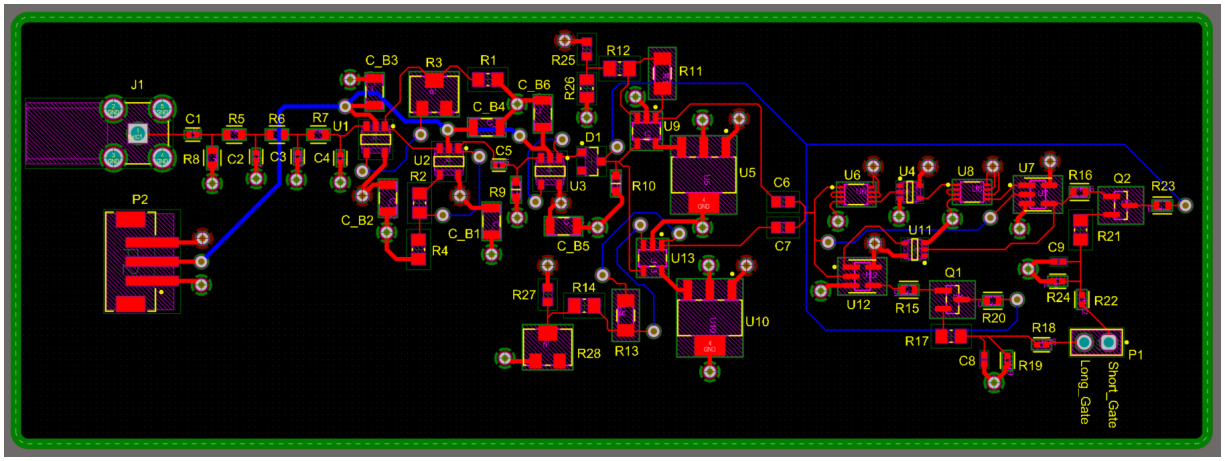

Figure A.6: The full charge comparison module that was created in PCB design software. The annotated gates can be seen in component P1, that should provide the voltage differences for each gate.

Bibliography

[1] D. E. Hogan and T. Kellison, "Nuclear terrorism," *The American Journal of the Medical Sciences*, vol. 323, no. 6, pp. 341–349, 2002, ISSN: 0002-9629. DOI: https://doi.org/10.1097/00000441-200206000-00006.

[2] S. F. MORENO, "Nuclear regulatory measures to prevent illicit use of nuclear materials and radioactive sources," *C&SPapersSeries*, p. 75, 2002.

[3] Y. Rojavin *et al.*, "Civilian nuclear incidents: An overview of historical, medical, and scientific aspects," *Journal of Emergencies, Trauma, and Shock*, vol. 4, no. 2, pp. 260–272, 2011.

[4] H. De Cauwer, D. G. Barten, D. Tin, L. J. Mortelmans, G. R. Ciottone, and F. Somville, "50 years of terrorism against the nuclear industry: A review of 91 incidents in the global terrorism database," *Prehospital and disaster medicine*, vol. 38, no. 2, pp. 199–206, 2023.

[5] D. T. Ingersoll, "Deliberately small reactors and the second nuclear era," *Progress in nuclear energy*, vol. 51, no. 4-5, pp. 589–603, 2009.

[6] N. Muellner, N. Arnold, K. Gufler, W. Kromp, W. Renneberg, and W. Liebert, "Nuclear energy-the solution to climate change?" *Energy Policy*, vol. 155, p. 112 363, 2021.

[7] D. S. Siqueira, J. de Almeida Meystre, M. Q. Hilário, D. H. D. Rocha, G. J. Menon, and R. J. da Silva, "Current perspectives on nuclear energy as a global climate change mitigation option," *Mitigation and Adaptation Strategies for Global Change*, vol. 24, pp. 749–777, 2019.

[8] P. Egidi, "Introduction to naturally occurring radioactive material," Oak Ridge National Lab., Grand Junction, CO (United States), Tech. Rep., 1997.

[9] A. J. Sigurdson and E. Ron, "Cosmic radiation exposure and cancer risk among flight crew," *Cancer investigation*, vol. 22, no. 5, pp. 743–761, 2004.

[10] Z. Koreshi and H. Khan, "Detector response from thermal neutron activation of concealed explosives," *IIUM Engineering Journal*, vol. 18, pp. 177–188, Dec. 2017. DOI: 10.31436/iiumej.v18i2.758.

[11] I. Jovanovic and A. S. Erickson, *Active Interrogation in Nuclear Security: Science, Technology and Systems*. Springer, 2018.

[12] K. Guzmán García, H. Vega-Carrillo, E. Gallego, J. González, A. Lorente, and S. Ibañez-Fernandez, "10 b+zns(ag) as an alternative to 3 he-based detectors for radiation portal monitors," *EPJ Web of Conferences*, vol. 153, p. 07 008, Jan. 2017. DOI: 10.1051/epjconf/201715307008.

[13] C. W. van Eijk, "New inorganic scintillators—aspects of energy resolution," *Nuclear Instruments and Methods in Physics Research Section A: Accelerators, Spectrometers, Detectors and Associated Equipment*, vol. 471, no. 1, pp. 244–248, 2001, Imaging 2000, ISSN: 0168-9002. DOI: https://doi.org/10.1016/S0168-9002(01)00983-4.

[14] A. Hristova, E. Vapirev, L. Tsankov, and V. Jordanov, "Compton edge energy calibration of organic detectors," *International journal of radiation applications and instrumentation. Part A. Applied radiation and isotopes*, vol. 41, no. 9, pp. 887–889, 1990.

[15] C. Sosa, S. Thompson, D. Chichester, S. Clarke, A. Di Fulvio, and S. Pozzi, "Energy resolution experiments of conical organic scintillators and a comparison with geant4 simulations," *Nuclear Instruments and Methods in Physics Research Section A: Accelerators, Spectrometers, Detectors and Associated Equipment*, vol. 898, pp. 77–84, 2018, ISSN: 0168-9002. DOI: https://doi.org/10.1016/j.nima.2018.04.058.

[16] e. a. Sacchetti, "3he-free neutron detectors and their applications," 2015. DOI: https://doi.org/10.1140/epjp/i2015-15053-1.

[17] J. Dumazert and C. Frangville, "Plastic scintillators," in M. Hamel, Ed. Springer Cham, 2021.

[18] J. Ahn, F. Guarnieri, and K. Furuta, *Resilience: A new paradigm of nuclear safety: From accident mitigation to resilient society facing extreme situations*. Springer Nature, 2017, pp. 251–252.

[19] M. J. Balmer, K. A. Gamage, and G. C. Taylor, "Comparative analysis of pulse shape discrimination methods in a 6li loaded plastic scintillator," *Nuclear Instruments and Methods in Physics Research Section A: Accelerators, Spectrometers, Detectors and Associated Equipment*, vol. 788, pp. 146–153, 2015.

[20] E. Arnqvist, *Cllbc scintillation detector gamma–ray and neutron response characterization: For tagged neutron time-of–flight measurements*, 2024.

[21] J. Glodo *et al.*, "New developments in scintillators for security applications," *Physics Procedia*, vol. 90, pp. 285–290, 2017, Conference on the Application of Accelerators in Research and Industry, CAARI 2016, 30 October – 4 November 2016, Ft. Worth, TX, USA, ISSN: 1875-3892. DOI: https://doi.org/10.1016/j.phpro.2017.09.012.

[22] S. Mianowski *et al.*, "Neutron hardness of ej-276 scintillation material," *Journal of Instrumentation*, vol. 15, no. 10, P10012, Oct. 2020. DOI: 10.1088/1748-0221/15/10/P10012. [Online]. Available: https://dx.doi.org/10.1088/1748-0221/15/10/P10012.

[23] J. Glodo *et al.*, "Selected properties of cs _{2} liycl _{6}, cs _{2} lilacl _{6}, and cs _{2} lilabr _{6} scintillators," *IEEE Transactions on Nuclear Science*, vol. 58, no. 1, pp. 333–338, 2011.

[24] C. Roca *et al.*, *Performance of large-scale 6li-doped pulse-shape discriminating plastic scintillators*, 2024. arXiv: 2405.19573 [physics.ins-det]. [Online]. Available: https://arxiv.org/abs/2405.19573.

[25] N. Zaitseva *et al.*, "Performance stability of plastics for neutron-gamma pulse shape discrimination," *Nuclear Instruments and Methods in Physics Research Section A: Accelerators, Spectrometers, Detectors and Associated Equipment*, vol. 1068, p. 169 731, 2024, ISSN: 0168-9002. DOI: https://doi.org/10.1016/j.nima.2024.169731.

[26] P. P. Guss, T. G. Stampahar, S. Mukhopadhyay, A. Barzilov, and A. Guckes, "Scintillation properties of a cs2lila (br6) 90%(cl6) 10%: Ce3+ (cllbc) crystal," in *Radiation Detectors: Systems and Applications XV*, SPIE, vol. 9215, 2014, pp. 27–41.

[27] S. Mianowski *et al.*, "Neutron hardness of ej-276 scintillation material," *Journal of Instrumentation*, vol. 15, no. 10, P10012, 2020.

[28] A. Giaz *et al.*, "Fast neutron measurements with 7li and 6li enriched clyc scintillators," *Nuclear Instruments and Methods in Physics Research Section A: Accelerators, Spectrometers, Detectors and Associated Equipment*, vol. 825, pp. 51–61, 2016.

[29] F. Brooks, "Development of organic scintillators," *Nuclear Instruments and Methods*, vol. 162, no. 1, pp. 477–505, 1979, ISSN: 0029-554X. DOI: https://doi.org/10.1016/0029-554X(79)90729-8.

[30] R. Batchelor, W. Gilboy, J. Parker, and J. Towle, "The response of organic scintillators to fast neutrons," *Nuclear Instruments and Methods*, vol. 13, pp. 70–82, 1961, ISSN: 0029-554X. DOI: https://doi.org/10.1016/0029-554X(61)90171-9.

[31] M. Moszyński, C. Gresset, J. Vacher, and R. Odru, "Properties of csf, a fast inorganic scintillator in energy and time spectroscopy," *Nuclear Instruments and Methods*, vol. 179, no. 2, pp. 271–276, 1981, ISSN: 0029-554X. DOI: https://doi.org/10.1016/0029-554X(81)90049-5.

[32] R. Heath, R. Hofstadter, and E. Hughes, "Inorganic scintillators: A review of techniques and applications," *Nuclear Instruments and Methods*, vol. 162, no. 1, pp. 431–476, 1979, ISSN: 0029-554X. DOI: https://doi.org/10.1016/0029-554X(79)90728-6.

[33] F. Brooks, R. Pringle, and B. Funt, "Pulse shape discrimination in a plastic scintillator," *IRE Transactions on Nuclear Science*, vol. NS-7, no. 2-3, pp. 35–38, 1960, Cited by: 83. DOI: 10.1109/TNS2.1960.4315733.

[34] N. Zaitseva *et al.*, "Recent developments in plastic scintillators with pulse shape discrimination," *Nuclear Instruments and Methods in Physics Research Section A: Accelerators, Spectrometers, Detectors and Associated Equipment*, vol. 889, pp. 97–104, 2018, ISSN: 0168-9002. DOI: https://doi.org/10.1016/j.nima.2018.01.093.

[35] N. Zaitseva *et al.*, "Plastic scintillators with efficient neutron/gamma pulse shape discrimination," *Nuclear Instruments and Methods in Physics Research Section A: Accelerators, Spectrometers, Detectors and Associated Equipment*, vol. 668, pp. 88–93, 2012, ISSN: 0168-9002. DOI: https://doi.org/10.1016/j.nima.2011.11.071.

[36] M. J. Weber and R. R. Monchamp, "Luminescence of bi4 ge3 o12: Spectral and decay properties," *Journal of Applied Physics*, vol. 44, no. 12, pp. 5495–5499, 1973.

[37] R. Hofstadter, "The detection of gamma-rays with thallium-activated sodium iodide crystals," *Physical Review*, vol. 75, no. 5, p. 796, 1949.

[38] A. Gektin and M. Korzhik, "Inorganic scintillators for detector systems," *Berlin: Springer*, pp. 20–77, 2017.

[39] G. McBeth, J. Lutkin, and R. Winyard, "A simple zero crossing pulse shape discrimination system," *Nuclear Instruments and Methods*, vol. 93, no. 1, pp. 99–102, 1971.

[40] M. L. Roush, M. Wilson, and W. F. Hornyak, "Pulse shape discrimination," *Nuclear Instruments and Methods*, vol. 31, no. 1, pp. 112–124, 1964.

[41] R. Winyard, J. Lutkin, and G. McBeth, "Pulse shape discrimination in inorganic and organic scintillators. i," *Nuclear Instruments and Methods*, vol. 95, no. 1, pp. 141–153, 1971.

[42] C. L. Morris, J. E. Bolger, G. W. Hoffmann, C. F. Moore, L. E. Smith, and H. A. Thiessen, "A digital technique for neutron-gamma pulse shape discrimination," *Nuclear Instruments and Methods*, vol. 137, no. 2, pp. 397–398, 1976.

[43] R. Aryaeinejad, J. K. Hartwell, and D. F. Spencer, "Comparison between digital and analog pulse shape discrimination techniques for neutron and gamma ray separation," in *IEEE Nuclear Science Symposium Conference Record, 2005*, IEEE, vol. 1, 2005, pp. 500–504.

[44] C. Sosa, M. Flaska, and S. A. Pozzi, "Comparison of analog and digital pulse-shape-discrimination systems," *Nuclear Instruments and Methods in Physics Research Section A: Accelerators, Spectrometers, Detectors and Associated Equipment*, vol. 826, pp. 72–79, 2016.

[45] I. Kuon and J. Rose, "Measuring the gap between fpgas and asics," in *Proceedings of the 2006 ACM/SIGDA 14th international symposium on Field programmable gate arrays*, 2006, pp. 21–30.

[46] B. Mindur, W. Dąbrowski, T. Fiutowski, P. Wiacek, and A. Zielińska, "An fpga based gemroc readout system," in *2012 18th IEEE-NPSS Real Time Conference*, IEEE, 2012, pp. 1–5.

[47] F. Simon, "Silicon photomultipliers in particle and nuclear physics," *Nuclear Instruments and Methods in Physics Research Section A: Accelerators, Spectrometers, Detectors and Associated Equipment*, vol. 926, pp. 85–100, 2019, Silicon Photomultipliers: Technology, Characterisation and Applications, ISSN: 0168-9002. DOI: https://doi.org/10.1016/j.nima.2018.11.042.

[48] G. F. Knoll, "Radiation detection and measurement," vol. 4th Edition, Jan. 1979.

[49] I. Obodovskiy, "Chapter 5 - passing of charged particles through matter," in *Radiation*, I. Obodovskiy, Ed., Elsevier, 2019, pp. 103–136, ISBN: 978-0-444-63979-0. DOI: https://doi.org/10.1016/B978-0-444-63979-0.00005-7.

[50] X. Zhang *et al.*, "Parameterization of multiple bragg curves for scanning proton beams using simultaneous fitting of multiple curves," *Physics in Medicine and Biology*, vol. 56, p. 7725, 2011. DOI: 10.1088/0031-9155/56/24/003.

[51] S. Gagnebin, "Experimental determination of absorbed dose to water in a scanned proton beam using a water calorimeter and an ionization chamber," Ph.D. dissertation, May 2010.

[52] H. Sakaguchi and J. Zenihiro, "Proton elastic scattering from stable and unstable nuclei — extraction of nuclear densities," *Progress in Particle and Nuclear Physics*, vol. 97, pp. 1–52, 2017, ISSN: 0146-6410. DOI: https://doi.org/10.1016/j.ppnp.2017.06.001.

[53] J. Mott and J. Daniel, "Interactions of electromagnetic radiation and subatomic particles with matter – part 2," *Clinical Oncology*, vol. 33, Mar. 2021. DOI: 10.1016/j.clon.2021.02.005.

[54] R. Van Dyck, F. Moore, D. Farnham, and P. Schwinberg, "New measurement of the proton-electron mass ratio," *International Journal of Mass Spectrometry and Ion Processes*, vol. 66, no. 3, pp. 327–337, 1985, ISSN: 0168-1176. DOI: https://doi.org/10.1016/0168-1176(85)80006-9.

[55] Y. Dahman, "Chapter 2 - generic methodologies for characterization**by yaser dahman, caroline halim, oswaldo matos, and louisa chan.," in *Nanotechnology and Functional Materials for Engineers*, ser. Micro and Nano Technologies, Y. Dahman, Ed., Elsevier, 2017, pp. 19–45, ISBN: 978-0-323-51256-5. DOI: https://doi.org/10.1016/B978-0-323-51256-5.00002-2.

[56] D. E. Groom and S. Klein, "Passage of particles through matter," *The European Physical Journal C-Particles and Fields*, vol. 15, no. 1-4, pp. 163–173, 2000.

[57] N. J. Carron, *An introduction to the passage of energetic particles through matter*. Taylor & Francis, 2006.

[58] M. Bolukbasi, S. Middleburgh, M. Dahlfors, and W. Lee, "Performance and economic assessment of enriched gadolinia burnable absorbers," *Progress in Nuclear Energy*, vol. 137, p. 103 752, 2021, ISSN: 0149-1970. DOI: https://doi.org/10.1016/j.pnucene.2021.103752.

[59] Y. Ding, Z. Zhang, J. Liu, Z. Wang, P. Zhou, and Y. Zhao, "A new gadolinium-loaded liquid scintillator for reactor neutrino detection," *Nuclear Instruments and Methods in Physics Research Section A: Accelerators, Spectrometers, Detectors and Associated Equipment*, vol. 584, no. 1, pp. 238–243, 2008, ISSN: 0168-9002. DOI: https://doi.org/10.1016/j.nima.2007.09.044.

[60] A. Z. Mesquita, I. C. Reis, V. F. de Almeida, and R. R. Rodrigues, "Boron-10 effect on the reactivity of the ipr-r1 triga research reactor," *Annals of Nuclear Energy*, vol. 132, pp. 64–69, 2019, ISSN: 0306-4549. DOI: https://doi.org/10.1016/j.anucene.2019.04.023.

[61] J. Bevins, "Characterization of a boron carbide heterojunction neutron detector," p. 193, Mar. 2011.

[62] B. C. Reed and D. Mihailidis, *the Physics of the Manhattan Project*. Springer, 2011.

[63] V. Venugopal and P. Bhagdikar, "De broglie wavelength and frequency of scattered electrons in the compton effect," *Physics Education*, vol. 29, p. 35, Mar. 2013.

[64] R. D. Evans and R. Evans, *The atomic nucleus*. McGraw-Hill New York, 1955, vol. 582.

[65] D.-M. Xia *et al.*, "Temperature dependence of the light yield of the lab-based and mesitylene-based liquid scintillators," *Chinese Physics C*, vol. 38, no. 11, p. 116 001, 2014.

[66] A. Kastalsky, S. Luryi, and B. Spivak, "Semiconductor high-energy radiation scintillation detector," *Nuclear Instruments and Methods in Physics Research Section A: Accelerators, Spectrometers, Detectors and Associated Equipment*, vol. 565, no. 2, pp. 650–656, 2006.

[67] P. A. Rodnyi, "Core–valence luminescence in scintillators," *Radiation Measurements*, vol. 38, no. 4, pp. 343–352, 2004, Proceedings of the 5th European Conference on Luminescent Detectors and Transformers of Ionizing Radiation (LUMDETR 2003), ISSN: 1350-4487. DOI: https://doi.org/10.1016/j.radmeas.2003.11.003.

[68] X. Wen and A. Enqvist, "Measuring the scintillation decay time for different energy deposited by gamma-rays and neutrons in a cs2liycl6:ce3+ detector," *Nuclear Instruments and Methods in Physics Research Section A: Accelerators, Spectrometers, Detectors and Associated Equipment*, vol. 853, pp. 9–15, 2017, ISSN: 0168-9002. DOI: https://doi.org/10.1016/j.nima.2017.02.019.

[69] R. Hawrami *et al.*, "Crystals for nuclear security applications," *IEEE Transactions on Nuclear Science*, vol. 63, pp. 509–512, Apr. 2016. DOI: 10.1109/TNS.2016.2522188.

[70] M. Smith *et al.*, "Fast neutron measurements using cs2liycl6:ce (clyc) scintillator," *Nuclear Instruments and Methods in Physics Research Section A: Accelerators, Spectrometers, Detectors and Associated Equipment*, vol. 784, pp. 162–167, 2015, Symposium on Radiation Measurements and Applications 2014 (SORMA XV), ISSN: 0168-9002. DOI: https://doi.org/10.1016/j.nima.2014.09.021.

[71] G. Bizarri, "Scintillation mechanisms of inorganic materials: From crystal characteristics to scintillation properties," *Journal of Crystal Growth*, vol. 312, no. 8, pp. 1213–1215, 2010, The 17th American Conference on Crystal Growth and Epitaxy The 14th US Biennial Workshop on Organometallic Vapor Phase Epitaxy/The 6th International Workshop on Modeling in Crystal Growth, ISSN: 0022-0248. DOI: https://doi.org/10.1016/j.jcrysgro.2009.12.063.

[72] J. B. Birks, *The theory and practice of scintillation counting: International series of monographs in electronics and instrumentation*. Elsevier, 2013, vol. 27.

[73] B. Valeur and M. N. Berberan-Santos, "A brief history of fluorescence and phosphorescence before the emergence of quantum theory," *Journal of Chemical Education*, vol. 88, no. 6, pp. 731–738, 2011.

[74] S. N. Ahmed, *Physics and engineering of radiation detection*. Academic Press, 2007.

[75] P. Landsberg, "Semiconductor physics | recombination processes," in *Encyclopedia of Modern Optics*, R. D. Guenther, Ed., Oxford: Elsevier, 2005, pp. 21–29, ISBN: 978-0-12-369395-2. DOI: https://doi.org/10.1016/B0-12-369395-0/00618-7.

[76] T. Shima and Y. Nagai, "Development of a photomultiplier tube with high quantum efficiency," *Nuclear Instruments and Methods in Physics Research Section A: Accelerators, Spectrometers, Detectors and Associated Equipment*, vol. 431, no. 1, pp. 185–193, 1999, ISSN: 0168-9002. DOI: https://doi.org/10.1016/S0168-9002(99)00259-4.

[77] P. Buzhan *et al.*, "The advanced study of silicon photomultiplier," in *Advanced technology and particle physics*, World Scientific, 2002, pp. 717–728.

[78] A. Otte, J. Hose, R. Mirzoyan, A. Romaszkiewicz, M. Teshima, and A. Thea, "A measurement of the photon detection efficiency of silicon photomultipliers," *Nuclear Instruments and Methods in Physics Research Section A: Accelerators, Spectrometers, Detectors and Associated Equipment*, vol. 567, no. 1, pp. 360–363, 2006, Proceedings of the 4th International Conference on New Developments in Photodetection, ISSN: 0168-9002. DOI: https://doi.org/10.1016/j.nima.2006.05.145.

[79] C. Burgess, "Optical spectroscopy | detection devices*," in *Encyclopedia of Analytical Science (Second Edition)*, P. Worsfold, A. Townshend, and C. Poole, Eds., Second Edition, Oxford: Elsevier, 2005, pp. 438–443, ISBN: 978-0-12-369397-6. DOI: https://doi.org/10.1016/B0-12-369397-7/00431-3.

[80] M. Guilhaus, "Mass spectrometry | time-of-flight," in *Encyclopedia of Analytical Science (Second Edition)*, P. Worsfold, A. Townshend, and C. Poole, Eds., Second Edition, Oxford: Elsevier, 2005, pp. 412–423, ISBN: 978-0-12-369397-6. DOI: https://doi.org/10.1016/B0-12-369397-7/00347-2.

[81] A. G. Wright, *The photomultiplier handbook*. Oxford University Press, 2017.

[82] B. G. Streetman, "18 - semiconductors and transistors," in *Reference Data for Engineers (Ninth Edition)*, W. M. Middleton and M. E. Van Valkenburg, Eds., Ninth Edition, Woburn: Newnes, 2002, pp. 18-1-18–27, ISBN: 978-0-7506-7291-7. DOI: https://doi.org/10.1016/B978-075067291-7/50020-0.

[83] R. Weissman, G. Christenson, P. N. Grillot, Y.-C. Shen, and D. Wynne, "Light-emitting diodes," in *Encyclopedia of Physical Science and Technology (Third Edition)*, R. A. Meyers, Ed., Third Edition, New York: Academic Press, 2003, pp. 539–556, ISBN: 978-0-12-227410-7. DOI: https://doi.org/10.1016/B0-12-227410-5/00377-X.

[84] M. e. a. Grodzicka, "Effective dead time of apd cells of sipm," in *2011 IEEE Nuclear Science Symposium Conference Record*, IEEE, 2011, pp. 553–562.

[85] F. Acerbi and S. Gundacker, "Understanding and simulating sipms," *Nuclear Instruments and Methods in Physics Research Section A: Accelerators, Spectrometers, Detectors and Associated Equipment*, vol. 926, pp. 16–35, 2019, Silicon Photomultipliers: Technology, Characterisation and Applications, ISSN: 0168-9002. DOI: https://doi.org/10.1016/j.nima.2018.11.118.

[86] M. Calvi, P. Carniti, C. Gotti, C. Matteuzzi, and G. Pessina, "Single photon detection with sipms irradiated up to 10Î4cm2 1mevequivalent neutron fluence," *Nuclear Instruments and Methods in Physics Research Section A: Accelerators, Spectrometers, Detectors and Associated Equipment*, vol. 922, pp. 243–249, 2019, ISSN: 0168-9002. DOI: https://doi.org/10.1016/j.nima.2019.01.013.

[87] N. Thanh *et al.*, *Multi-pixel photon counter for operating the tabletop cosmic-ray detector under loosely controlled conditions*, Jun. 2021. DOI: 10.48550/arXiv.2106.08603.

[88] S. Gundacker and A. Heering, "The silicon photomultiplier: Fundamentals and applications of a modern solid-state photon detector," vol. 65, no. 17, 17TR01, Aug. 2020. DOI: 10 . 1088 / 1361 - 6560 / ab7b2d. [Online]. Available: https://dx.doi.org/10.1088/1361-6560/ab7b2d.

[89] J. Li, P. Fan, C. Zhu, M. Wang, Z. Wei, and Y. Xia, "Optimization of pulse shape discrimination based on frequency domain for sipm-based nail scintillator detector," *Journal of Instrumentation*, vol. 19, no. 03, P03014, 2024.

[90] H. Saleh, A. Yahya, M. Sayed, and M. Ashour, "Pulse shape discrimination techniques based on cross-correlation and principal component analysis," *International Journal of Computer Applications*, vol. 975, p. 8887, 2012.

[91] M. Hubbard, M. Taggart, and P. Sellin, "Exploration of fourier based algorithms and detector designs for pulse shape discrimination," *Nuclear Instruments and Methods in Physics Research Section A: Accelerators, Spectrometers, Detectors and Associated Equipment*, vol. 930, pp. 64–73, 2019.

[92] M. J. Balmer, K. A. Gamage, and G. C. Taylor, "Comparative analysis of pulse shape discrimination methods in a 6li loaded plastic scintillator," *Nuclear Instruments and Methods in Physics Research Section A: Accelerators, Spectrometers, Detectors and Associated Equipment*, vol. 788, pp. 146–153, 2015, ISSN: 0168-9002. DOI: https://doi.org/10.1016/j.nima.2015.03.089.

[93] H. Singh and R. Mehra, "Optimization of digital neutron-gamma discrimination methods in time and frequency domain," *Journal of Instrumentation*, vol. 19, no. 02, P02025, 2024.

[94] B. Seitz, D. Bennett, and F. Thomson, "Pulse shape discrimination of clyc, cllbc and ej-276 with sipm readout," in *EPJ Web of Conferences*, EDP Sciences, vol. 288, 2023, p. 06 010.

[95] N. Zaitseva *et al.*, "Pulse shape discrimination in impure and mixed single-crystal organic scintillators," *IEEE Transactions on Nuclear Science*, vol. 58, no. 6, pp. 3411–3420, 2011.

[96] A. T. Lintereur, J. H. Ely, J. A. Stave, and B. S. McDonald, "Neutron and gamma ray pulse shape discrimination with polyvinyltoluene," Pacific Northwest National Lab.(PNNL), Richland, WA (United States), Tech. Rep., 2012.

[97] P. Chuan *et al.*, "A study on the impact of pulse shaping parameters on zero-crossing method performance for neutron/gamma discrimination," *IEEE Transactions on Nuclear Science*, vol. 70, no. 11, pp. 2464–2470, 2023.

[98] C.-M. Chang, J. W. Cates, and C. S. Levin, "Time-over-threshold for pulse shape discrimination in a time-of-flight/depth of interaction phoswich pet detector," in *2016 IEEE Nuclear Science Symposium, Medical Imaging Conference and Room-Temperature Semiconductor Detector Workshop (NSS/MIC/RTSD)*, IEEE, 2016, pp. 1–3.

[99] J. Jung, Y. Choi, K. bom Kim, S. Lee, and H.-j. Choe, "An improved time over threshold method using bipolar signals," *Physics in Medicine & Biology*, vol. 63, no. 13, p. 135 002, 2018.

[100] R. Harn, A. Osovizky, Y. Kadmon, A. Manor, and M. Ghelman, "Analog pulse shape discrimination based on time duration and pulse height," in *EPJ Web of Conferences*, EDP Sciences, vol. 253, 2021, p. 11 008.

[101] A. Roy *et al.*, "Evaluation of the constant fraction time-over-threshold (cf-tot) method for neutron-gamma pulse shape discrimination," *Journal of Instrumentation*, vol. 17, no. 05, P05028, 2022.

[102] M. Lee *et al.*, "Pulse pileup correction method for gamma-ray spectroscopy in high radiation fields," *Nuclear Engineering and Technology*, vol. 52, no. 5, pp. 1029–1035, 2020, ISSN: 1738-5733. DOI: https://doi.org/10.1016/j.net.2019.12.003.

[103] P. Horowitz, W. Hill, and I. Robinson, *The art of electronics*. Cambridge university press Cambridge, 1989, vol. 2.

[104] Y. Zou, F. Villa, D. Bronzi, S. Tisa, A. Tosi, and F. Zappa, "Planar cmos analog sipms: Design, modeling, and characterization," *Journal of Modern Optics*, vol. 62, Jun. 2015. DOI: 10.1080/09500340.2015.1049572.

[105] J. Szyduczyński, D. Kościelnik, and M. Miśkowicz, "Time-to-digital conversion techniques: A survey of recent developments," *Measurement*, vol. 214, p. 112 762, 2023, ISSN: 0263-2241. DOI: https://doi.org/10.1016/j.measurement.2023.112762.

[106] B. Haraoubia, "2 - analog-to-digital and digital-to-analog converters," in *Non-Linear Electronics 2*, B. Haraoubia, Ed., Elsevier, 2019, pp. 99–190, ISBN: 978-1-78548-301-1. DOI: https://doi.org/10.1016/B978-1-78548-301-1.50002-7.

[107] D. Crecraft and S. Gergely, "7 - analog-to-digital and digital-to-analog conversion," in *Analog Electronics*, D. Crecraft and S. Gergely, Eds., Oxford: Butterworth-Heinemann, 2002, pp. 156–179, ISBN: 978-0-7506-5095-3. DOI: https://doi.org/10.1016/B978-075065095-3/50007-6.

[108] B. Wang, X. Sun, Y. Li, C. Li, Y. Du, and K. Hu, "A compact and highly integrated 128-channel fpga-based readout electronics for nuclear imaging application," *Nuclear Instruments and Methods in Physics Research Section A: Accelerators, Spectrometers, Detectors and Associated Equipment*, vol. 1064, p. 169 452, 2024, ISSN: 0168-9002. DOI: https://doi.org/10.1016/j.nima.2024.169452.

[109] B. Haraoubia, "1 - flip-flops," in *Non-Linear Electronics 2*, B. Haraoubia, Ed., Elsevier, 2019, pp. 1–97, ISBN: 978-1-78548-301-1. DOI: https://doi.org/10.1016/B978-1-78548-301-1.50001-5.

[110] V. J. Verma, A. K. Mishra, D. Vaithiyanathan, and B. Kaur, "Review of different flip-flop circuits and a modified flip-flop circuit for low voltage operation," in *2022 IEEE 3rd Global Conference for Advancement in Technology (GCAT)*, IEEE, 2022, pp. 1–5.

[111] R. Bannatyne and G. Viot, "Introduction to microcontrollers," in *WESCON/97 Conference Proceedings*, IEEE, 1997, pp. 564–574.

[112] D. V. Perepelitsa, "Johnson noise and shot noise," *Dept. of Physics, MIT*, 2006.

[113] R. F. Voss, "1/f (flicker) noise: A brief review," in *33rd Annual Symposium on Frequency Control*, IEEE, 1979, pp. 40–46.

[114] S. Hsu and R. Whittier, "Characterization of burst noise in silicon devices," *Solid-State Electronics*, vol. 12, no. 11, pp. 867–878, 1969, ISSN: 0038-1101. DOI: https://doi.org/10.1016/0038-1101(69)90044-6.

[115] *A standard fast, 12-stage, 51mm (2inch) tube*, XP2262, Rev. 1, Photonis, Sep. 1998.

[116] *Photomultiplier tube r1828-01*, R1828-01, Rev. 1, Hamamatsu, Feb. 2025.

[117] *Photomultiplier tube r7724*, R7724, Rev. 1, Hamamatsu, Jan. 2021.

[118] *Photomultiplier tube r1924a*, R1924A, Rev. 1, Hamamatsu, Oct. 2022.

[119] *Afbr-s4n44p164m 4-4 nuv-mt silicon photomultiplier array*, AFBR-S4N44P164M, Rev. 1, Broadcom, Jul. 2025.

[120] M. Kołodziej *et al.*, *First experimental test of a coded-mask gamma camera for proton therapy monitoring*, 2024. arXiv: 2501.00666 [physics.med-ph]. [Online]. Available: https://arxiv.org/abs/2501.00666.

[121] *Silicon photomultiplier (sipm) 4-side scaleable arrays*, ARRAYJ60035-64P-PCB, Rev. 9, SensL, Apr. 2023.

[122] *Psd plastic scintillator ej-276d and ej-276g*, EJ276, Rev. 1, Eljen, Aug. 2023.

[123] *High resolution dual mode cllbc scintillators*, CLLBC, Rev. 2, Scionix/BNC, Nov. 2018.

[124] *High resolution dual mode clyc scintillators*, CLYC, Rev. 2, Scionix/BNC, Jan. 2022.

[125] G. Bertrand, M. Hamel, S. Normand, and F. Sguerra, "Pulse shape discrimination between (fast or thermal) neutrons and gamma rays with plastic scintillators: State of the art," *Nuclear Instruments and Methods in Physics Research Section A Accelerators Spectrometers Detectors and Associated Equipment*, vol. 776, pp. 114–128, Mar. 2015. DOI: 10.1016/j.nima.2014.12.024.

[126] S. A. Dazeley *et al.*, "A 6li-doped pulse shape sensitive plastic scintillator for ton-scale detector applications,"

[127] W.-F. Su, Y.-C. Fu, and W.-P. Pan, "Thermal properties of high refractive index epoxy resin system," *Thermochimica Acta*, vol. 392-393, pp. 385–389, 2002, MATERIAL CHARACTERIZATION BY THERMAL ANALYSIS AND CALORIMETRY. A collection of Papers Scheduled for the 28th North American Thermal Analysis Society Conference Orlando, FL 4-6 October 2000., ISSN: 0040-6031. DOI: https://doi.org/10.1016/S0040-6031(02)00124-7.

[128] S. Hyeon, M. Hammig, and M. Jeong, "Improving light collection efficiency using partitioned light guide on pixelated scintillator-based gamma-ray imager," *Nuclear Engineering and Technology*, vol. 54, no. 5, pp. 1760–1768, 2022, ISSN: 1738-5733. DOI: https://doi.org/10.1016/j.net.2021.12.002.

[129] S. Querchfeld, J. Rautenberg, and K.-H. Kampert, "Development of a highly efficient pmt winston-cone system for fluorescence measurement of extensive air showers," 2015.

[130] M. Safari, F. Abbasi davani, and H. Afarideh, "Differentiation method for localization of compton edge in organic scintillation detectors," Oct. 2016. DOI: 10.22034/rpe.2020.104839.

[131] M. L. Lockhart, D. Henzlova, T. L. Burr, S. Croft, and A. Favalli, "252cf yield calibration method for nuclear material accountancy and safeguards practitioners," *Nuclear Instruments and Methods in Physics Research Section A: Accelerators, Spectrometers, Detectors and Associated Equipment*, vol. 1056, p. 168 648, 2023, ISSN: 0168-9002. DOI: https://doi.org/10.1016/j.nima.2023.168648.

[132] J. F. Dicello, W. Gross, and U. Kraljevic, "Radiation quality of californium-252," *Physics in Medicine and Biology*, vol. 17, no. 3, p. 345, 1972. DOI: 10.1088/0031-9155/17/3/301.

[133] S. Bastola, "Spontaneous fission spectrum of neutrons from 252 cf with kinetic energies less than 1 mev," 2012.

[134] C. H. Lee, J. Son, T. H. Kim, S. Lee, and Y.-K. Kim, "Measurement of neutron energy spectrum emitted by cf-252 source using time-of-flight method," in *Transactions of the Korean Nuclear Society Autumn Meeting*, 2016.

[135] R. Mcelroy Jr and S. Cleveland, "The dd neutron generator as an alternative to the am (li) isotopic neutron source in active neutron coincidence counting for international nuclear safeguards," Oak Ridge National Laboratory (ORNL), Oak Ridge, TN (United States), Tech. Rep., 2018.

[136] R. Lang *et al.*, "Characterization of a deuterium–deuterium plasma fusion neutron generator," *Nuclear Instruments and Methods in Physics Research Section A: Accelerators, Spectrometers, Detectors and Associated Equipment*, vol. 879, pp. 31–38, 2018, ISSN: 0168-9002. DOI: https://doi.org/10.1016/j.nima.2017.10.001.

[137] C. E. Moss, W. L. Myers, G. M. Sundby, D. L. Chichester, and J. P. Johnson, "Survey of neutron generators for active interrogation," Los Alamos National Laboratory (LANL), Los Alamos, NM (United States), Tech. Rep., 2017.

[138] R. Remetti, L. Lepore, and N. Cherubini, "Development and experimental validation of a monte carlo modeling of the neutron emission from a d-t generator," *Nuclear Instruments and Methods in Physics Research Section A: Accelerators, Spectrometers, Detectors and Associated Equipment*, vol. 842, pp. 7–13, 2017, ISSN: 0168-9002. DOI: https://doi.org/10.1016/j.nima.2016.10.031.

[139] A. Wehmeyer, R. Radel, and G. Kulcinski, "Optimizing neutron production rates from d-d fusion in an inertial electrostatic confinement device," *ANS Topical Meeting on Fusion Energy*, vol. 47, pp. 14–16, Oct. 2004. DOI: 10.13182/FST05-A861.

[140] P. V. Raja, "Performance studies of silicon and 4h-silicon carbide radiation detectors for fusion plasma diagnostics," Ph.D. dissertation, Feb. 2019. DOI: 10.13140/RG.2.2.12302.02880.

[141] P. Basu, R. Sarangapani, and B. Venkatraman, "Compact shielding design for 740 gbq 241am-be neutron source transport container," *Radiation Physics and Chemistry*, vol. 170, p. 108 670, 2020.

[142] A. Waheed *et al.*, "Optimization of moderator assembly for neutron flux measurement: Experimental and theoretical approaches," *Nuclear Science and Techniques*, vol. 28, p. 61, Sep. 2016. DOI: 10.1007/s41365-017-0213-z.

[143] *720 digitizer family*, DT5720, Rev. 3, CAEN, Nov. 2019.

[144] *730 digitizer family*, DT5730, Rev. 6, CAEN, Nov. 2019.

[145] *742 digitizer family*, DT5742, Rev. 3, CAEN, Dec. 2019.

[146] R. Coulon, V. Gressier, and C. Michotte, "Test of a digitizer to process the pulse signal from the 3 photomultiplier tubes of a tdcr liquid scintillation counter," *Applied Radiation and Isotopes*, vol. 192, p. 110 598, 2023, ISSN: 0969-8043. DOI: https://doi.org/10.1016/j.apradiso.2022.110598.

[147] R. Guida, B. Mandelli, and M. Corbetta, "Effects of gas mixture quality on gem detectors operation," in *Journal of Physics: Conference Series*, IOP Publishing, vol. 1498, 2020, p. 012 036.

[148] V. Buridon *et al.*, "Natif radiation portal monitor performances optimization by means of multi-parametric analysis," in *Conférence internationale R&I CBRNE*, 2024.

[149] *Lmh6629 ultra-low noise, high-speed operational amplifier with shutdown*, LMH6629, Rev. 1, Texas Instruments, Dec. 2014.

[150] *Opa820 unity-gain stable, low-noise, voltage-feedback operational amplifier*, OPA820, Rev. 1, Texas Instruments, Dec. 2016.

[151] *280mhz, 2.9ns comparatorfamily with rail-to-rail inputsvand cmos outputs*, LTC6752, Rev. C, Linear Technology, Nov. 2014.

[152] *Sn74lvc2g74 single positive-edge-triggered d-type flip-flop with clear and preset*, SN74LVC2G74, Rev. 1, Texas Instruments, Oct. 2021.

[153] *Small signal mosfet*, 2N7002E, Rev. 1, ONSemi, Apr. 2007.

[154] *Sn74lvc1g14 single schmitt-trigger inverter*, SN74LVC1G14, Rev. 1, Texas Instruments, Oct. 2025.

[155] *Sn74lvc1g08 single 2-input positive-and gate*, SN74LVC1G08, Rev. 1, Texas Instruments, May 2019.

[156] *Tdc7200 time-to-digital converter for time-of-flight applications in lidar, magnetostrictive and flow meters*, TDC7200, Rev. 1, Texas Instruments, Mar. 2016.

[157] *Surface-mount oscillator*, XO57CRECNA16M, Rev. 1, Vishay Dale, Jul. 2025.

[158] *Time-to-digital converter for time-of-flight applications in lidar, magnetostrictive and flow meters*, TDC7200, Rev. 1, Texas Instruments, Feb. 2016.

[159] M. Engelhardt, "Ltspice/switcher cad iii," 2007.

[160] F. Acerbi and S. Gundacker, "Understanding and simulating sipms," *Nuclear Instruments and Methods in Physics Research Section A: Accelerators, Spectrometers, Detectors and Associated Equipment*, vol. 926, pp. 16–35, 2019, Silicon Photomultipliers: Technology, Characterisation and Applications, ISSN: 0168-9002. DOI: https://doi.org/10.1016/j.nima.2018.11.118.

[161] *Tdc7201 time-to-digital converter for time-of-flight applications in lidar, range finders, and adas*, TDC7201, Rev. 1, Texas Instruments, May 2016.

[162] M. Wiebusch, "Design and implementation of a compact analog constant fraction discriminator for high-resolution timing in gamma-ray spectroscopy," *Journal of Instrumentation*, vol. 19, no. 12, p. C12009, 2024.

[163] F. Ferrulli, N. Dinar, L. G. Manzano, M. Labalme, and M. Silari, "Characterization of stilbene and ej-276 scintillators coupled with a large area sipm array for a fast neutron dose rate detector," *Nuclear Instruments and Methods in Physics Research Section A: Accelerators, Spectrometers, Detectors and Associated Equipment*, vol. 1010, p. 165 566, 2021.

[164] F. Ren *et al.*, "Detection of 10 to 300 kev fast neutron using clyc, cllb and cllbc scintillators," *Journal of Instrumentation*, vol. 19, no. 08, P08025, 2024.

[165] N. Kaneshige *et al.*, "Cllbc high temperature scintillation characterization and detector integration," *IEEE Transactions on Nuclear Science*, vol. 70, no. 7, pp. 1357–1361, 2023.

[166] F. Shen, Y. Pan, Q. Fu, S. Lin, T. Huang, and W. Wang, "Psd performance of ej-276 and ej-301 scintillator readout with sipm array," *Nuclear Instruments and Methods in Physics Research Section A: Accelerators, Spectrometers, Detectors and Associated Equipment*, vol. 1039, p. 167 148, 2022.

[167] C. Weber, I. Fabry, V. Huhn, A. Siepe, and W. von Witsch, "Accurate determination of the fast-neutron detection efficiency for organic scintillators using a collimated neutron beam," *Nuclear Instruments and Methods in Physics Research Section A: Accelerators, Spectrometers, Detectors and Associated Equipment*, vol. 488, no. 1, pp. 307–313, 2002, ISSN: 0168-9002. DOI: https://doi.org/10.1016/S0168-9002(02)00432-1.